Investigations of the Synthesis, Growth, Assembly and Properties of Inorganic and Carbon Nanostructures

A Thesis

Submitted for the Degree of

DOCTOR OF PHILOSOPHY

by

NEENU VARGHESE

CHEMISTRY AND PHYSICS OF MATERIALS UNIT
JAWAHARLAL NEHRU CENTRE FOR ADVANCED SCIENTIFIC RESEARCH
(A Deemed University)
Bangalore – 560 064

SEPTEMBER 2011

DECLARATION

I hereby declare that the matter embodied in the thesis entitled "**Investigations of the Synthesis, Growth, Assembly and Properties of Inorganic and Carbon Nanostructures**" is the result of investigations carried out by me at the Chemistry and Physics of Materials Unit, Jawaharlal Nehru Centre for Advanced Scientific Research, Bangalore, India under the supervision of Prof. C.N.R. Rao and it has not been submitted elsewhere for the award of any degree or diploma.

In keeping with the general practice in reporting scientific observations, due acknowledgment has been made whenever the work described is based on the findings of other investigators.

Neenu Varghese

CERTIFICATE

I hereby certify that the matter embodied in this thesis entitled "**Investigations of the Synthesis, Growth, Assembly and Properties of Inorganic and Carbon Nanostructures**" has been carried out by Ms. Neenu Varghese at the Chemistry and Physics of Materials Unit, Jawaharlal Nehru Centre for Advanced Scientific Research, Bangalore, India under my supervision and it has not been submitted elsewhere for the award of any degree or diploma.

Prof. C.N.R. Rao
(Research Supervisor)

Acknowledgements

I am extremely grateful to Prof. C. N. R. Rao, FRS for suggesting me research problems and guiding me throughout. He has been a constant source of inspiration for me. I greatly admire his enthusiasm towards science. I express my hearty gratitude to him for giving me an opportunity to work under his guidance.

I would like to express my sincere thanks to Dr. A. Govindaraj who has helped me a great deal in carrying out various experiments.

I would like to thank JNCASR for providing me all the facilities.

I thank the past and present chairmen of CPMU, Prof. C. N. R. Rao and Prof. G. U. Kulkarni for providing all the facilities in the department.

I am thankful to Basavaraj, Usha Madam, Anil, Vasu, Selvi, Srinath, Srinivas, Mahesh, Basavaraj and Srinivasa Rao for their help with the various characterization techniques. I am thankful to Prof. A. Sundaresan for magnetic measurement facility and Dr. Ranjan Datta for TEM measurements.

I thank Prof. A.K. Sood, Dr. Prabal Maiti, Prof. Milan Sanyal for colloborative work.

I am thankful to the faculty members of IISc and JNC for their courses. In particular, I would like to thank Prof. D. D. Sharma, Prof. S. Ramasesha, Prof. Uday Maitra, Prof. T. N. Guru Row, Prof. E. D. Jemmis, Prof. S. chandrashekar, Prof. S. chandrashekaran, Prof. S. A. Shivasankar, Prof. S. Yasonath, Prof. B. Bagchi, Prof. M. S. Hegde, Prof. S. Ramakrishnan, Prof. A. M. Umarji, Prof. P.

K. Das, Prof. A. G. Samuelson, Prof. S. Ranganathan from IISc and Prof. M. Eswaramoorthy, Prof. A. Sundaresan, Prof. G. U. Kulkarni, Prof. Swapan Pati and Dr.Tapas Kumar Maji from JNC.

I thank Mr. Nitesh for help in magnetic measurements and Dr. Prashant for electrical mesurements.

I would like to thank Dr. Kanishka, Dr. Vivek, Dr. Nusrat, Umesh and Hitesh for working with me in various research problems.

I would like to thank all my lab members Vivek, Chandu, Kalyani, Bhat, Tiru, Gomathi, Rakesh, Claudy, Sahu, Kanishka, Late, Sandeep, Sundarayya, Prashant, Subrahmanyam, Leela, Basant, Anupama, Barun, Urmi, Kalyan, Manu, Matte, Shashi, Gopal, Ajmala, Moses, Prashant, Manju, Bello, Umesh, Nusrat and Hitesh for their fruitful discussions, help and co-operation.

I would like to thank my Int Ph.D batchmates in JNC and IISc for making the course work time wonderful.

I am thankful to computer lab staff for their help.

I would like to thank Mrs. Rao and Mr. Sanjay for encouraging words and hospitality . I am thankful to all academic staff members and office members.

I am thankful to all work shop members.

Special thanks to all my collaborators and teachers.

I would like to thank my friends Limi, Jilu, Jiby, Shameema, Linta, Nicky, Neena, Reji, Lakshmi, Vivek, Leela, Subbu, Josena, Datta, Urmi, Nitesh, Kalyan, Guru, Madhu, Raju, Pranab, Anupama, Kalyani, Sonia, Gopal, Shashi, Ajmala, Claudy, Gomathi, Selvi, Ashly, Krishnan, Priya and all JNC friends.

Heartfelt thanks to my parents, parents-in-law, Minu, Basil, Arun, Annu and Aiswarya for their love and support.

I am thankful to Ashik, my husband for being there for me always.

Preface

The thesis contains seven chapters of which the first chapter gives a brief overview of the synthesis, properties and self-assembly of nanomaterials. The other six chapters deal with various aspects of nanomaterials such as synthesis, growth kinetics, assembly and properties of inorganic and carbon nanostructures.

Chapter 2 deals with the study of growth kinetics of metallic and semiconducting nanomaterials by a combined use of small angle X-ray scattering, transmission electron microscopy and various spectroscopic techniques. The growth of nanocrystals of gold, CdSe, CdS and platinum has been studied to check the validity of Ostwald ripening to be the growth mechanism. The role of the capping agent (surface) has been examined in the case of Pt nanocrystal growth. Assembly of gold nanorods and the disintegration of gold nanocrystalline films have been investigated by isothermal titration calorimetry (ITC) and UV-vis spectroscopy is described in chapter 3.

Chapter 4 deals with the selectivity in the interaction of electon-donor and -acceptor molecules with graphene and single walled carbon nanotubes studied using ITC and Raman spectroscopy. Electron-acceptor molecules are found to interact more strongly with graphene and SWNTs than the -donor molecules. Study on the binding of DNA nucleobases and nucleosides with graphene by ITC is described in chapter 5. Purines generally bind more strongly.

Synthesis of cadmium oxide nanostructures and magnetic nickel nanofilms

formed at the organic-aqueous interface and characterizations are described in chapter 6. Chapter 7 deals with the synthesis and disintegration of fibrillar aggregates formed by the amyloid peptide structural motif diphenylalanine, insulin and bovine serum albumin at the organic-aqueous interface.

Contents

CHAPTER 1

Nanomaterials: A Brief Overview

1.1 Introduction

Nanoscience involves the study of properties and phenomena on the scale of 1-100 nm (1 nm = 10^{-9} m). Nanotechnology involves the design, fabrication and application of nanomaterials, and the fundamental understanding of the relationships between physical properties or phenomena and materials dimensions. On nanometer scale, materials or structures may possess new physical properties or exhibit new physical phenomena which vary with change in their size and shape. Nanoscale materials often exhibit behavior that is intermediate between that of a macroscopic solid and an atomic or molecular species. This is partly due to the high surface to volume ratio of these materials and partly due to the size induced quantum confinement of the electrons. Due to these special properties, the research on this area is evolving and expanding very rapidly.

The study on nanomaterials is a new subject although they were used from ancient times. Chinese are known to use Au nanoparticles as an inorganic dye to introduce red color into their ceramic porcelains more than thousand years ago [1]. Colloidal gold was used for treatment of arthritis. The secret behind the color of the Lycurgus cup, a roman glass artifact dated to 4 AD, that appears red in transmitted light and green in reflected light was found to be due to Au and Ag nanocrystals in glass. Use of colloidal gold has a long history, though a comprehensive study

on the preparation and properties of colloidal gold was done in the middle of the 19th century by Michael Faraday [2]. He established that several dyes were indeed made of metal particles. After a thorough study of gold sols, Faraday concluded *". . . the gold is reduced in exceedingly fine particles which becoming diffuse, produce a beautiful fluid. . . the various preparations of gold, whether ruby, green, violet or blue. . . consist of that substance in a metallic divided state"*. Thus, colloidal metal particles in sols came to be known as divided metals. Figure 1.1 shows gold colloids prepared by Faraday. Now nanometer scale structures represent a rapidly expanding and challenging area of research that crosses the borders between many areas of physical sciences and engineering due to the ability to see and manipulate matter on the nanoscale and understanding of atomic scale interactions.

Figure 1.1: Gold colloids prepared by Michael Faraday

In a metal, electrons are highly delocalized over large space (i.e. least confined). This is a result of the fact that the separation between the valence and conduction bands vanishes, giving the metal its conducting properties. As we decrease the size of the metal and confine its electronic motion, the separation between the valence and the conduction bands becomes comparable to or larger than kT, and the

metal becomes a semiconductor. More confinement increases the energy separation further, and the material becomes an insulator. In the size domain at which the metal-to-insulator transition occurs, new properties are expected to be observed which are possessed neither by the metal nor by the molecules or atoms forming the metal [3].

1.2 Propertis of nanomaterials

1.2.1 Electronic properties

Bulk metals possess a partially filled electronic band and their ability to conduct electrons is due to the availability of a continuum of energy levels above E_F , the fermi level. These levels can easily be populated by applying an electric field and the electrons now behave as delocalized Bloch waves ($\lambda \approx$ 5-10 $\mathring{A}$) [4]. When a metal is divided finely, the continuum of the electronic states breaks down and the sample ultimately becomes insulating. The discreteness of energy levels do not physically manifest themselves as long as the gap is less than k_bT , the thermal energy at temperature T . The discreteness of the levels can be measured in terms of average spacing between the successive quantum levels, δ, given by

$$\delta = \frac{4E_F}{3n_e}$$

and is known as the Kubo gap [5]. Here, n_e is the number of valence electrons in the cluster (a contribution of one valence electron per constituent atom is assumed). In the case of semiconductors, a reduction in the size of the system causes the energy levels at the band edge to become discrete, with interlevel spacings similar to metals. This effectively increases the bandgap of the semiconductor [6]. The issues

at hand are sketched schematically in Figure 1.2. Additional complications are

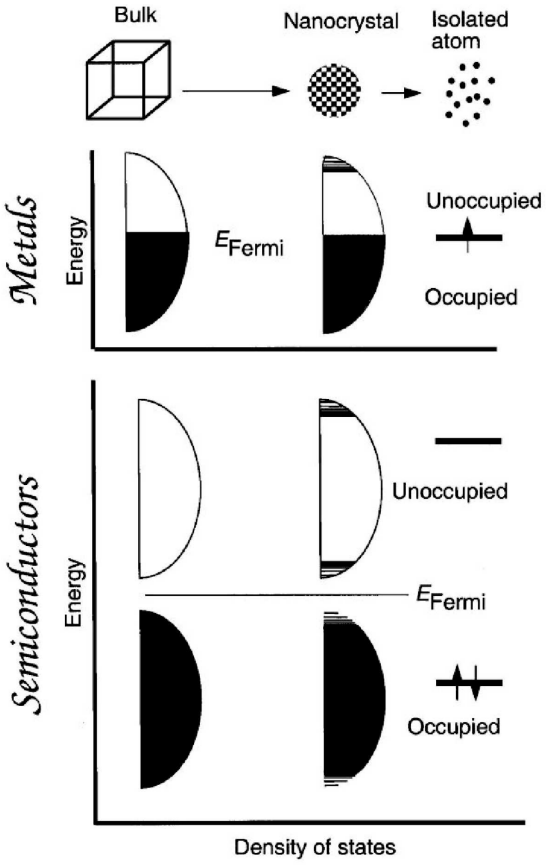

Figure 1.2: Schematic illustration of the changes in the electronic structure accompanying a reduction in size, in metals and semiconductors [7].

introduced by the strongly directional covalent bonds present in a semiconductor. Accompanying the appearance of the discrete levels are other consequences such as the change from metallic to van der Waals type of bonding, lowering of the melting point, and perhaps most significantly, a metal-insulator transition. The whole gamut of such changes are generally called as quantum size effects [8].

1.2.2 Optical properties

In noble metals, the decrease in size below the electron mean free path (the distance the electron travels between scattering collisions with the lattice centers) gives rise to intense absorption in the visible-near UV [9–12]. This results from the coherent oscillation of the free electrons from one surface of the particle to the other and is called the surface plasmon absorption. A schematic illustration of the electric field component of an incoming light wave inducing a polarization of the free or itinerant electrons with respect to the heavier core is shown in Figure 1.3 [11]. This gives these metallic nanoparticles brilliant color in colloidal solution that intrigued scientists in the 17th century. It was Faraday who showed that the intense color is due to metallic gold in colloidal form [2]. In 1908 Mie explained the phenomena by solving Maxwells equations for the absorption and scattering of electromagnetic radiation by spherical metallic particles [13]. This theory has been used to calculate the spectra of particles smaller than the wavelength of light for nanoparticles whose metallic dielectric function is known and which are embedded in an environment of known dielectric constant [10, 14, 15]. Colloidal metallic nanoparticles are of interest because of their use as catalysts, photocatalysts, sensors, ferrofluids, and because of their applications in optoelectronics, electronic and magnetic devices [16–19].

The shape dependence of the surface plasmon absorption was studied by Gans [19]. For nanorods two absorption bands are seen: one is due to the coherent electronic oscillation along the short axis (the transverse absorption band), and the other (the longitudinal band) is at a longer wavelength, which is more intense and results from the coherent electronic oscillation along the long axis. UV-Vis spectrum of the gold nanorods of aspect ratio 4.1 is shown in Figure 1.4 [20]. The

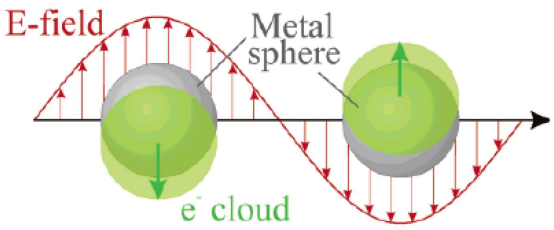

Figure 1.3: Schematic of plasmon oscillation for a sphere, showing the displacement of the conduction electron charge cloud relative to the nuclei [11].

absorption maximum of the latter band is sensitive to the rod length. Transverse band appear at a lower wavelength ($\approx$ 520 nm) and longitudinal shifts to longer wavelengths as increase in length of the nanorods.

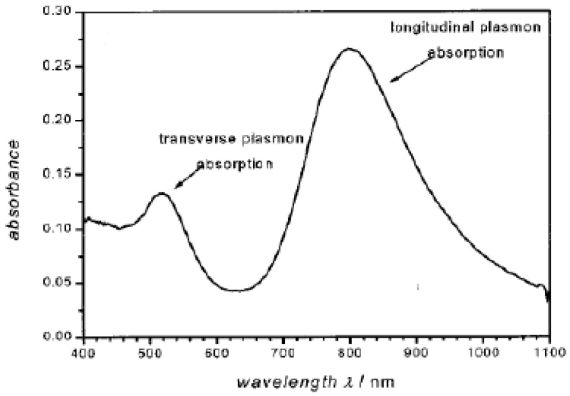

Figure 1.4: UV-Vis spectrum of gold nanorods of aspect ratio 4.1 [20].

Figure 1.5 shows colors of gold nanorods of different aspect ratios and the corresponding optical spectra [21]. This absorption is over 1000 times stronger than the strongest absorption of molecular dyes and is responsible for enhancing other linear and nonlinear processes involving the interaction of these nanoparticles with electromagnetic radiation [22], e.g., fluorescence, surface-enhanced Raman scattering, and second harmonic generation. Furthermore, the fact that the absorption intensity and wavelength maximum of these nanocrystals are sensitive to the dielectric

constant of the environment makes them potentially useful as sensors.

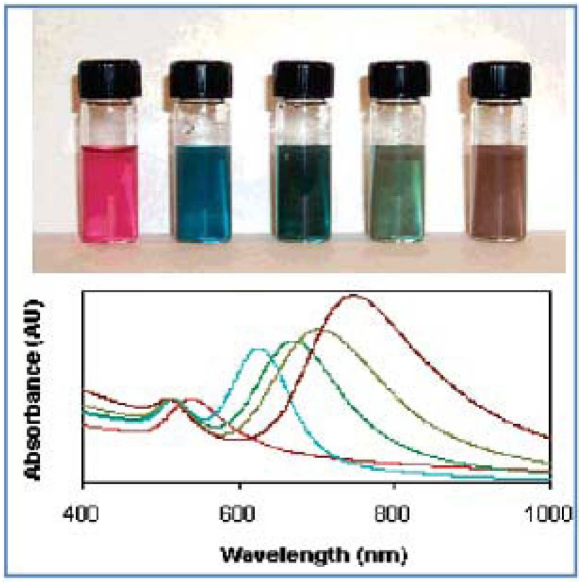

Figure 1.5: Image of photochemically prepared gold nanorods solution, and corresponding UV-Vis spectrum [21].

In semiconductor nanocrystals, changes in optical properties result from the further confinement of the electronic motion to a length scale that is comparable to the mean free path of the electrons in the bulk material. Reduction in nanocrystal-size beyond the bulk excitonic Bohr radius induces a larger band gap that causes blue-shifts in the absorption wavelength [23]. The absorption band can be systematically varied across ranges of a few 100 nm by changing the size of the semiconductor nanocrystal. As an example, the absorption spectra of CdSe nanocrystals of various sizes are shown in Figure 1.6 [24]. The excitonic nature of the absorption band permits direct correlation of the band gap of the semiconductor nanocrystal with the absorption edge.

In addition to the interesting absorption properties, the semiconductor nanocrystals also exhibit strong photoluminescence (PL) properties due to the nonradiative recombination of the electron-hole pairs. The emission from monodisperse semi-

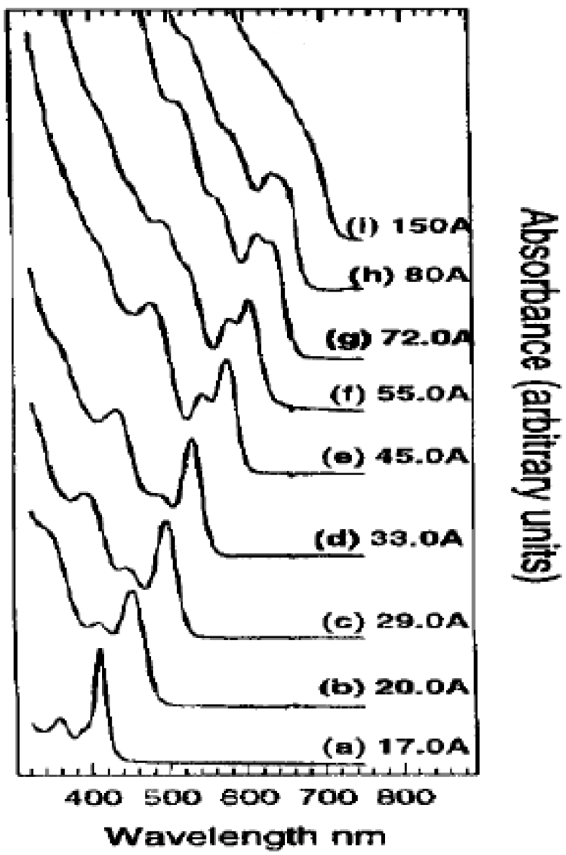

Figure 1.6: Optical absorption spectra of CdSe nanocrystals with varying diameters [24].

conductor nanocrystals such as CdSe is intense, narrow and can be brought about by excitation in a broad range of wavelengths [25]. The emission can be tuned by altering the diameter of the nanocrystal. Fluorescence from semiconductor nanocrystals are superior to conventional dyes in several respects. The emission peaks are intense, narrow, and are tunable. Further, Stokes shifts much larger than those of conventional dyes are possible. Employing nanocrystals of different sizes, but of the same material, emission at widely different wavelengths can be brought about by excitation at a single wavelength. The earlier factors have led to the exploration of a wide range of applications for luminescent semiconductor nanocrystals. For example, CdSe nanocrystals with green and red emission (of 3

and 5 nm diameter, respectively) can be used to produce white light by mixing them with the blue emission from an LED. White emission is also observed from extremely small CdSe nanocrystals [26]. These properties have led to the exploration of a wide range of applications for luminescent semiconductor nanocrystals [27].

1.2.3 Magnetic properties

Ferromagnetic particles become unstable when the particle size reduces below a certain size, since the surface energy provides a sufficient energy for domains to spontaneously switch polarization directions. As a result, ferromagnetics become paramagnetics. However, nanometer sized ferromagnetic turned to paramagnetic behaves differently from the conventional paramagnetic and is referred to as superparamagnetics. Nanometer sized ferromagnetic particles of up to N = 10^5 atoms ferromagnetically coupled by exchange forces, form a single domain [28], with a large single magnetic moment μ with up to 10^5 Bohr magnetons, μ_B. Bean and Livingston demonstrated that these clusters or particles at elevated temperatures can be analogously described as paramagnetic atoms or molecules, however with much larger magnetic moments [29]. The magnetization behavior of single domain particles in thermodynamic equilibrium at all fields is identical with that of atomic paramagnetism, except that an extremely large moment is involved, and thus large susceptibilities are involved. Also, the magnetization curve must show no hysteresis, since that is not a thermal equilibrium property.

Superparamagnetism was first predicted to exist in small ferromagnetic particles below a critical size by Frankel and Dorfman [30]. This critical size was estimated to be 15 nm in radius for a spherical sample of the common ferromag-

netic materials [31]. Superparamagnetic behavior is caused by thermal flipping of the anisotropic barrier to magnetization reversal. Below a certain temperature, called the blocking temperature, temperature-induced flipping or relaxation can be arrested and the nanocrystals acquire a finite coercivity. In Figure 1.7, magnetic measurements indicating size-dependent changes in the blocking temperature of $CoFe_2O_4$ nanoparticles are shown.

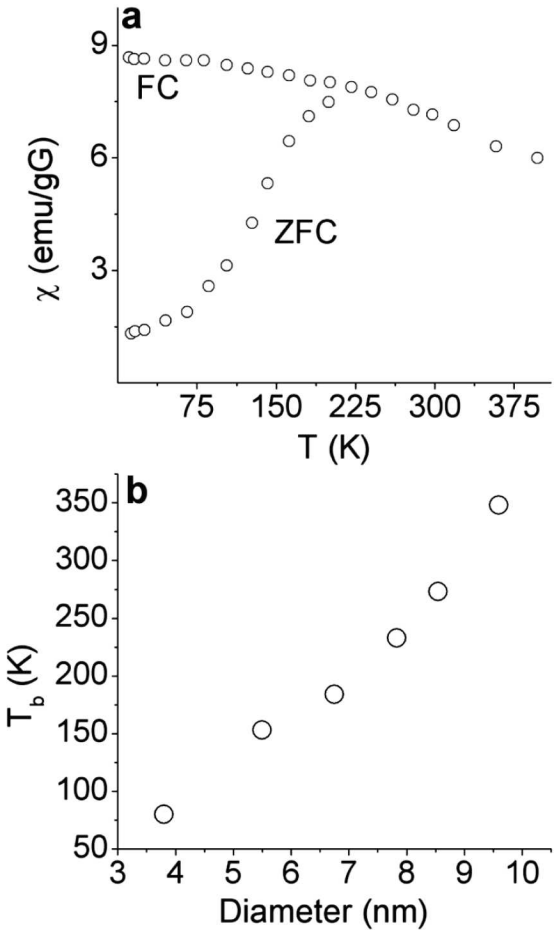

Figure 1.7: (a) Magnetic susceptibility vs. temperature for $CoFe_2O_4$ nanoparticles under field cooled and zero-field cooled conditions. The applied field is 2,000 G. (b) shows the variation of blocking temperature (T_b) with diameter of nanoparticles [32]

Many metal oxide nanoparticles are known to show evidence for the presence of

ferromagnetic interactions at low temperatures. This is specially true of nanoparticles of antiferromagnetic oxides such as MnO, CoO, and NiO [33, 34]. A layer of uncompensated spins at the surface is responsible for the ferromagnetic interactions observed at low temperatures in normally antiferromagnetic oxides. What one normally observes is a divergence in the zero-field cooled and field cooled magnetization data at low temperatures. The materials show magnetic hysteresis below a blocking temperature typical of superparamagnetic materials. The blocking temperature generally increases with the particle size.

It has been found recently that nanoparticles of all metal oxides, including those which are normally nonmagnetic such as Al_2O_3, SnO_2, and TiO_2, show ferromagnetic features in terms of magnetic hysteresis at room temperature due to surface effects [35].

1.3 Synthesis of nanocrystals

Many techniques, including both top-down and bottom-up approaches, have been developed and applied for the synthesis of nanoparticles. Top-down methods rely on continuous breakup of bulk matter while the bottom-up methods builds up nanomaterials from their constituent atoms. The top-down and bottom-up approaches can also be considered as physical and chemical methods, respectively. Many of the physical methods involve the evaporation of a solid material to form a supersaturated vapor from which homogenous nucleation of nanoparticles occurs. In these methods, the size of the particles is controlled by temporarily inactivating the source of evaporation, or by slowing the rate by introducing gas molecules to collide with the particles. The growth generally occurs rapidly, from milliseconds to seconds, requiring a precise control over experimental parameters. Different va-

rieties of the physical methods employed for the synthesis of nanocrystals include inert gas condensation, arc discharge, ion sputtering, laser ablation, pyrolysis etc.

Chemical methods have emerged to be indispensable for synthesizing nanocrystals of various types of materials. These methods are generally carried out under mild conditions and are relatively straightforward. Nanodimensional materials in the form of embedded solids, liquids, and foams have also been prepared by chemical means and such materials have been in use for some time. Any chemical reaction resulting in a sol consists of three steps - seeding, particle growth, and growth termination by capping. The relative rates of the steps can be altered by changing parameters such as concentrations and temperature.

Metal nanocrystals by reduction

A variety of reducing agents are used to reduce soluble metal salts to obtain the corresponding metals. By terminating the growth with appropriate surfactants or ions, metal nanoparticles are produced. Nanocrystals of a variety of metals have been made by borohydride reduction [36]. The basic reaction involves the hydrolysis of the borohydride accompanied by the evolution of hydrogen. Thus, Pt nanocrystals with mean diameter 2.8 nm were prepared by the reduction of chloroplatinic acid with sodium borohydride. Homiyama and coworkers [37] made Cu sols by the borohydride reduction of Cu salts. Green and O'Brien [38] prepared Cr and Ni nanoparticles by carrying out the reduction with Li or Na borohydride at high temperatures in coordinating solvents. Schiffrin and coworkers [39] developed a two-phase method to reduce noble metals. This method, popularly known as the Brust method, has been widely used to prepare organosols. In this method, aqueous metal ions are transferred to a toluene layer by the use of tetraoctylammonium

bromide, a phase transfer catalyst which is also capable of acting as a stabilizing agent. The Au complex transferred to toluene is reacted with alkanethiols to form polymeric thiolates. Aqueous borohydride is added to this mixture to bring about the reduction that is modulated by the interface of toluene and water. The thiol molecules also serve as capping agents.

The citrate route to colloidal Au, first described by Hauser and Lynn [40], is a popular method to prepare Au hydrosols. Synthesis by the citrate method involves the addition of chloroauric acid to a boiling solution of sodium citrate [36]. A wine red color indicates the onset of reduction. The average diameter of the nanoparticles can be varied over a range of 10-100 nm by varying the concentration ratio between chloroauric acid and sodium citrate. The citrate method has been extended to synthesize Pt and Ag nanoparticles [41, 42].

The reduction with alcohols has been used as a method to prepare metallic nanocrystals. Palladium acetate refluxed with ethanol in the presence of PVP yields Pd nanocrystals of 6 nm diameter [43, 44]. Teranishi and Miyake [45] have prepared monodisperse PVP covered Pd nanocrystals of various sizes in the 25nm range, by employing ethanol as the reducing agent and varying its power by diluting with water. Nanoparticles of Ag, Au, Pd, and Cu have been prepared by ethyl alcohol reduction of metal salts under refluxing conditions in the presence of PVP [45]. Other metal sols prepared by alcohol reduction include Pt, Au, and Rh [46]. Particles of Co, Ni, Cu, Au, Ag, and their alloys in the size range of 100 nm to a few microns have been obtained by polyol method [47–49].

Exceedingly fine Au nanoparticles with diameters between 1 and 2 nm have been made by reduction of $HAuCl_4$ with tetrakishydroxymethylphosphonim chloride (THPC) [50]. THPC also acts as a capping agent. Similarly, Au nanoparticles, free from surfactants, have been synthesized by the reduction of the aurate ion by

sodium napthalenide in diglyme [51]. Cu and Pt nanoparicles have been made by using hydrazine hydrate as a reducing agent [52]. By using tetrabutylammonium borohydride or its mixture with hydrazine, Peng and coworkers [53] have obtained monodisperse nanocrystals of Au, Cu, Ag and Pt.

Solvothermal synthesis

The solvothermal method provides a means of using solvents at temperatures well above their boiling points, by carrying out the reaction in a sealed vessel. The pressure generated in the vessel due to the solvent vapors elevates the boiling point of the solvent. Typically, solvothermal methods make use of solvents such as ethanol, toluene, and water, and are widely used to synthesize zeolites, inorganic open-framework structures, and other solid materials. Qian and coworkers [54] have reported several solvothermal routes to chalcogenide nanocrystals. CdS nanocrystals of 6 nm diameter have been made using cadmium sulphate/nitrate as the Cd source, thiourea as the S source and ethylene glycol as the solvent. The reaction was carried out for 12 h at 180 °C. Chen and Fan [55] have prepared transition metal dichalcogenides (MS_2; M = Fe, Co, Ni, Mo; S = S or Se) with diameters in the range 4-200 nm by a hydrothermal route (water as solvent). Fe, Co, and Ni chalcogenides were obtained by treating the corresponding halide with $Na_2S_2O_3$ (sodium thiosulphate) or Na_2SeSO_3 (sodium selenosulphate) for 12 h at 140-150 °C. Mo chalcogenides were prepared starting from Na_2MoO_4, sodium thio or seleno sulphate and hydrazine.

CdSe nanocrystals have been prepared solvothermally by reacting Cd stearate with elemental Se in toluene in the presence of tetralin (see Figure 1.8) [56]. The key step in the reaction scheme is the aromatization of tetralin to naphthalene in

the presence of Se, producing H_2Se.

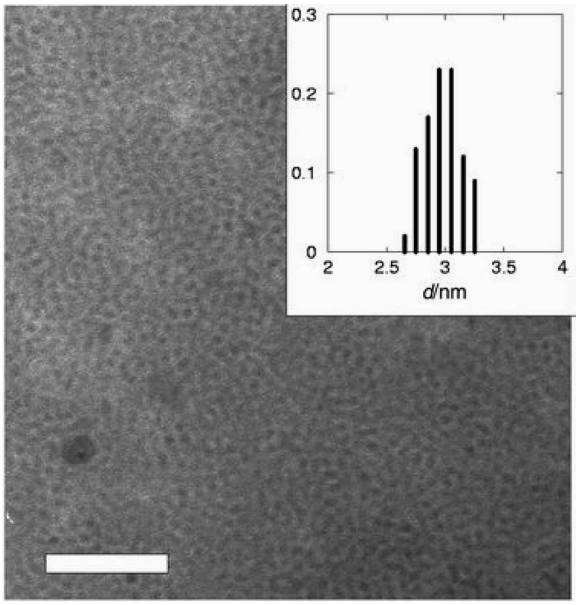

Figure 1.8: TEM image of CdSe nanocrystals synthesized by solvothermal method. The scale bar corresponds to 50 nm. The inset shows a histogram of particle size distribution [56].

CdS nanocrystals are similarly prepared by the reaction of a Cd salt with S in the presence of tetralin. Wei *et al.* report a green synthetic route for CdSe nanoparticles in aqueous solution using Se powder as the selenium source [57]. CdS nanocrystals of $\approx$ 6 nm diameter have also been prepared in an aqueous solution containing pepsin at room temperature [58]. Nanocrystals of chalcogenides can be prepared under solvothermal conditions starting with the elements. Thus, ZnSe nanocrystals of 12-16 nm are prepared by reacting the elements in pyridine. By reacting Zn and Se in ethylenediamine, a complex ZnSe(en) is obtained [59]. This compound gets thermally decomposed to yield ZnSe nanoparticles. ZnS nanoparticles in the 3-18 nm size range have been obtained by Qian and coworkers [60] by treating Zn and S in pyridine. Sardar and Rao [61] have prepared GaN nanoparticles of various sizes under solvothermal conditions, employing gallium cupferronate

($Ga(C_6H_5N_2O_2)_3$) or chloride ($GaCl_3$) as the gallium source and hexamethyldisilyzane as the nitriding agent and toluene as solvent.

Photochemical synthesis

Photochemical synthesis of nanoparticles is carried out by the light-induced decomposition of a metal complex or the reduction of a metal salt by photogenerated reducing agents such as solvated electrons. The former is called photolysis and the latter radiolysis. The formation of photographic images on a AgBr film is a familiar photolysis reaction. Henglein, Belloni, and their coworkers have pioneered the use of photolysis and radiolysis for the preparation of nanoscale metals [62]. Metals such as Cd and Tl have been obtained by photolysis. PVP-covered Au nanocrystals are produced by the reduction of $HAuCl_4$ in formamide by UV-irradiation [63]. The reaction is free radical mediated, with the radicals being generated by photodegradation of formamide. This provides a route to ion-free reduction of $HAuCl_4$. Radiolysis of Ag salts in the presence of polyphosphates produces extremely small clusters that are stable in solution for several hours.

Arrested precipitation

Nanocrystals can be obtained from solutions that precipitate the bulk matter under conditions unfavorable for the growth of particulates in the precipitate. For example, the precipitation of metal salts by chalcogens can be arrested by employing a high pH. The groups of Brus, Henglein, and Weller have prepared CdS nanocrystals by adopting this strategy [64–66]. Typically, $CdSO_4$ is reacted with $(NH_4)_2S$ in water at high pH to obtain CdS particles of diameter around 5 nm. Other sulfur sources such as H_2S and Na_2S are also used to obtain CdS. Capping agents (e.g.,

sodium polyphosphate) stabilize such dispersions. In addition to water, methanol, acetonitrile and such solvents can be used to obtain CdS and ZnS nanocrystals by arrested precipitation [67]. Better control over particle size is attained by the use of stronger capping agents. Preparation of water soluble thiolate capped PbS nanocrystals has been investigated by Cornacchio *et al.* [68].

Thermolysis

Thermolysis routes are related to chemical vapor deposition (CVD)-based methods to prepare thin films. By carrying out thermolysis reactions in high boiling solvents in the presence of capping agents, nanocrystals of various materials are obtained. Thermal decomposition provides remarkable control over size and is well suited for scale up to gram quantities.

Murray and coworkers [69] described a method for synthesizing CdSe nanocrystals by reacting a metal alkyl (dimethylcadmium) with TOPSe (tri-n-octylphosphine selenide) in TOP (tri-n-octylphosphine), a coordinating solvent that also acts as the capping agent. Fischer and coworkers [70] prepared TOPO-capped CdSe nanocrystals starting from less dangerous Cd precursors, while Guyot-Sionnest and coworkers [71] used dimethylzinc and a mixture of TOPO and hexadecylamine as capping agents to synthesize ZnSe nanocrystals. PbSe nanocrystals are prepared by the thermolysis of lead oleate and TOPSe in diphenylether-TOP [72]. Hyeon and coworkers [73] have prepared a series of metal sulphide nanoparticles such as ZnS, PbS and MnS by the thermolysis of metal-oleylamine complexes in the presence of S and oleylamine. ZnSe nanocrystals have been synthesized in a hot mixture of a long chain alkylamine and alkylphosphines [74]. PbS nanocrystals have been obtained by reacting $PbCl_2$-oleylamine complex with S-oleylamine complex without

the use of any solvents [75].

There are various other methods for the synthesis of nanocrystals including electrochemical synthesis, sonochemical synthesis, synthesis in microemulsions etc.

1.4 Growth kinetics of nanocrystals in solution

For the fabrication of nanoparticles, a small size is not the only requirement. For any practical application, the processing conditions need to be controlled in such a way that resulting nanoparticles have the following characteristics: (i) identical size of all particles, (ii) identical shape or morphology, (iii) identical chemical composition and crystal structure and (iv) individually dispersed [23]. Better understanding of the growth mechanism and careful control of the growth parameters are required to meet these characteristics.

In solution when the concentration of the growth species increases above the equilibrium concentration, initially there will be no nucleation. Nucleation occurs when the concentration reaches the minimum saturation required to overcome the critical energy barrier, and the nucleation rate increases very rapidly as the concentration increases further. Once nuclei are formed, growth occurs simultaneously. Above the minimum concentration, nucleation and growth are inseparable processes; however, these two processes proceed at different speeds. When the concentration decreases below this specific concentration, which corresponds to the critical energy, no more nuclei would form, whereas the growth will proceed until the concentration of growth species has attained the equilibrium concentration or solubility (see Figure 1.9) [76].

There are various mechanisms by which particles grow in solution [76]. As a result of the large surface area present for small particles, surface excess en-

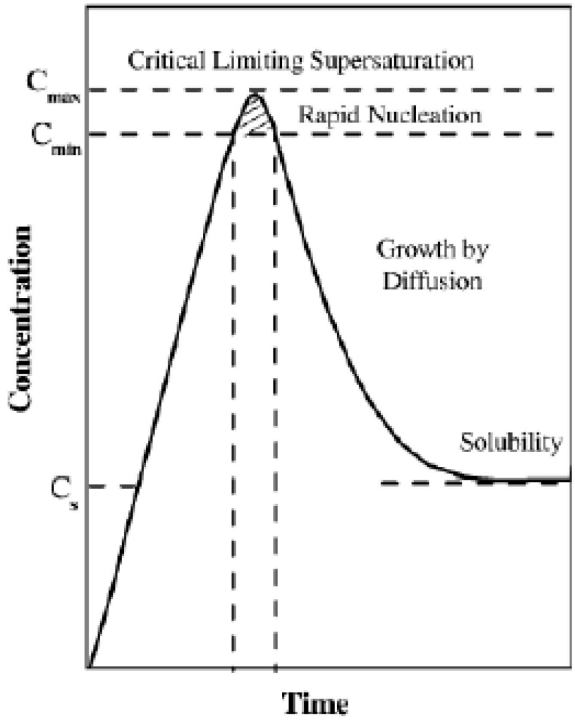

Figure 1.9: Schematic illustrating the processes of nucleation and subsequent growth [76].

ergy becomes more important in very small particles, constituting a non-negligible percentage of the total energy. Hence, for a solution that is initially not in thermodynamic equilibrium, a mechanism that allows the formation of larger particles at the cost of smaller particles reduces the surface energy and hence plays a key role in the growth of nanocrystals. A colloidal particle grows by a sequence of monomer diffusion towards the surface followed by reaction of the monomers at the surface of the nanocrystal. Coarsening effects, controlled either by mass transport or diffusion, are often termed the Ostwald ripening process. This diffusion limited Ostwald ripening process is the most predominant growth mechanism and was first quantified by Lifshitz and Slyozov [77], followed by a related work by Wagner [78], known as the LSW theory.

The diffusion process is dominated by the surface energy of the nanoparticle.

The interfacial energy is the energy associated with an interface due to differences between the chemical potential of atoms in an interfacial region and atoms in neighboring bulk phases. For a solid species present at a solid/liquid interface, the chemical potential of a particle increases with decreasing particle size, the equilibrium solute concentration for a small particle is much higher than for a large particle. The resulting concentration gradients lead to transport of the solute from the smaller particles to the larger particles. The equilibrium concentration of the nanocrystal in the liquid phase is dependent on the local curvature of the solid phase. Differences in the local equilibrium concentrations, due to variations in curvature, set up concentration gradients and provide the driving force for the growth of larger particles at the expense of smaller particles [79]. In case of Ostwald ripening the dependence of the particle size on time is given by

$$D^3 - D_0^3 = Kt$$

Where D and D_0 are the average particle diameter at time t and at time t=0 respectively. The rate const K is given by $K = 8\gamma d V_m^2 C_\infty / 9RT$, where d is the diffusion constant at temperature T, V_m the molar volume, γ the surface energy, and C_∞ the equilibrium concentration at a flat surface.

Besides the diffusion process, another important process in the growth of any particle is the reaction at the surface where the units of diffusing particles are assimilated into the growing nanocrystal. When the diffusion of growth species from the bulk to the growth surface is sufficiently rapid the growth rate is controlled by the surface process. In that case the growth rate is limited by the surface reaction

of the monomers and the rate law would be given by

$$D^2 \propto t$$

While in the preceding two sections, we have discussed the two limiting cases, in practice it is to be expected that both diffusion and surface reaction will contribute to the growth process in real experimental conditions. Specifically, several recent reports [80, 81] have stressed that the growth in a variety of realistic systems does not belong to either of the two limits, namely the diffusion or the reaction-limited regimes, but is controlled by a combination of diffusion and reaction at the surface

$$BD^3 + CD^2 + const = t$$

where, $B = AT/exp(-E_a/k_BT)$, $A \propto 1/(D_0\gamma V_m^2 C_\infty)$ and $C \propto T/(k_d\gamma V_m^2 C_\infty)$, k_d is the rate constant of surface reaction.

For better understanding of the growth mechanism of nanocrystals in solution thorough studies using techniques such as Small Angle X-ray Scattering (SAXS), Transmission Electron Microscopy (TEM), optical spectroscopy, etc. are required.

1.5 Self assembly of nanomaterials

The development of rational approaches for multidimensional interconnection of nanoscale building blocks into desired nanostructures is a significant challenge in the realization of advanced nanodevices [82, 83]. Self assembly driven by various interactions is an effective strategy for forming versatile soft nanocrystal assembly motifs [84–88]. Understanding factors governing the creation of nanocrystal assemblies would allow the design of desired nanostructures for optical, microelectronic,

chemical and biological applications [89]. Monofunctionalized nanoparticles can be used as molecular building blocks to react with other chemicals such as polymers, to give rise to nanomaterials linked with covalent bonds [90]. Nanoparticles encapsulated within cross-linked polymers undergo a sphere to chain transition induced by the micelle transition [91]. Ordered self-assembly of Au nanocrystals and Fe_2MnO_4 nanocubes into two- and three-dimensional (3-D) arrays from water soluble nanocrystal micelles have been observed [92]. The method involves drying water soluble Au nanocrystal micelles synthesized by a surfactant encapsulation technique. A spontaneous formation of nanoparticle strip patterns have been observed on dewetting a dilute film of polymer coated nanoparticles floating on a water surface [93]. Au nanoparticle monolayers and multilayers have been constructed on a gold surface using coordination chemistry of metal ions [94]. Au nanoparticle networks can be prepared by functionalizing them with azobenzene derivatives [95]. Gold nanocrystals produced electrochemically in the presence of PVP spontaneously order into 1D or 2D arrays [96]. Hybridization of branched DNA trimers and Au nanoparticle DNA conjugates has been employed to produce discrete self-assembled nanoparticle dendrimers [97]. The effect of disorder on the phase behavior of DNA-linked gold nanoparticle assemblies has been studied [98]. Variation in the length of the DNA linker results in different melting temperatures of the DNA-linked nanoparticle assemblies. By controlling the size distribution of magnetic Co nanocrystals, mesoscopic patterns with columnar and labyrinth structures are achieved [99]. Self-assembly of triangular and hexagonal CdS nanocrystals into complex structures such as rods and arrows has been observed [100]. Ring-like structures of semiconductors are found to occur by the self-assembly of nanocrystals in aqueous media [101, 102]. Self-assembly of NRs is also controllable via careful control over experimental conditions such as the concentration, pH, ion strength

and size distribution of NRs as well as the parameters affecting water evaporation [103–106] or by virtue of Langmuir-Blodgett [LB] techniques [107]. Self-assembly of Au nanorods driven by surfactants [108] and DNA molecules [109] have been demonstrated. Figure 1.10 shows self assembled gold nanorods by DNA hybridization [109].

Figure 1.10: Transmission electron micrographs of bundles of DNA linked gold nanorods [109].

End to end assembly of gold nanorods

The assembly of nanomaterial across extended length scales is a key challenge to the integration of functional nanodevices and nanomaterials. The real value of nanotechnology is to develop advanced nanodevices of superior function and properties. While most of the ordered structures published recently are based on colloidal particles [110–115], nanorods with anisotropic properties and longitudinal mode on optical excitations have also attracted great attention. The assembly of gold nanorods (GNRs) is attractive for several important applications, including

surface-enhanced Raman scattering (SERS) and fluorescence sensing [116–118]. El-Sayed *et al.* have organized GNRs into one-, two- and three-dimensional structures by controlling the evaporation of solvent [108]. Murphy *et al.* have demonstrated that electrostatic interactions lead to the organization of GNRs into self-assembled monolayers [119, 120].

The structure of the gold nanorods plays an important role in their end to end self assembly. Figure 1.11 shows a high-resolution TEM image of a Au nanorod oriented along [110]. The facets enclosing the nanorods are identified from the electron diffraction pattern, and the side facets are {110} and {100} with approximately equivalent surface area and the growth direction is [001]. The ends of the nanorods are terminated by the (001) and {111} facets of small areas [121]. The surfactant cetyl trimethylammonium bromide (CTAB) preferentially binds to the {100} faces, along the length of the rods, compared to the end {111} Au faces, due to the size of the CTAB head group [122, 123]. The binding of the large $[NMe_3]^+$ headgroup of CTAB and associated long alkyl chain can be more readily accommodated at the {100} side edges than within the plane of individual close-packed {111} faces, where the Au-Au spacings are too small to facilitate epitaxy. As the nanorods grow in length, the area of the side faces increases, and this facilitate the assembly of a bilayer of CTAB molecules as shown in Figure 1.12 at the crystal surface [124]. This makes the binder molecule unsuccessful at displacing the CTAB bound to the length of the gold nanorods, and thus it preferentially bound to the {111} ends of the rods, resulting in preferential end-to-end linkages [122, 124].

It has been demonstrated that some approaches are available for controlled assembly of GNRs [125]. For example, interactions between deoxyribonucleic acid (DNA) and its complementary strand have been used to assemble gold nanowires on a solid surface [126] or in solution [109]. Gold nanorods have been linked to

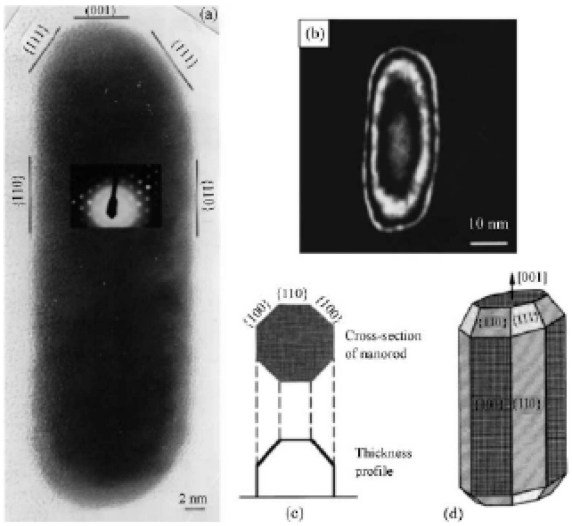

Figure 1.11: (a) High-resolution TEM image of a gold nanorod showing the facetted crystal structure of the rod. (b) Dark-field TEM image of a gold nanorod. (c) Cross-section and the corresponding profile of crystal thickness and (d) structural model [121].

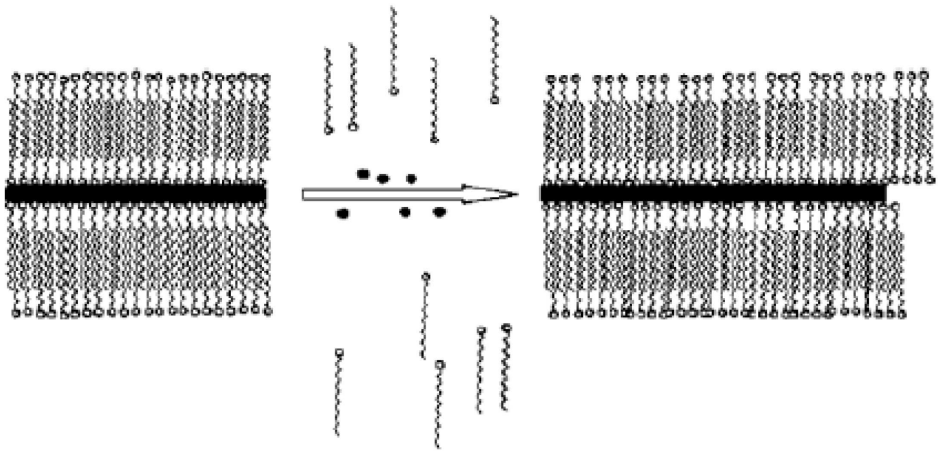

Figure 1.12: bilayer of CTAB (squiggles) on the gold nanorod (black rectangle) surface [124].

form 1-D chains using various linker molecules such as 3-mercaptopropionic acid, cysteine, Glutathione, alkanedithiols, biotin-streptavidin connectors etc [127–131]. Figure 1.13 shows the TEM image of the chains of gold nanorods formed by the

interaction with cysteine and the corresponding change in the UV-Vis spectra.

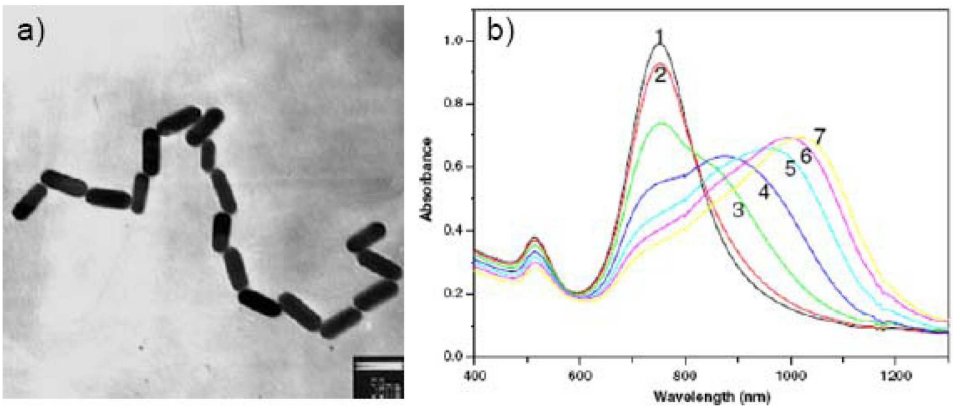

Figure 1.13: (a) TEM images and (b) UV-Vis spectra of chains of gold nanorods in the presence of cysteine [125].

As the nanorods are linked to form chains the longitudinal surface plasmon band shifts to longer wavelengths as shown in Figure 1.13 [125].

1.6 Nanocrystalline film at liquid-liquid Interface

Ultrathin films of metal nanocrystals constitute a novel class of materials with a unique combination of nominally zero and two dimensionalities. Interfaces are an important means to generate two-dimensional self assemblies of nanocrystals, providing a constrained environment for organized assembly. The air-water interface has been exploited for the preparation of films of metals and semiconductors, which have potential applications in nanodevices. For example, Chi *et al.* [132] have reported the preparation of monolayers of Au_{55} nanocrystals by spreading its chloroform sol over the aqueous layer in an LB trough and then transferring it onto a substrate. Large-scale ordered arrays of such nanocrystals have been obtained by Brown *et al.* [133]. Sastry and co-workers synthesized hydrophobically modified Au nanoparticles and organized them into lamellar films by the LB method [134].

Properties of thin films obtained by the LB technique are determined by the nature of the substrate as well as the reaction conditions, and the films are generally polycrystalline.

Unlike the air-water interface, the liquid-liquid (organic-aqueous) interface has not been investigated sufficiently. Nanocrystalline films can be prepared by a simple one-step synthesis at the liquid-liquid interface wherein an organometallic compound dissolved in an organic layer reacts with the reducing agent present in the aqueous layer at the interface as shown in Figure 1.14 [135]. A careful examination has shown that the material formed at the interface is an ultrathin nanocrystalline film consisting of closely packed metal nanocrystals coated with the organic species present at the interface [136]. The film at the interface is essentially freestanding and can be deposited onto a substrate for further investigation or could be converted to either an organosol or a hydrosol by using appropriate capping agents [136, 137].

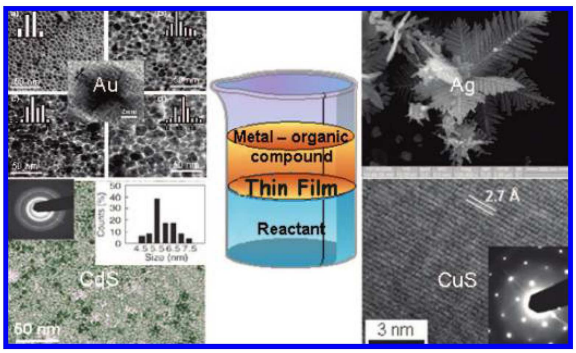

Figure 1.14: Schematic showing the formation of film at liquid-liquid interface [135].

Figure 1.15 shows nanocrystalline film of Au formed at the toluene-water interface by the reaction of $Au(PPh_3)Cl$ in toluene and alkaline solution of tetrakis (hydroxymethyl) phosphoniumchloride (THPC) in water. With the addition of a few micromoles of capping agents such as dodecanethiol or octylamine to the

Figure 1.15: Nanocrystalline film of Au formed at the toluene-water interface (middle). When dodecanethiol is added to the toluene layer, the film breaks up forming an organosol(left) while mercaptoundecanoic acid added to water it produces a hydrosol (right) [137].

toluene layer, the Au film at the interface disappeared within minutes, accompanied by a distinctive pink coloration in the top layer as shown in Figure 1.15 (Left) that is characteristic of an Au organosol. Similarly, the addition of a few micromoles of mercaptoundecanoic acid (MUA) to the aqueous solution results in the complete dissolution of the film after a few hours and the transfer of its contents to the aqueous layer as in Figure 1.15 (Right) [137].

1.7 Carbon nanostructures

1.7.1 Carbon nanotubes

The well known crystalline allotropes of carbon are diamond and graphite. The new carbon allotrope, fullerenes were discovered by Kroto *et al.* [138] in 1985 while investigating the nature of carbon present in interstellar space. Iijima [139] observed in 1991 that nanotubules of graphite were deposited on the negative electrode during the direct current arcing of graphite for the preparation of fullerenes. These nanotubes are concentric graphitic cylinders closed at either end due to the presence of five-membered rings. Nanotubes can be either multi-walled (MWNTs)

or single-walled nanotubes (SWNTs).

Synthesis

Ever since the discovery of the carbon nanotubes, several ways of preparing them have been explored. Various methods including electrochemical synthesis, laser ablation, chemical vapour deposition and pyrolysis of precursor molecules [140, 141] have been used to synthesize the carbon nanotubes. The nanotubes are generally obtained by the arc method or hydrocarbon pyrolysis. They are multi-walled, having several graphitic sheets or layers. Single-walled nanotubes (SWNTs) were first prepared by metal-catalyzed DC arcing of graphite rods [142, 143] in a He atmosphere. The graphite anode was filled with metal powders (Fe, Co or Ni) and the cathode was made of pure graphite. SWNTs generally occur in the web-like material deposited behind the cathode. Schematic of arc discharge set-up is shown in Figure 1.16. Various metal catalysts have been used to make SWNTs by this

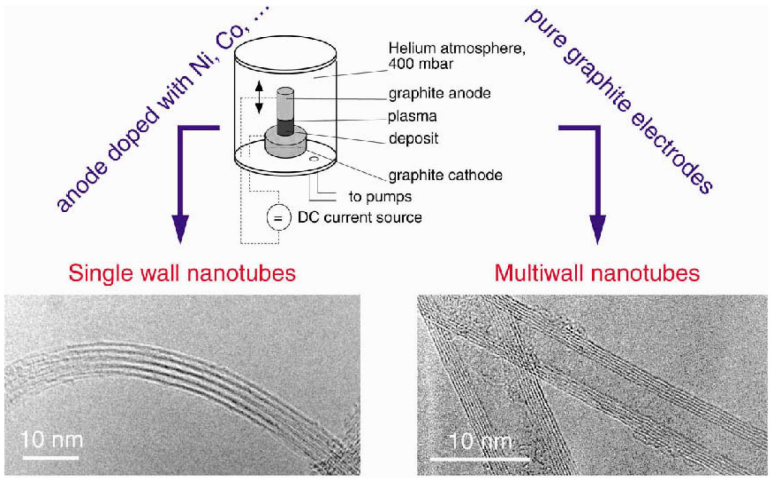

Figure 1.16: Experimental set-up of an arc discharge apparatus

route. Dai *et al.* [144] prepared SWNTs by the disproportionation of CO at 1200 °C over Mo particles of a few nanometers diameter dispersed in a fumed alumina

matrix. Saito *et al.* [145] compared SWNTs produced by using different catalysts and found that a Co or a Fe/Ni bimetallic catalyst gives rise to tubes forming a highway-junction pattern. SWNTs are also prepared by using various oxides Y_2O_3, La_2O_3, CeO_2 as catalysts [146]. Journet *et al.* [147] obtained ≈80% yield of SWNTs in the arc, by using a mixture of 1 at.% Y and 4.2 at.% Ni as catalyst. Arc evaporation of graphite rods filled with Ni and Y_2O_3 in a He atmosphere (660 torr) gives rise to web-like deposits on the chamber walls near the cathode, consisting of SWNT bundles. SWNTs have been produced in more than 70% yield by the condensation of a laser-vaporized carbon-nickel-cobalt mixture at 1200 °C [148]. Under controlled conditions of pyrolysis, dilute hydrocarbon-organometallic mixtures yield SWNTs [149]. Pyrolysis of metallocene-acetylene mixtures at 1100 °C yields SWNTs [149, 150]. Pyrolysis of acetylene in mixture with $Fe(CO)_5$ at 1100 °C gives good yields of SWNTs. Pyrolysis of ferrocene-thiophene mixtures also yield SWNTs, but the yield appears to be somewhat low. Pyrolysis of benzene and thiophene along with ferrocene gives a high yield of SWNTs [151]. The decomposition of CO on a silica-supported Co-Mo catalyst also yields SWNTs [152]. In CoMoCAT process, SWNTs are grown by CO disproportionation at 700 - 950 °C [153]. The experimental set up for producing carbon nanotubes by CoMoCAT method is given in Figure 1.17.

Structure

A SWNT can be visualized by cutting the C_{60} structure across the middle and adding a cylinder of graphite of the same diameter. If C_{60} is bisected normal to a five-fold axis, an armchair tube is formed, and if it is bisected normal to a three-fold axis, a zigzag tube is formed [154]. Armchair and zigzag tubes are non-chiral. In addition to these, a variety of chiral tubes can be formed with the screw axis along

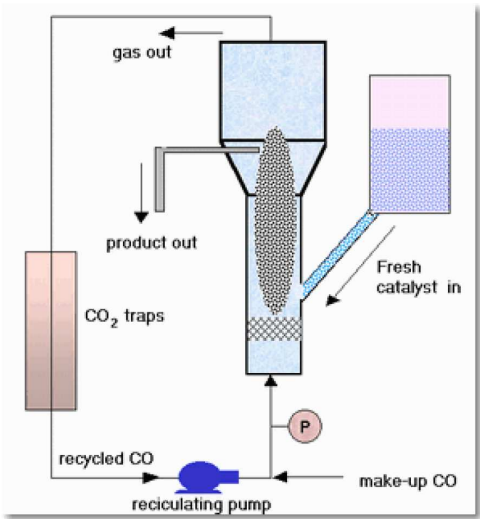

Figure 1.17: Schematic diagram of a CoMoCat apparatus

the axis of the tube. Nanotubes can be defined by a chiral angle θ and a chiral vector C_h by the equation,

$$C_h = na_1 + ma_2$$

where a_1 and a_2 are unit vectors in a 2D graphene lattice and n and m are integers (See Figure 1.18). The vector C_h connects two crystallographically equivalent sites

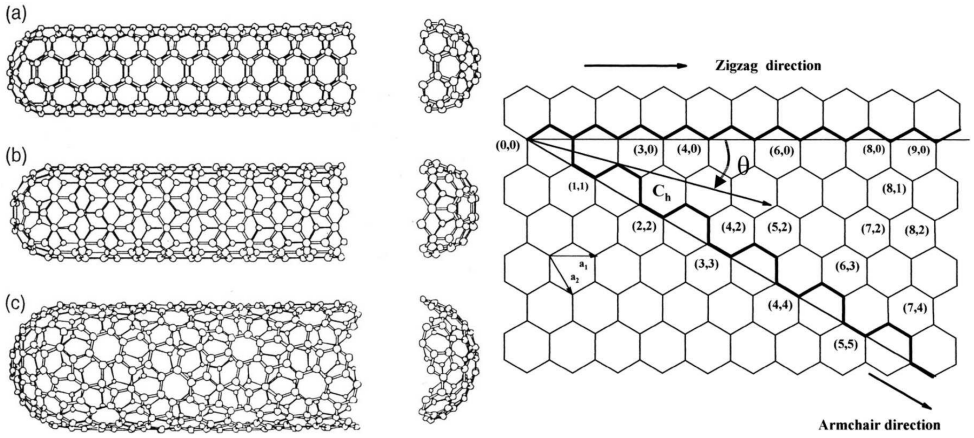

(a) (b)

Figure 1.18: (a) Models of (a) armchair, (b) zigzag, and (c) chiral nanotubes and (b) A 2D graphene sheet showing chiral vector C_h and chiral angle.

on a 2D graphene sheet and the chiral angle is the angle it makes with respect to the zigzag direction, (See Figure 1.18). A tube is formed by rolling up the graphene sheet in such a way that the two points connected by the chiral vector coincide. Calculations for the electronic structure of SWNTs [155] show that about 1/3 of the nanotubes are metallic and 2/3 are semiconducting, depending on the nanotube diameter and chiral angle. It can be shown that metallic conduction in a (n,m) carbon nanotube is achieved when

$$2n + m = 3q$$

, where q is an integer. All armchair carbon nanotubes are metallic.

1.7.2 Graphene

Graphene is the name given to a flat monolayer of carbon atoms tightly packed into a two-dimensional (2D) honeycomb lattice, and is a basic building block for graphitic materials of all other dimensionalities [156]. Theoretically, graphene has been studied for sixty years and is widely used for describing properties of various carbon-based materials. Graphene was an academic material as it was widely believed that 2D crystals are unstable. Geim and co-workers [157] in 2005 showed that a single layer of graphene is indeed stable, thus opening a new area of fascinating physics and chemistry. Depending on their dimensions and physical properties, graphene stacks are classified into three categories: single layer graphene, few layer graphene or FLG and graphite.

Synthesis

A large majority of the studies of graphene have been directed towards synthesis. Since micromechanical cleavage of HOPG was first employed to obtain single layer graphene (SG), various methods including epitaxial growth on an insulator surface such as SiC and chemical vapor deposition (CVD) on surfaces of transition metals such as Ni and Cu have been employed [158, 159]. Graphene layers can be grown on different transition metal substrates by decomposing a variety of hydrocarbons such as methane, ethylene, acetylene and benzene with the number of layers varying with the hydrocarbon and reaction parameters. Hydrazine reduction of single layer graphene oxide seems to be an effective means of obtaining a dispersion of SG in solvents such as DMF. Many of the above methods are, however, not suitable to make large quantities of graphene samples. Bi- and few-layer graphenes can be obtained by different chemical procedures such as thermal exfoliation of graphite oxide, reduction of graphene oxide with reducing agents such as hydrazine under microwave irradiation, and microwave solvothermal treatment of graphene oxide [158, 159]. The most common method of preparing graphene samples seems to be through the reduction of graphene oxide. An arc-discharge method involving evaporation of graphite electrodes in a hydrogen atmosphere has been reported for preparing graphene flakes [160]. The presence of H_2 during the arc-discharge process terminates the dangling carbon bonds with hydrogen and prevents the formation of closed structures, such as rolling of sheets into nanotubes and graphitic polyhedral particles.

Graphene is characterized by different microscopy and related techniques. While transmission electron microscopy (TEM) and scanning electron microscopy (SEM) are used to obtain graphene morphology, scanning tunneling microscopy (STM)

and atomic force microscopy (AFM) are used to observe the atomic arrangement and the layer thickness of graphene.

1.7.3 Raman spectroscopy of carbon nanotubes and graphene

Raman spectroscopy has historically played an important role in the study and characterization of graphitic materials [161–164], being widely used in the last four decades to characterize pyrolytic graphite, carbon fibers, glassy carbon, pitch based graphitic foams, nanographite ribbons, fullerenes, carbon nanotubes, and graphene. For sp^2 nanocarbons, Raman spectroscopy can give information about crystallite size, clustering of the sp^2 phase, the presence of sp^2 - sp^3 hybridization and chemical impurities, mass density, optical energy gap, elastic constants, doping, defects and other crystal disorder, edge structure, strain, number of graphene layers, nanotube diameter, nanotube chirality and metallic vs. semiconductor behavior. The following paragraphs describe three aspects of Raman spectra (see Figure 1.19), which are sensitive enough to provide unique information about the similarities and differences between the various carbon nanostructures. The various Raman features are discussed including the G-band at ≈ 1582 cm^{-1}, which is common to all sp^2 carbon forms, the radial breathing mode (RBM) that makes the diameter and optical transition energy analysis of nanotubes possible, and the D and G′ bands that are significant in providing information about the electronic and geometrical structure through the double resonance process.

The G Band. The stretching of the C-C bond in graphitic materials gives rise to the so-called G-band Raman feature which is common to all sp^2 carbon systems (see Figure 1.19). This spectral feature is similar for graphenes and nanotubes but yet has properties capable of distinguishing one carbon nanotstructure from

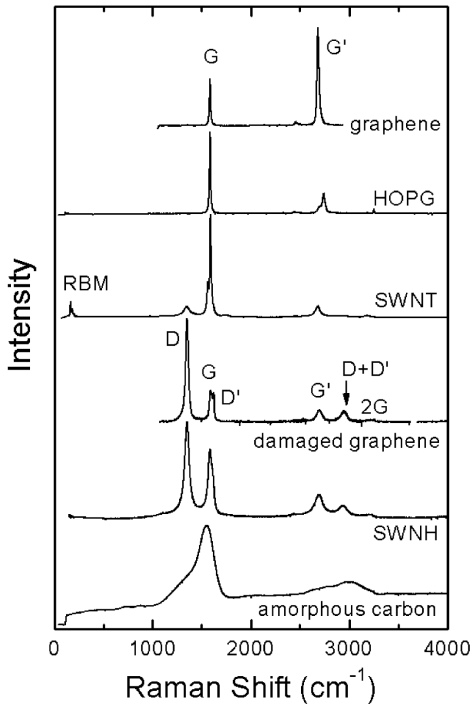

Figure 1.19: Raman spectra from different types of sp^2 nanocarbons. The graphene related structures are labeled next to their respective spectra.

another. The G-band is highly sensitive to strain effects in sp^2 nanocarbons and can be used to probe any modification to the flat geometric structure of graphene, such as the strain induced by external forces, by one graphene layer on another in few layer graphene or in multiwall nanotubes, or even by the curvature of the side wall when growing a SWNT. Curvature effects which occurs in carbon nanotubes, give rise to multiple peaks in the G-band spectrum for a SWNT, [165] while a single peak is observed for a 2D graphene sheet. This curvature dependence generates a diameter dependence, thus making the G band a probe also for the tube diameter.

The Kohn anomaly is observed in metallic and semimetallic systems, where real electron-hole pair creation can occur by a phonon excitation (pG) process, thus strongly influencing the G-band frequency and the spectral width of graphene and metallic SWNTs. These effects in metallic SWNTs are stronger than those

in graphene because of the quantum confinement effect, and this process depends sensitively on diameter and chiral angle [166]. In graphenes these effects depend sensitively on the number of graphene layers. Semiconducting SWNTs also exhibit a phonon energy renormalization due to electron-phonon coupling, but this renormalization effect is weaker than that in graphene and for metallic SWNTs. Consequently, while the G band line width in graphene and metallic SWNTs is strongly sensitive to whether the Fermi energy matches the energy of the Kohn anomaly, [166] in semiconducting SWNTs the G band line width is basically independent of doping.

The Radial Breathing Mode (RBM) The radial breathing mode is especially important in two ways: (1) for the determination of the diameter of a nanotube through the dependence of ω_{RBM} on d_t, and (2) for relating the ω_{RBM} and the resonant optical transition energies E_{ii} for a given tube.

Experimental data on the radial breathing mode frequency taken by many authors have been fit using the relation $\omega_{RBM} = \frac{A}{d_t} + B$. For the water-assisted supergrowth samples, values of A = 227 nm.cm^{-1} and B=0.3 cm^{-1} are obtained. This result is in remarkably good agreement with elasticity theory parametrized by the graphite elastic properties, thus directly connecting one-dimensional carbon nanotubes and their two-dimensional counterpart graphene from which nanotubes are conceptually derived.

Dispersive G′ Band: the Double Resonance Process All kinds of sp^2 carbon materials exhibit a strong Raman feature which appears in the range 2500-2800 cm^{-1}, as shown in Figure 1.19. Together with the G band (1582 cm^{-1}), this spectrum is a Raman signature of graphitic sp^2 materials and is called the G′ band to emphasize that it is a Raman-allowed mode for sp^2 carbons. Interestingly, the G′ band is a second-order two-phonon process and, intriguingly, it exhibits a strong

frequency dependence on the excitation laser energy E_{laser}. The G′ band in particular is a second-order process related to a phonon near the K point in graphene, activated by double resonance (DR) processes, [167, 168] which are responsible for its dispersive nature and cause a strong dependence on any perturbation to the electronic and/or phonon structure of graphene. For this reason, the G′ feature provides a very sensitive probe for characterizing specific sp^2 nanocarbons.

Disorder-Induced D Band. The presence of disorder in sp^2-hybridized carbon systems leads to rich and intriguing phenomena in their resonance Raman spectra, thus making Raman spectroscopy one of the most sensitive and informative techniques to characterize disorder in sp^2 carbon materials. Raman spectroscopy has thus become a key tool and is widely used to identify disorder in the sp^2 network of different carbon structures, such as diamond like carbon, amorphous carbon, nanostructured carbon, as well as carbon nanofibers, nanotubes, and nanohorns [164, 169, 170].

References

[1] H. Zhao and Y. Ning. Techniques used for the preparation and application of gold powder in ancient china. *Gold Bull.*, 33(3):103–105, 2000.

[2] M Faraday. The bakerian lecture: experimental relations of gold (and other metals) to light. *Philos Trans R Soc London*, 147:145–181, 1857.

[3] M. A. El-Sayed. Some interesting properties of metals confined in time and nanometer space of different shapes. *Acc. Chem. Res.*, 34(4):257–264, 2001.

[4] P. Braunstein, G. Oro, and P.R. Raithbay. *Metal clusters in Chemistry, Wiley-VCH, Weinheim*. 1998.

[5] R. Kubo. Electronic properties of metallic fine particles. i. *J. Phys. Soc. of Jpn*, 17(6):975–986, 1962.

[6] S.V. Gaponenko. *Optical Properties Of Semiconductor Nanocrystals, Cambridge University Press, Cambridge*. 1998.

[7] C. N. R. Rao, P. J. Thomas, and G. U. Kulkarni. *Nanocrystals: Synthesis,Properties and Applications; Springer-Verlag: Berlin*. 2007.

[8] W. P. Halperin. Quantum size effects in metal particles. *Rev. Mod. Phys.*, 58(3):533–606, 1986.

[9] U. Kreibig and M. Vollmer. *Springer: Berlin*. 1995.

[10] G. C. Papavassiliou. Optical properties of small inorganic and organic metal particles. *Prog. Solid State Chem.*, 12(3-4):185 – 271, 1979.

[11] K. L. Kelly, E. Coronado, L. L. Zhao, and G. C. Schatz. The optical properties of metal nanoparticles: the influence of size, shape, and dielectric environment. *J. Phys. Chem. B*, 107(3):668–677, 2003.

[12] S. Link and M. A. El-Sayed. Shape and size dependence of radiative, nonradiative and photothermal properties of gold nanocrystals. *Int. Rev. Phy. Chem.*, 19(3):409 – 453, 2000.

[13] G. Mie. Beitrge zur optik trber medien, speziell kolloidaler metallsungen. *Ann. Phys.*, 330(3):377–445, 1908.

[14] J. A. Creighton and D. G. Eadon. Ultraviolet-visible absorption spectra of the colloidal metallic elements. *J. Chem. Soc., Faraday Trans.*, 87:3881–3891, 1991.

[15] P. Mulvaney. Surface plasmon spectroscopy of nanosized metal particles. *Langmuir*, 12(3):788–800, 1996.

[16] H. Hirai, H. Wakabayashi, and M. Komiyama. Polymer-protected copper colloids as catalysts for selective hydration of acrylonitrile. *Chem. Lett.*, 12(7):1047–1050, 1983.

[17] P. A. Brugger, P. Cuendet, and M. Graetzel. Ultrafine and specific catalysts affording efficient hydrogen evolution from water under visible light illumination. *J. Am. Chem. Soc.*, 103(11):2923–2927, 1981.

[18] J. M. Thomas. Colloidal metals: past, present and future. *Pure Appl. Chem.*, 60(10):1517–1528, 1988.

[19] R. Gans. *Ann. Phys.,*, 47:270, 1915.

[20] S. Link and M. A. El-Sayed. Spectral properties and relaxation dynamics of surface plasmon electronic oscillations in gold and silver nanodots and nanorods. *J. Phys. Chem. B*, 103(40):8410–8426, 1999.

[21] F. Kim, J. H. Song, and P. Yang. Photochemical synthesis of gold nanorods. *J. Am. Chem. Soc.*, 124(48):14316–14317, 2002.

[22] G. T. Boyd, Z. H. Yu, and Y. R. Shen. Photoinduced luminescence from the noble metals and its enhancement on roughened surfaces. *Phys. Rev. B*, 33(12):7923–7936, 1986.

[23] G. Cao. *Nanostructures & Nanomaterials: Synthesis, Properties & Applications, Imperial College Press, London,*. 2004.

[24] C. B. Murray, C. R. Kagan, and M. G. Bawendi. Synthesis and characterization of monodisperse nanocrystals and close-packed nanocrystal assemblies. *Ann. Rev. Mater. Sci.*, 30:545–610, 2000.

[25] A. J. Sutherland. Quantum dots as luminescent probes in biological systems. *Curr. Opn. Sol. Stat. Mater. Sci.*, 6(4):365 – 370, 2002.

[26] M. J. Bowers, J. R. McBride, and S. J. Rosenthal. White-light emission from magic-sized cadmium selenide nanocrystals. *J. Am. Chem. Soc.*, 127(44):15378–15379, 2005.

[27] M. Nirmal and L. Brus. Luminescence photophysics in semiconductor nanocrystals. *Acc. Chem. Res.*, 32(5):407–414, 1999.

[28] J. P. Bucher, D. C. Douglass, and L. A. Bloomfield. Magnetic properties of free cobalt clusters. *Phys. Rev. Lett.*, 66(23):3052–3055, 1991.

[29] C.P. Bean and I.S. Jacobs. Superparamagnetism. *J. Appl. Phys.*, 30(4):S120, 1959.

[30] J. Frankel and J. Dorfinan. Spontaneous and induced magnetisation in ferromagnetic bodies. *Nature*, 126(3173):274, 1930.

[31] C. Kittel. Theory of the structure of ferromagnetic domains in films and small particles. *Phys. Rev.*, 70(11-12):965–971, 1946.

[32] C. Liu, A. J. Rondinone, and Z. J. Zhang. Synthesis of magnetic spinel ferrite $CoFe_2O_4$ nanoparticles from ferric salt and characterization of the size-dependent superparamagnetic properties. *Pure Appl. Chem.*, 72(1-2):37–45, 2000.

[33] M. Ghosh, E. V. Sampathkumaran, and C. N. R. Rao. Synthesis and magnetic properties of coo nanoparticles. *Chem. Mater.*, 17(9):2348–2352, 2005.

[34] M. Ghosh, K. Biswas, A. Sundaresan, and C. N. R. Rao. Mno and nio nanoparticles: synthesis and magnetic properties. *J. Mater. Chem.*, 16:106–111, 2006.

[35] A. Sundaresan, R. Bhargavi, N. Rangarajan, U. Siddesh, and C. N. R. Rao. Ferromagnetism as a universal feature of nanoparticles of the otherwise nonmagnetic oxides. *Phys. Rev. B*, 74(16):161306, 2006.

[36] J. Turkevich, P. Cooper Stevenson, and J. Hillier. A study of the nucleation and growth processes in the synthesis of colloidal gold. *Discuss. Faraday Soc.*, 11:55–75, 1951.

[37] H. Hirai, H. Wakabayashi, and M. Komiyama. Polymer-protected copper

colloids as catalysts for selective hydration of acrylonitrile. *Chem. Lett.*, 12(7):1047–1050, 1983.

[38] M. Green and P. O'Brien. The preparation of organically functionalised chromium and nickel nanoparticles. *Chem. Commun.*, pages 1912–1913, 2001.

[39] M. Brust, M. Walker, D. Bethell, D. J. Schiffrin, and R. Whyman. Synthesis of thiol-derivatised gold nanoparticles in a two-phase liquid-liquid system. *J. Chem. Soc., Chem. Commun.*, pages 801–802, 1994.

[40] E.A. Hauser and J.E. Lynn. *Experiments in Colloid Chemistry, (McGraw-Hill, New York*. 1940.

[41] D. N. Furlong, A. Launikonis, W. H. F. Sasse, and J. V. Sanders. Colloidal platinum sols. preparation, characterization and stability towards salt. *J. Chem. Soc., Faraday Trans. 1*, 80:571–588, 1984.

[42] A. Harriman, G. R. Millward, P. Neta, M. C. Richoux, and J. M. Thomas. Interfacial electron-transfer reactions between platinum colloids and reducing radicals in aqueous solution. *J. Phys. Chem.*, 92(5):1286–1290, 1988.

[43] J. S. Bradley, J. M. Millar, and E. W. Hill. Surface chemistry on colloidal metals: a high-resolution nmr study of carbon monoxide adsorbed on metallic palladium crystallites in colloidal suspension. *J. Am. Chem. Soc.*, 113(10):4016–4017, 1991.

[44] J. S. Bradley, E. W. Hill, S. Behal, C. Klein, A. Duteil, and B. Chaudret. Preparation and characterization of organosols of monodispersed nanoscale palladium. particle size effects in the binding geometry of adsorbed carbon monoxide. *Chem. Mater.*, 4(6):1234–1239, 1992.

[45] T. Teranishi, H. Hori, and M. Miyake. Esr study on palladium nanoparticles. *J. Phys. Chem. B*, 101(30):5774–5776, 1997.

[46] Y. Wang and N. Toshima. Preparation of PdPt bimetallic colloids with controllable core/shell structures. *J. Phys. Chem. B*, 101(27):5301–5306, 1997.

[47] P. Y. Silvert, R. Herrera-Urbina, N. Duvauchelle, V. Vijayakrishnan, and K. T. Elhsissen. Preparation of colloidal silver dispersions by the polyol process. part 1-synthesis and characterization. *J. Mater. Chem.*, 6:573–577, 1996.

[48] Ram Seshadri and C.N.R. Rao. Preparation of monodispersed, submicron gold particles. *Mater. Res. Bull.*, 29(7):795 – 799, 1994.

[49] P. Saravanan, T. A. Jose, P. J. Thomas, and G. U. Kulkarni. Submicron particles of Co, Ni and CoNi alloys. *Bull. Mater. Sci.*, 24(5):515521, 2001.

[50] D. G. Duff, A. Baiker, and P. P. Edwards. A new hydrosol of gold clusters. *J. Chem. Soc., Chem. Commun.*, (1):96–98, 1993.

[51] M. Schulz-Dobrick, K. V. Sarathy, and M. Jansen. Surfactant-free synthesis and functionalization of gold nanoparticles. *J. Am. Chem. Soc.*, 127(37):12816–12817, 2005.

[52] P. R. Van Rheenen, M. J. McKelvy, and W. S. Glaunsinger. Synthesis and characterization of small platinum particles formed by the chemical reduction of chloroplatinic acid. *J. Solid State Chem.*, 67(1):151 – 169, 1987.

[53] N. R. Jana and X. Peng. Single-phase and gram-scale routes toward nearly monodisperse Au and other noble metal nanocrystals. *J. Am. Chem. Soc.*, 125(47):14280–14281, 2003.

[54] S.-H. Yu, J. Yang, Z.-H. Han, Y. Zhou, R.-Y. Yang, Y.-T. Qian, and Y.-H. Zhang. Controllable synthesis of nanocrystalline CdS with different morphologies and particle sizes by a novel solvothermal process. *J. Mater. Chem.*, 9:1283–1287, 1999.

[55] Chen and R. Fan. Low-temperature hydrothermal synthesis of transition metal dichalcogenides. *Chem. Mater.*, 13(3):802–805, 2001.

[56] U. K. Gautam, M. Rajamathi, F. Meldrum, P. Morgan, and R. Seshadri. A solvothermal route to capped CdSe nanoparticles. *Chem. Commun.*, pages 629–630, 2001.

[57] D.-W. Deng, J.-S. Yu, and Y. Pan. Water-soluble CdSe and CdSe/CdS nanocrystals: A greener synthetic route. *J. Colloid Interface Sci.*, 299(1):225 – 232, 2006.

[58] L. Yang, Q. Shen, J. Zhou, and K. Jiang. Biomimetic synthesis of CdS nanocrystals in aqueous solution of pepsin. *Mater. Chem. Phys.*, 98(1):125 – 130, 2006.

[59] J.H. Zhan, X.G. Yang, W.X. Zhang, D. W. Wang, Y. Xie, and Y. T. Qian. A solvothermal route to wurtzite ZnSe nanoparticles. *J. Mater. Res.*, 15(3):629–632, 2000.

[60] Y. Li, Y. Ding, Y. Qian, Y. Zhang, and L. Yang. A solvothermal elemental reaction to produce nanocrystalline ZnSe. *Inorg. Chem.*, 37(12):2844–2845, 1998.

[61] K. Sardar and C.N.R. Rao. New solvothermal routes for GaN nanocrystals. *Adv. Mater.*, 16(5):425–429, 2004.

[62] P. Braunstein, G. Oro, and P. R. Raithbay. *Metal clusters in Chemistry,vol.2, Wiley-VCH, Weinheim.* 1998.

[63] M. Y. Han, L. Zhou, C. H. Quek, S. F. Y. Li, and W. Huang. Room temperature coulomb staircase on pure and uniform surface-capped gold nanoparticles. *Chem. Phys. Lett.*, 287(1-2):47 – 52, 1998.

[64] R. Rossetti, J. L. Ellison, J. M. Gibson, and L. E. Brus. Size effects in the excited electronic states of small colloidal CdS crystallites. *J. Chem. Phys.*, 80(9):4464, 1984.

[65] C. H. Fischer and A. Henglein. Photochemistry of colloidal semiconductors. preparation and photolysis of cadmium sulfide sols in organic solvents. *J. Phys. Chem.*, 93(14):5578–5581, 1989.

[66] T. Vossmeyer, L. Katsikas, M. Giersig, I. G. Popovic, K. Diesner, A. Chemseddine, A. Eychmueller, and H. Weller. CdS nanoclusters: Synthesis, characterization, size dependent oscillator strength, temperature shift of the excitonic transition energy, and reversible absorbance shift. *J. Phys. Chem.*, 98(31):7665–7673, 1994.

[67] R. Rossetti, R. Hull, J. M. Gibson, and L. E. Brus. Excited electronic states and optical spectra of ZnS and CdS crystallites in the ≈15 to 50 $|AA$ size range: Evolution from molecular to bulk semiconducting properties. *J. Chem. Phys.*, 82(1):552, 1985.

[68] A. L. P. Cornacchio and N. D. Jones. Thiolate-capped PbS nanocrystals in water: sensitivity to o_2, ph and concentration, an alternate pathway for crystal growth and a top-down synthesis. *J. Mater. Chem.*, 16:1171–1177, 2006.

[69] C. B. Murray, D. J. Norris, and M. G. Bawendi. Synthesis and characterization of nearly monodisperse cde (e = sulfur, selenium, tellurium) semiconductor nanocrystallites. *J. Am. Chem. Soc.*, 115(19):8706–8715, 1993.

[70] J. Hambrock, A. Birkner, and R. A. Fischer. Synthesis of CdSe nanoparticles using various organometallic cadmium precursors. *J. Mater. Chem.*, 11:3197–3201, 2001.

[71] M. A. Hines and P. Guyot-Sionnest. Bright uv-blue luminescent colloidal ZnSe nanocrystals. *J. Phys. Chem. B*, 102(19):3655–3657, 1998.

[72] C. B. Murray, S. Sun, W. Gaschler, H. Doyle, T. A. Betley, and C. R. Kagan. Colloidal synthesis of nanocrystals and nanocrystal superlattices. *IBM J. Res. Dev.*, 45(1):47 –56, 2001.

[73] J. Joo, H. Bin Na, T. Yu, J. H. Yu, Y. W. Kim, F. Wu, J. Z. Zhang, and T. Hyeon. Generalized and facile synthesis of semiconducting metal sulfide nanocrystals. *J. Am. Chem. Soc.*, 125(36):11100–11105, 2003.

[74] P. D. Cozzoli, L. Manna, M. L. Curri, S. Kudera, C. Giannini, M. Striccoli, and A. Agostiano. Shape and phase control of colloidal znse nanocrystals. *Chem. Mater.*, 17(6):1296–1306, 2005.

[75] L. Cademartiri, J. Bertolotti, R. Sapienza, D. S. Wiersma, G. von Freymann, and G. A. Ozin. Multigram scale, solventless, and diffusion-controlled route to highly monodisperse PbS nanocrystals. *J. Phys. Chem. B*, 110(2):671–673, 2006.

[76] C. N. R. Rao, A. Muller, and A. K. Cheetham. *Nanomaterials Chemistry:*

Recent Developments and New Directions, Wiley-VCH Verlag GmbH & Co. 2007.

[77] I.M. Lifshitz and V.V. Slyozov. The kinetics of precipitation from supersaturated solid solutions. *J. Phys.Chem. Solids*, 19(1-2):35 – 50, 1961.

[78] C. Wagner. *Z. Elektrochem.*, 65:581, 1961.

[79] T. Sugimoto. Preparation of monodispersed colloidal particles. *Adv. Colloid Interface Sci.*, 28:65 – 108, 1987.

[80] D. V. Talapin, A. L. Rogach, M. Haase, and H. Weller. Evolution of an ensemble of nanoparticles in a colloidal solution: theoretical study. *J. Phys. Chem. B*, 105(49):12278–12285, 2001.

[81] R. Viswanatha, S. Sapra, B. Satpati, P. V. Satyam, B. N. Dev, and D. D. Sarma. Understanding the quantum size effects in ZnO nanocrystals. *J. Mater. Chem.*, 14:661–668, 2004.

[82] Y. Huang, X. Duan, Q. Wei, and C. M. Lieber. Directed Assembly of One-Dimensional Nanostructures into Functional Networks. *Science*, 291(5504):630–633, 2001.

[83] I. W. Hamley. Nanotechnology with soft materials. *Angew. Chem. Int. Ed.*, 42(15):1692–1712, 2003.

[84] A. P. Alivisatos, K. P. Johnsson, X. G. Peng, T. E. Wilson, C. J. Loweth, M. P. Bruchez, and P. G. Schultz. Organization of 'nanocrystal molecules' using DNA. *Nature*, 382:609–611, 1996.

[85] P. C. Ohara, J. R. Heath, and W. M. Gelbart. Self-assembly of submicrometer rings of particles from solutions of nanoparticles. *Angew. Chem. Int. Ed.*, 36(10):1078–1080, 1997.

[86] B. A. Korgel and D. Fitzmaurice. Self-assembly of silver nanocrystals into two-dimensional nanowire arrays. *Adv. Mater.*, 10(9):661–665, 1998.

[87] M. Li, H. Schnablegger, and S. Mann. Coupled synthesis and self-assembly of nanoparticles to give structures with controlled organization. *Nature*, 402:393–395, 1999.

[88] T. L. Breen, J. Tien, R. J. Scott, Oliver, T. Hadzic, and G. M. Whitesides. Design and Self-Assembly of Open, Regular, 3D Mesostructures. *Science*, 284(5416):948–951, 1999.

[89] A. N. Shipway, E. Katz, and I. Willner. Nanoparticle arrays on surfaces for electronic, optical, and sensor applications. *ChemPhysChem*, 1(1):18–52, 2000.

[90] Q. Dai, J. G. Worden, J. Trullinger, and Q. Huo. A nanonecklace synthesized from monofunctionalized gold nanoparticles. *J. Am. Chem. Soc.*, 127(22):8008–8009, 2005.

[91] Y. Kang, K. J. Erickson, and T. A. Taton. Plasmonic nanoparticle chains via a morphological, sphere-to-string transition. *J. Am. Chem. Soc.*, 127(40):13800–13801, 2005.

[92] H. Fan, E. Leve, J. Gabaldon, A. Wright, R. E. Haddad, and C. J. Brinker. Ordered two- and three-dimensional arrays self-assembled from water-soluble nanocrystalmicelles. *Adv. Mater.*, 17(21):2587–2590, 2005.

[93] J. Huang, F. Kim, A. R. Tao, S. Connor, and P. Yang. Spontaneous formation of nanoparticle stripe patterns through dewetting. *Nat. Mater.*, 4(12):896–900, 2005.

[94] M. Wanunu, R. Popovitz-Biro, H. Cohen, A. Vaskevich, and I. Rubinstein. Coordination-based gold nanoparticle layers. *J. Am. Chem. Soc.*, 127(25):9207–9215, 2005.

[95] D. S. Sidhaye, S. Kashyap, M. Sastry, S. Hotha, and B. L. V. Prasad. Gold nanoparticle networks with photoresponsive interparticle spacings. *Langmuir*, 21(17):7979–7984, 2005.

[96] S. Huang, H. Ma, X. Zhang, Fe. Yong, X. Feng, W. Pan, X. Wang, Y. Wang, and S. Chen. Electrochemical synthesis of gold nanocrystals and their 1D and 2D organization. *J. Phys. Chem. B*, 109(42):19823–19830, 2005.

[97] S. A. Claridge, S. L. Goh, J. M. J. Frchet, S. C. Williams, C. M. Micheel, and A. P. Alivisatos. Directed assembly of discrete gold nanoparticle groupings using branched dna scaffolds. *Chem. Mater.*, 17(7):1628–1635, 2005.

[98] N. C. Harris and C. Kiang. Disorder in dna-linked gold nanoparticle assemblies. *Phys. Rev. Lett.*, 95(4):046101(1–4), 2005.

[99] V. Germain and M-P. Pileni. Size distribution of cobalt nanocrystals: A key parameter in formation of columns and labyrinths in mesoscopic structures. *Adv. Mater.*, 17(11):1424–1429, 2005.

[100] J. H. Warner and R. D. Tilley. Synthesis and self-assembly of triangular and hexagonal CdS nanocrystals. *Adv. Mater.*, 17(24):2997–3001, 2005.

[101] B. Liu and H. C. Zeng. Semiconductor rings fabricated by self-assembly of nanocrystals. *J. Am. Chem. Soc.*, 127(51):18262–18268, 2005.

[102] C. N. R. Rao, A. Govindaraj, and S. R. C. Vivekchand. Inorganic nanomaterials: current status and future prospects. *Annu. Rep. Prog. Chem., Sect. A: Inorg. Chem.*, 102:20–45, 2006.

[103] B. Nikoobakht, Z. L. Wang, and M. A. El-Sayed. Self-assembly of gold nanorods. *J. Phys. Chem. B*, 104(36):8635–8640, 2000.

[104] N. R. Jana, L. A. Gearheart, S. A. Obare, C. J. Johnson, K. J. Edler, S. Mann, and C. J. Murphy. Liquid crystalline assemblies of ordered gold nanorods. *J. Mater. Chem.*, 12(10):2909–2912, 2002.

[105] N. R. Jana. Shape effect in nanoparticle self-assembly. *Angew. Chem.*, 116(12):1562–1566, 2004.

[106] C. J. Orendorff, P. L. Hankins, and C. J. Murphy. pH-triggered assembly of gold nanorods. *Langmuir*, 21(5):2022–2026, 2005.

[107] S.-W. Chung, G. Markovich, and J. R. Heath. Fabrication and alignment of wires in two dimensions. *J. Phys. Chem. B*, 102(35):6685–6687, 1998.

[108] B. Nikoobakth, Z. L. Wang, and M. A. El-Sayed. Isothermal titration calorimetry: application to structure-based drug design. *J. Phys. Chem. B*, 104(36):8635–8640, 2000.

[109] E. Dujardin, L. B. Hsin, C. R. C. Wang, and S. Mann. DNA-driven self-assembly of gold nanorods. *Chem. Commun.*, (14):1264–1265, 2001.

[110] C. A. Mirkin, R. L. Letsinger, R. C. Mucic, and J. J. Storhoff. A DNA-based method for rationally assembling nanoparticles into macroscopic materials. *Nature*, 382(6592):607–609, 1996.

[111] C. M. Niemeyer, W. Burger, and J. Peplies. Covalent DNAStreptavidin conjugates as building blocks for novel biometallic nanostructures. *Angew. Chem. Int. Ed.*, 37(16):2265–2268, 1998.

[112] J. J. Storhoff and C. A. Mirkin. Programmed materials synthesis with DNA. *Chem. Rev.*, 99(7):1849–1862, 1999.

[113] C. B. W. Garcia, Y. Zhang, S. Mahajan, F. DiSalvo, and U. Wiesner. Self-assembly approach toward magnetic silica-type nanoparticles of different shapes from reverse block copolymer mesophases. *J. Am. Chem. Soc.*, 125(44):13310–13311, 2003.

[114] A. D. Ormonde, E. C. M. Hicks, J. Castillo, and R. P. Van Duyne. Nanosphere lithography: fabrication of large-area ag nanoparticle arrays by convective self-assembly and their characterization by scanning UVVisible extinction spectroscopy. *Langmuir*, 20(16):6927–6931, 2004.

[115] H. Lee, A. M. Purdon, V. Chu, and R. M. Westervelt. Controlled assembly of magnetic nanoparticles from magnetotactic bacteria using microelectromagnets arrays. *Nano Lett.*, 4(5):995–998, 2004.

[116] C. J. Orendorff, A. Gole, T. K. Sau, and C. J. Murphy. Surface-enhanced raman spectroscopy of self-assembled monolayers: sandwich architecture and nanoparticle shape dependence. *Anal. Chem.*, 77(10):3261–3266, 2005.

[117] C. J. Murphy, T. K. Sau, A. M. Gole, C. J. Orendorff, J. Gao, L. Gou, S. E.

Hunyadi, and T. Li. Anisotropic metal nanoparticles: synthesis, assembly, and optical applications. *J. Phys. Chem. B*, 109(29):13857–13870, 2005.

[118] C.-Z. Li, K. B. Male, S. Hrapovic, and J. H. T. Luong. Fluorescence properties of gold nanorods and their application for DNA biosensing. *Chem. Commun.*, pages 3924–3926, 2005.

[119] A. Gole, C. J. Orendorff, and C. J. Murphy. Immobilization of gold nanorods onto acid-terminated self-assembled monolayers via electrostatic interactions. *Langmuir*, 20(17):7117–7122, 2004.

[120] A. Gole and C. J. Murphy. Polyelectrolyte-coated gold nanorods: synthesis, characterization and immobilization. *Chem. Mater.*, 17(6):1325–1330, 2005.

[121] Z. L. Wang, M. B. Mohamed, S. Link, and M. A. El-Sayed. Crystallographic facets and shapes of gold nanorods of different aspect ratios. *Surface Science*, 440(1-2):L809 – L814, 1999.

[122] B. Nikoobakht and M. A. El-Sayed. Evidence for bilayer assembly of cationic surfactants on the surface of gold nanorods. *Langmuir*, 17(20):6368–6374, 2001.

[123] C. J. Johnson, E. Dujardin, S. A. Davis, C. J. Murphy, and S. Mann. Growth and form of gold nanorods prepared by seed-mediated, surfactant-directed synthesis. *J. Mater. Chem.*, 12:1765–1770, 2002.

[124] J. Gao, C. M. Bender, and C. J. Murphy. Dependence of the gold nanorod aspect ratio on the nature of the directing surfactant in aqueous solution. *Langmuir*, 19(21):9065–9070, 2003.

[125] X. Hu, W. Cheng, T. Wang, E. Wang, and S. Dong. Well-ordered end-to-end linkage of gold nanorods. *Nanotechnology*, 16(10):2164, 2005.

[126] J. N. K. Mbindyo, B. D. Reiss, B. R. Martin, C. D. Keating, M. J. Natan, and T. E.Mallouk. DNA-directed assembly of gold nanowires on complementary surfaces. *Adv. Mater.*, 13(4):249–254, 2001.

[127] K. G. Thomas, S. Barazzouk, B. I. Ipe, S. T. S. Joseph, and P. V. Kamat. Uniaxial plasmon coupling through longitudinal self-assembly of gold nanorods. *J. Phys. Chem. B*, 108(35):13066–13068, 2004.

[128] S. Zhang, X. Kou, Z. Yang, Q. Shi, G. D. Stucky, L. Sun, J. Wang, and C. Yan. Nanonecklaces assembled from gold rods, spheres, and bipyramids. *Chem. Commun*, (18):1816–1818, 2007.

[129] P. K. Sudeep, S. T. S. Joseph, and K. G. Thomas. Selective detection of cysteine and glutathione using gold nanorods. *J. Am. Chem. Soc.*, 127(18):6516–6517, 2005.

[130] S. T. S. Joseph, B. I. Ipe, P. Pramod, and K. G. Thomas. Gold nanorods to nanochains: Mechanistic investigations on their longitudinal assembly using α,ω-alkanedithiols and interplasmon coupling. *J. Phys. Chem. B*, 110(1):150–157, 2006.

[131] K. K. Caswell, J. N. Wilson, U. H. F Bunz, and C. J. Murphy. Preferential end-to-end assembly of gold nanorods by biotin-streptavidin connectors. *J. Am. Chem. Soc.*, 125(46):13914–13915, 2003.

[132] L. F. Chi, S. Rakers, M. Hartig, H. Fuchs, and G. Schmid. Preparation

and characterization of langmuir monolayers and langmuir-blodgett films of nanosized au_{55}-clusters. *Thin Solid Films*, 327-329:520 – 523, 1998.

[133] J. J. Brown, J. A. Porter, C. P. Daghlian, and U. J. Gibson. Ordered arrays of amphiphilic gold nanoparticles in langmuir monolayers. *Langmuir*, 17(26):7966–7969, 2001.

[134] M. Sastry, A. Gole, and V. Patil. Lamellar langmuir-blodgett films of hydrophobized colloidal gold nanoparticles by organization at the air-water interface. *Thin Solid Films*, 384(1):125 – 131, 2001.

[135] C. N. R. Rao and K. P. Kalyanikutty. The liquid-liquid interface as a medium to generate nanocrystalline films of inorganic materials. *Acc. Chem. Res.*, 41(4):489–499, 2008.

[136] C. N. R. Rao, G. U. Kulkarni, P. J. Thomas, V. V. Agrawal, and P. Saravanan. Films of metal nanocrystals formed at aqueous-organic interfaces. *J. Phys. Chem. B*, 107(30):7391–7395, 2003.

[137] V. V. Agrawal, G. U. Kulkarni, and C. N. R. Rao. Nature and properties of ultrathin nanocrystalline gold films formed at the organic-aqueous interface. *J. Phys. Chem. B*, 109(15):7300–7305, 2005.

[138] H. W. Kroto, J. R. Heath, S. C. O'Brien, R. F. Curl, and R. E. Smalley. C_{60}: Buckminsterfullerene. *Nature*, 318:162–163, 1985.

[139] S. Iijima. Helical microtubules of graphitic carbon. *Nature*, 354:56–58, 1991.

[140] W. K Hsu, J. P. Hare, M. Terrones, H.W. Kroto, D. R. M. Walton, and P. J. F. Harris. Condensed-phase nanotubes. *Nature*, 377:687, 1995.

[141] M. Endo, K. Takeuchi, S. Igarashi, K. Kobori, M. Shiraishi, and H. W. Kroto. The production and structure of pyrolytic carbon nanotubes (PCNTs). *J. Phys. Chem. Solids*, 54(12):1841 – 1848, 1993.

[142] S. Iijima and T. Ichihashi. Single-shell carbon nanotubes of 1-nm diameter. *Nature*, 363:603 – 605, 1993.

[143] D. S. Bethune, C. H. Klang, M. S. de Vries, G. Gorman, R. Savoy, J. Vazquez, and R. Beyers. Cobalt-catalysed growth of carbon nanotubes with single-atomic-layer walls. *Nature*, 363:605 – 607, 1993.

[144] H. Dai, A. G. Rinzler, P. Nikolaev, A. Thess, D. T. Colbert, and R. E. Smalley. Single-wall nanotubes produced by metal-catalyzed disproportionation of carbon monoxide. *Chem. Phys. Lett.*, 260(3-4):471 – 475, 1996.

[145] Y. Saito, M. Okuda, and T. Koyama. Carbon nanocapsules and single-wall nanotubes formed by arc evaporation. *Surf. Rev. Lett.*, 3(1):863–867, 1996.

[146] Y. Saito, K. Kawabata, and M. Okuda. Single-layered carbon nanotubes synthesized by catalytic assistance of rare-earths in a carbon arc. *J. Phys. Chem.*, 99(43):16076–16079, 1995.

[147] C. Journet, W. K. Maser, P. Bernier, Loiseau, M. Lamy de la Chapelle, S. Lefrant, P. Deniard, R. Lee, and J. E. Fischer. Large-scale production of single-walled carbon nanotubes by the electric-arc technique. *Nature*, 388:756–758, 1997.

[148] A. Thess, R. Lee, P. Nikolaev, H. Dai, P. Petit, J. Robert, C. Xu, Y. H. Lee, S. G. Kim, A. G. Rinzler, D. T. Colbert, G. E. Scuseria, D. Tomnek, J. E.

Fischer, and R. E. Smalley. Crystalline ropes of metallic carbon nanotubes. *Science*, 273(5274):483–487, 1996.

[149] B. C. Satishkumar, A. Govindaraj, R. Sen, and C. N. R. Rao. Single-walled nanotubes by the pyrolysis of acetylene-organometallic mixtures. *Chem. Phys. Lett.*, 293(1-2):47 – 52, 1998.

[150] S. Seraphin and D. Zhou. Singlewalled carbon nanotubes produced at high yield by mixed catalysts. *Appl. Phys. Lett.*, 64(16):2087(1–3), 1994.

[151] F. Li H. M. Cheng and, G. Su, H. Y. Pan, L. L. He, X. Sun, , and M. S. Dresselhaus. Large-scale and low-cost synthesis of single-walled carbon nanotubes by the catalytic pyrolysis of hydrocarbons. *Appl. Phys. Lett.*, 72(25):3282(1–3), 1998.

[152] B. Kitiyanan, W. E. Alvarez, J. H. Harwell, and D. E. Resasco. Controlled production of single-wall carbon nanotubes by catalytic decomposition of CO on bimetallic Co-Mo catalysts. *Chem. Phys. Lett.*, 317(3-5):497 – 503, 2000.

[153] http://www.ou.edu/engineering/nanotube.

[154] C. N. R. Rao, A. Muller, and A. K. Cheetham. *The Chemistry of Nanomaterials, WileyVCH Verlag GmbH & Co.* 2004.

[155] M. S. Dresselhaus and P. C. Eklund. Phonons in carbon nanotubes. *Appl. Phys. Lett.*, 49(6):705 – 814, 2000.

[156] A. K. Geim and K. S. Novoselov. The rise of graphene. *Nat. Mater.*, 6:183 – 191, 2007.

[157] K. S. Novoselov, D. Jiang, F. Schedin, T. J. Booth, V. V. Khotkevich, S. V. Morozov, and A. K. Geim. Two-dimensional atomic crystals. *Proc. Natl. Acad. Sci. U.S.A.*, 102(30):10451–10453, 2005.

[158] C.N.R. Rao, A.K. Sood, K.S. Subrahmanyam, and A. Govindaraj. Graphene: The new two-dimensional nanomaterial. *Angew. Chem. Int. Ed.*, 48(42):7752–7777, 2009.

[159] S. Park and R. S. Ruoff. The rise of graphene. *Nat. Nanotechnol.*, 4:217 – 224, 2009.

[160] K. S. Subrahmanyam, L. S. Panchakarla, A. Govindaraj, and C. N. R. Rao. Simple method of preparing graphene flakes by an arc-discharge method. *J. Phys. Chem. C*, 113(11):4257–4259, 2009.

[161] M. S. Dresselhaus, G. Dresselhaus, K. Sugihara, I. L. Spain, and H. A. Goldberg. *Graphite Fibers and Filaments. (Springer-Verlag, Berlin), vol.5.* 1988.

[162] L.M. Malard, M.A. Pimenta, G. Dresselhaus, and M.S. Dresselhaus. Raman spectroscopy in graphene. *Phys. Rep.*, 473(5-6):51 – 87, 2009.

[163] M. S. Dresselhaus, A. Jorio, M. Hofmann, G. Dresselhaus, and R. Saito. Perspectives on carbon nanotubes and graphene raman spectroscopy. *Nano Lett.*, 10(3):751–758, 2010.

[164] A. C. Ferrari and J. Robertson. Raman spectroscopy of amorphous, nanostructured, diamondlike carbon, and nanodiamond. *Phil. Trans. R. Soc. Lond. A*, 362(1824):2477–2512, 2004.

[165] M.S. Dresselhaus, G. Dresselhaus, R. Saito, and A. Jorio. Raman spectroscopy of carbon nanotubes. *Phys. Rep.*, 409(2):47 – 99, 2005.

[166] K. Sasaki, R. Saito, G. Dresselhaus, M. S. Dresselhaus, H. Farhat, and J. Kong. Curvature-induced optical phonon frequency shift in metallic carbon nanotubes. *Phys. Rev. B*, 77(24):245441, 2008.

[167] R. Saito, A. Jorio, A. G. Souza Filho, G. Dresselhaus, M. S. Dresselhaus, and M. A. Pimenta. Probing phonon dispersion relations of graphite by double resonance raman scattering. *Phys. Rev. Lett.*, 88(2):027401, 2001.

[168] J. Jiang, R. Saito, Ge. G. Samsonidze, A. Jorio, S. G. Chou, G. Dresselhaus, and M. S. Dresselhaus. Chirality dependence of exciton effects in single-wall carbon nanotubes: Tight-binding model. *Phys. Rev. B*, 75(3):035407, 2007.

[169] M. A. Pimenta, G. Dresselhaus, M. S. Dresselhaus, L. G. Cancado, A. Jorio, and R. Saito. Studying disorder in graphite-based systems by raman spectroscopy. *Phys. Chem. Chem. Phys.*, 9:1276–1290, 2007.

[170] A. Jorio, M. Dresselhaus, and G. Dresselhaus. *Carbon Nanotubes. Advanced Topics in the Synthesis, Structure, Properties and Applications; Springer: Berlin/Heidelberg, Vol. 111, pp 495-530.* 2008.

CHAPTER 2

Growth Kinetics of Metallic and Semiconducting Nanomaterials by a Combined Use of Small Angle X-ray Scattering and Other Techniques*

Summary

This chapter describes the results of detailed investigations of the growth kinetics of metallic and semiconducting nanocrystals by the combined use of small angel X-ray scattering and transmission electron microscopy along with other spectroscopic techniques.The growth of gold nanocrystals prepared by the reduction of tetrachloroauric acid by tetrakis(hydroxymethyl)phosphonium chloride, which allows slow reduction, is investigated by small-angle X-ray scattering and isothermal titration calorimetry in combination with transmission electron microscopy. The growth of the nanocrystals does not follow the diffusion-limited Ostwald ripening but instead follows a sigmoidal rate curve. The activation energy obtained from the temperature-dependent growth study is very small. The heat change associated with the growth is determined for the first time as approximately 10 kcal mol^{-1} per 1 nm increase in the nanocrystal diameter.

The growth of capped CdSe and CdS nanocrystals formed by the reaction of

*Papers based on this work have been published in *Small* **(2008)**, *Chem-Asian J* **(2008)**, *Phys. Chem. Chem. Phys.* **(2011)**

selenium or sulphur with cadmium stearate in toluene solution in the presence of dodecanthiol or trioctylphosphine oxide has been investigated by a variety of techniques to obtain reliable data. Although certain qualitative observations suggest growth of the nanocrystals to be controlled by diffusion-limited Ostwald ripening, we have found it is necessary to include the surface reaction term in the growth equation. Thus, the growth of CdSe and CdS nanocrystals have contributions from both diffusion and surface reaction, with a D^3+D^2 type behavior, independent of the capping agent.

In order to examine the applicability of the diffusion-limited Ostwald ripening model to the growth kinetics of nanocrystals, platinum nanocrystals prepared by two different methods have been investigated. One of the methods of synthesis involved the reduction of chloroplatinic acid by sodium citrate while in the other method reduction was carried out in the presence of a capping agent polyvinylpyrrolidone (PVP). Growth of platinum nanocrystals prepared by citrate reduction in the absence of any capping agent follows a Ostwald ripening growth with a D^3 dependence. In the presence of PVP as the capping agent, the growth of platinum nanocrystals does not follow the Ostwald ripening model, making it necessary to include a surface reaction term in the growth equation. Thus, the growth of platinum nanocrystals in the presence of PVP has contributions both from diffusion and surface reaction, exhibiting a D^3+D^2 type behavior.

2.1 Introduction

Nanocrystals constitute an important class of nanomaterials and chemical routes have proved to be more useful for the synthesis of these materials [1, 2]. The growth mechanism of nanocrystals has recently attracted the attention of a few workers [3]. One of the popular mechanisms employed to explain the growth kinetics of nanocrystals is the diffusion-limited Ostwald ripening process following the Lifshitz-Slyozov-Wagner (LSW) theory [4, 5]. Thus, studies of the growth of ZnO and TiO_2 nanocrystals by Searson and coworkers [6–8] have revealed Ostwald ripening to be the dominant mechanism. Peng *et al.* [9] examined the growth of CdSe and InAs nanocrystals by employing UV-visible absorption spectroscopy to determine the size of nanocrystals and the band widths of the photoluminescence spectra to determine their size distribution. These workers observed a focusing and defocusing effect of the size distribution similar to that expected in Ostwald ripening. Qu *et al.* [10] found a diffusion-limited mechanism in the last stage of the growth in the case of CdSe nanocrystals. Based on an *in situ* transmission electron microscopy (TEM) investigation, Mohamed *et al.* [11] reported a diffusion-controlled growth of small gold nanoclusters. The study of Kondow *et al.* on platinum nanoparticles generated by laser ablation showed that Ostwald ripening was the growth mechanism in the absence of any surfactant [12]. Simonsen *et al.* [13] employed transmission electron microscopy (TEM) for a *in situ* study of Pt nanoparticle sintering on a Al_2O_3 support and observed the growth of the particles to follow the Ostwald ripening process.

There are a few reports in literature where the growth kinetics of nanocrystals are found to deviate from the simple diffusion limited Ostwald ripening model. Thus, Seshadri *et al.* [14] proposed the growth of gold nanoparticles to be essentially

stochastic wherein the nucleation and growth steps are well separated. A recent study of the nucleation and growth of gold nanocrystals by small angle X-ray scattering (SAXS) and UV-vis spectroscopy over very short time scale suggests a surface reaction-limited growth of nanocrystals in the presence of an alkanoic acid [15]. To study the fast growth kinetics, these workers used tetrabutylammonium borohydride as the reducing agent. Theoretical investigations suggest that the growth of nanocrystals could be controlled by the diffusion of particles as well as the reaction at the surface [16]. Thus, Viswanatha *et al.* [17] observed the growth of the ZnO nanocrystals in water to follow a growth mechanism intermediate between diffusion-control and surface reaction-control. These workers also reported the growth kinetics of the ZnO nanocrystals in the absence of any capping agent to deviate from diffusion-controlled Ostwald ripening [18].

Growth kinetics of nanocrystals in the presence of capping agents is controlled by several factors, and signatures of either the diffusion or the reaction- controlled regimes are seen. The effect of capping agents on the growth of nanocrystals has been examined by a few workers [9, 10, 19–25]. For example, the growth of ZnO nanocrystals in the presence of poly(vinyl pyrollidone) (PVP) was reported to show deviations from Ostwald ripening [19]. To our knowledge, information of the mechanism of the growth of nanorods, especially in the presence of capping agents is limited. A useful study in this context is that of Peng and Peng [26, 27] who examined the growth kinetics of CdSe nanorods by UV-vis spectroscopy and TEM images and found the diffusion-controlled model to be valid when the monomer concentration was sufficiently high. At low monomer concentrations, the aspect ratio of the rod decreased due to intra-particle diffusion on the surface of the nanocrystal. Thoma *et al.* [28] have observed anisotropic growth of CdSe in the presence of a surfactant. Based on TEM studies, Pacholski *et al.* [29] proposed

that small ZnO nanoparticles are converted to rods by the oriented attachment mechanism assisted by Ostwald ripening. Based on the estimation of nanorod lengths from XRD peak broadening, Zhu *et al.* [30] have found the growth kinetics of oleic acid-capped ZnO nanorods to deviate from Ostwald ripening.

2.2 Scope of the present investigations

2.2.1 Gold nanocrystals

In view of the limited knowledge of the growth mechanism of metal nanocrystals, we considered it important to investigate the growth kinetics of gold nanocrystals by employing appropriate reagents. We have carried out an *in situ* investigation of the kinetics of growth of gold nanocrystals wherein the growth occurs over relatively long periods of time. For this purpose, we have employed tetrakis(hydroxymethyl)-phosphonium chloride (THPC) as the reducing agent to reduce tetrachloroauric acid ($HAuCl_4$) in aqueous solution to yield a wine-red hydrosol [14, 31]. The use of THPC as the reducing agent has permitted us to study the growth kinetics over period of a few hours, unlike stronger reducing agents such as $NaBH_4$ that require one to study the kinetics over a few minutes. We have employed small angle X-ray scattering (SAXS) to obtain the growth kinetics data, starting with different initial concentrations of $HAuCl_4$. SAXS provides a direct probe to determine the size and shape of nanomaterials and the sampling size is very much larger than that in TEM measurements. Additionally, SAXS is most suited for an *in situ* study of the growth of gold nanocrystals. We have also cross-checked the size distribution of the gold nanocrystals determined by SAXS by TEM at a few points of growth. While TEM is the most direct means to obtain the size distribution of nanostructures,

it is not possible to carry out *in situ* measurements, especially when the initial nanostructures are small in size. Furthermore, the sampling size in TEM is rather small, making statistical averaging or determination of the distribution function less certain. UV-vis spectroscopy is not quite suitable for the determination of the size distribution of metal nanocrystals, the method being sensitive to change in electronic structure, shape, etc.

Our study has enabled us to obtain good kinetic data on the growth of gold nanocrystals. The data, however, do not conform to diffusion-limited Ostwald ripening. We have carried out isothermal titration calorimetric (ITC) measurements on the growth of the gold nanocrystals to obtain an estimate of the heat change associated with the growth, an aspect not examined hitherto in literature.

2.2.2 CdSe and CdS nanocrystals

In order to understand the growth mechanism of II-VI semiconductor nanocrystals, we considered it valuable to investigate the growth kinetics of CdSe and CdS nanocrystals over relatively long periods by employing a variety of techniques. Most of the studies of the growth kinetics of CdSe and CdS nanocrystals reported in the literature are based on UV-vis and photoluminescence (PL) spectroscopies, which are indirect and are strongly affected by the change in the electronic structure of the nanomaterials. We have therefore employed SAXS along with TEM, and UV-vis and PL spectroscopies for our study of the growth kinetics of CdSe and CdS nanocrystals. Employing such independent techniques is important because of the limitations of each of the techniques. We have obtained the size distribution of the nanocrystals by TEM at different times of growth since it is a direct probe to obtain the size, shape, and size distribution of nanostructures.

We have employed a solvothermal reaction between cadmium stearate [$Cd(st)_2$] and selenium or sulfur powder, in the presence of dodecanethiol or trioctylphosphine oxide (TOPO) in toluene and a catalytic amount of tetralin [32, 33]. We have obtained growth-kinetic data starting with different initial concentrations of $Cd(st)_2$, and report the results of this study in this article. Our study has provided good kinetic data on the growth of CdSe and CdS nanocrystals. The data, however, do not conform to diffusion-limited Ostwald ripening in both cases. The growth mechanism in both CdSe and CdS nanocrystals deviates from the diffusion-limited LSW model, requiring the inclusion of an additional contribution from a surface process.

2.2.3 Platinum nanocrystals: Role of the surface

Ostwald ripening as well as other growth models have been reported for both metallic and semiconducting nanomaterials in solution in the literature. It was also seen that surface plays an important role in determining the mechanism. It was of interest to see why Ostwald ripening is not observed as the growth mechanism in the case of nanoparticles and how the surface plays a role when there is a deviation from this mechanism. With this purpose, we have studied the growth kinetics of platinum nanocrystals prepared by two different procedures. In the first synthesis, the platinum nanoparticles were prepared by the reduction of hexachloroplatinate solutions by sodium citrate [34]. In the second synthesis, chloroplatinic acid was reduced in ethylene glycol in the presence of polyvinylpyrrolidone (PVP) as the capping agent [35]. We have employed SAXS along with TEM to investigate the growth kinetics.

2.3 Experimental section

Gold nanocrystals

Gold sols were prepared following the method of Duff *et al.* [31] using alkaline solutions of THPC to reduce $HAuCl_4$. Typically, to an aqueous solution of NaOH (6.25 mL, 25 mM) in a 50 mL beaker, THPC (250 μL, 480 μL of 80% THPC diluted to 10 mL) was added. After 5 min, $HAuCl_4$ (125 μL, 0.006 mmol) was added rapidly while shaking the beaker. In order study the effect of concentration of $HAuCl_4$ on growth of the gold nanocrystals, we also carried out the reactions with 250 μL (0.012 mmol) and 375 μL (0.018 mmol) of 50 mM $HAuCl_4$ solutions. The sols thus produced were typically very dilute, making the study of their growth a more tractable problem. The volume fraction of the particles was of the order of 10^{-4}. Variable temperature measurements over the 276-323 K range were carried out with the $HAuCl_4$ solution (250 μL, 0.012 mmol).

CdSe nanocrystals

To carry out the growth study, CdSe nanocrystals were prepared by the reaction of cadmium stearate and selenium powder in toluene at 250 °C under solvothermal conditions as reported in the literature [32]. The reaction was stopped at different times (1, 2, 3, 4, 5, and 10 h) and the products were analyzed by using TEM and SAXS, and UV-vis and photoluminescence spectroscopies. In a typical synthesis, cadmium stearate (0.2 g, 0.29 mmol) and selenium powder (0.023 g, 0.29 mmol) were added to toluene (20 mL), followed by the addition of tetralin (30.4 μL) and 1-dodecanethiol (17.4 μL). The reaction mixture was sealed in a teflon-lined autoclave (60% filling fraction) and maintained at 250 °C in a hot air oven. The

solid products obtained at different times after the reaction were precipitated with the addition of 2-propanol. The precipitate was collected by centrifugation and redissolved in toluene. To study the effect of the concentration of the reactants on the growth process, we prepared CdSe nanocrystals at a lower concentration of cadmium stearate (0.05 g, 0.07 mmol) keeping the other reaction parameters the same. The samples were taken out after different reaction times (2, 3, 4, 5, and 10 h) for investigation. To study the effect of the capping on the growth process, we prepared CdSe nanocrystals using trioctylphosphine oxide, TOPO, as capping agent (0.0038 g, 0.00 9 mmol) instead of 1-dodecanethiol keeping the other reaction parameters the same. The samples were taken out after different reaction times (2, 3, 4, 5, and 10 h) for investigation.

CdS nanocrystals

To carry out the growth study, CdS nanocrystals were prepared by the reaction of cadmium stearate and sulfur powder in toluene at 250 °C under solvothermal conditions as reported in the literature [33]. The reaction was stopped at different times (1, 2, 3, 4, 5, and 10 h) and the products were analyzed by using TEM and SAXS, and UV-vis and photoluminescence spectroscopies. In a typical synthesis, cadmium stearate (0.05 g, 0.07 mmol) was dissolved in toluene (20 mL), and sulfur powder (2.4 mg, 0.07 mmol), tetralin (30.4 μL), and 1-dodecanethiol (17.4 μL) were added under stirring. The reaction mixture was sealed in a teflon-lined autoclave (60% filling fraction) and maintained at 250 °C in a hot air oven. The solid products obtained at different times after the reaction, were precipitated with the addition of 2-propanol. The precipitate was collected by centrifugation and redissolved in toluene.

Platinum nanocrystals

Platinum nanoparticles were prepared by the reduction of chloroplatinic acid by sodium citrate by the procedure reported in the literature [34]. In a typical reaction, 4 mL of 19.3 mM H_2PtCl_6 solution was added to 110 mL of distilled water and was brought to boiling temperature. To the boiling solution, 10 mL of aqueous solution containing 0.15 g of sodium citrate was added and the mixture was refluxed. Small aliquots were collected from the reaction mixture after different reaction times and were cooled in an ice bath to stop the growth. These solutions were used for further measurements.

In the second procedure, platinum nanocrystals were prepared by the reduction in ethylene glycol as reported in the literature [35]. In a typical synthesis, 1 mL of 80 mM H_2PtCl_6 solution in ethylene glycol was rapidly added to 7 mL ethylene glycol which was held at 160 °C that contained both $NaNO_3$ and poly(vinyl pyrrolidone) (PVP). The concentration of $NaNO_3$ and PVP were 33 mM and 30 mM respectively. The mixture was stirred and maintained at 160 °C for the growth. Small aliquots were collected from the reaction mixture after different reaction times and were cooled in an ice bath to stop the growth. Acetone was added to these solutions to precipitate the nanocrystals. The precipitate was collected by centrifugation, dried and redissolved in ethanol for further measurements.

Small Angle X-ray Scattering (SAXS) measurements

The average diameter and diameter distribution of the nanocrystals could be readily obtained by SAXS [36–38]. We performed SAXS measurements with a Bruker-AXS NanoSTAR instrument modified and optimized for solution scattering (See Figure 2.1). The instrument has X-ray tube (Cu Kα radiation, operated at 45 kV/35 mA),

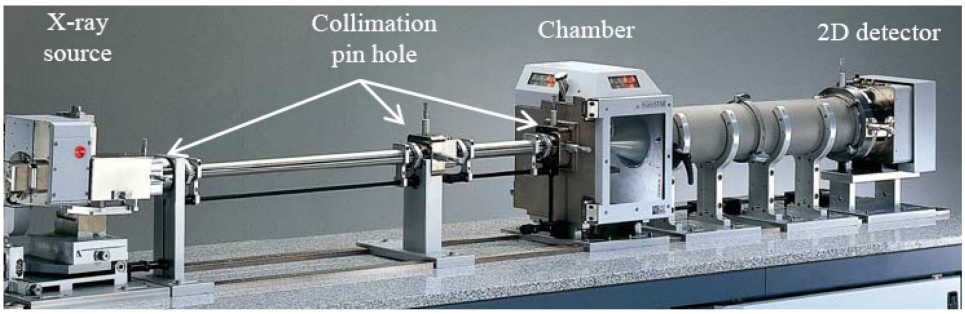

Figure 2.1: SAXS instrument

cross-coupled Gobel mirrors, three pinhole collimation, evacuated beam path, and a 2D gas-detector (HI-STAR) [38]. We recorded the SAXS data in the q range of 0.007 to 0.21Å^{-1}, (i.e, 2θ = 0.1 to 3 °). Solutions of the gold nanocrystals in water were used for the measurements. The nanocrystals in solution was sealed in quartz capillaries (diameter of about 2 mm) for SAXS measurements. Temperature variation studies were carried out by a special heating-cooling sample stage supplied by Bruker-AXS. The concentration of the nanocrystals was sufficiently low to neglect interparticle interference effects. Experimental SAXS data were fitted by the Bruker-AXS DIFFRAC^{plus} NANOFIT software using a solid spherical model. The form factor of the spheres used in this software is that due to Rayleigh [39].

Isothermal titration calorimetric (ITC) experiments

Isothermal titration calorimetric (ITC) experiments were performed using a Microcal VP-ITC instrument at 30 °C [40]. The instrument consists of two identical cells, one for sample and the other for reference (distilled water) and both the cells were maintained at the same temperature. As soon as the gold nanocrystals are formed in beaker, hydrosol was filled in the sample cell of the calorimeter and 2 mL of distilled water taken in the syringe were injected in equal intervals of 5 min-

utes to the sample cell with 1.47 mL capacity. Heat changes for the growth were measured over the 10 to 750 min range. For ITC experiment we have prepared gold hydrosols with two different concentrations of $HAuCl_4$, that is, 250 μL (0.012 mmol) of 50 mM and 375 μL (0.018 mmol) of 50 mM respectively.

TEM measurements

The products obtained after different reaction periods were taken on holey carbon-coated Cu grids for TEM investigations with a JEOL (JEM3010) microscope operating with an accelerating voltage of 300 kV. The diameter distributions were obtained from the magnified micrograph by using a DigitalMicrograph 3.4 software. Typically, 150-200 well separated nanocrystals from three or four micrographs of the same sample were used to obtain the size distribution.

UV-vis and photoluminescence spectroscopies

The UV-vis spectroscopy measurements were performed using a Perkin-Elmer Lambda 900 UV/VIS/NIR spectrophotometer. The nanocrystals were dissolved in toluene, and the solution was used to carry out the UV-vis measurements. Photoluminescence spectra of these solutions were recorded with a Perkin-Elmer model LS55 luminescence spectrophotometer. The average diameter of the nanocrystals was calculated from the absorption peak position using the sizing curves given in the literature [41]. The sizing curves provided the diameter of CdSe and CdS nanocrystals, which was calculated by using TEM and XRD and the first absorption peak position.

2.4 Results and discussion

2.4.1 Gold nanocrystals

In situ SAXS measurements of the gold hydrosols prepared with different concentrations of $HAuCl_4$ were carried out over the 10-700 min range with an exposure time of 600 sec in order to obtain good signal-to-noise ratios. Figure 2.2a and b shows typical intensity vs. scattering vector plots in the logarithmic scale for different times of growth in the case of gold hydrosols prepared respectively with 125 μL (0.006 mmol) and 375 μL (0.018 mmol) of 50 mM $HAuCl_4$ solutions. The

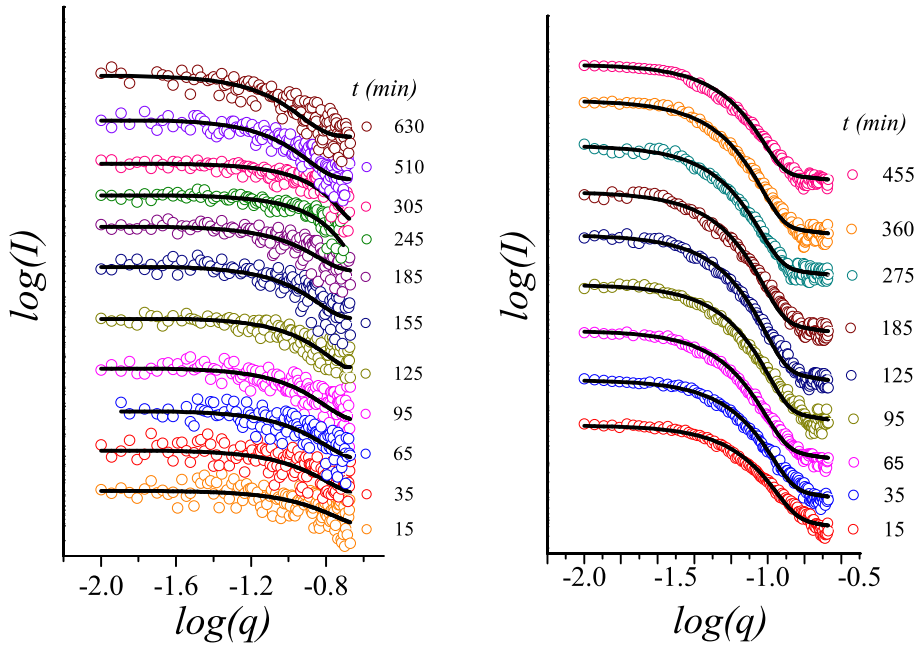

(a) (b)

Figure 2.2: SAXS data for the growth of gold nanocrystals prepared from the solution of (a) 125 μL (0.006 mmol) and (b) 375 μL (0.018 mmol) of 50 mM $HAuCl_4$ after different reaction times. Solid lines are the spherical model fits to the experimental data.

changes observed in SAXS patterns clearly indicate that the nanocrystals grow as

a function of time at both the concentrations of $HAuCl_4$. In order to estimate the average diameter and diameter distribution of gold nanocrystals, we have fitted the experimental SAXS data to the spherical model mentioned in experimental section. The scattering contrast for X-rays is given by the electron density difference between the particle and the solvent. Since gold has higher contrast than the solvent, only the gold particles need to be considered for analysis. In the case of a diluted assembly of spherical particles, neglecting particle interaction, the scattering intensity is given by

$$I(q) \propto \int f(r)V(r)^2P(q,r)dr \tag{2.1}$$

where V(r) and P(q,r) are the volume and form factor, respectively, of a sphere of radius r. The form factor of the sphere is given by

$$P(q,r) = \left[\frac{3\sin(qr) - qr\cos(qr)}{(qr)^3}\right]^2 \tag{2.2}$$

In equation (2.2), q is the scattering vector ($q = 4\pi \sin\theta/\lambda$), where θ is scattering angle and λ is X-ray wave length), and r is the radius of the sphere. To obtain the particle size distribution, we used the Gaussian distribution, $f(r)$, where

$$f(r) = \frac{1}{\sigma\sqrt{2\pi}}e^{-\frac{(r-r_0)^2}{2\sigma^2}} \tag{2.3}$$

Least square refinement yields two parameters, r and σ, where the latter is the standard deviation. The solid curves in the Figure 2.2 are the sphere model fits of the experimental SAXS data. The fits with the experimental patterns are quite good, yielding the average diameter and the diameter distributions for different growth times.

We have estimated the diameter, D, of the gold nanocrystals after different

times of growth from the SAXS data, and show the time evolution of the standard deviation of the diameter distribution, σ_D (i.e., the half-width of the diameter distribution) in Figure 2.3a and b in the case of nanocrystals prepared with two different concentrations of $HAuCl_4$. The insets in Figure 2.3a and b represent the corresponding time evolution of the diameter distribution. With the lower concentration of $HAuCl_4$, the width of the diameter distribution changes periodically with time as can be seen from Figure 2.3a. Initially, the monomer concentration is sufficient to make the growth rate fast and all the nuclei present in the solution grow at the same rate, rendering the width of the distribution narrow. After some time, there will be a shortage of the monomer in solution and the growth rates of the different sizes of nanocrystals in the solution become different, making the distribution broader. Nanocrystals which are smaller than the critical nuclear size then undergo dissolution, thereby increasing the monomer concentration in the solution, and again giving rise to a narrow diameter distribution. Interestingly, we find the width of the diameter distribution to be nearly constant with the time of growth in the case of gold nanocrystals prepared with higher concentrations of $HAuCl_4$ (Figure 2.3b). Thus, when the concentration of $HAuCl_4$ is high, the nanocrystals present in the solution grow at the same rate. As a result, the width of the distribution curves is constant throughout the process. This permits us to merge the diameter distributions at different times by dividing the distribution by the corresponding mean diameter (i.e., by scaling the mean diameter at different times).

Figure 2.4a and b show plots of the normalized frequency (normalized by the maximum counts) against $D/ < D >$ in the case of gold nanocrystals prepared with two concentrations of $HAuCl_4$, 125 μL (0.006 mmol) and 375 μL (0.018 mmol) of 50 mM $HAuCl_4$ respectively. In the case of the nanocrystals prepared with the

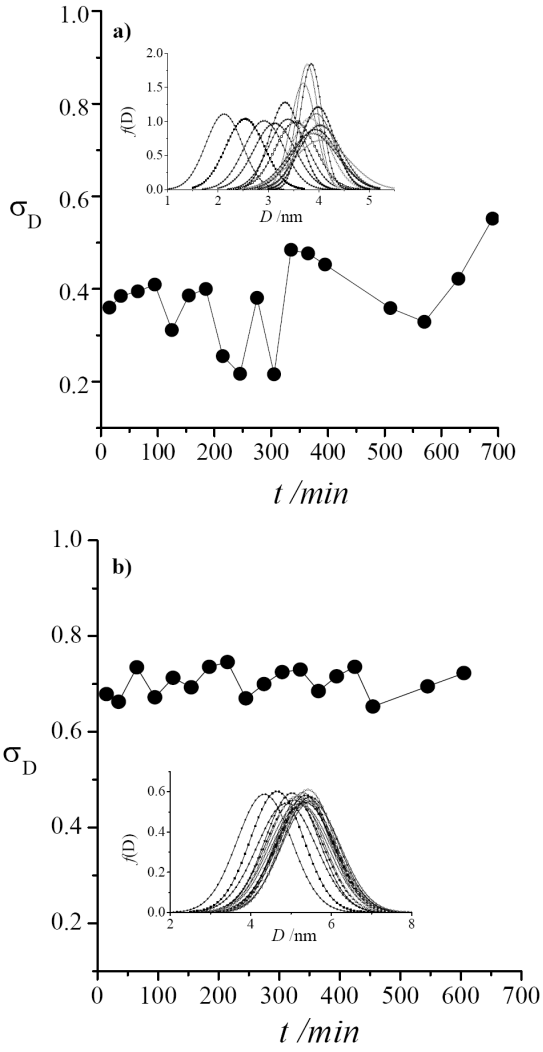

Figure 2.3: Time evolution of the σ_D of diameter distribution of the gold nanocrystals prepared from (a) 125 μL (0.006 mmol), and (b) 375 μL (0.018 mmol) of 50mM $HAuCl_4$. Insets represent the corresponding time evolution of diameter distribution of the gold nanocrystals. The distributions are obtained from the spherical model fits to the experimental SAXS data, recorded after different reaction times (15-690 min). The first curve (closed circles) is at 15 min and the last (open stars) is at 690 min in (a) and 605 min in (b).

lower concentration of $HAuCl_4$, we do not obtain as good a universal curve (Figure 2.4a) as with the higher concentration (Figure 2.4b). In the case of the latter, all the data collapse to a nice single curve that can be represented by the Gaussian

distribution function (solid line).

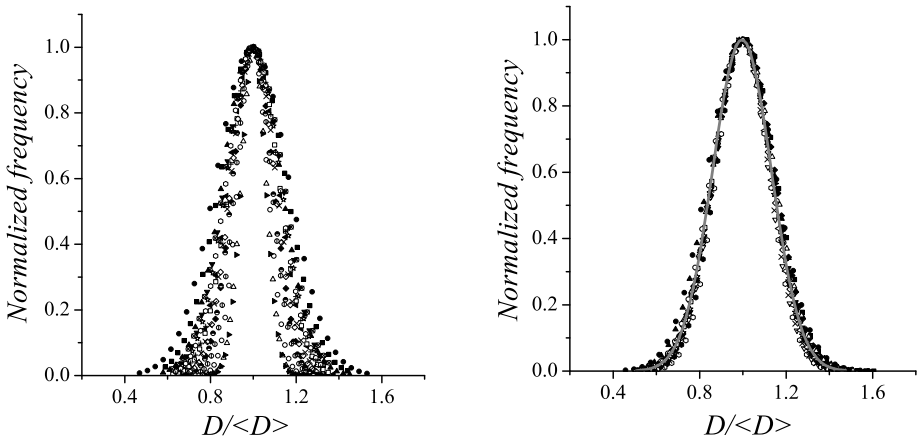

(a) (b)

Figure 2.4: Universal diameter distribution curves of gold nanocrystals obtained by scaling the mean diameter at different times (15-690 min): nanocrystals prepared from a) 125 μL (0.006 mmol) and b) 375 μL (0.018 mmol) of 50 mM $HAuCl_4$. Different symbols represent the size distributions obtained after different times of reaction by scaling the mean diameter. Solid curve in (b) represents the Gaussian distribution function.

We have plotted the average diameter of gold nanocrystals prepared with three different concentrations of $HAuCl_4$ against time in Figure 2.5. The diameter of the gold nanocrystals varies from 2.1 to 4 nm, from 3.1 to 5.2 nm and from 4.3 to 5.4 nm respectively when the starting $HAuCl_4$ concentration is 0.006, 0.012 and 0.018 mmol. With increasing concentration of $HAuCl_4$, the diameter of gold nanocrystals increases, higher monomer concentrations favoring the formation of bigger gold nanocrystals. The growth process saturates early when the concentration of $HAuCl_4$ is high.

We have carried out TEM measurements at a few points during the growth. In Figure 2.6, we show the typical TEM images of gold nanocrystals prepared with 0.012 mmol of $HAuCl_4$ after different periods of growth to illustrate how the size of

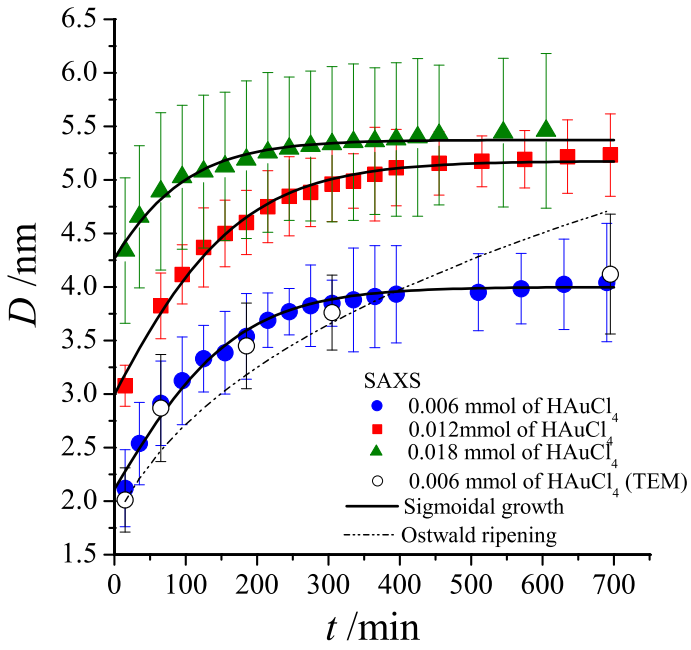

Figure 2.5: Time evolution of the average diameter (D) of the gold nanocrystals obtained from SAXS for different concentrations of $HAuCl_4$ (solid symbols). TEM data are shown by open circles. Error bars indicating the standard deviations of the average diameter are shown. Solid curves represent the sigmoidal growth model fits to the experimental data. Dotted curve is the Ostwald ripening model fit to the experimental data.

the gold nanocrystals increases with increasing the growth time. We have estimated the average diameter and the diameter distribution of gold nanocrystals at different stages of the growth from the TEM images. We have plotted the average diameter obtained from TEM images in Figure 2.5 (open symbols) in the case of 0.012 mmol of $HAuCl_4$. Although the TEM data are not expected to as statistically satisfactory as SAXS, the diameter distributions obtained from TEM and SAXS after 15, 65, 185, and 690 min of growth are in good agreement.

The diameter distribution of gold nanocrystals obtained from SAXS and TEM are both symmetric and are best described by Gaussian distribution. The LSW

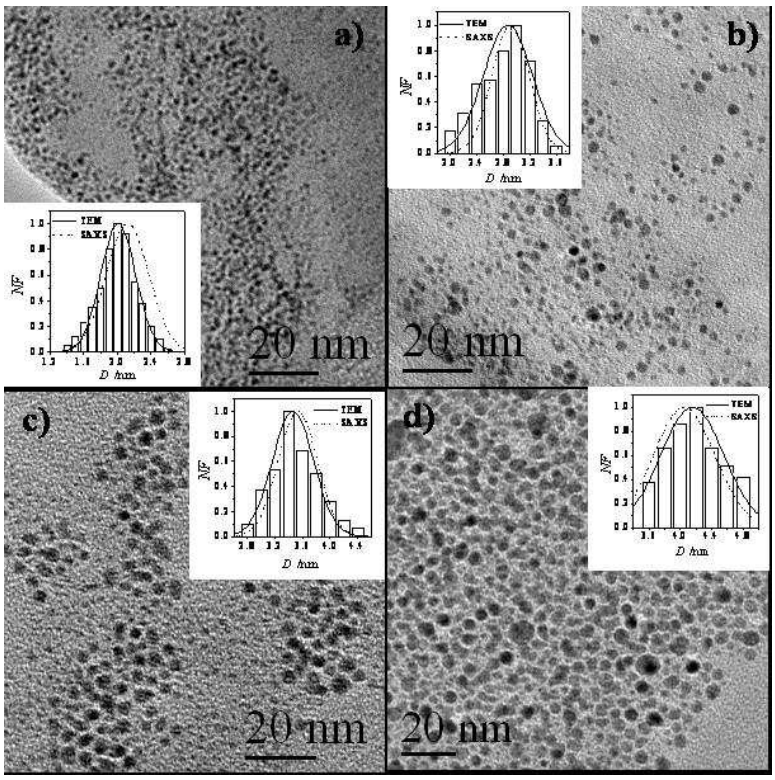

Figure 2.6: TEM images of gold nanocrystals prepared from 125 μL (0.006 mmol) of 50 mM $HAuCl_4$, obtained after a) 15, b) 65, c) 185, and d) 630 min of growth. Insets compare the diameter distributions obtained from TEM and SAXS for the same time of growth. NF: normalized frequency.

theory of growth, on the other hand, predicts an asymmetric size distribution. It is possible to obtain a more symmetric size distribution within the LSW theory when the volume fraction is high. In our study, the volume fraction is only of the order of 10^{-4}, and it, therefore, appears that the growth mechanism is different from Ostwald ripening. If the diffusion-limited Ostwald ripening according to LSW theory [4, 5] was the sole contributor for the growth, the rate law would be given by

$$D^3 - D_0^3 = Kt \tag{2.4}$$

where D is the average diameter at time t and D_0 is the average initial diameter

of the nanocrystals. The rate const K is given by $K = 8\gamma d V_m^2 C_\infty / 9RT$, where d is the diffusion constant at temperature T, V_m the molar volume, γ the surface energy, and C_∞ the equilibrium concentration at a flat surface. We tried to fit the D(t) data obtained from SAXS to the Ostwald ripening model in the case of the gold nanocrystals prepared with different concentrations of $HAuCl_4$ and found that it was not possible to fit the D(t) data by Equation (2.4). A typical fit to the Equation (2.4) of the D(t) data of the gold nanocrystals is shown in Figure 2.5 by the broken curve. The fit is unsatisfactory with a reduced χ^2 of 0.14 and a coefficient of determination, R^2, of 0.536. This result suggests that the growth process is different from the diffusion-limited Ostwald ripening. We have tried to fit the D(t) data of the gold nanocrystals to the surface-limited reaction model ($D^2 \propto t$) or a combined model ($BD^3 + CD^2 + const = t$) which contains both diffusion limited and surface-limited growth [17, 42]. We have found that the fit of the data either to the surface reaction model or to a combined model to be unsatisfactory.

In order to fit the experimental D(t) data of the gold nanocrystals, we have, therefore, used a sigmoidal growth model [14]

$$< D >= \frac{D_0}{(1 - \frac{D_0}{D_\infty})exp(-\gamma t) + \frac{D_0}{D_\infty}} \tag{2.5}$$

where D_0 is average initial diameter of the nanocrystals, D_∞ the mean diameter at infinite time and γ the rate constant. The remarkable goodness of fits (for example, $\chi^2 = 0.004$ and $R^2 = 0.987$ for gold nanocrystals prepared with 0.006 mmol of $HAuCl_4$) over the entire range of experimental data by the sigmoidal growth equation is shown by thick solid curve in the Figure 2.5. The values of D_0, D_∞ and γ are 2.1 nm, 4 nm, and 0.011 min^{-1}; 3 nm, 5.2 nm, and 0.010 min^{-1}; and

4.3 nm, 5.4 nm, and 0.012 min^{-1} for gold nanocrystals prepared with 0.006, 0.012 and 0.018 mmol of $HAuCl_4$, respectively.

In a sigmoidal growth process, there is first an induction period when small nuclei are formed, followed by the growth or propagation step. After the growth process, there will be a termination step when the reacting species get exhausted. The fits for D(t) data for the gold nanocrystals to the sigmoidal growth model suggest that there are three stages of the total process, nucleation, growth and the saturation. It also implies that nucleation and growth process are well separated. In principle, the higher the monomer concentration, faster is the nucleation process [27]. Thus, when the $HAuCl_4$ concentration is high, the initial nucleation process occurs faster and the growth process saturates early ($t \approx 150$ min). The particle size varies from 4.3 to 5.4nm at the highest concentration of $HAuCl_4$ in the present study as can be seen in from Figure 2.5 (solid green triangles). When the concentration of $HAuCl_4$ or the monomer concentration is small, the nucleation rate becomes slow and the available gold atoms present in the solution allows the growth of the particle to occur over a longer period ($t \approx 320$ min). The particle size here varies from 2.1 to 4 nm (see Figure 2.5, solid blue circles).

We have examined the effect of temperature on the growth kinetics of gold nanocrystals by carrying out *in situ* SAXS experiments under different temperatures. In Figure 2.7a, we show the result obtained with a starting $HAuCl_4$ concentration of 0.012 mmol. The diameter of the gold nanocrystals varies from 2.7 to 4.3, from 3.1 to 5.1, and from 3.2 to 5.8 nm at 276, 298, and 323K respectively. Thus, the diameter of the gold nanocrystals increases with the increasing temperatures for a given time. In Figure 2.7a, we also show the sigmoidal fit to the experimental D(t) data (see solid black curves). From these data, we have derived the values of γ in Equation (2.5) at different temperatures. A plot of $\ln(\gamma)$ against inverse

temperature is given in Figure 2.7b. This plot yields an activation energy for the growth process of one kcal mol^{-1}.

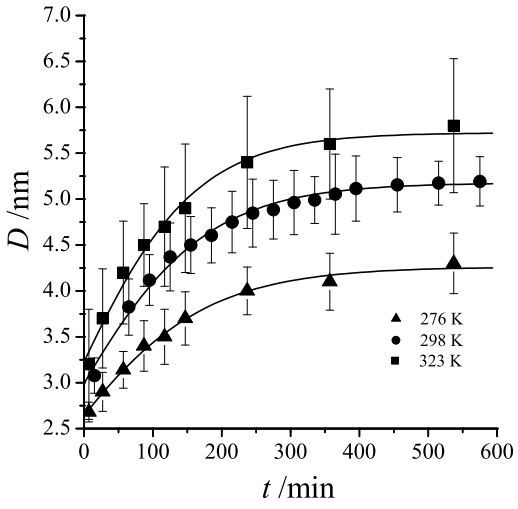

(a)

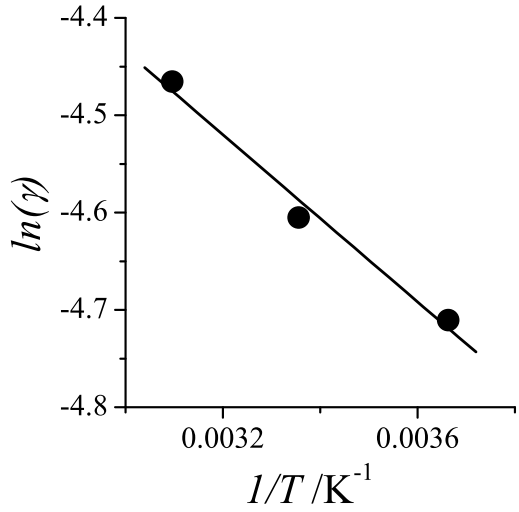

(b)

Figure 2.7: (a) Time evolution of the average diameter (D) of gold nanocrystals prepared from 250 μL (0.012 mmol) of 50 mM $HAuCl_4$ as function of temperature, obtained from SAXS. Error bars indicating the standard deviations of the average diameter are shown. (b) Arrhenius plot for the variation of γ.

We have also derived the activation energy by the temperature variation of the half width of the diameter distribution, σ. The plot of $\ln(\sigma)$ against 1/T (Figure 2.8) gives an activation energy of 3.4 kcal mol^{-1}. Clearly the growth of gold nanocrystals, under the reaction conditions employed, is associated with a low activation energy. The activation energy for the nucleation process could, however, be high, but we have not examined this regime of the dynamics.

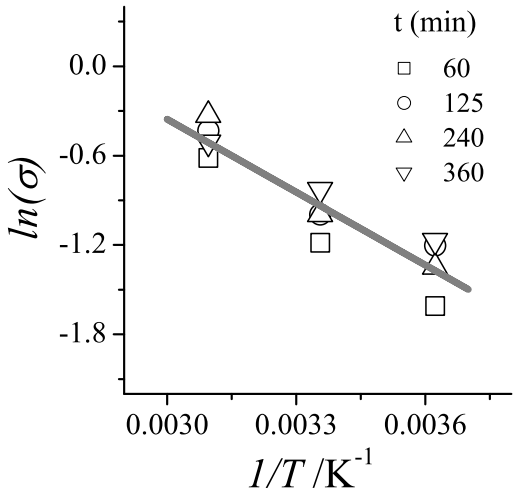

Figure 2.8: Arrhenius plot for σ

In order to understand the thermodynamics of the growth of gold nanocrystals, we have measured the change in heat associated with the growth of gold nanocrystals prepared with starting $HAuCl_4$ concentrations of 0.012 and 0.018 mmol by carrying out ITC measurements (see Figure 2.9). The heat change associated with growth is exothermic as expected and the curves in Figure 2.9 shows a variation opposite to that of the diameter in Figure 2.5. In the case of gold nanocrystals prepared with 0.018 mmol of $HAuCl_4$, the heat change saturates around t≈135 min; compared to 300 min in the case of gold nanocrystals prepared with 0.012 mmol of $HAuCl_4$. The heat change associated with the growth of gold nanocrys-

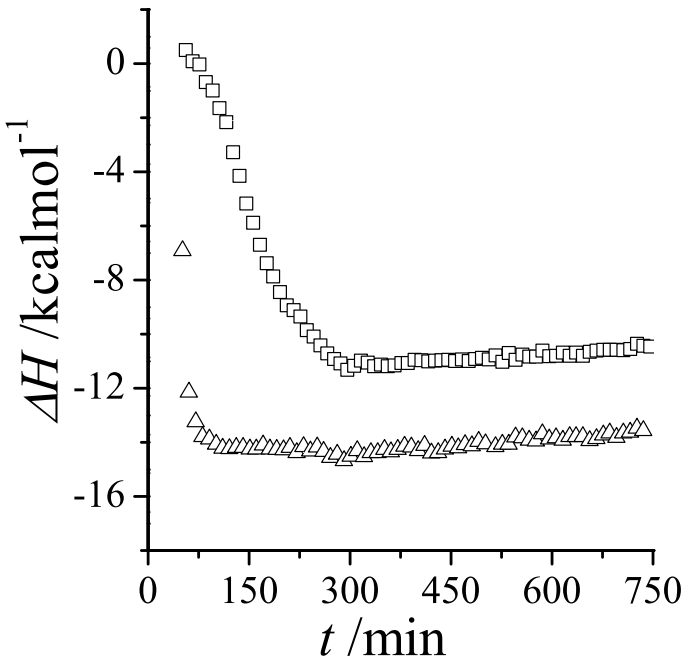

Figure 2.9: Time evolution of the heat change associated with the growth of gold nanocrystals prepared with different concentrations of HAuCl4 obtained from ITC: 0.012 mmol of $HAuCl_4$ (squares) and 0.018 mmol of $HAuCl_4$ (triangles).

tals prepared from the higher concentration of $HAuCl_4$ is larger than that found with the lower concentration. These results indicate a close relation between the variation of heat change and of the nanocrystal diameter.

In Figure 2.10, we have plotted heat change associated with the growth against nanocrystal diameter by making use of the data in Figure 2.5. The heat change varies linearly with the diameter and saturates at large diameters. From the linear regime (correlation coefficients, R of 0.98 and 0.99 for 0.012 and 0.018 mmol concentrations of $HAuCl_4$, respectively), we obtain for first time, the value of heat change per nm of growth of nanocrystal. Thus, the value obtained from the slope of the linear fits are 11 and 10 kcal mol^{-1} per nm for the growth of gold nanocrystals for the starting $HAuCl_4$ concentrations of 0.012 and 0.018 mmol, respectively.

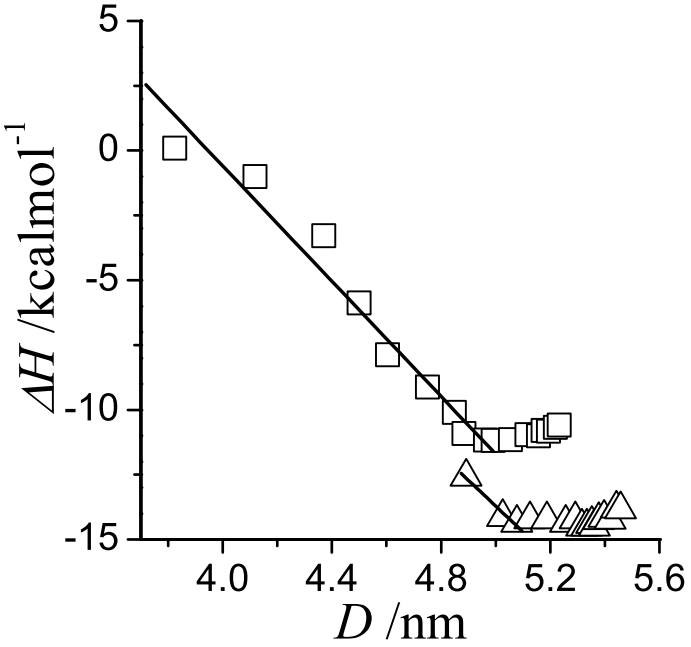

Figure 2.10: Plots of heat change associated with the growth against the diameter of the gold nanocrystal obtained from SAXS (Figure 2.5). Solid lines are the linear fit to the experimental data over the growth range.

2.4.2 CdSe and CdS nanocrystals

SAXS measurements on the growth of dodecanethiol capped CdSe nanocrystals were carried out at different initial concentrations of $Cd(st)_2$. Figure 2.11a and b shows typical logarithmic scale plots of intensity versus scattering vector for different times of growth in the case of nanocrystals prepared with 0.05 g (0.07 mmol) and 0.2 g (0.29 mmol) of $Cd(st)_2$, respectively. The changes observed in the SAXS patterns clearly indicate that the nanocrystals grow as a function of time at both concentrations of $Cd(st)_2$ investigated. To estimate the average diameter and diameter distribution of CdSe nanocrystals, we have fitted the experimental SAXS data to the spherical model mentioned in the Experimental Section. The scattering contrast for X-rays is given by the electron-density difference between the particle

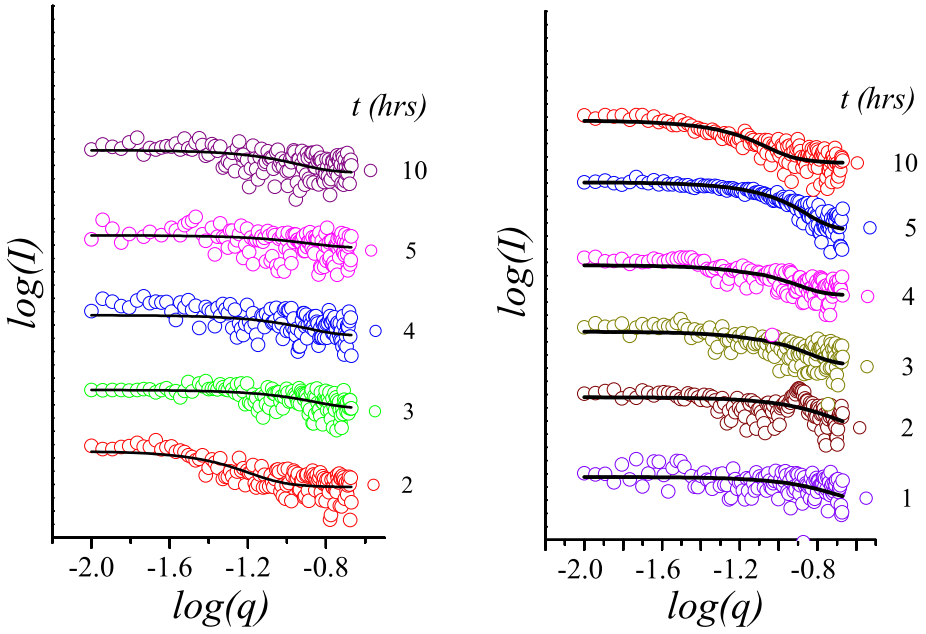

(a) (b)

Figure 2.11: SAXS data for the growth of CdSe nanocrystals prepared from (a) 0.05 g (0.07 mmol), and (b) 0.2 g (0.29 mmol) of cadmium stearate after different times of the reaction. Solid lines are the spherical model fits to the experimental data.

and the solvent. As CdSe has a higher contrast than the solvent, only the CdSe particles need to be considered for analysis. In the case of a diluted assembly of spherical particles, neglecting particle interaction, the scattering intensity is given by Equation (2.1). The solid curves in Figure 2.11 are the sphere-model fits of the experimental SAXS data. The fits with the experimental patterns are quite good, yielding the average diameter, as well as the diameter distributions for different growth times.

We have estimated the diameter, D, of the CdSe nanocrystals after different periods of growth from the SAXS data, and show the time evolution of the diameter distribution in Figure 2.12(a) in the case of nanocrystals prepared with 0.2 g (0.29

mmol) of $Cd(st)_2$. Figure 2.12(b) represents the corresponding time evolution of the standard deviation of the diameter distribution, σ_D (i.e. half-width of the diameter distribution). The width of the diameter distribution increases up to a certain time, undergoes a sudden drop, and finally reaches a maximum value. We have observed a similar fluctuation in the diameter distribution in the case of CdSe nanocrystals prepared from a lower concentration of $Cd(st)_2$. Such focusing and defocusing of the diameter and length distributions has been noticed earlier in the case of CdSe nanoparticles [9] and of ZnO nanorods [43]. When the monomer concentration gets depleted, arising from the faster growth of the nanocrystals, the smaller nanocrystals start to shrink, while the bigger ones keep growing. The size distribution, therefore, becomes broader (e.g., t=3 hrs). Dissolution of the small nanocrystals again enriches the monomer concentration in the solution, with the growth of the bigger nanocrystals continuing through the diffusion of the monomer from solution to the nanocrystals surface, giving rise to a focusing of the diameter distribution (e.g., t=4 to 5 hrs). The focusing and defocusing of the diameter distribution is, thus, dependent on the variation of the monomer concentration in the solution, indicating that the growth of CdSe nanocrystals occurs, at least partly, by diffusion of monomer from the solution to the surface of the nanocrystals.

We have carried out TEM measurements at a few points during the growth of the CdSe nanocrystals. Figure 2.13 shows typical TEM images of CdSe nanocrystals prepared with (0.2 g, 0.29 mmol) of $Cd(st)_2$ after different periods of growth to illustrate how the size of the CdSe nanocrystals increases with increasing growth time. We have estimated the average diameter and the diameter distribution of CdSe nanocrystals at different stages of the growth from the TEM images. Although the TEM data are not statistically as satisfactory as SAXS, the diameter

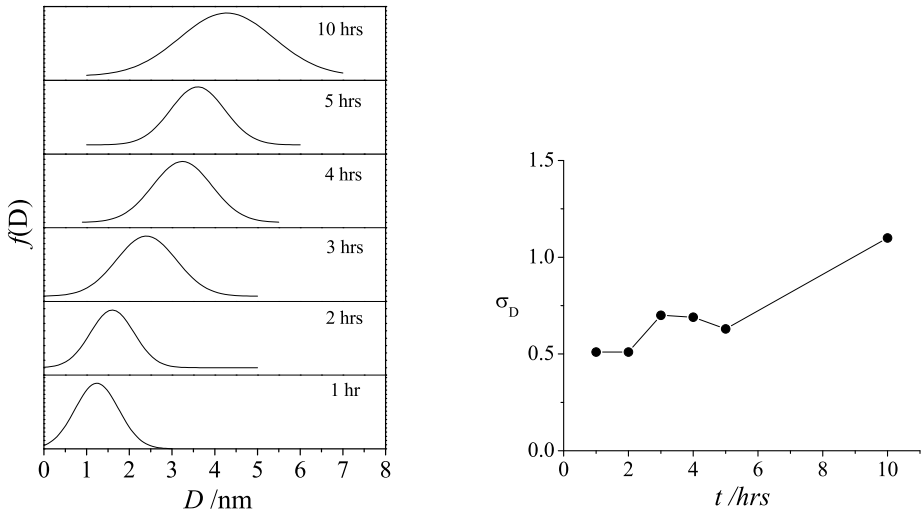

(a) (b)

Figure 2.12: (a) Time evolution of diameter distribution of the CdSe nanocrystals prepared from 0.2g (0.29 mmol) of cadmium stearate and (b) the corresponding time evolution of the standard deviation, σ_D, of diameter distribution. The distributions are obtained from the spherical model fits to the experimental SAXS data, recorded after different reaction times (1-10 hrs).

distributions obtained from TEM and SAXS after 3, 4, 5, and 10 h of growth show good agreements.

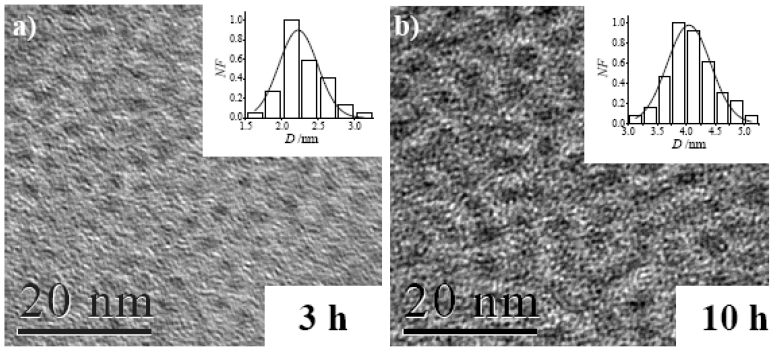

Figure 2.13: TEM images of CdSe nanocrystals prepared from 0.2 g (0.29 mmol) of cadmium stearate obtained after a) 3 and b) 10 hrs of growth. Insets show the diameter distributions obtained from TEM. NF: normalized frequency.

We have also carried out UV-vis and PL spectroscopy measurements to obtain additional information on the growth kinetics of CdSe nanocrystals. Figure 2.14a and b, respectively represent the time evolution of UV-vis and PL spectra of the CdSe nanocrystals prepared from 0.2 g (0.29 mmol) of $Cd(st)_2$. The UV-vis spectra show three clearly resolved bands at approximately 410, 458, and 505 nm after 3 h of the reaction, which is consistent with that reported in the literature [9, 32, 44]. With increasing reaction time, the absorption bands of CdSe nanocrystals are red-shifted from 400 to 600 nm as the particle size increases. We have calculated the average diameters of the CdSe nanocrystals after different times of the reaction from the UV-vis spectra following the method described in the Experimental Section.

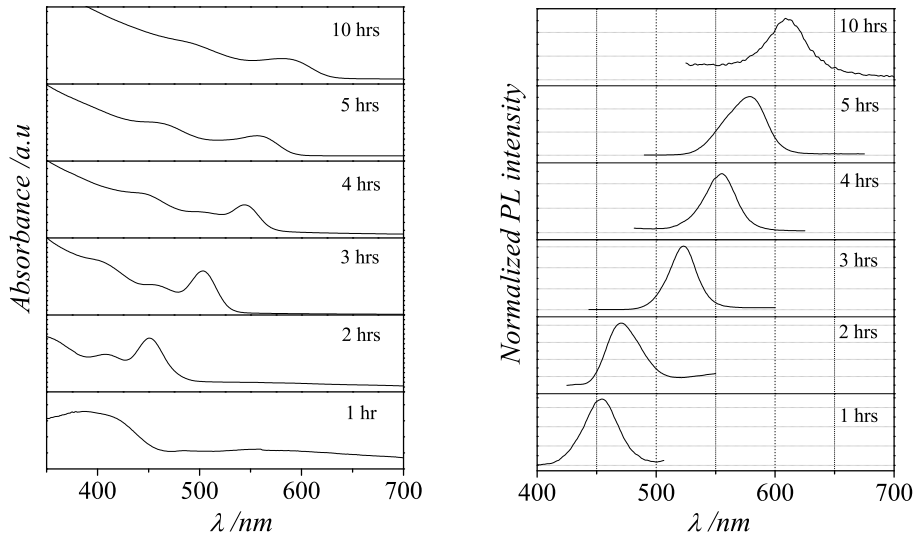

(a) (b)

Figure 2.14: (a) UV-vis spectra and (b) photoluminescence spectra of CdSe nanocrystals prepared from 0.2 g (0.29 mmol) of cadmium stearate obtained after different time of growth (1-10hrs).

The PL spectra of CdSe nanocrystals in Figure 2.14(b) show clearly resolved

band-edge luminescence (e.g., 518 nm band after 3 h of reaction), which is consistent with the literature [9, 10, 32, 44]. The PL band of CdSe nanocrystals is red-shifted from 455 to 615 nm with increasing reaction time. The width of the PL spectra also provides information about the particle size distribution [10]. The width of the PL band changes with an increase in reaction time similar to the relationship observed for the width of diameter distribution with time (Figure 2.12). The diameter distributions derived from PL bands are similar to those from SAXS, showing a broadening and narrowing of the PL bandwidth with reaction time [10]. Surprisingly, the PL bands become symmetric (t=1, 3, 4, and 10 h) and asymmetric (t=2 and 5 h) during the growth of the particle. The LSW theory of growth predicts an asymmetric size distribution [4, 42]. Thus, the PL data reveal that the diffusion-limited reaction contributes to the growth of CdSe nanocrystals.

In Figure 2.15, we have shown the time evolution of the average diameter obtained from SAXS (filled circles), TEM (open circles) and UV-vis spectroscopy (open triangles) of the CdSe nanocrystals prepared with two different concentrations of $Cd(st)_2$. The diameters obtained from different techniques are in close agreement. The diameter of the CdSe nanocrystals varies from 1 to 2.1 nm and from 1.3 to 4.4 nm when the starting $Cd(st)_2$ concentrations are 0.07 and 0.29 mmol, respectively. With increasing concentration of $Cd(st)_2$, the diameter of CdSe nanocrystals increases, with higher monomer concentrations favoring the formation of bigger CdSe nanocrystals.

Although some qualitative evidence for the diffusion-limited growth of CdSe nanocrystals is provided by the observation of the focusing and defocusing diameter distribution, a better insight is obtained from the time evolution of the average diameter of nanocrystals. If the diffusion-limited Ostwald ripening according to LSW theory [4, 5] were the sole contributor for the growth, the rate law would be

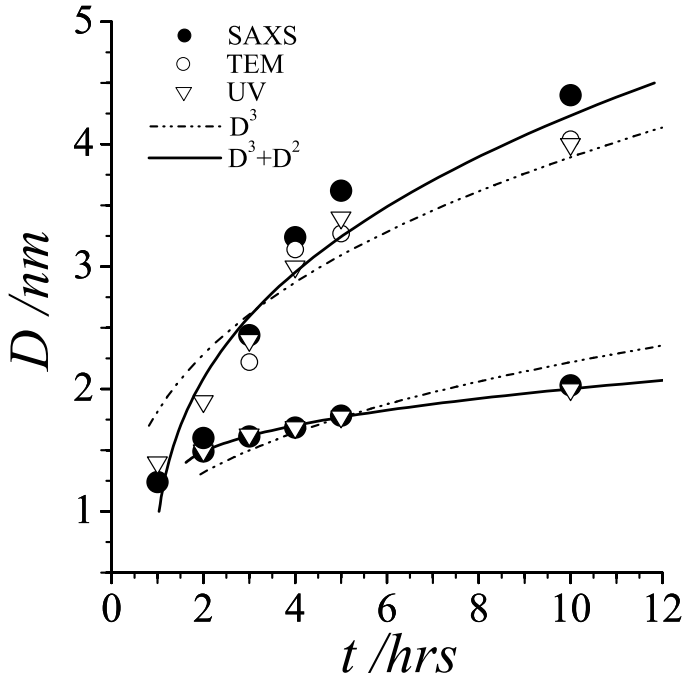

Figure 2.15: Time evolution of the average diameter (D) of the CdSe nanocrystals obtained from SAXS for different concentrations cadmium stearate (filled circles). TEM data are shown by open circles. Average diameter calculated from UV-vis spectra are given by open triangles. Solid curves represent fits of the data to the combined surface and diffusion growth model. Dotted curve is the Ostwald ripening model fit to the experimental data.

given by Equation (2.4). We have tried to fit the D(t) data of the CdSe nanocrystals obtained from SAXS, TEM, and UV-vis spectroscopy to the Ostwald-ripening model and found that it was not possible to obtain a good fit of the D(t) data by using Equation (2.4). A typical fit, using Equation (2.4), of the D(t) data of the CdSe nanocrystals obtained, is shown in Figure 2.15 by the broken curve. The fit is not satisfactory with a coefficient of determination, R^2, of 0.33 and 0.58 for 0.07 and 0.29 mmol of $Cd(st)_2$, respectively. The growth process clearly deviates from diffusion-limited Ostwald ripening. We have tried to fit the D(t) data to the surface-limited reaction model ($D^2 \propto t$) or by varying the value of the exponent

(n in $D^n \propto t$), and found that the fit of the data was unsatisfactory to both the surface-reaction model and to a variable-n model[3, 12]. To fit the experimental D(t) data of the CdSe nanocrytals, we have, therefore, used a model which contains both the diffusion- limited and surface-limited growth, [17, 42, 43] shown in Equation (2.6)

$$BD^3 + CD^2 + const = t \tag{2.6}$$

where, $B = AT/exp(-E_a/k_BT)$, $A \propto 1/(D_0\gamma V_m^2 C_\infty)$ and $C \propto T/(k_d\gamma V_m^2 C_\infty)$, k_d is the rate constant of surface reaction. The goodness of fits with R^2=0.99 and 0.97 for the lower and higher concentrations of $Cd(st)_2$, respectively, over the entire range of experimental data by the combined diffusion and surface reaction-control model is shown by the thick solid curve in Figure 2.15. The observed improvement to the fitting of the data suggests that the growth of the CdSe nanocrystals appears to have contributions from the surface reaction as well.

We have studied the effect of a capping agent on the growth kinetics of CdSe nanocrystals. For this purpose, we have employed trioctylphosphine oxide (TOPO) in place of dodecanethiol keeping the other conditions same at the time of the reaction. We have estimated the diameters and diameter distributions of TOPO-capped CdSe nanocrystals after different times of the reaction by using SAXS, TEM, UV-vis, and photoluminescence, as was undertaken for the dodecanethiol-capped CdSe nanocrystals. In Figure 2.16, we show the average diameter of TOPO-capped CdSe nanocrytals obtained from SAXS, TEM, and UV-vis spectroscopy after different times of the reaction. Diameters obtained from the different techniques show close agreement. The diameter of the CdSe nanocrystals varies from 1.1 to 2.7 nm when the starting $Cd(st)_2$ concentration is 0.29 mmol. In the presence of TOPO, the increase in diameter is somewhat smaller compared to that observed in the do-

decanethiol capped case. We have found the Ostwald ripening model [Equation (2.4)] to be unsatisfactory for the data with TOPO as capping agent. Utilising the surface-limited reaction model or by variation of the exponent (n in $D^n \propto t$), does not provide a good agreement with the experimentally obtained results. We have therefore used the combined model, Equation (2.6), containing both diffusion-limited and surface-limited growth. The fit is good over the entire range of the data (R^2=0.997, solid curve in Figure 2.16). Thus, the growth of the TOPO-capped CdSe also follows the combined diffusion and surface reaction-control model.

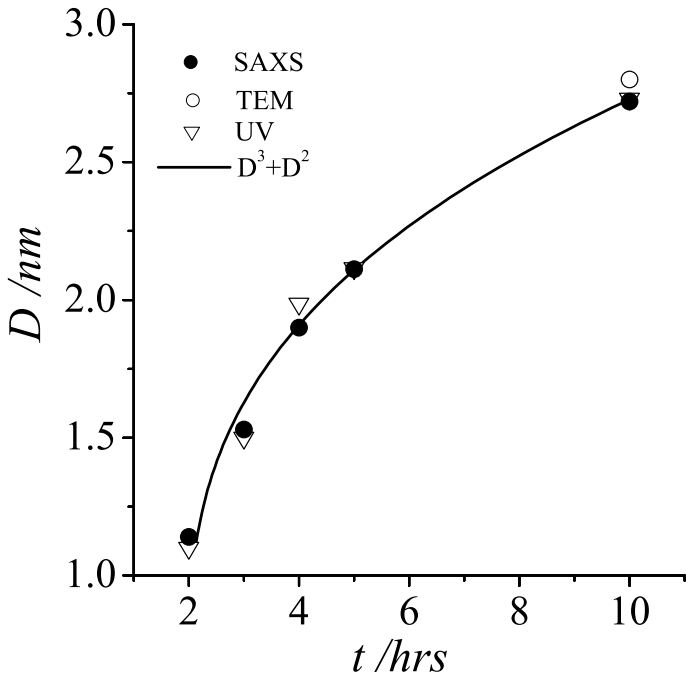

Figure 2.16: Time evolution of the average diameter (D) of the CdSe nanocrystals obtained from SAXS using TOPO as the capping agent (filled circles). TEM data are shown by open circles. Average diameter calculated from UV-vis spectra are given by open triangles. Solid curves represent the combined surface and diffusion growth model fits to the experimental data.

We have carried out studies on the growth kinetics of the dodecanethiol-capped

CdS nanocrystals by a combined use of SAXS, TEM, and UV-vis and photoluminescence spectroscopy. Figure 2.17 shows typical intensity versus scattering vector plots in the logarithmic scale for different times of growth in the case of CdS nanocrystals prepared with 0.05 g (0.07 mmol) of $Cd(st)_2$. To estimate the average diameter and diameter distribution of CdS nanocrystals, we have fitted the experimental SAXS data to the spherical model. The width of the diameter distribution obtained from SAXS shows the similar focusing and defocusing observed in the case of CdSe nanocrystals.

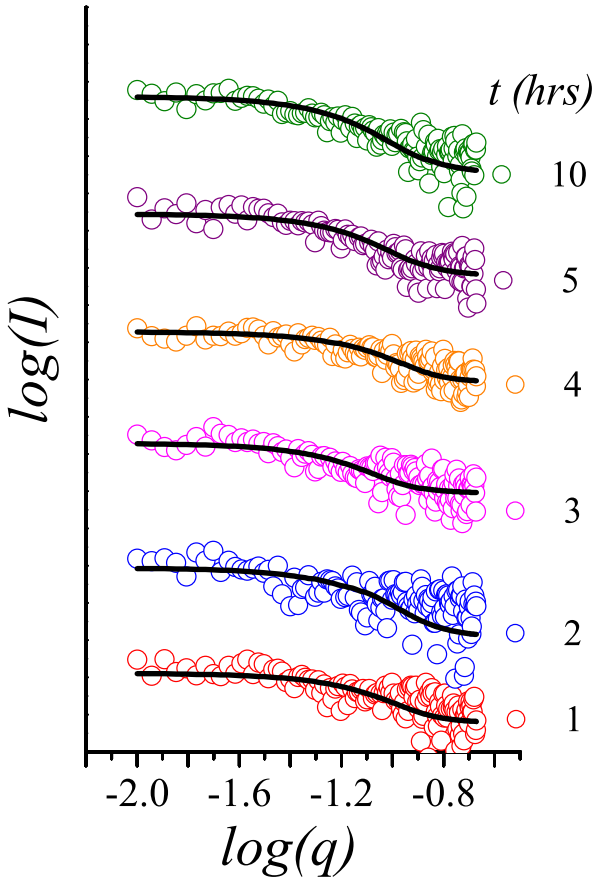

Figure 2.17: SAXS data for the growth of CdS nanocrystals prepared from a) 0.05 g (0.07 mmol) of cadmium stearate after different times of the reaction. Solid lines are the spherical model fits to the experimental data.

We have also carried out TEM measurements on the CdS nanocrystals at a few points during the growth, and Figure 2.18 shows typical TEM images of CdS nanocrystals prepared with 0.05 g (0.07 mmol) of $Cd(st)_2$ after different periods of growth. We have estimated the average diameter and the diameter distribution of CdS nanocrystals at different stages of the growth from the TEM images. Although the TEM data are not expected to be as statistically satisfactory as SAXS, the diameter distributions obtained from TEM and SAXS after 4 and 10 h of growth are in good agreement.

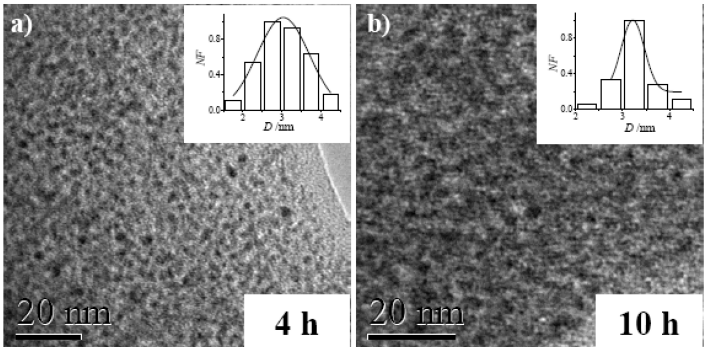

Figure 2.18: TEM images of CdS nanocrystals prepared from 0.05 g (0.07 mmol) of cadmium stearate obtained after a) 4 and b) 10 hrs of growth. Insets show the diameter distributions obtained from TEM. NF: normalized frequency.

Figure 2.19 represents the time evolution of UV-Vis spectra of the CdS nanocrystals prepared from 0.05 g (0.07 mmol) of $Cd(st)_2$. The UV-Vis spectra show one transition (e.g., 375 nm band after 3 h of the reaction) that is consistent with the literature [44]. With increasing reaction time, the absorption bands of CdS nanocrystals are red-shifted from 360 to 390 nm as the particle size increases. The PL spectra of CdS are not as good as those obtained from CdSe. The bandedge luminescence is obtained to be about 370 nm after 2 h of the reaction.

Figure 2.20 shows the plot of the average diameter obtained from SAXS (filled circles), TEM (open circles), and UV-Vis spectroscopy (filled triangles) of CdS

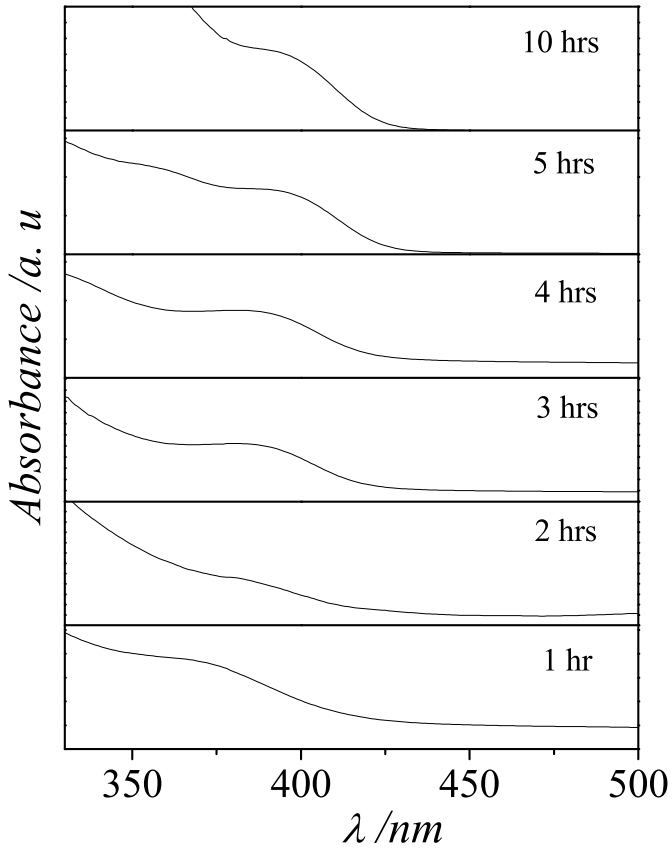

Figure 2.19: UV-vis spectra of CdS nanocrystals prepared from 0.05g (0.07 mmol) of cadmium stearate obtained after different time of growth (1-10hrs).

nanocrystals against time. Diameters obtained from different techniques exhibit close agreement. The diameter of the CdS nanocrystals varies from 2.3 to 3.1 nm when the starting $Cd(st)_2$ concentration is 0.07 mmol.

We tried to fit the D(t) data to the Ostwald- ripening model [Equation (2.4)], yet an unsatisfactory fit was obtained having an R^2 value of only 0.85. A typical fit of the D(t) data to Equation (2.4) of the CdS nanocrystals is shown in Figure 2.20

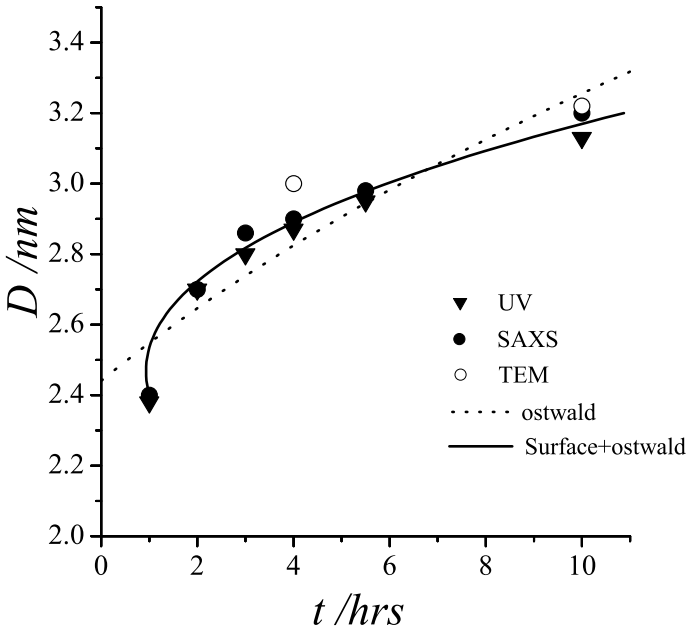

Figure 2.20: Time evolution of the average diameter (D) of the CdS nanocrystals obtained from SAXS for 0.05 g (0.07 mmol) of cadmium stearate (filled circles). TEM data are shown by open circles. Average diameter calculated from UV-vis spectra are given by filled triangles. Solid curves represent the combined surface and diffusion growth model fits to the experimental data. Dotted curve is the Ostwald ripening model fit to the experimental data.

by the broken curve. The growth process clearly deviates from the diffusion-limited Ostwald ripening model. We found a good fit of the data only with the combined model, shown in Equation (2.6), accounting for both diffusion- limited and surface-limited growth. The fit is good over the entire range of the data (R^2=0.99, solid curve in Figure 2.20). Thus, the growth of the CdS deviates sufficiently from the diffusion-limited Ostwald-ripening model, and follows a mechanism involving both diffusion-control and surface- reaction control. The presence of a capping agent gives rise to a barrier to diffusion. The contribution of the surface reaction, therefore, comes into picture. Thus, the growth of capped CdSe and CdS nanocrystals clearly occurs through a combination of diffusion and surface-reaction processes.

2.4.3 Platinum nanocrystals: Role of the Surface

Results of the SAXS measurements on the growth of platinum nanocrystals prepared by the citrate reduction are shown in Figure 2.21 with logarithmic plots of intensity vs. scattering vector for different times of growth.

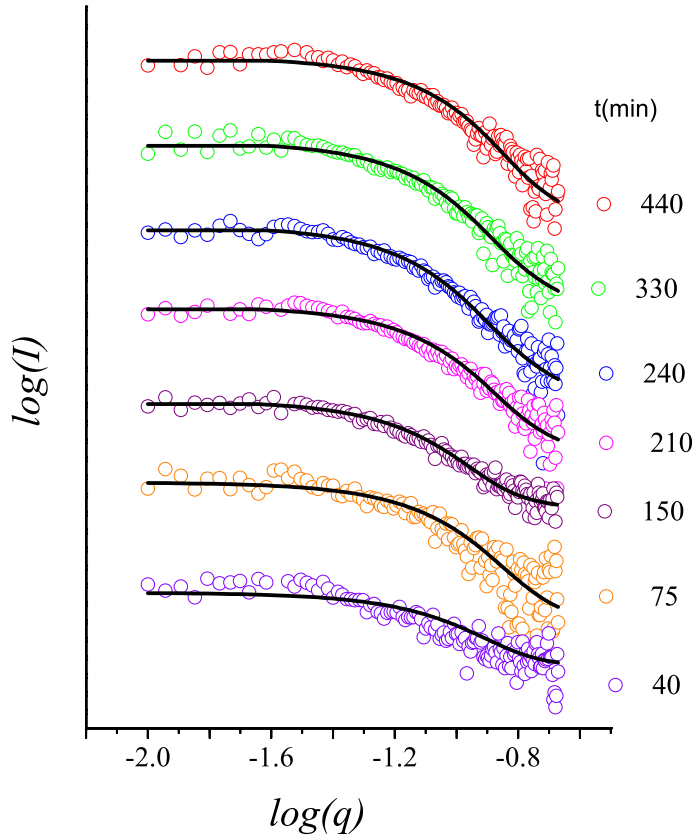

Figure 2.21: SAXS data for the growth of platinum nanocrystals prepared by the reduction with sodium citrate after different reaction times. Solid lines are the spherical model fits to the experimental data.

The changes observed in the SAXS patterns indicate that the nanocrystals grow as a function of time. In order to estimate the average diameter and diameter distribution of platinum nanocrystals, the experimental SAXS data is fitted to the spherical model mentioned in experimental section. The scattering contrast

for X-rays is given by the electron density difference between the particle and the solvent. Since platinum has much higher contrast than the solvent, only the platinum particles are considered for analysis. In the case of a dilute assembly of spherical particles, neglecting particle interaction, the scattering intensity is given by Equation (2.1). Solid curves in the Figure 2.21 are fits of the experimental SAXS data to the sphere model. The fits with the experimental pattern are quite good, yielding the average diameter as well as the diameter distributions for different growth times.

We have estimated the diameter, D, of the platinum nanocrystals after different periods of growth from the SAXS data, and have shown the time evolution of the diameter distribution in Figure 2.22. The width of the diameter distribution increases first and then decreases for different times of growth. Such focusing and defocusing of the diameter and length distributions [9, 43] occurs when the monomer concentration gets depleted due to the faster growth of the nanocrystals and the smaller nanocrystals shrink as the bigger ones grow. The size distribution, therefore, becomes broader. Dissolution of the small nanocrystals again enriches the monomer concentration in the solution, with the growth of the bigger nanocrystals continuing through the diffusion of the monomer from solution to the nanocrystals surface resulting in the focusing of the diameter distribution. Focusing and defocusing of the diameter distribution is thus dependent on the variation of the monomer concentration in the solution and indicates that the growth of platinum nanocrystals occurs mainly by the diffusion of monomer from solution to surface of the nanocrystals.

We have carried out TEM measurements during the growth of the platinum nanocrystals. In Figure 2.23, we show typical TEM images of platinum nanocrystals prepared after 40 and 440 minutes of growth to illustrate how the size of the

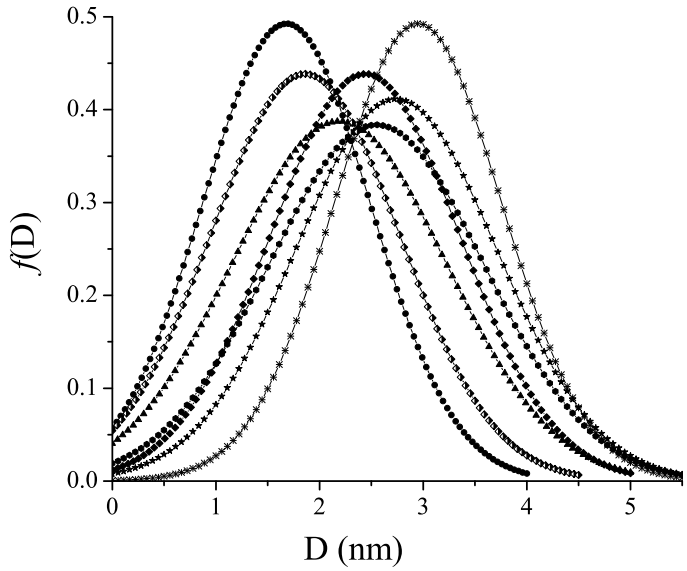

Figure 2.22: Time evolution of diameter distribution of the platinum nanocrystals prepared by reduction with sodium citrate. The distributions are obtained from the spherical model fits to the experimental SAXS data, recorded after different reaction times.

platinum nanocrystals increases with increasing time. We have estimated the average diameter and the diameter distribution of platinum nanocrystals at different stages of the growth from the TEM images. The diameter distributions obtained from TEM and SAXS show good agreement. Figure 2.24 shows the time evolution of the average diameter of the platinum nanocrystals obtained from SAXS (filled squares) and TEM (open circles). The diameters obtained from the two techniques are comparable, the values varying between 1.2 and 2.9 nm over a period of 440 minutes.

Although some evidence for the diffusion-limited growth of platinum nanocrystals is provided by the observation of the focusing and defocusing diameter distribution, a better insight is obtained from the time evolution of the average diameter of nanocrystals. If the diffusion-limited Ostwald ripening according to LSW the-

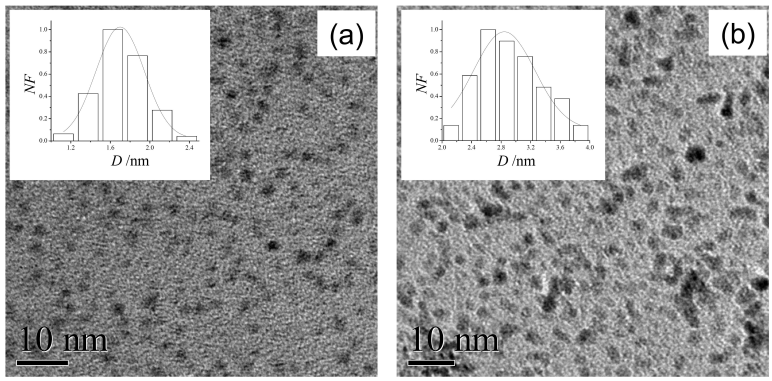

Figure 2.23: TEM images of platinum nanocrystals prepared by the reduction with sodium citrate after (a) 40 and (b) 440 minutes of growth. Insets show the diameter distributions. NF is the normalized frequency.

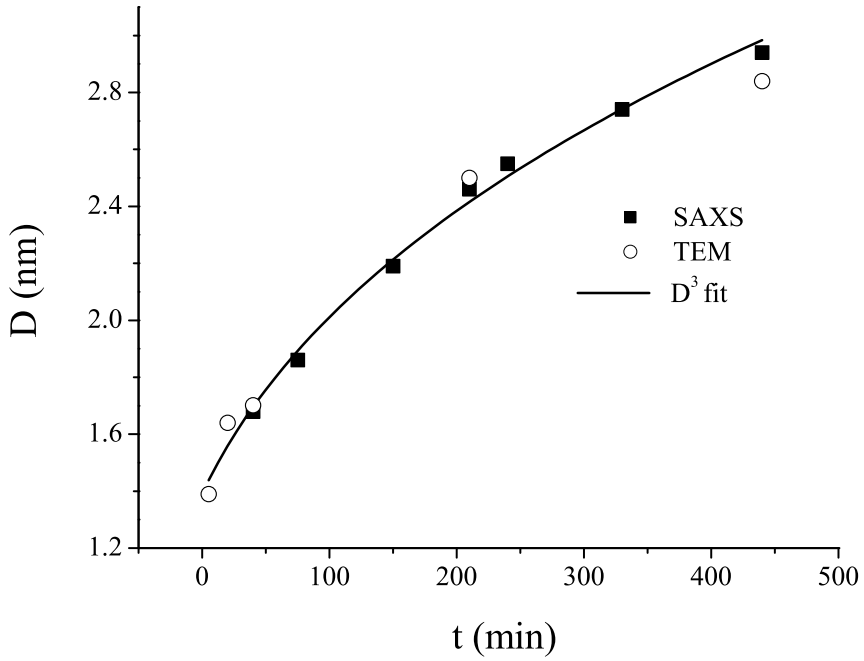

Figure 2.24: Time evolution of the average diameter (D) of the platinum nanocrystals obtained from SAXS (filled circles). TEM data are shown by open circles. Solid curve represents fit of the data to the diffusion-limited Ostwald ripening growth model.

ory [4, 5] were the sole contributor for the growth, the rate law would be given by Equation (2.4). We fitted the D(t) data of the platinum nanocrystals obtained from

SAXS and TEM to the Ostwald ripening model by Equation (2.4). The goodness of fits with $R^2 = 0.99$ over the entire range of experimental data by the Ostwald ripening model is shown by solid curve in Figure 2.24.

We have studied the effect of capping agent on the growth kinetics of platinum nanocrystals by employing the second procedure for the synthesis. In this procedure, particles were prepared by ethylene glycol reduction of the platinum salt in the presence of PVP as the capping agent. Figure 2.25 shows typical intensity vs. scattering vector plots in the logarithmic scale for different times obtained from SAXS measurements.

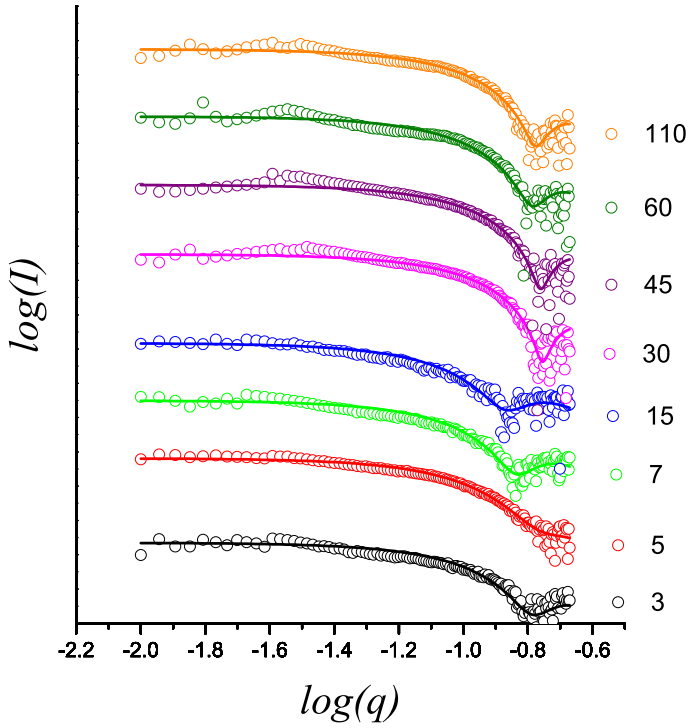

Figure 2.25: SAXS data for the growth of platinum nanocrystals prepared by ethylene glycol reduction in the presence of PVP after different times of the reaction. Solid lines are the spherical model fits to the experimental data.

We have fitted the experimental SAXS data to the spherical model and also

carried out TEM measurements on the platinum nanocrystals at a few points during the growth. We show typical TEM images of the nanocrystals after 3 and 110 minutes of growth in Figure 2.26. The diameter distributions obtained from TEM and SAXS show good agreement with the diameter varying from 3.2 to 4.8 nm over 120 minutes.

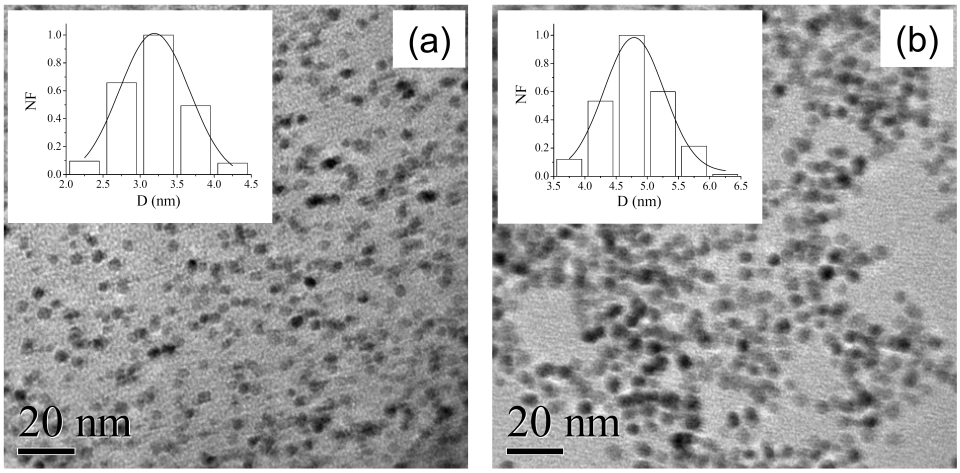

Figure 2.26: TEM images of platinum nanocrystals prepared by ethylene glycol reduction in the presence of PVP after (a) 3 and (b) 110 minutes of growth. Insets show the diameter distributions. NF is the normalized frequency.

We have plotted the average diameter obtained from SAXS (filled squares) and TEM (open circles) of platinum nanocrystals against time in Figure 2.27. We have tried to fit the D(t) data to the Ostwald ripening model [Equation (2.4)], but found to be unsatisfactory, the R^2 value being 0.87. A typical fit of the D(t) data to Equation (2.4) of the platinum nanocrystals is shown in Figure 2.27 by the broken curve. The growth process clearly deviates from diffusion-limited Ostwald ripening. We, therefore, fitted the D(t) data to the surface-limited reaction model ($D^2 \propto t$) or by varying the value of the exponent (n in $D^n \propto t$) and found that the fit of the data was unsatisfactory to both the surface reaction model and to a variable n model. In order to fit the experimental D(t) data of the platinum

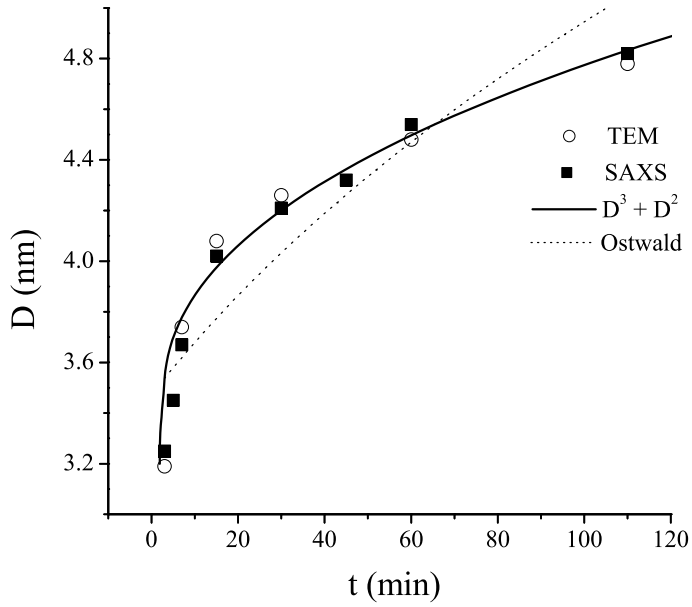

Figure 2.27: Time evolution of the average diameter (D) of the platinum nanocrystals prepared by ethylene glycol reduction in the presence of PVP obtained from SAXS (filled squares). TEM data are shown by open circles. Dotted curve is the Ostwald ripening model fit to the experimental data. Solid curve represents the combined surface and diffusion growth model fits to the experimental data.

nanocrytals, we, therefore, used a model which contains both the diffusion-limited and surface-limited growth, [17, 42, 43] which is given by Equation (2.6). We obtained a good fit ($R^2 = 0.992$) over the entire range of experimental data by the combined diffusion and surface reaction control model of Equation (2.6) as shown by solid curve in Figure 2.27. In the presence of PVP, the growth of the platinum nanocrystals involves contributions from surface reaction as well.

2.5 Conclusions

A systematic study of the growth of gold nanocrystals formed by the reduction of $HAuCl_4$ by THPC, has been carried out by employing SAXS. The rate of the

growth was sufficiently slow to follow the grow kinetics over a long period, 10 min after the initiation of the reaction. Thus, the data represent the kinetics of the growth immediately after the nucleation that probably occurs within a minute or so. With increasing concentration of $HAuCl_4$, the diameter of the gold nanocrystal increases and the growth process saturates early when the concentration of $HAuCl_4$ is high. The growth kinetics of gold nanocrystals cannot be explained by diffusion-limited Ostwald ripening, but are satisfactorily fitted with sigmoidal growth. Interestingly, the activation energy for the growth of gold nanocrystals is very small with the reactants and reaction conditions employed in the present study. ITC measurements show the growth process of gold nanocrystals to be exothermic, and give an estimate of the heat change of $\approx$10 kcal mol^{-1} per 1 nm of growth for a diameter in the 3-5nm range.

A systematic study of the growth of capped CdSe and CdS nanocrystals has been carried out by a combined use of SAXS, TEM, UV-Vis, and PL spectroscopies to obtain reliable data on the growth kinetics. The rate of growth was sufficiently slow to follow the kinetics over a long period. Thus, the data represent the kinetics of the growth immediately after the nucleation, which probably occurs within a minute or so. With an increase in the concentration of the starting metal precursor, $Cd(st)_2$, the diameter of the CdSe nanocrystals increases. Focusing and defocusing of the diameter distribution, and the asymmetric nature of the PL band of the nanocrystals, reveal that the diffusion of the monomer contributes towards the growth of the nanocrystals. However, the best fits of the D(t) data is found to be a D^3+D^2 model, suggesting that the growth mechanism of capped CdSe and CdS nanocrystals involves both diffusion and surface reactions. The presence of a capping agent, gives rise to a barrier to diffusion, thereby rendering the contribution of the surface reaction relevant.

Diffusion-limited Ostwald ripening satisfactorly explains the growth of platinum nanocrystals in the absence of any capping agent. It is to be noted that platinum nanocrystals formed by the reduction of sodium citrate do not have any strongly binding capping agent. Thus, we find that in the presence of PVP, there is need to take a surface reaction term into account in addition to the Ostwald ripening. Growth of the nanocrystals mainly occurs by the diffusion of monomers from solution to the nanocrystal surface or by the reaction at the surface where the diffusing species get assimilated into the growing nanocrystals. Diffusion and surface reaction are limiting cases in nanocrystal growth. The presence of a capping agent such as PVP gives rise to a barrier to diffusion and the contribution of the surface reaction, therefore, becomes significant.

References

[1] C. N. R. Rao, P. J. Thomas, and G. U. Kulkarni. *Nanocrystals: Synthesis, Properties and Applications,Springer, Berlin, Germany.* 2007.

[2] C. N. R. Rao and A. Govindaraj. *Nanotubes and Nanowires; RSC Nanoscience & Nanotechnology series; Royal Society of Chemistry:Cambridge, U.K.,.* 2005.

[3] C. N. R. Rao, A. Muller, and A. K. Cheetham. *Nanomaterials Chemistry: Recent Developments and New Directions, Wiley-VCH Verlag GmbH & Co.* 2007.

[4] I.M. Lifshitz and V.V. Slyozov. The kinetics of precipitation from supersaturated solid solutions. *J. Phys.Chem. Solids*, 19(1-2):35 – 50, 1961.

[5] C. Wagner. *Z. Elektrochem.*, 65:581, 1961.

[6] E. M. Wong, J. E. Bonevich, and P. C. Searson. Growth kinetics of nanocrystalline ZnO particles from colloidal suspensions. *J. Phys. Chem. B*, 102(40):7770–7775, 1998.

[7] Z. Hu, D. J. Escamilla Ramrez, B. E. Heredia Cervera, G. Oskam, and P. C. Searson. Synthesis of ZnO nanoparticles in 2-propanol by reaction with water. *J. Phys. Chem. B*, 109(22):11209–11214, 2005.

[8] G. Oskam, A. Nellore, R. L. Penn, and P. C. Searson. The growth kinetics of TiO_2 nanoparticles from titanium(IV) alkoxide at high water/titanium ratio. *J. Phys. Chem. B*, 107(8):1734–1738, 2003.

[9] X. Peng, J. Wickham, and A. P. Alivisatos. Kinetics of II-VI and III-V colloidal semiconductor nanocrystal growth: focusing of size distributions. *J. Am. Chem. Soc.*, 120(21):5343–5344, 1998.

[10] L. Qu, W. W. Yu, and X. Peng. In situ observation of the nucleation and growth of CdSe nanocrystals. *Nano Lett.*, 4(3):465–469, 2004.

[11] M. B. Mohamed, Z. L. Wang, and M. A. El-Sayed. Temperature-dependent size-controlled nucleation and growth of gold nanoclusters. *J. Phys. Chem. A*, 103(49):10255–10259, 1999.

[12] F. Mafun, J.-y. Kohno, Y. Takeda, and T. Kondow. Formation of stable platinum nanoparticles by laser ablation in water. *J. Phys. Chem. B*, 107(18):4218–4223, 2003.

[13] S. B. Simonsen, I. Chorkendorff, S. Dahl, M. Skoglundh, J. Sehested, and S. Helveg. Direct observations of oxygen-induced platinum nanoparticle ripening studied by in situ TEM. *J. Am. Chem. Soc.*, 132(23):7968–7975, 2010.

[14] R. Seshadri, G. N. Subbanna, V. Vijayakrishnan, G. U. Kulkarni, G. Anantha krishna, and C. N. R. Rao. Growth of nanometric gold particles in solution phase. *J. Phys. Chem.*, 99(15):5639–5644, 1995.

[15] B. Abcassis, F. Testard, O. Spalla, and P. Barboux. Probing in situ the nucleation and growth of gold nanoparticles by small-angle x-ray scattering. *Nano Lett.*, 7(6):1723–1727, 2007.

[16] D. V. Talapin, A. L. Rogach, M. Haase, and H. Weller. Evolution of an ensemble of nanoparticles in a colloidal solution: theoretical study. *J. Phys. Chem. B*, 105(49):12278–12285, 2001.

[17] R. Viswanatha, P. K. Santra, C. Dasgupta, and D. D. Sarma. Growth mechanism of nanocrystals in solution: ZnO, a case study. *Phys. Rev. Lett.*, 98(25):255501, 2007.

[18] R. Viswanatha, H. Amenitsch, and D. D. Sarma. Growth kinetics of ZnO nanocrystals: a few surprises. *J. Am. Chem. Soc.*, 129(14):4470–4475, 2007.

[19] R.Viswanatha and D.D. Sarma. Study of the growth of capped ZnO nanocrystals: A route to rational synthesis. *Chem. Eur. J*, 12(1):180–186, 2005.

[20] N. S. Pesika, Z. Hu, K. J. Stebe, and P. C. Searson. Quenching of growth of ZnO nanoparticles by adsorption of octanethiol. *J. Phys. Chem. B*, 106(28):6985–6990, 2002.

[21] C. R. Bullen and P. Mulvaney. Nucleation and growth kinetics of CdSe nanocrystals in octadecene. *Nano Lett.*, 4(12):2303–2307, 2004.

[22] W. W. Yu and X. Peng. Formation of high-quality CdS and Other II-VI semiconductor nanocrystals in noncoordinating solvents: Tunable reactivity of monomers. *Angew. Chem. Int.Ed.*, 41(13):2368–2371, 2002.

[23] L. Qu and X. Peng. Control of photoluminescence properties of CdSe nanocrystals in growth. *J. Am. Chem. Soc.*, 124(9):2049–2055, 2002.

[24] Q. Dai, D. Li, H. Chen, S. Kan, H. Li, S. Gao, Y. Hou, B. Liu, and G. Zou. Colloidal CdSe nanocrystals synthesized in noncoordinating solvents with the addition of a secondary ligand: exceptional growth kinetics. *J. Phys. Chem. B*, 110(33):16508–16513, 2006.

[25] E. M. Wong, P. G. Hoertz, C. J. Liang, B. M. Shi, G. J. Meyer, and P. C. Searson. Influence of organic capping ligands on the growth kinetics of ZnO nanoparticles. *Langmuir*, 17(26):8362–8367, 2001.

[26] Z. A. Peng and X. Peng. Mechanisms of the shape evolution of CdSe nanocrystals. *J. Am. Chem. Soc.*, 123(7):1389–1395, 2001.

[27] Z. A. Peng and X. Peng. Nearly monodisperse and shape-controlled CdSe nanocrystals via alternative routes: nucleation and growth. *J. Am. Chem. Soc.*, 124(13):3343–3353, 2002.

[28] S. G. Thoma, A. Sanchez, P. P. Provencio, B. L. Abrams, and J. P. Wilcoxon. Synthesis, optical properties, and growth mechanism of blue-emitting CdSe nanorods. *J. Am. Chem. Soc.*, 127(20):7611–7614, 2005.

[29] C. Pacholski, A. Kornowski, and H.Weller. Self-assembly of ZnO: From nanodots to nanorods. *Angew. Chem., Int. Edit.*, 41(7):1188–1191, 2002.

[30] Z. Zhu., T. Andelman, M. Yin, T. L. Chen, S. N. Ehrlich, S. P. O'Brien, and R. M. Osgood. Synchrotron x-ray scattering of ZnO nanorods: Periodic ordering and lattice size. *J. Mater. Res.*, 20:1033, 2005.

[31] D. G. Duff, A. Baiker, and P. P. Edwards. A new hydrosol of gold clusters. *J. Chem. Soc., Chem. Commun.*, (1):96–98, 1993.

[32] U. K. Gautam, M. Rajamathi, F. Meldrum, P. Morgan, and R. Seshadri. A solvothermal route to capped CdSe nanoparticles. *Chem. Commun.*, pages 629–630, 2001.

[33] U. K. Gautam, R. Seshadri, and C. N. R. Rao. A solvothermal route to CdS nanocrystals. *Chem. Phys. Lett.*, 375(5-6):560 – 564, 2003.

[34] P. A. Brugger, P. Cuendet, and M. Graetzel. Ultrafine and specific catalysts affording efficient hydrogen evolution from water under visible light illumination. *J. Am. Chem. Soc.*, 103(11):2923–2927, 1981.

[35] T. Herricks, J. Chen, and Y. Xia. Polyol synthesis of platinum nanoparticles: control of morphology with sodium nitrate. *Nano Lett.*, 4(12):2367–2371, 2004.

[36] J. S. Pedersen. Analysis of small-angle scattering data from colloids and polymer solutions: modeling and least-squares fitting. *Advances in Colloid and Interface Science*, 70:171 – 210, 1997.

[37] P. Lindner and Th. Zemb. *Neutrons, X-rays and Light: Scattering Methods Applied to Soft Condensed Matter, North-Holland, New York*. 2002.

[38] J. S. Pedersen. A flux- and background-optimized version of the NanoSTAR small-angle X-ray scattering camera for solution scattering. *J. Appl. Crystallogr.*, 37(3):369–380, 2004.

[39] L. Rayleigh. *Proc. Roy. Soc. London, Ser. A*, 84:25–46, 1911.

[40] J. E. Ladbury and B. Z. Chowdhry. Sensing the heat: the application of isothermal titration calorimetry to thermodynamic studies of biomolecular interactions. *Chem. Biol.*, 3(10):791–801, 1996.

[41] W. W. Yu, L. Qu, W. Guo, and X. Peng. Experimental determination of the extinction coefficient of CdTe, CdSe, and CdS nanocrystals. *Chem. Mater.*, 15(14):2854–2860, 2003.

[42] C. N. R. Rao, A. Muller, and A. K. Cheetham. *Nanomaterials Chemistry: Recent Developments and New Directions, Wiley-VCH Verlag GmbH & Co.* 2007.

[43] K. Biswas, B. Das, and C. N. R. Rao. Growth kinetics of ZnO nanorods: Capping-dependent mechanism and other interesting features. *J. Phys. Chem. C*, 112(7):2404–2411, 2008.

[44] C. B. Murray, D. J. Norris, and M. G. Bawendi. Synthesis and characterization

of nearly monodisperse CdE (E = sulfur, selenium, tellurium) semiconductor nanocrystallites. *J. Am. Chem. Soc.*, 115(19):8706–8715, 1993.

CHAPTER 3

An Isothermal Calorimetric Investigation of the Assembly and Disassembly of Nanomaterials*

Summary

Interaction of gold nanorods with cysteine as well as 3-mercaptopropionic acid (MPA) has been investigated by isothermal titration calorimetry (ITC), in combination with electronic absorption spectroscopy and electron microscopy. The assembly process with MPA show two steps, the first due to the binding of MPA to gold nanorods through the sulfur atom, and the second due to assembly of the MPA capped gold nanorods through the formation of cyclic hydrogen bonded dimers between the MPA molecules. In the case of cysteine only a single step is observed in ITC, due to the binding of the molecules to gold nanorods.

Disintegration of gold nanofilms formed at the organic-aqueous interface by alkanethiols of different chain lengths has been monitored by isothermal titration calorimetry. The process involves two steps, the first step being the exothermic gold film-thiol interaction and the second step includes the endothermic disordering process followed by further thiol capping of isolated gold particles. The rate of interaction of the thiols with the film is found to decrease with decreasing chain length.

*Papers based on this work have been published in *Chem. Phys. Lett.* **(2008)**, *Langmuir* **(2008)**

3.1 Introduction

Calorimetry is the principal source of thermodynamic data. It is an important technique due to the fact that practically all physical, chemical and biological processes are accompanied by heat exchanges. Calorimetry has, therefore, become a powerful tool in many fields of science and technology. Isothermal titration calorimetry (ITC) is a technique wherein one can measure the energetics of biochemical or molecular interactions at constant temperature [1–4]. It is an ultrasensitive technique which can monitor precise changes in heat in a chemical reaction and resolve the binding stoichiometry, binding heat and binding constant in one experiment. In determining these thermodynamic parameters, one compound in solution is generally added in small increments to a solution containing its binding partner, and the heat change is measured for each addition of the compound solution [1]. Determination of accurate thermodynamic parameters from such ITC data requires that the experimental isotherms be modeled in terms of the chemical processes that occur upon mixing the two solutions, taking into account how each process contributes to the measured heat. Owing to these unique strengths, ITC has been widely used to quantify various interactions. ITC has been used to study various interactions such as conformational transitions in macromolecules, protein-ligand binding [4], nucleic acid recognition, enzyme kinetics [5], drug design [6], structure-energy correlations, investigation of micelles [7] etc. [8, 9]. We were interested to use ITC to study various interactions of nanoparticles. There have been few studies which use ITC as a tool to study nanomaterials interactions. For example, Sastry *et al.* studied the binding of DNA bases and PNA base monomers to gold nanoparticles using ITC [10]. Rao *et al.* used ITC to calculate and compare the interaction energy of various nucleobases with single walled carbon nanotubes [11]. In the

present study we have used isothermal titration calorimetry to monitor the heat change associated with various processes such as assembly of gold nanorods and disintegration of gold nanofilm at the liquid-liquid interface by various alkanethiols.

3.2 Scope of the present investigations

3.2.1 Assembly of gold nanorods

Self-assembly of nanostructures constitutes an important aspect in nanoscience and nanotechnology and several chemical strategies have been employed to create assemblies of nanoparticles [12, 13]. Gold nanorods have been assembled using DNA, surfactants and various linker molecules [14–20]. Linking has major consequences on the electronic spectra of the nanorods [16]. Thus when gold nanoparticles are packed closely to form a film, the surface plasmon resonance band of the gold film shifts progressively to longer wavelengths depending on the interparticle separation [21]. Gold nanorods exhibit another unique feature in the electronic spectra, in that they show transverse and longitudinal surface plasmon absorption bands [22]. The transverse band does not vary with the aspect ratio of the nanorods while the longitudinal plasmon band shifts to longer wavelength with increase in aspect ratio. Accordingly, on linking gold nanorods by mercaptopropionic acid (MPA) or cysteine to give rise to chains or necklaces, the longitudinal surface plasmon resonance band shifts significantly to longer wavelengths [16, 17].

Formation of chains and necklaces of gold nanorods using organic linker molecules would involve two processes: (1) interaction of the linker molecules with the gold nanorods and (2) formation of the extended chains or necklaces. When thiolcarboxylic acid (MPA) and cysteine are used as linkers, the first process involves the

formation of the metal-sulfur bond which is an exothermic reaction. The formation of necklaces would also involve an exothermic process. We have investigated the process of assembly of gold nanorods to form necklaces by isothermal titration calorimetry in combination with spectroscopic and transmission electron microscopic studies. For this purpose, we have employed 3-mercapatopropionic acid as the linker molecule wherein the linkage occurs through the formation of six-membered dimeric hydrogen bonded rings between the carboxylic groups [16] and also cysteine where electrostatic interactions lead to the assembly [17] as shown below.

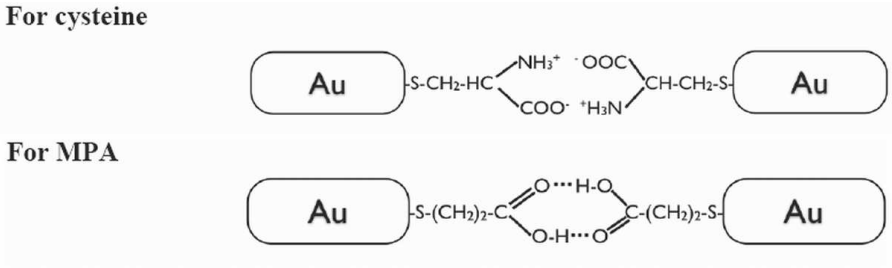

3.2.2 Disintegration of gold nanofilms by alkanethiols

Mesoscalar assemblies of metal nanocrystals are of considerable interest since both short and long range interactions coexist in these systems and compete to give rise to a host of interesting structural, optical, electrical, magnetic and other properties [23–30]. A number of studies have aimed to explore their potential in technological applications [31–35]. A nanocrystal assembly, analogous to an atomic lattice, derives its properties from the nature of the nanocrystal (also called a superatom [36]), from its geometric arrangement, and from the nature of the material in the intervening space. Specifically in the case of a simple two dimensional hexagonal assembly, the main variables are the nanocrystal diameter, the interparticle separation and the nature of the spacer molecule as well as the domain size. There are

several reports on the synthesis of well-defined two-dimensional assemblies formed by suitably derivatizing the nanocrystals [37], by assembling at the air-water interface [38, 39] or by growing nanocrystals in predefined locations [40, 41]. These methods have enabled a greater degree of control on the structural and physical properties of nanocrystal assemblies.

We have been interested in investigating the disintegration process of metal nanocrystal assemblies caused by a variation in the interparticle distance. For this purpose, we have prepared nanocrystalline gold films at the liquid-liquid interface [42]. Unlike the literature procedures that involve at least two steps, this is a simple one-step synthesis, wherein an organometallic compound dissolved in an organic layer reacts with a reducing agent present in the aqueous layer at the interface. The film formed at the interface is an ultrathin nanocrystalline film consisting of closely packed metal nanocrystals, a few nanometers in diameter [43]. The film at the interface can be transferred to a toluene layer as an organosol by the addition of small amounts of alkanethiols. In the present study, we have investigated how heat changes associated with the disintegration process reflects the effects of changing interparticle separation between the gold nanocrystals when the film interacts with alkanethiols of different chain lengths, $CH_3(CH_2)_nSH$. The study not only provides an insight into the collective behavior of the nanocrystals in the film and its dependence on the interparticle distance but also throws light on the nature of interaction of alkanethiols with metal nanoparticle assemblies. Thus, we find that the interaction between the nanoparticles decreases linearly with the increase in the separation between the nanoparticles as determined by the length of the alkane chain.

3.3 Experimental section

Isothermal titration calorimetry (ITC)

In ITC, the experiment is performed at a constant temperature [1]. A schematic diagram of a standard ITC instrument is shown in Figure 3.1. The instrument consists of two identical cells (volume typically 0.5 - 1.5 mL) housed in an isothermal jacket. These two cells are kept at thermal equilibrium (T = 0, see Figure 3.1) throughout the experiment. One cell is filled with water (for experiments performed in aqueous solvents) or buffer solution, and acts purely as a reference. The other (the sample cell) is filled with one component of the interaction to be investigated. Prior to use, solutions are degassed under vacuum (140 mbar, 8 min) to eliminate air bubbles. The basis of the experiment is to measure the heat energy per unit time (expressed in μW) that must be added to the sample cell to maintain zero temperature difference between the two cells at the designated temperature for an experiment.

When the second component is introduced in a series of aliquots (typically injections of 5-25 μL to give a total added volume of 50-250 μL) to the sample cell, an enthalpic change results. If the interaction is exothermic, less heat per unit time will be required by the sample cell to keep the two cells in thermal equilibrium; if the interaction is endothermic, the opposite effect will be observed. ITC uses a cell feedback network (CFB) to differentially measure and compensate for heat produced or absorbed between the sample and reference cell. The cells are in contact with thermopile/thermocouple circuits regulated by an interactive feedback control system, so the highly sensitive response to fluctuations in temperature between the cells and between the jacket and the cells can be detected. After each

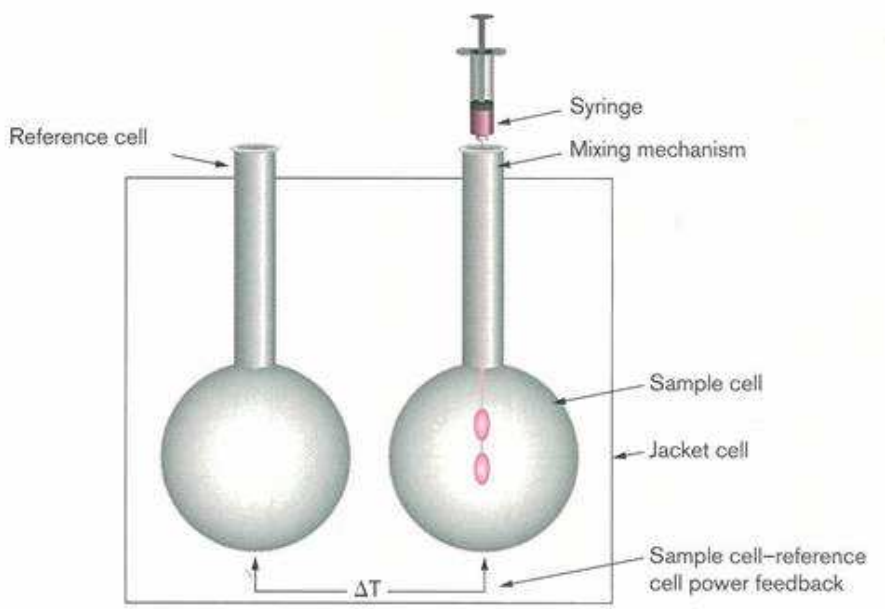

Figure 3.1: A schematic diagram of ITC instrument

addition, the heat released or absorbed as a result of the reaction is monitored by the isothermal titration calorimeter as a peak of power against time for each injection. Addition of the second component is automated and occurs from a precision syringe driven by a computer-controlled stepper motor. The contents of the sample cell are stirred to effect rapid mixing of the reactants. Mixing of the interacting species, by stirring or by diffusion after fast injection is very rapid and response times of instruments to incremental heats are typically less than 10 s. The amount of titrand required per experiment depends on the magnitude of the heat change. As the substrate in the cell becomes saturated with ligands, the heat signal diminishes until only background heat of dilution is observed.

ITC observations are plotted as the power in μcal/sec needed to maintain the reference and the sample cell at an identical temperature as shown in figure 3.2.

The raw data for an experiment consists of a series of spikes of heat flow (power),

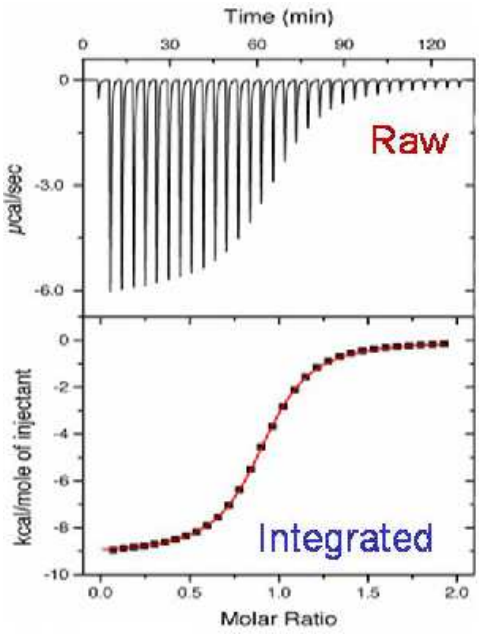

Figure 3.2: Raw data and integrated plot in ITC

with every spike corresponding to a ligand injection. These heat flow spikes/pulses are integrated with respect to time, giving the total heat effect per injection. The data is acquired by computer software developed by MicroCal LLC.

Assembly of gold nanorods

The gold nanorods were prepared using the photochemical method described in the literature [44]. In a typical preparation, 1.78 mg of tetraoctylammonium bromide was added to 6 mL 0.08 M aqueous solution of cetyl trimethylammonium bromide (CTAB), followed by the addition of 120 μL of 0.1 M hydrogen tetracholoaurate, 130 μL of acetone and 90 μL of cyclohexane. A small amount of silver nitrate solution (90 μL of 0.01 M) was added to the above mixture and the solution was taken in a quartz tube and irradiated with UV light for 14 hours. The resulting solution

was blue in color and centrifuged at 7000 rpm for 15 minutes. The precipitate was collected, dispersed in distilled water and centrifuged at 7000 rpm twice. The resulting solution was used for the further experiments.

The prepared gold nanorods were characterized using UV-visible spectroscopy and transmission electron microscopy (TEM). All the UV-visible spectral experiments were performed using a Perkin-Elmer Lamda 900 UV/VIS/NIR spectrometer while the TEM images were recorded using JEOL JEM 3010 instrument fitted with a Gatan CCD camera at an accelerating voltage of 300 kV.

We have used mercaptopropionic acid (MPA) and cysteine as linkers to study the assembly process. The end to end assembly of nanorods can be followed by UV-vis spectroscopy as the longitudinal plasmon band shifts to higher wavelengths with chain formation. We carried out the assembly of gold nanorods in isothermal titration calorimeter to monitor the heat changes associated with the assembly process. The UV-vis and TEM measurements were done after the experiments in ITC to confirm the chain formation. The calorimetric experimental details are as follows.

Isothermal titration calorimetric (ITC) experiments were performed using a Microcal VP-ITC instrument at 30 °C [1]. In a typical titration, 2 μL of 0.57 mM solution of cysteine or MPA taken in the syringe were injected in equal intervals of 5 minutes to a solution of 1.59 nM solution of gold nanorods which was taken in the sample cell with 1.47 mL capacity. A total of 130 μL of cysteine or MPA was added to gold nanorod solution. The heat change to the first injection was not considered in the calculations [1]. The concentration of gold nanorods was calculated using the molar extinction coefficient of the surface plasmon resonance band of gold nanorods [45]. The reference cell of the microcalorimeter was filled with distilled water and both the cells were maintained at the same temperature.

When cysteine/MPA is injected to the sample cell containing gold nanorods, the difference in heat needed to keep both the sample cell and reference cell at the same temperature is monitored. After the titration the samples were analyzed using UV-visible spectroscopy and transmission electron microscopy. Control experiments were carried out by titrating cysteine or MPA with distilled water under the same conditions and were subtracted with the experimental data to remove the dilution effects of the injectant.

Disintegration of gold films by alkanethiols

In a typical experiment, the sample cell of the microcalorimeter was filled with 0.9 mL of 6.25 mM solution of NaOH and 37.5 μL of 50 mM solution of THPC. 0.85 mL of 1.5 mM solution of $Au(PPh_3)Cl$ in toluene was added to the cell and the solution was kept undisturbed for 23 hours for the formation of the film. The reference cell was filled with 0.9 mL distilled water and 0.85 mL toluene and both cells were maintained at the same temperature. A syringe of 280 μL capacity was filled with 1.73 M solution of the alkanethiol. 5 μL of 1.73 M solution of alkanethiol taken in the syringe were injected in equal intervals of 5 minutes to the mixture (film) in the sample cell and the heat changes for each injection was measured. Control experiments were carried out by the addition of same concentration of alkanethiol to a 0.9 mL distilled water and 0.85 mL toluene taken in the sample cell and subtracted with the experimental data to remove the dilution effects of alkanethiol.

3.4 Results and discussion

3.4.1 Assembly of gold nanorods

The as-prepared gold nanorods were characterized using UV-visible spectroscopy and transmission electron microscopy (TEM). The TEM images of the as prepared nanorods are shown in Figure 3.3a. All the nanorods were well separated as it is seen

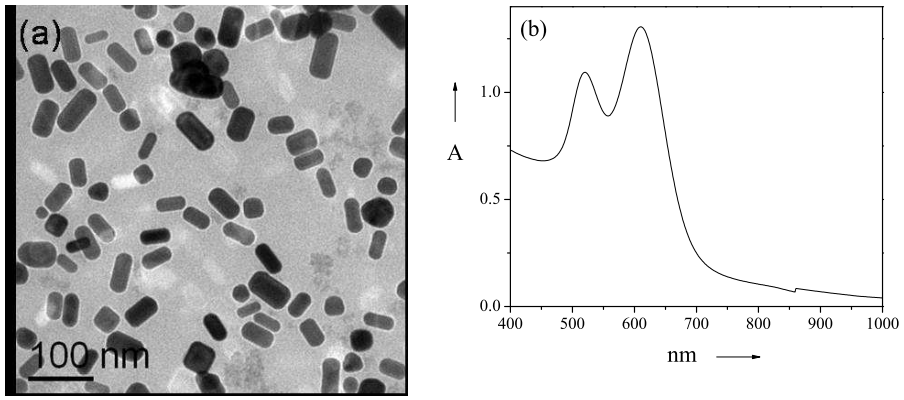

(a) (b)

Figure 3.3: (a) TEM micrographs and (b) UV-visible spectra of gold nanorods

in the figure. The average length of the nanorods is 40 nm and it average diameter is 18 nm. UV-vis spectra show two bands due to surface plasmon resonance. The transverse surface plasmon band appeared around 520 nm and longitudinal band was around 605 nm as shown in Figure 3.3b.

The additions of the linkers lead to the end to end assembly which is evidenced by UV-vis spectroscopy. Figure 3.4a shows the changes in optical spectra with time after the addition of mercaptopropionic acid to the as prepared gold nanorods. Each spectrum is recorded in the interval of 5 min after the initial addition of MPA. As the nanorods are assembled to form chains the longitudinal band shifted to higher

wavelengths. The TEM image recorded after the addition of MPA reveals the presence of assembled nanorods as can be seen from Figure 3.4b.

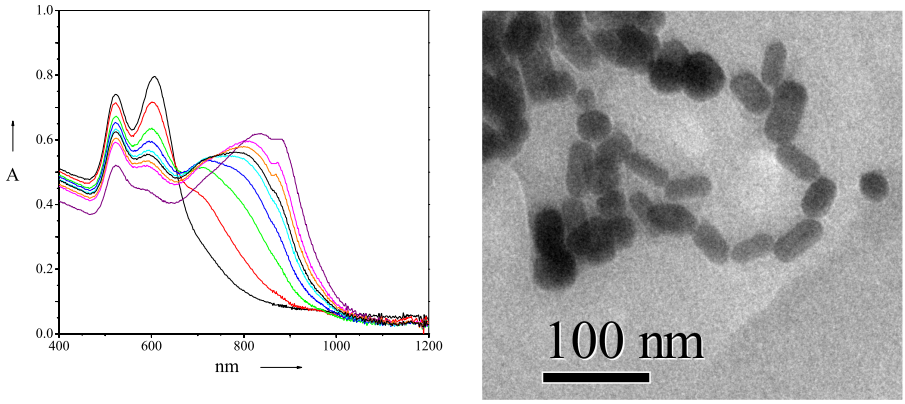

(a) (b)

Figure 3.4: (a) Change in UV-visible spectra of gold nanorods with the addition of 3-mercaptopropionic acid and (b) TEM image of the assembled nanorods

In ITC, we first carried out the study of the linking of gold nanorods to form necklaces by interactions with cysteine. The raw data obtained during the injections of cysteine to gold nanorods are shown in Figure 3.5a. At each injection, an exothermic reaction occurs. Figure 3.5(b) shows the integrated plot of the data in Figure 3.5a, achieved by integrating each peak and normalizing with respect to the concentration of cysteine added.

The integrated plot gives the dependence of the heat exchange at each injection in kcal/mole of cysteine on the molar ratio of cysteine to that of gold nanorods. The data in Figure 3.5(b) were obtained after accounting for dilution effects. We observe that the exothermicity of the peaks decreases from one injection to the next due to the binding of cysteine molecules to the gold nanorods forming Au-S bonds. The number of free sites available on the gold nanorods for the binding of cysteine decreases as the reaction progresses, thereby reducing the exothermicity

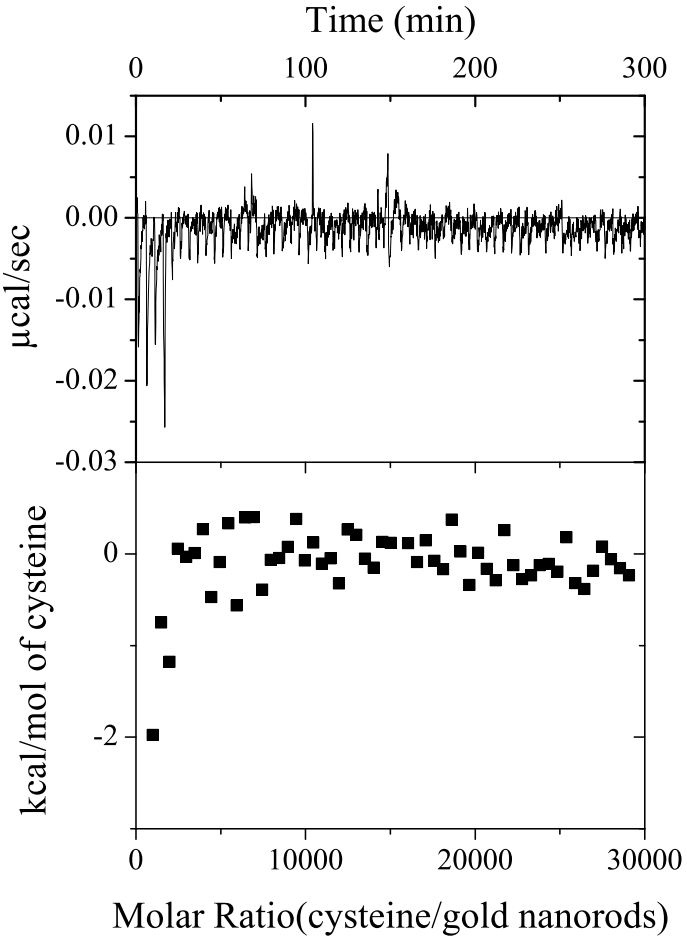

Figure 3.5: (a) Raw calorimetric data obtained by the titration of 0.57 mM cysteine with 1.59 nM gold nanorod solution and (b) binding isotherm plot obtained by integrating each peak in raw data and normalizing with cysteine concentration

with progressive injections. The actual formation of chains or necklaces of gold nanorods occurs by weak electrostatic interaction of the cysteine molecules which cannot be detected by ITC [46]. We therefore observe only a one step process corresponding to the binding of thiol to Au nanorods.

The process of assembly occurring through the interaction of the gold nanorods with cysteine is directly evidenced in the electronic absorption spectra and transmission electron microscopic images. Figure 3.6 shows how the electronic absorp-

tion spectra of the as-prepared nanorods changes after the addition of cysteine.

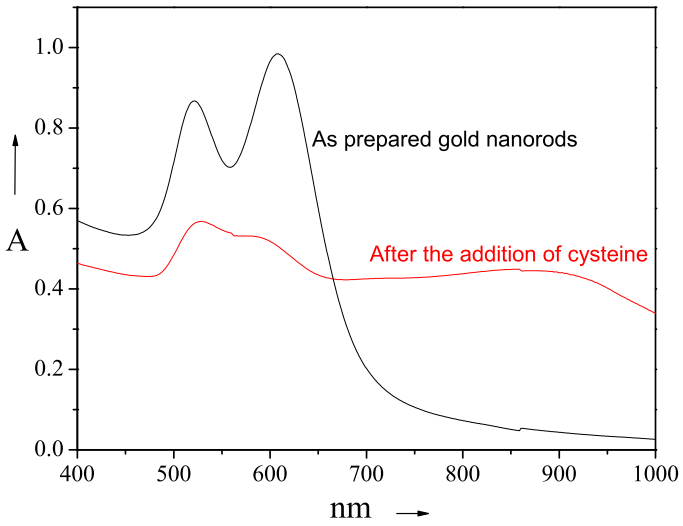

Figure 3.6: UV-visible spectra of gold nanorods before and after calorimetric titration with cysteine

The nanorods show the transverse and longitudinal surface plasmon resonance bands at 520 and 605 nm respectively before the addition of cysteine. After the addition of cysteine, the intensity of the longitudinal surface plasmon band decreases and a new broad band appears in the region 800-900 nm due to formation of chains or necklaces arising from the linking of the gold nanorods by the electrostatic interaction between cysteine molecules. The TEM image in Figure 3.7a shows the presence of randomly oriented Au nanorods in the as-prepared gold nanorods. The formation of necklaces of nanorods after the addition of cysteine is evidenced in the image shown in Figure 3.7b.

The thermodynamics of interaction of cysteine molecules with the gold nanorods can be understood based on the calorimetric data obtained. Assuming that the energy released is due to the formation of Au-S bond only, since the energy associated

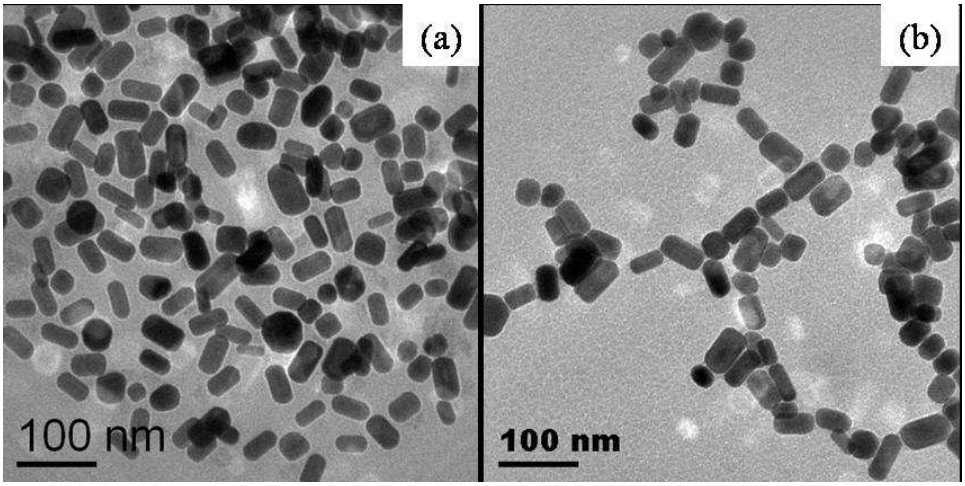

Figure 3.7: TEM micrographs of gold nanorods (a) before and (b) after calorimetric titration with cysteine.

with electrostatic interaction is negligible [34], the number of cysteine molecules bonded to each nanorod can be estimated. The binding of thiol to the gold nanorods involves the following reaction:

$$\text{R-S-H} + \text{Au} \rightarrow \text{R-S-Au} + \tfrac{1}{2}\ \text{H}_2$$

From the bond energies of RS-H, RS-Au, H-H bond which are 87 kcal/mole, 40 kcal/mole and 104 kcal/mole respectively, the net enthalpy of binding of thiol to Au is -5 kcal/mole [47]. The total heat liberated in the cysteine titration is -966 kcal per mole of Au nanorods. The average number of cysteine molecules attached to Au nanorods thus works out to be around 193.

The results of our calorimetric studies of the interaction of the thiol carboxylic acid, MPA, with gold nanorods are quite different from those with cysteine. In the case of MPA, we observe two steps in the calorimetric data as can be seen in Figure 3.8.

To understand the binding process of MPA with the gold nanorods, we performed separate experiments wherein the reaction was stopped at different stages (after 12 and 22 injections) and the product analyzed using TEM and UV-visible

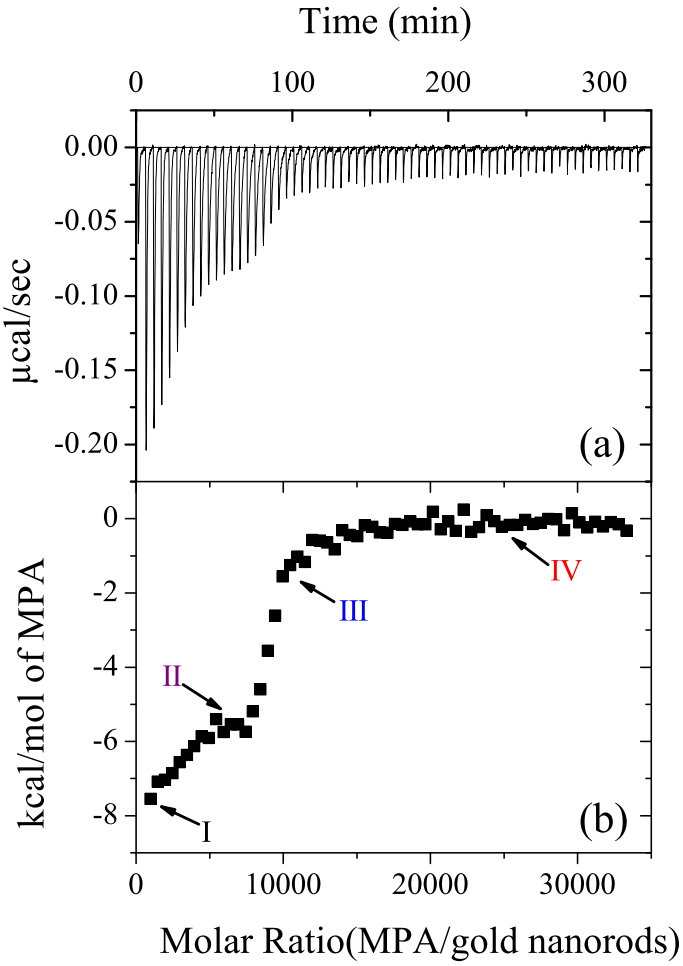

Figure 3.8: (a) Raw calorimetric data obtained by the titration of 0.57 mM 3-mercaptopropionic acid (MPA) with 1.59 nM gold nanorod solution and (b)binding isotherm plot obtained by integrating each peak in raw data and normalizing with MPA concentration.

spectroscopy. Figure 3.9 shows the absorption spectra of Au nanorods taken at different stages during the binding process indicated in Figure 3.8(b). The longitudinal plasmon resonance band does not shift after the first few injections of MPA (point II), and shows significant shifts after 22 injections (point III). We assign the first step in the calorimetric data to the binding of MPA molecules to Au nanorods or the formation of Au-S bonds. The second step corresponds to the binding of

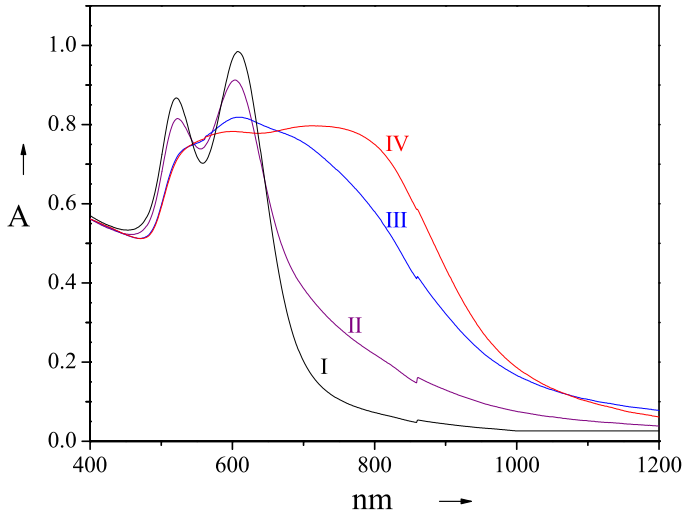

Figure 3.9: UV-visible spectra of gold nanorods taken at different stages of the calorimetric titration with MPA as indicated in Figure 3.8(b).

gold nanorods to form chains or necklaces through the formation of six-membered cyclic hydrogen bonded units between the carboxylic acid groups of MPA. In Figure 3.10, we show the TEM image of the as prepared gold nanorods and the necklaces formed by the nanorods after the addition of MPA. Such an occurrence of two steps has been noted in the dynamics of gold nanorod-alkanedithiol interaction [19].

Using an approach similar to that illustrated for cysteine, we have calculated the average number of MPA molecules attached to each Au nanorod. The heat released in the first step (Figure 3.8) is -3650 kcal/mole of Au nanorods. The number of MPA molecules binding to each gold nanorod is therefore around 730. The heat released in the second step is -3015 kcal per mole of gold nanorods. As intermolecular hydrogen bonding between MPA molecules releases approximately -15 kcal/mole, the number of hydrogen bonded units or the number of gold nanorods in the necklace cannot be greater than 200.

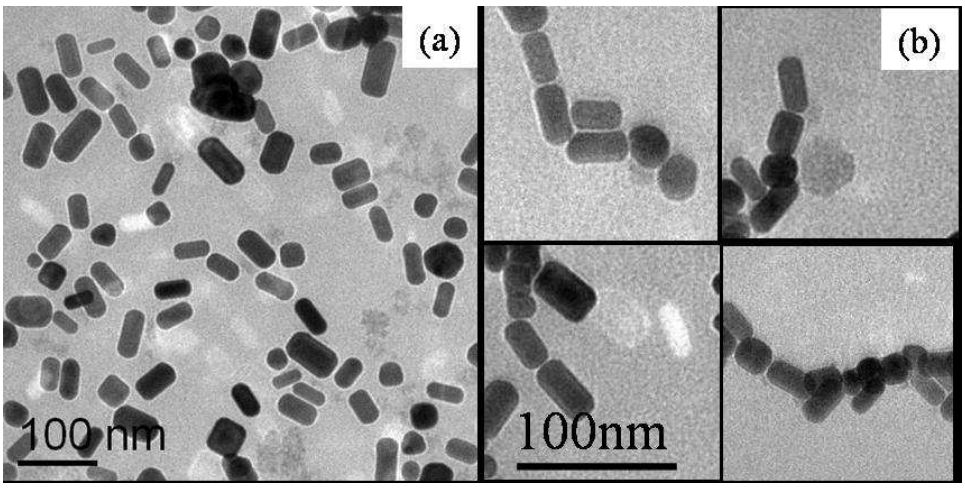

Figure 3.10: TEM micrographs of gold nanorods (a) before and (b) after the titration with MPA

3.4.2 Disintegration of gold films by alkanethiols

The film formed at the liquid-liquid interface was examined by UV-vis spectroscopy and TEM. Figure 3.11 shows the optical spectra and corresponding TEM images of the nanocrystalline films and the changes on perturbation through sonication or interaction with an alkanethiol. The spectrum corresponding to a nanocrystalline film obtained at the liquid-liquid interface at room temperature exhibits a broad band centered at 700 nm, with a weak shoulder at around 540 nm. While the absorption band around 540 nm is characteristic of surface plasmons from uncoupled nanocrystals, the higher wavelength band at 700 nm is a typical response from an assembly of interacting nanocrystals [48]. As evident from the corresponding TEM image (Figure 3.11), the nanocrystalline film consists of close-packed assembly of particles with ≈ 1 nm spacing due to the organic shell. The collective absorption is affected when the nanocrystalline film is subjected to ultrasonication as can be seen in spectrum b of Figure 3.11. There is a rise in absorption at 540 nm followed by an ill-defined broad feature. With the addition of alkanethiol a well-defined band

around 530 nm (spectrum c of Figure 3.11) is obtained, typical of uncoupled colloidal gold nanocrystals. Accordingly, the TEM image shows isolated nanocrystals.

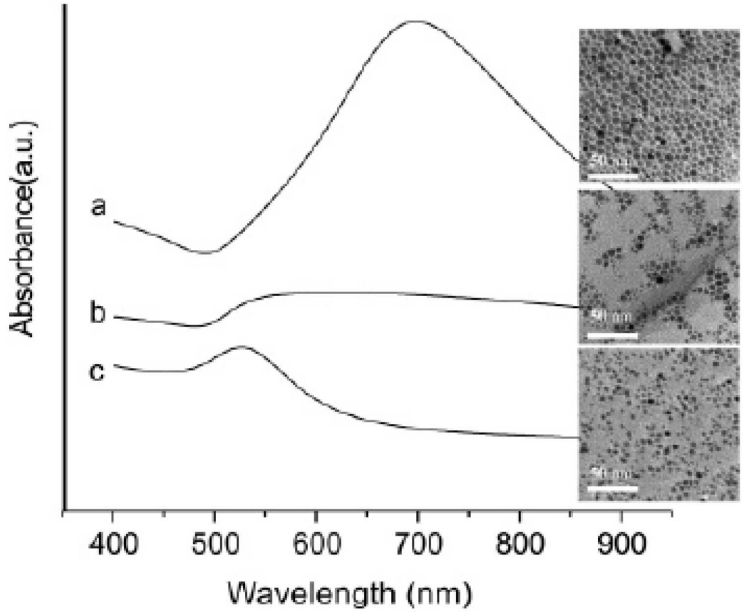

Figure 3.11: Optical absorption spectra of (a) an Au nanocrystalline film prepared at the liquid-liquid interface and deposited on a glass substrate, (b) a sol obtained by sonicating the film in toluene for 3 min, (c) a sol obtained by derivatizing the nanocrystals from the film using hexadecanethiol in toluene. The corresponding TEM images are shown.

Figure 3.12 shows typical data obtained from the isothermal titration calorimetric experiments with two alkanethiols. The integrated plot of the ITC data is given after accounting for the dilution effects of alkanethiols. The additions of small amounts of alkanethiol give rise to an exothermic reaction (initial points in the curve). With increase in the thiol concentration the exothermicity decreases and the process eventually becomes endothermic. After a few injections the process again becomes exothermic. This is seen as a peak in the heat versus concentration plot (Figure 3.12).

Comparison of the disintegration process by two alkanethiols of different chain

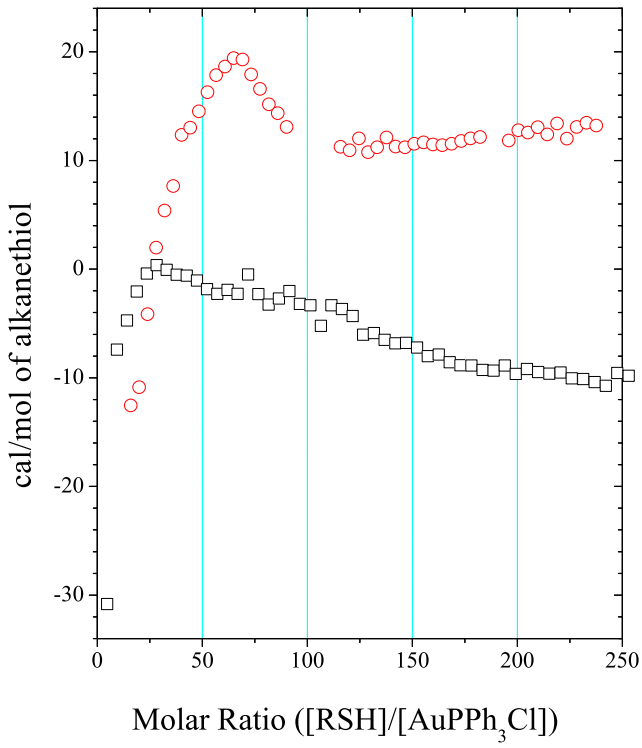

Figure 3.12: Heat content change per mole of the alkanethiols obtained by isothermal titration calorimetric (ITC) experiments versus the molar ratio of alkanethiol (a) C_4 thiol, (b) C_{12} thiol to $Au(PPh_3)Cl$.

length (C_4, C_{12}) shows that the peak appears at different concentrations for different alkanethiols. For longer alkanethiols the peak appeared at lower concentration. The position of the peak relates to the effectiveness of the thiol in disintegrating the film. We have plotted the concentration at which the peak appears against the number of carbon atoms in the alkane chain, n in Figure 3.13. We see a near linear relationship with the peak appearing at low concentration with the increase in chain length.

The mechanism of the disintegration of the film can be explained as follows with

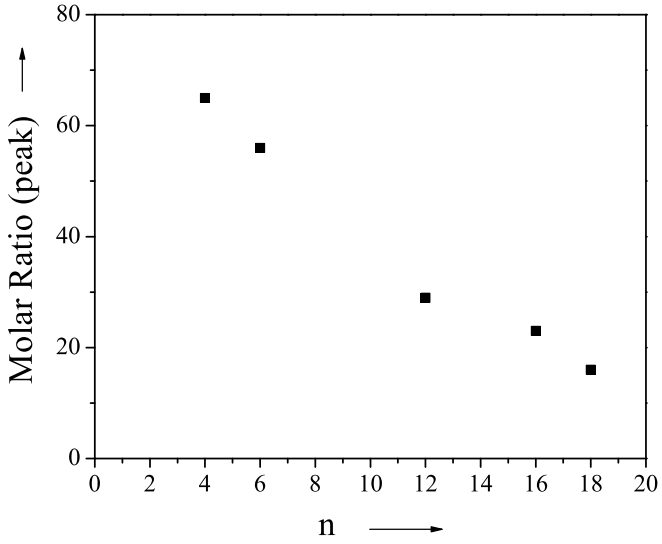

Figure 3.13: Dependence of the molar ratio of the alkanethiol to $Au(PPh_3)Cl$ at which the peak appears due to maximum endothermicity on the number of carbon atoms in the alkanethiol, n.

the help of Figure 3.14. When alkanethiols were added initially to the nanocrystalline film, the thiol group attaches to the gold nanocrystals forming Au-S bond. This step (stage 1 in Figure 3.14) corresponds to the exothermic process seen in figure 3.12. As more alkanethiols were added to the film the number of available sites for binding on the gold nanoparticles of the film decreases which decreases the exothermicity with progressive injections. Also as the alkanethiols attaches to the nanoparticles in the film the spacing between the particles increases and the film starts to disintegrate. The endothermic process corresponds to disordering or disintegration of the film (stage 2). The more is the length of the alkane chain, the more efficient will be the disintegration process since the spacing between nanoparticles is directly proportional to the alkanethiol length. The stage 2 is more complex. After the disordering or disintegration of the film isolated nanoparticles get created

which are then capped by the thiol molecules present in the solution. Hence the last step is again exothermic as indeed seen in Figure 3.12.

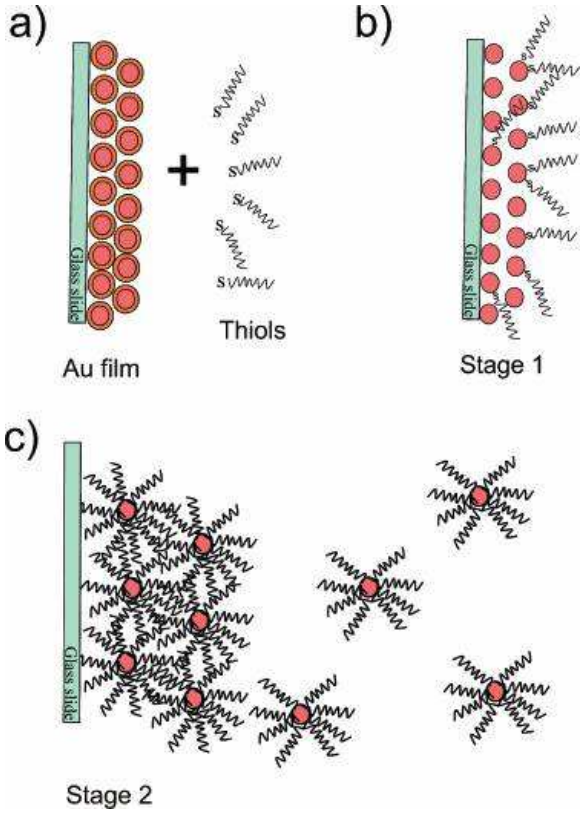

Figure 3.14: A Schematic showing the process of thiol adsorption and increasing disorder in the nanocrystalline film.

3.5 Conclusions

Isothermal titration calorimeter has been a wonderful tool to measure various interactions of nanomaterials. The process of assembly of gold nanorods and disintegration of nanocrystalline film were carried out in ITC and heat changes for these processes were monitored. In the assembly process, ITC experiments were able to distinguish different kind of binding interactions. Isothermal titration calorimetric measurements on the interaction of the thiolcarboxylic acid, MPA, establishes the

occurrence of two steps in the assembling process associated with the binding of gold nanorods to the sulfur atom of linker molecules and the formation of the necklace structure. The shifts of the longitudinal plasmon absorption band of the gold nanorods in the electron absorption spectrum as well as transmission electron microscope images carried out at different states of ITC measurements provide direct evidence for the occurrence of the assembly of gold nanorods at the stage expected from ITC measurements. ITC measurements on the binding of cysteine with gold nanorods show only a single step due to the binding of the molecules, since the process of assembly occurs by electrostatic interaction. Thus, measurements in the cysteine-Au nanorod systems indirectly support the mechanism for the second step found in the MPA-Au nanorod system. The heat change associated with the disintegration of gold nanocrystalline film formed at the liquid-liquid interface by different alkanethiols was monitored using ITC. The study gave insight to the mechanism of the disintegration and the effectiveness of the different alkanethiols in the process.

References

[1] J. E. Ladbury and B. Z. Chowdhry. Sensing the heat: the application of isothermal titration calorimetry to thermodynamic studies of biomolecular interactions. *Chem. Biol.*, 3(10):791–801, 1996.

[2] I. Jelesarov and H. R. Bosshard. Isothermal titration calorimetry and differential scanning calorimetry as complementary tools to investigate the energetics of biomolecular recognition. *J. Mol. Recognit.*, 12(1):3–18, 1999.

[3] A. Ababou and J. E. Ladbury. Survey of the year 2004: literature on applications of isothermal titration calorimetry. *J. Mol. Recognit.*, 19(1):79–89, 2006.

[4] A. A. Saboury. A review on the ligand binding studies by isothermal titration calorimetry. *J. Iran. Chem. Soc.*, 3(1):1–21, 2006.

[5] S. D. Spencer and R. B. Raffa. Isothermal titration calorimetric study of RNase-A kinetics (cCMP $\rightarrow$ 3'-CMP) involving end-product inhibition. *Pharm. Res.*, 21(9):1642–1647, 2004.

[6] J. E. Ladbury. Isothermal titration calorimetry: application to structure-based drug design. *Thermochim. Acta*, 380(2):209–215, 2001.

[7] K. Beyer, D. Leine, and A. Blume. The demicellization of alkyltrimethylammonium bromides in 0.1 M sodium chloride solution studied by isothermal titration calorimetry. *Colloids and Surfaces B: Biointerfaces*, 49(1):31–39, 2006.

[8] O. Okhrimenko and I. Jelesarov. A survey of the year 2006 literature on

applications of isothermal titration calorimetry. *J. Mol. Recognit.*, 21(1):1–19, 2008.

[9] M. J. Cliff, A. Gutierrez, and J. E. Ladbury. A survey of the year 2003 literature on applications of isothermal titration calorimetry. *J. Mol. Recognit.*, 17(6):513–523, 2004.

[10] A. Gourishankar, S. Shukla, K. N. Ganesh, and M. Sastry. Isothermal titration calorimetry studies on the binding of DNA bases and PNA base monomers to gold nanoparticles. *J. Am. Chem. Soc.*, 126(41):13186–13187, 2004.

[11] A. Das, A. K. Sood, P. K. Maiti, M. Das, R. Varadarajan, and C.N.R. Rao. Binding of nucleobases with single-walled carbon nanotubes: Theory and experiment. *Chem. Phys. Lett.*, 453(4-6):266–273, 2008.

[12] C. N. R. Rao, A. Muller, and A. K. Cheetham. *Recent Advances in the Chemistry of Nanomaterials, Wiley-VCH Verlag GmbH & Co.* 2004.

[13] C. N. R. Rao, G. U. Kulkarni, P. J. Thomas, and P. P. Edwards. Metal nanoparticles and their assemblies. *Chem. Soc. Rev.*, 29(1):27–35, 2000.

[14] E. Dujardin, L. B. Hsin, C. R. C. Wang, and S. Mann. DNA-driven self-assembly of gold nanorods. *Chem. Commun.*, (14):1264–1265, 2001.

[15] B. Nikoobakth, Z. L. Wang, and M. A. El-Sayed. Isothermal titration calorimetry: application to structure-based drug design. *J. Phys. Chem. B*, 104(36):8635–8640, 2000.

[16] K. G. Thomas, S. Barazzouk, B. I. Ipe, S. T. S. Joseph, and P. V. Kamat. Uniaxial plasmon coupling through longitudinal self-assembly of gold nanorods. *J. Phys. Chem. B*, 108(35):13066–13068, 2004.

[17] S. Zhang, X. Kou, Z. Yang, Q. Shi, G. D. Stucky, L. Sun, J. Wang, and C. Yan. Nanonecklaces assembled from gold rods, spheres, and bipyramids. *Chem. Commun*, (18):1816–1818, 2007.

[18] K. K. Caswell, J. N. Wilson, U. H. F Bunz, and C. J. Murphy. Preferential end-to-end assembly of gold nanorods by biotin-streptavidin connectors. *J. Am. Chem. Soc.*, 125(46):13914–13915, 2003.

[19] S. T. S. Joseph, B. I. Ipe, P. Pramod, and K. G. Thomas. Gold nanorods to nanochains: Mechanistic investigations on their longitudinal assembly using α,ω-alkanedithiols and interplasmon coupling. *J. Phys. Chem. B*, 110(1):150–157, 2006.

[20] R. Voggu, P. Suguna, S. Chandrasekaran, and C. N. R. Rao. Assembling covalently linked nanocrystals and nanotubes through click chemistry. *Thermochim. Acta*, 443(1-3):118–121, 2007.

[21] C. N. R. Rao, G. U. Kulkarni, P. J. Thomas, V. V. Agrawal, and P. Saravanan. Films of metal nanocrystals formed at aqueous-organic interfaces. *J. Phys. Chem. B*, 107(30):7391–7395, 2003.

[22] S. Link, M. B. Mohamed, and M. A. El-Sayed. Simulation of the optical absorption spectra of gold nanorods as a function of their aspect ratio and the effect of the medium dielectric constant. *J. Phys. Chem. B*, 103(16):3073–3077, 1999.

[23] Z. L. Wang. Structural analysis of self-assembling nanocrystal superlattices. *Adv. Mater.*, 10(1):13–30, 1998.

[24] C. N. R. Rao, P. J. Thomas, and G. U. Kulkarni. *Nanocrystals: Synthesis,Properties and Applications; Springer-Verlag: Berlin.* 2007.

[25] A. H. Rechberger, A. Leitner, J. R. Krenn, B. Lamprecht, and L. Aussenegg. Optical properties of two interacting gold nanoparticles. *Opt.Commun.*, 220(1-3):137–141, 2003.

[26] U. Kreibig and M. Vollmer. *Optical Properties of Metal Clusters; Springer-Verlag: Berlin.* 1995.

[27] J. B. Pelka, M. Brust, P. Gierlowski, W. Paszkowicz, and N. Schell. Structure and conductivity of self-assembled films of gold nanoparticles. *Appl. Phys. Lett.*, 89(6):063110(1–3), 2006.

[28] R. H. Terrill, T. A. Postlethwaite, C.-h. Chen, C.-D. Poon, A. Terzis, A. Chen, J. E. Hutchison, M. R. Clark, and G. J. Wignall. Monolayers in three dimensions: NMR, SAXS, thermal, and electron hopping studies of alkanethiol stabilized gold clusters. *J. Am. Chem. Soc.*, 117(50):12537–12548, 1995.

[29] W. P. Wuelfing, S. J. Green, J. J. Pietron, D. E. Cliffel, and R. W. Murray. Electronic conductivity of solid-state, mixed-valent, monolayer-protected au clusters. *J. Am. Chem. Soc.*, 122(46):11465–11472, 2000.

[30] M. P. Pileni, Y. Lalatonne, D. Ingert, I. Lisiecki, and A. Courty. Self assemblies of nanocrystals: preparation, collective properties and uses. *Faraday Discuss.*, 125:251–264, 2004.

[31] A. J. Haes, S. Zou, G. C. Schatz, and R. P. VanDuyne. A nanoscale optical

biosensor: The long range distance dependence of the localized surface plasmon resonance of noble metal nanoparticles. *J. Phys. Chem. B*, 108(1):109–116, 2004.

[32] Y. Joseph, I. Besnard, M. Rosenberger, B. Guse, J. M.and Wild U. Nothofer, H. G.and Wessels, A. Knop-Gericke, D. Su, R. Schlogl, A. Yasuda, and T. Vossmeyer. Self-assembled gold nanoparticle/alkanedithiol films: Preparation, electron microscopy, XPS-Analysis, charge transport, and vapor-sensing properties. *J. Phys. Chem. B*, 107(30):7406–7413, 2003.

[33] N. Krasteva, I. Besnard, B. Guse, R. E. Bauer, K. Mullen, A. Yasuda, and T. Vossmeyer. Self-assembled gold nanoparticle/dendrimer composite films for vapor sensing applications. *Nano Lett.*, 2(5):551–555, 2002.

[34] Y. Lu, G. L. Liu, and L. P. Lee. High-density silver nanoparticle film with temperature-controllable interparticle spacing for a tunable surface enhanced raman scattering substrate. *Nano Lett.*, 5(1):5–9, 2005.

[35] A. Yu, Z. Liang, J. Cho, and F. Caruso. Nanostructured electrochemical sensor based on dense gold nanoparticle films. *Nano Lett.*, 3(9):1203–1207, 2003.

[36] E. Roduner. Size matters: why nanomaterials are different. *Chem. Soc. Rev.*, 35(7):583–592, 2006.

[37] C. P. Collier, T. Vossmeyer, and J. R. Heath. Nanocrystal superlattices. *Annu. Rev. Phys. Chem.*, 49:371–404, 1998.

[38] J. R. Heath, C. M. Knobler, and D. V. Leff. Pressure/temperature phase diagrams and superlattices of organically functionalized metal nanocrystal mono-

layers: The influence of particle size, size distribution, and surface passivant. *J. Phys. Chem. B*, 101(2):189–197, 1997.

[39] B. Kim, S. L. Tripp, and A. Wei. Self-organization of large gold nanoparticle arrays. *J. Am. Chem. Soc.*, 123(32):7955–7956, 2001.

[40] N. Chandrasekharan and P. V. Kamat. Assembling gold nanoparticles as nanostructured films using an electrophoretic approach. *Nano Lett.*, 1(2):67–70, 2001.

[41] C. L. Haynes, A. D. McFarland, L. Zhao, R. P. Van Duyne, G. C. Schatz, L. Gunnarsson, J. Prikulis, B. Kasemo, and M. Kall. Nanoparticle optics: The importance of radiative dipole coupling in two-dimensional nanoparticle arrays. *J. Phys. Chem. B*, 107(30):7337–7342, 2003.

[42] C. N. R. Rao, G. U. Kulkarni, V. V. Agrawal, U. K. Gautam, M. Ghosh, and U. Tumkurkar. Use of the liquid-liquid interface for generating ultrathin nanocrystalline films of metals, chalcogenides, and oxides. *J. Colloid Interface Sci.*, 289(2):305–318, 2005.

[43] V. V. Agrawal, G. U. Kulkarni, and C. N. R. Rao. Nature and properties of ultrathin nanocrystalline gold films formed at the organic-aqueous interface. *J. Phys. Chem. B*, 109(15):7300–7305, 2005.

[44] F. Kim, J. H. Song, and P. Yang. Photochemical synthesis of gold nanorods. *J. Am. Chem. Soc.*, 124(48):14316–14317, 2002.

[45] C. J. Orendorff and C. J. Murphy. Quantitation of metal content in the silver-assisted growth of gold nanorods. *J. Phys. Chem. B*, 110(9):3990–3994, 2006.

[46] H. Joshi, P. S. Shirude, V. Bansal, K. N. Ganesh, and M. Sastry. Isothermal titration calorimetry studies on the binding of amino acids to gold nanoparticles. *J. Phys. Chem. B*, 108(31):11535–11540, 2004.

[47] A. Ulman. Formation and structure of self-assembled monolayers. *Chem. Rev.*, 96(4):1533–1554, 1996.

[48] L. Gunnarsson, T. Rindzevicius, J. Prikulis, B. Kasemo, Mi. Kll, S. Zou, and G. C. Schatz. Confined plasmons in nanofabricated single silver particle pairs: experimental observations of strong interparticle interactions. *J. Phys. Chem. B*, 109(3):1079–1087, 2005.

CHAPTER 4

Selectivity in the Interaction of Electron Donor and Acceptor Molecules with Graphene and Single-Walled Carbon Nanotubes*

Summary

Interaction of electron donor and acceptor molecules with graphene samples prepared by different methods as well as with single-walled carbon nanotubes (SWNTs) has been investigated by isothermal titration calorimetry (ITC) and spectroscopic techniques. The ITC interaction energies of the graphene samples and SWNTs with electron acceptor molecules are higher than those with electron donor molecules. Thus, tetracyanoethylene (TCNE) shows the highest interaction energy with both graphene and SWNTs. The interaction energy with acceptor molecules varies with the electron affinity as well as with the charge-transfer transition energy for different aromatics. Metallic SWNTs interact reversibly with electron acceptor molecules, resulting in the opening of a gap.

*A paper based on this work has been published in *J. Phys. Chem. C* **(2009)**

4.1 Introduction

Recent investigations of the interaction of electron donor and acceptor molecules with single-walled carbon nanotubes (SWNTs) have shown that molecular charge-transfer affects the electronic structure of the nanotubes [1–4]. Thus, by the interaction of tetracyanoethylene (TCNE) and tetrathiafulvalene (TTF), it has been possible to introduce metallic to semiconducting transition in SWNTs and vice versa, but specificity of interaction with respect to the electronic nature of the SWNTs is not established. Interaction of electron donor and acceptor molecules with few-layer graphene has been investigated using Raman spectroscopy and other techniques. Molecular charge transfer interaction between these molecules and graphene causes marked changes in the electronic structure of graphene [5, 6]. The softening and stiffening of the G-band in Raman spectra of graphene were observed on the interaction with the donor and acceptor molecules respectively. The magnitude of the shifts in the G-band increased depending on the increase in donating or accepting power of these molecules and the concentration. First-principles calculations based on the DFT-GGA method suggest the interaction of graphene with donor and acceptor molecules to involve charge-transfer, giving rise to the associated Raman band shifts [7].

4.2 Scope of the present investigations

It is of essence to carry out a comparative investigation of the interaction of donor and acceptor molecules with graphene and SWNTs in terms of the relative interaction energies. For this purpose, we have employed isothermal titration calorimetry (ITC) to measure the heats of interaction of a few electron donor and acceptor molecules with graphene and SWNTs. ITC is known to be a sensitive tool to study

such binding interactions, as illustrated in the case of nucleobases [8, 9]. ITC may not provide actual interaction energies, but gives trends in interaction energies. Since SWNTs prepared by arc discharge and other methods constitute mixtures of semiconducting and metallic species [10], we have investigated the interaction of pure metallic nanotubes, specially prepared by a new method and of pure semiconducting (CoMoCAT) nanotubes with donor and acceptor molecules, in order to examine the specificity of interaction. Besides showing that electron-withdrawing molecules interact more strongly with graphene and SWNTs, the present study demonstrates that doping by charge-transfer changes the Fermi level of SWNTs, to create a band gap in the initially metallic SWNTs. In the case of graphene also, a band gap is opened through charge-transfer by electron acceptor molecules.

4.3 Experimental section

Isothermal titration calorimetric experiments were carried out with graphene samples prepared by three different methods, namely thermal exfoliation of graphitic oxide (EG) [11], arc discharge of graphite in hydrogen (HG) [12] and conversion of nanodiamond (DG) [13]. Dodecylamide derivatives of EG (EG-A) and DG (DG-A) were prepared by the literature procedure [14, 15]. The graphene samples were characterized by atomic force microscopy (AFM), transmission electron microscopy (TEM), field-emission scanning electron microscopy (FESEM) and Raman spectroscopy. The EG, DG and HG samples contained 3-4, 5-6 and 2-3 layers, respectively. The surface area of the HG sample is small ($\approx 400\ m^2g^{-1}$) compared to DG ($\approx 800\ m^2g^{-1}$) and EG ($\approx 1100\ m^2g^{-1}$). EG-A, DG-A and HG dispersed in toluene were used in the experiments.

ITC experiments were carried out with 1 mg mL^{-1} dispersions of graphene.

The graphene dispersion was taken in the sample cell of the isothermal titration calorimeter and the reference cell filled with toluene. 10 mM solutions of tetracyanoethylene (TCNE), tetracyanoquinodimethane (TCNQ), 2,4,7-trinitrofluorenone (TNF), tetrathiafulvalene (TTF), N,N-dimethyl para-phenylenediamine (DMPD) and N,N,N',N'-tetramethyl para-phenylenediamine (TMPD) were prepared in toluene. In each experiment, 10 μL of 10 mM of each of these solutions taken in syringe was added in equal intervals of 3 minutes to the sample cell and the heat changes measured after each addition. The experiments were carried out at a constant temperature 26 °C. Control experiments were performed by titrating the respective molecules against toluene under the same conditions and the data so obtained were subtracted from the experimental data to eliminate the dilution effect.

SWNT samples were prepared by the arc discharge method and purified by successive acid and hydrogen treatment [16, 17]. Metallic SWNTs were prepared by DC arc evaporation of a graphite rod containing the Ni+Y_2O_3 catalyst, under a continuous flow of helium bubbled through $Fe(CO)_5$ [18, 19]. The samples so obtained were nearly pure metallic SWNTs (around 95%). SWNT samples dispersed in ortho-dichlorobenzene (DCB) were sonicated for 1 hour to obtain 1 mg mL^{-1} solutions. The CoMoCAT nanotubes purchased from Southwest Nanotechnologies, Inc. (around 92% semiconducting) were also dispersed in ortho-dichlorobenzene (DCB) by sonication to obtain 1 mg mL^{-1} solutions. Interaction of SWNTs with donor and acceptor molecules was studied in DCB solvent in the same manner as the graphene samples. In order to compare the results obtained with graphene and SWNTs, graphene samples (EG, EG-A and HG) were also dispersed in DCB by sonication for 1 hour to obtain 1 mg mL^{-1} solutions. These solutions were used to study the interaction with TCNE.

4.4 Results and discussion

Interaction with graphene

The changes in the Raman spectra of graphene on interaction with electron donor and acceptor molecules have been studied. Figure 4.1 shows the shifts in the G-band position of Raman spectra of graphene with TCNE and TTF of varying concentrations. The stiffening and softening of the G-band is observed on interaction with TCNE and TTF respectively. The shifts in the G-band increases with increase in the concentrations of the donor and acceptor molecules [6].

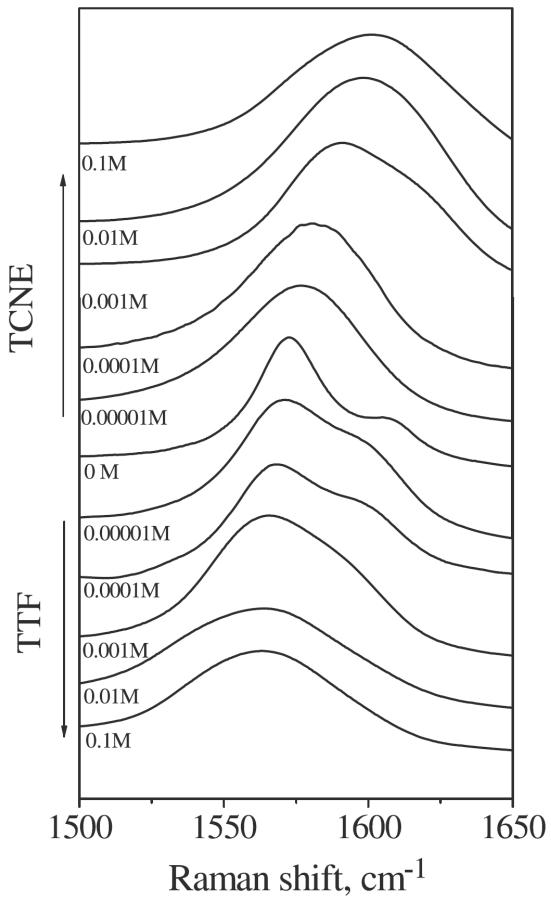

Figure 4.1: Shifts in the Raman G-band of graphene caused by interaction with varying concentrations of TTF and TCNE [6].

We carried out ITC measurements on the interaction of graphenes with donor and acceptor molecules. Figure 4.2 shows typical data obtained with 1.0 mg mL^{-1} solutions of EG-A in toluene with TCNE and TTF. Raw ITC data for the blank

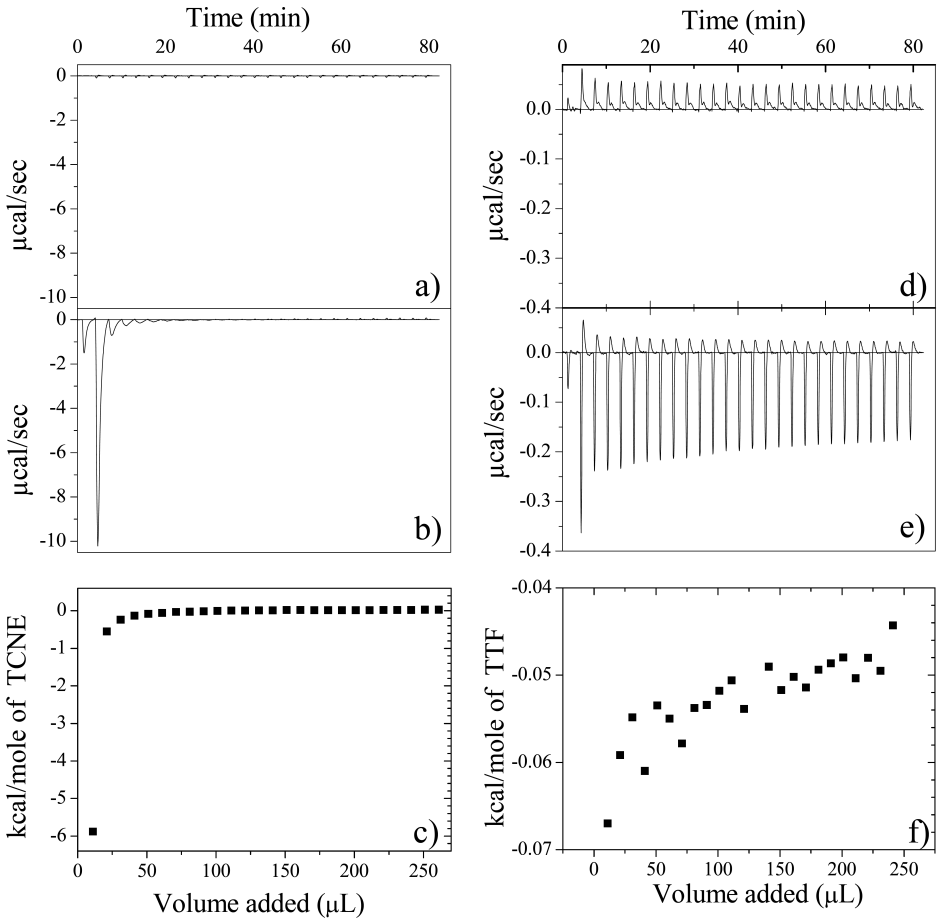

Figure 4.2: ITC data recorded for the interaction of TCNE and TTF with EG-A. ITC response for the blank titration with TCNE (a) and TTF (d). The raw ITC data for the titration of TCNE and TTF with 1.0 mg mL^{-1} of EG-A is shown in (b) and (e). (c) and (f) show the integrated heat of reaction at each injection of TCNE and TTF respectively.

titration of 10 mM TCNE and TTF against toluene are shown in Figures 4.2a and d. Figures 4.2b and e show the raw data for the titration of 10 mM TCNE and TTF solutions against 1.0 mg mL^{-1} EG-A solution. The ITC response in

the TCNE and TTF titrations against EG-A is exothermic as shown in Figures 4.2b and e. In order to eliminate dilution effects, heats from the blank titration data were subtracted from the molecule-graphene titration data. Figures 4.2c and f show the integrated heat changes (enthalpy changes in kcal mol^{-1}) after each injection of TCNE and TTF respectively after correcting for the heat of dilution. The exothermicity of the peaks reduces with progressive injection as the number of free sites for the binding of molecules available on the graphene decreases. The heat of reaction curve should ideally be sigmoidal in shape, but the limited solubility of graphene in toluene does not permit to record the initial part of the sigmoidal curve. Absolute binding energies cannot therefore be obtained from the present data. The relative affinities of the different electron donor and acceptor molecules can, however, be estimated from the heat liberated in the initial injections since all the experiments were performed under similar conditions. The relative binding energies obtained from the initial points of the integrated heat plots in the case of EG-A and HG are listed in Table 4.1. The trend in the relative binding energies of electron acceptor molecules with EG-A obtained from ITC measurements is, TCNE > TCNQ > TNF. Interaction energies of electron donor molecules with the graphene samples are considerably lower, the highest value being with N,N-dimethyl para-phenylenediamine (DMPD). The interaction energy of TTF is lower than that of DMPD. In the case of the interaction of TCNE with the different graphene samples, the highest ITC interaction energy is found to be with EG-A (-5.9 kcal mol^{-1}) and the lowest with DG-A (-1.6 kcal mol^{-1}). It is noteworthy that the surface area of EG is highest amongst the graphene samples [20].

Since the data for SWNTs were obtained in DCB solvent, we wanted to compare the data of graphenes in the same solvent. For this purpose, we carried out the isothermal titration calorimetric expriments of graphene prepared by different

	EG-A[(a)]	HG[(a)]	SWNT[(b)]
TCNE	-5.88[(c)]	-4.2	-4.25
TCNQ	-0.24		-0.32
TNF	-0.12	-0.30	-0.06
DMPD	-0.40	-0.12	-7.4
TTF	-0.07		-0.18

Table 4.1: Energies of interaction of graphene and SWNTs with electron donor and acceptor molecules obtained from ITC measurements (in kcal mol^{-1}). Concentration of graphene and SWNTs was 1 mg mL^{-1} in all the cases. (a) in toluene solvent (b) in ortho-dichlorobenzene (DCB) solvent (c) with DG-A the value is -1.6.

methods with TCNE. The relative interaction energies of TCNE in DCB solvent are -1.4 kcal mol^{-1}, -0.7 kcal mol^{-1}, -0.6 kcal mol^{-1} with EG-A, EG and HG respectively, giving the trend EG-A > EG > HG. This trend parallels that of the surface area.

Interaction energies of graphene with different donor and acceptor molecules have been calculated by employing first-principles calculations using a linear combination of atomic orbital DFT methods implemented in the SIESTA package [7]. This study shows evidence for charge transfer between graphene and the donor and acceptor molecules. According to this study, the interaction energies of graphene with TCNE and TCNQ are greater than that with TTF. This is consistent with the results from our ITC studies. The calculations also show that a gap develops in the electronic structure of graphene on interaction with these molecules.

Interaction with SWNTs

Interaction of single-walled carbon nanotubes with electron donor and acceptor molecules causes significant changes in the electronic and Raman spectra. Electron-donating molecules such as tetrathiafulvalene and aniline cause changes opposite to those caused by electron-withdrawing molecules such as nitrobenzene and tetra-

cyanoethylene. Figure 4.3 shows the shifts in Raman G-band of the SWNTs on interaction with various electron donor and acceptor molecules. SWNTs became more mettalic on interaction with electron-donating molecules and more semiconducing on interaction with acceptor molecules [1].

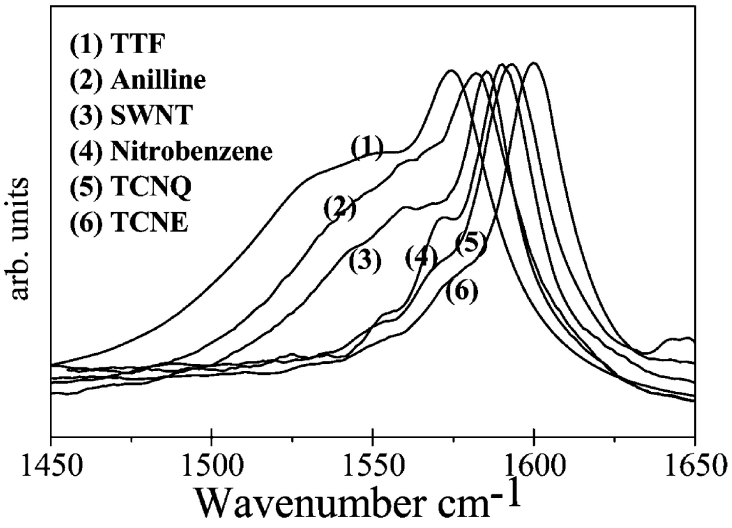

Figure 4.3: G-bands in the of Raman spectra of SWNTs on interaction with electron donor and acceptor molecules [1].

We have obtained ITC interaction energies of SWNTs with donor and acceptor molecules by a procedure similar to that with graphene by using orthodichlorobenzene (DCB) as the solvent. Typical data obtained for 1.0 mg mL^{-1} solutions of SWNTs in DCB interacting with TCNE and TTF are given in Figure 4.4. Raw data for the titration of 10 mM TCNE and TTF solutions against the 1.0 mg mL^{-1} SWNT solution are given in Figures 4.4 b and e. The ITC response in the titrations is exothermic as revealed by Figures 4.4 b and e. The integrated heat changes after each injection of TCNE and TTF respectively (after correcting for the heat of dilution) are shown in Figures 4.4 c and f. Just as in the case of graphene, exothermicity of the peaks reduces with progressive injection. The energies of interaction calculated from the initial points of the integrated heat plots are listed

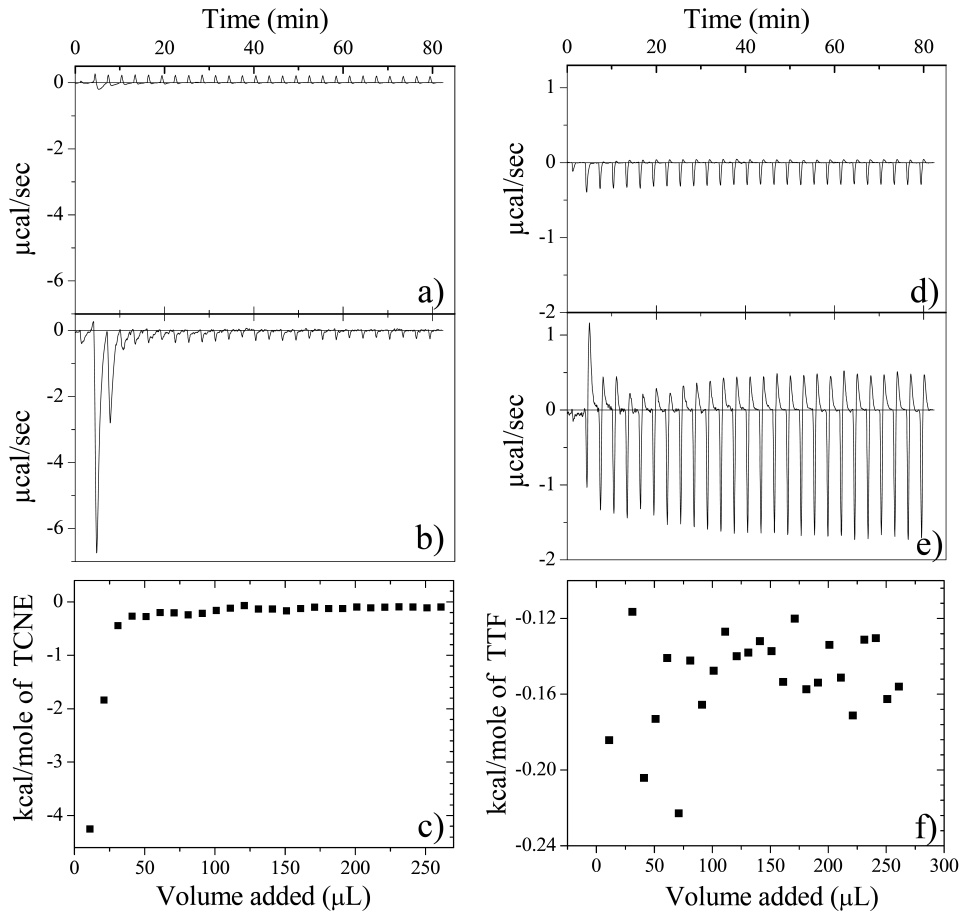

Figure 4.4: ITC data recorded for the interaction of TCNE and TTF with SWNTs. ITC response for the blank titration with TCNE (a) and TTF (d). The raw ITC data for the titration of TCNE and TTF with 1.0 mg mL^{-1} of SWNT is shown in (b) and (e). (c) and (f) show the integrated heat of reaction at each injection for TCNE and TTF respectively.

in Table 4.1. It is interesting that for electron acceptor molecules, the trend in the ITC interaction energies with SWNTs is the same as that with graphene (TCNE > TCNQ > TNF). Among the donor molecules, DMPD shows higher interaction energy than TTF. The interaction energy of SWNTs (-4.3 kcal mol^{-1}) with TCNE is generally larger than for the graphene samples. First-principles calculations of Pati in this laboratory (personal communication) have shown the interaction energy of SWNTs with TCNQ to be greater than that with TTF. SWNTs exhibit

higher interaction energy than graphene.

Interaction energies of graphene as well as SWNTs with electron acceptor molecules increase progressively with the electron affinities of the acceptors as can be seen in Figure 4.5(a) [21]. This result confirms that charge-transfer between the acceptor molecules and graphene or SWNTs contributes significantly to the interaction energy. Indirect confirmation of this conclusion is also provided by the fact that the interaction energy varies systematically with the charge-transfer transition energy, hν_{CT}, of the acceptors with an aromatic such as anthracene [22–24] as shown in figure 4.5(b).

Interaction with metallic SWNTs

SWNTs prepared by arc-discharge and other methods contain a mixture of metallic and semiconducting species,[10] the proportion of semiconducting nanotubes being around 66%. The interaction energies that we have given in Table 4.1 correspond to the mixture of metallic and semiconducting SWNTs. It would be more instructive if one were able to determine the interaction energy between the donor and acceptor molecules with pure metallic or semiconducting nanotubes. ITC measurements on the interaction of metallic SWNTs with donor and acceptor molecules reveal the interaction energy to be high in the case of TCNE (-7.4 kcal mol^{-1}), the energy varying in the order TCNE > TNF > TCNQ in the case of the acceptor molecules (Table 4.2).

Interaction energies of acceptor molecules with metallic SWNTs are generally higher than with the as-prepared SWNTs (containing the mixture of metallic and semiconducting species). The interaction energy of metallic nanotubes with a donor molecule such as TTF is negligible and could not be measured by ITC. This re-

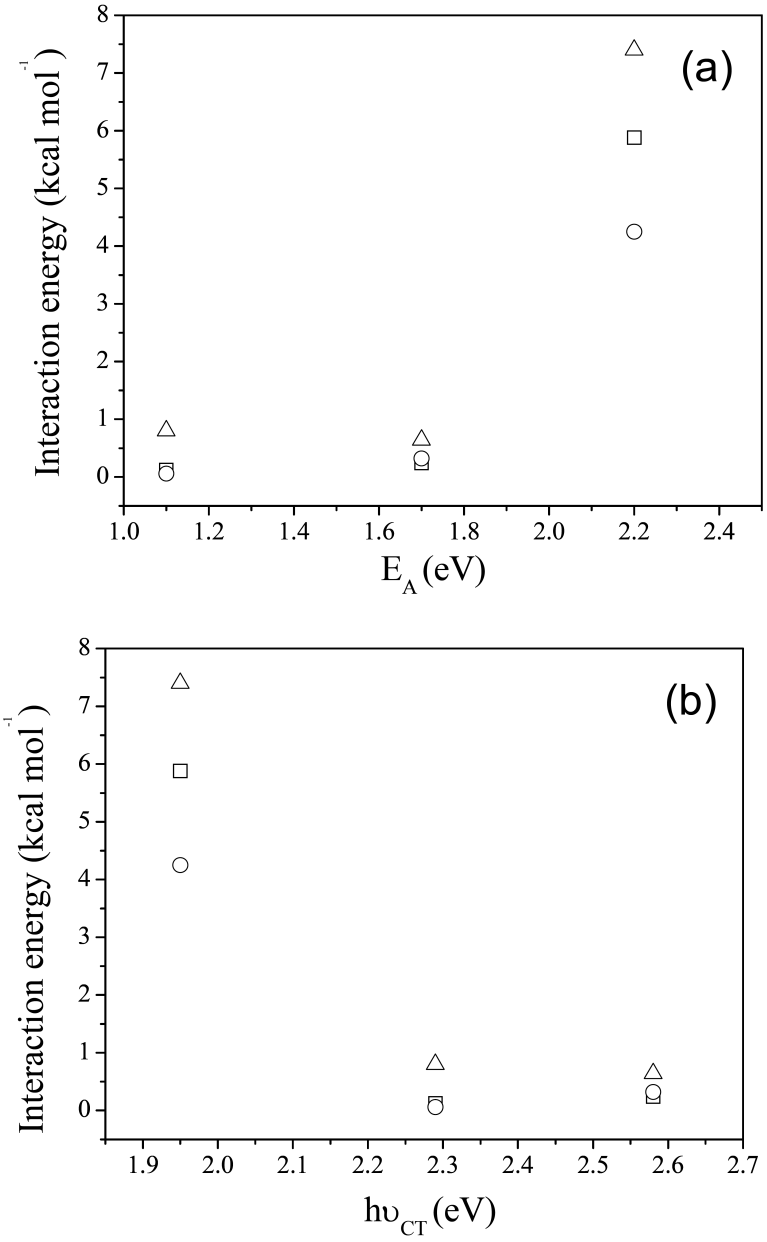

Figure 4.5: Variation of interaction energies of EG-A and SWNTs with electron acceptors (a) with the electron affinity of acceptors, E_A, (b) and with the charge-transfer transition energy, h_{CT}, with anthracene (EG-A, squares ; SWNTs, circles ; metallic SWNTs, triangles).

sult shows that metallic nanotubes specifically interact with electron-withdrawing molecules. In order to understand the nature of this interaction, we examined the

	SWNT$^{(a)}$	Metallic SWNT
TCNE	-4.25	-7.4
TCNQ	-0.32	-0.64
TNF	-0.06	-0.80
TTF	-0.18	+0.07

Table 4.2: Energies of interaction of SWNTs with electron donor and acceptor molecules obtained from ITC measurements (in kcal mol^{-1}). Concentration of SWNTs was 1 mg mL^{-1} in all the cases. (a) mixture containing 66% semiconducting and 33% metallic SWNTs

effect of acceptor and donor molecules on the Raman spectrum of metallic SWNTs. In Figure 4.6, we show the Raman G-band of metallic nanotubes before and after the interaction with TCNE (10 mM). On interaction with TCNE, the feature around 1540 cm^{-1} due to the metallic species [1, 25] disappears completely and the band maximum shifts to 1582 cm^{-1}. This change in the Raman spectrum corre-

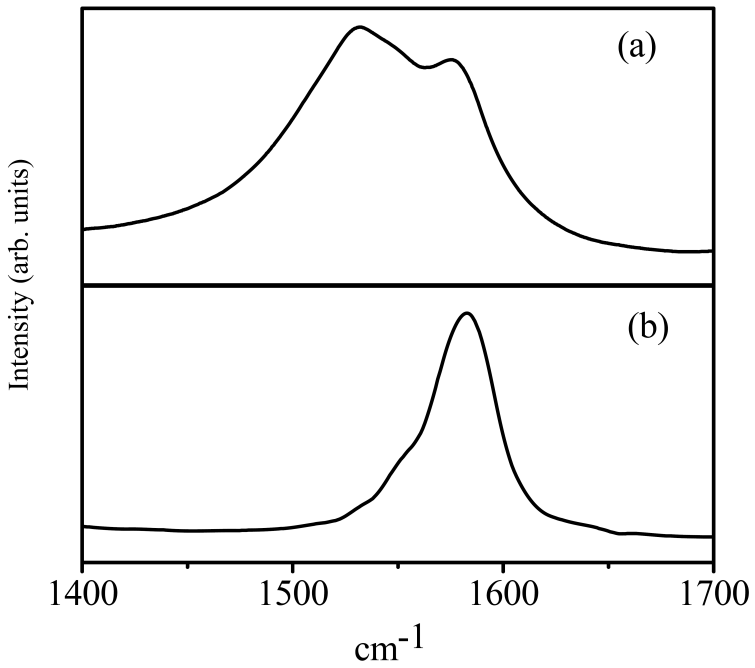

Figure 4.6: Raman G-band of (a) metallic SWNTs and (b) metallic SWNTs after interaction with TCNE (10mM).

sponds to the opening of a gap due to change in the Fermi level of SWNTs, giving

	Metallic SWNT$^{(a)}$	Semiconducting SWNT$^{(b)}$
TCNE	-7.4	-0.22
TCNQ	-0.64	+2.9
TTF	+0.07	-2.3
DMPD	+0.47	-1.9
TTMPD	-0.05	-2.9

Table 4.3: Energies of interaction of SWNTs with electron donor and acceptor molecules obtained from ITC measurements (in kcal mol^{-1}). Concentration of SWNTs was 1 mg mL^{-1} in all the cases. (a) nanotubes prepared by arc discharge method, (b) CoMoCAT nanotubes.

rise to an apparent metal-semiconductor transition. Electron-donating molecules have no effect on the Raman spectrum of metallic SWNTs. First-principles calculations also show that metallic (9,0) SWNTs develop a gap on interaction with TCNE. Electron-donating molecules, however, specifically interact with semiconducting nanotubes.

Interaction with semiconducting SWNTs

After the interaction of donor and acceptor molecules with metallic nanotubes and the mixture of metallic and semiconducting nanotubes has been carried out, it was our interest to measure the interacion of these molecules with pure semiconducting molecules with ITC. For this purpose, we used CoMoCAT nanotubes which are mainly semiconducting. The interaction energies obtained for the semiconducting molecules with donor and acceptor molecules are shown in Table 4.3. The donor molecules are found to interact strongly with the semiconducting nanotubes, the energy varying in the order TMPD > TTF > DMPD. The interaction of acceptor molecules like TCNE and TCNQ with the semiconducting nanotubes is negligible.

4.5 Conclusions

In conclusion, ITC provides a satisfactory means to investigate the interaction of graphene as well as SWNTs with electron donor and acceptor molecules. Although ITC does not provide absolute interaction energies, it gives trends in interaction energy which are of value. Interaction energies of electron acceptor molecules (TCNE, TCNQ and TNF) with graphene samples are higher than those of electron donor molecules (TTF and DMPD). Among the different graphene samples, the functionalized graphene EG-A shows the highest interaction energy. The studies carried out by us are on few-layer graphenes, but it would be somewhat difficult to investigate single-layer graphenes in this manner owing to its agglomeration in solid state. Interaction energies of SWNTs obtained from ITC are generally higher than those with graphene samples. Here again, TCNE gives the highest interaction energy. Metallic SWNTs interact specifically with electron acceptor molecules, such as TCNE, the interaction energy being higher than with as-prepared SWNTs (containing a mixture of metallic and semiconducting species). On interaction of metallic SWNTs with TCNE, the metallic feature in the Raman G-band disappears, due to the opening of a gap through molecular charge transfer. It would be worthwhile to study the interaction of pure semiconducting SWNTs with donor and acceptor molecules. Semiconducting nanotubes are found to interact more strongly with electron donor molecules than with the acceptor molecules.

References

[1] R. Voggu, C. S. Rout, A. D. Franklin, T. S. Fisher, and C. N. R. Rao. Extraordinary sensitivity of the electronic structure and properties of single-walled carbon nanotubes to molecular charge-transfer. *J. Phys. Chem. C*, 112(34):13053–13056, 2008.

[2] H. J. Shin, S. M. Kim, S. M. Yoon, A. Benayad, K. K. Kim, S. J. Kim, H. K. Park, J.Y. Choi, and Y. H. Lee. Tailoring electronic structures of carbon nanotubes by solvent with electron-donating and -withdrawing groups. *J. Am. Chem. Soc.*, 130(6):2062–2066, 2008.

[3] F. Tournus, S. Latil, M. I. Heggie, and J. C. Charlier. π -stacking interaction between carbon nanotubes and organic molecules. *Phys. Rev. B*, 72(7):075431, 2005.

[4] M. S. Strano, C. A. Dyke, M. L. Usrey, P. W. Barone, M. J. Allen, H. Shan, C. Kittrell, R. H. Hauge, J. M. Tour, and R. E. Smalley. Electronic Structure Control of Single-Walled Carbon Nanotube Functionalization. *Science*, 301(5639):1519–1522, 2003.

[5] B. Das, R. Voggu, C. S. Rout, and C. N. R. Rao. Changes in the electronic structure and properties of graphene induced by molecular charge-transfer. *Chem. Commun.*, pages 5155–5157, 2008.

[6] R. Voggu, B. Das, C. S. Rout, and C. N. R. Rao. Effects of charge transfer interaction of graphene with electron donor and acceptor molecules examined using raman spectroscopy and cognate techniques. *J. Phys.: Condens. Matter*, 20(47):472204, 2008.

[7] A. K. Manna and S. K. Pati. Tuning the electronic structure of graphene by molecular charge transfer: A computational study. *Chem. Asian. J*, 4(6):855–860, 2009.

[8] J. E. Ladbury and B. Z. Chowdhry. Sensing the heat: the application of isothermal titration calorimetry to thermodynamic studies of biomolecular interactions. *Chem. Biol.*, 3(10):791–801, 1996.

[9] A. Das, A. K. Sood, P. K. Maiti, M. Das, R. Varadarajan, and C.N.R. Rao. Binding of nucleobases with single-walled carbon nanotubes: Theory and experiment. *Chem. Phys. Lett.*, 453(4-6):266–273, 2008.

[10] C. N. R. Rao and A. Govindaraj. *Nanotubes and Nanowires; RSC Nanoscience & Nanotechnology series; Royal Society of Chemistry:Cambridge, U.K.,*. 2005.

[11] H. C. Schniepp, J. Li, M.J. McAllister, H. Sai, M. Herrera-Alonso, D. H. Adamson, R. K. Prud'homme, R. Car, D. A. Saville, and I. A. Aksay. Functionalized single graphene sheets derived from splitting graphite oxide. *J. Phys. Chem. B*, 110(17):8535–8539, 2006.

[12] K. S. Subrahmanyam, L. S. Panchakarla, A. Govindaraj, and C. N. R. Rao. Simple method of preparing graphene flakes by an arc-discharge method. *J. Phys. Chem. C*, 113(11):4257–4259, 2009.

[13] O. E. Andersson, B. L. V. Prasad, H. Sato, T. Enoki, Y. Hishiyama, Y. Kaburagi, M. Yoshikawa, and S. Bandow. Structure and electronic properties of graphite nanoparticles. *Phys. Rev. B*, 58(24):16387–16395, 1998.

[14] K. S. Subrahmanyam, S. R. C. Vivekchand, A. Govindaraj, and C. N. R.

Rao. A study of graphenes prepared by different methods: characterization, properties and solubilization. *J. Mater. Chem.*, 18:1517–1523, 2008.

[15] C. N. R. Rao, K. Biswas, K. S. Subrahmanyam, and A. Govindaraj. Graphene, the new nanocarbon. *J. Mater. Chem.*, 19:2457–2469, 2009.

[16] C. Journet, W. K. Maser, P. Bernier, A. Loiseau, M. Lamy de laChapelle, S. Lefrant, P. Deniard, R. Lee, and J. E. Fischer. Large-scale production of single-walled carbon nanotubes by the electric-arc technique. *Nature*, 388:756–758, 1997.

[17] S. R. C. Vivekchand, A. Govindaraj, M. M. Seikh, and C. N. R. Rao. New method of purification of carbon nanotubes based on hydrogen treatment. *J. Phys. Chem. B*, 108(22):6935–6937, 2004.

[18] R. Voggu, A. Govindaraj, and C. N. R. Rao. A new method of obtaining high enrichment of metallic single-walled carbon nanotubes, arxiv:0903.5359v1. *Condens. Matter*, 2009.

[19] R. Voggu, S. Ghosh, A. Govindaraj, and C. N. R. Rao. New strategies for the enrichment of metallic single-walled carbon nanotubes. *J. Nanosci. Nanotechnol*, 10(6):4102–4108, 2010.

[20] K.S. Subrahmanyam, R. Voggu, A. Govindaraj, and C.N.R. Rao. A comparative raman study of the interaction of electron donor and acceptor molecules with graphene prepared by different methods. *Chem. Phys. Lett.*, 472(1-3):96 – 98, 2009.

[21] G. Briegleb. Electron affinity of organic molecules. *Angew. Chem., Int. Ed.*, 3(9):617–632, 1964.

[22] M. J. S. Dewar and H. Rogers. π-complexes. II. charge transfer spectra of π-complexes formed by tetracyanoethylene with polycyclic aromatic hydrocarbons and with heteroaromatic boron compounds. *J. Am. Chem. Soc.*, 84(3):395–398, 1962.

[23] D. S. Acker and W. R. Hertler. Substituted quinodimethans. I. preparation and chemistry of 7,7,8,8-tetracyanoquinodimethan. *J. Am. Chem. Soc.*, 84(17):3370–3374, 1962.

[24] A. R. Lepley. π-complex interactions between trinitrofluorenone and polycyclic aromatic hydrocarbons. *J. Am. Chem. Soc.*, 84(18):3577–3582, 1962.

[25] A. Das, A. K. Sood, A. Govindaraj, A. M. Saitta, M. Lazzeri, F. Mauri, and C. N. R Rao. Doping in carbon nanotubes probed by raman and transport measurements. *Phys. Rev. Lett.*, 99(13):136803, 2007.

CHAPTER 5

Binding of DNA Nucleobases and Nucleosides with Graphene*

Summary

Interaction of two different samples of graphene with DNA nucleobases and nucleosides is investigated by isothermal titration calorimetry. The relative interaction energies of the nucleobases decrease in the order guanine (G) > adenine (A) > cytosine (C) > thymine (T) in aqueous solution, although the positions of C and T seem to be interchangeable. The same trend is found with the nucleosides. Interaction energies of the A-T and G-C pairs are somewhere between those of the constituent bases. Theoretical calculations including van der Waals interaction and solvation energies give the trend G > A ≈ T > C. The magnitudes of the interaction energies of the nucleobases with graphene are similar to those found with single-walled carbon nanotubes.

*A paper based on this work has been published in *ChemPhysChem* **(2009)**

5.1 Introduction

The interaction of DNA nucleobases with nanostructures has attracted much attention recently [1–5]. Binding of DNA bases and peptide nucleic acid (PNA) base monomers to gold nanoparticles has been examined by isothermal titration calorimetry and the strength of interaction varies in the order cytosine (C)> guanine (G)> adenine (A)> thymine (T) [1]. Interaction strengths of nucleobases with single-walled carbon nanotubes (SWNTs) and graphene have been estimated theoretically [5–8]. The experimental binding energies of nucleobases with SWNTs decrease in the order $T > A > C$, in agreement with calculations showing a trend of $G > T > A > C$ [5]. This trend is obtained from theory only when solvation effects are included. It would be of interest to compare this trend with that of the interaction of nucleobases with graphene. The binding of nucleobases with gold nanoparticles would involve specific capping interactions of the amino or other functional groups of the nucleobases with the metal particles. This would not be the case with SWNTs and graphene. Some theoretical studies have examined the binding of nucleobases with graphene. The trend of the calculated interaction energies shows some variations, especially in case of cytosine and thymine. For example, the interaction energies of the DNA nucleobases with graphene [6] and SWNTs [7] have been calculated using the plane-wave pseudopotential approach within the local density approximation (LDA) of density functional theory and found the sequence of interaction energy to be $G > A \approx T \approx C$. Antony *et al.* [8] have calculated the interaction energy of the DNA nucleobases with graphene with the dispersion-corrected density functional theory (DFT-D) method and obtained the order $G > A > T > C$. The single solute adsorption isotherm study of DNA nucleobases at the graphite-water interface shows the adsorption strength to vary

as $G > A > T > C$ [9].

5.2 Scope of the present investigations

In the present experimental investigation, binding of DNA nucleobases and nucleosides with graphene has been explored by employing isothermal titration calorimetry (ITC) since this technique is a useful tool to study binding interactions in aqueous media [10]. The trend in the interaction energies found by experiment have been compared with that from theoretical calculations and also that reported for SWNTs. The theoretical calculations employed by us include van der Waals energy as well as the solvation energy.

5.3 Experimental section

Isothermal titration calorimetric experiments were carried out with two graphene samples (Graphene I and Graphene II) prepared by different methods. Graphene I was prepared by the exfoliation of graphitic oxide by the method reported in the literature [11]. According to this method, graphitic oxide was prepared by reacting graphite (500 mg, Alfa Aesar, 2-15 mm) with a mixture of concentrated nitric acid (9 mL) and sulfuric acid (18 mL) with potassium chlorate (10 g) at room temperature for 5 days. Thermal exfoliation of graphitic oxide was carried out in a long quartz tube at 1050 ^0C under an argon atmosphere. The samples were characterized using X-ray diffraction (XRD), atomic force microscopy (AFM) and Raman spectroscopy. The samples contained 3-4 layers on average. In order to solubilize graphene in water, concentrated nitric acid (2 mL), concentrated sulfuric acid (2 mL) and water (20 mL) were added to graphene (10 mg) and subsequently

heated in a microwave oven for 10 min under hydrothermal conditions. Further, the sample was heated at 100 ^{0}C for 12 h. The product was washed with distilled water and centrifuged repeatedly to remove traces of acid [12]. Finally the graphene was dispersed in Milli-Q water and this solution was used for further experiments.

Graphene II was prepared by reduction of graphitic oxide by hydrazine. Graphitic oxide was prepared by the same method described earlier and was filtered, washed with distilled water and dried in oven at 40-45 ^{0}C for 2 days. It was then dissolved in distilled water by probe sonication while hydrazine (2 mL) was added to the mixture dropwise. A black precipitate was formed in the solution which was washed and dried. The product so obtained was examined by XRD, AFM and other measurements which showed it to contain 6-7 layers. The surface area of graphene II is smaller ($\approx 400\ m^2g^{-1}$) compared to graphene I ($\approx 1000\ m^2g^{-1}$). The graphene was dispersed in Milli-Q water by sonicating 1.0 mgmL^{-1} solution of graphene in water for 2 h. The solution was kept undisturbed for 15 min and the supernatant liquid was collected and this solution was used for further experiments.

ITC experiments were carried out with two different concentrations of graphene I solutions (1.0 mgmL^{-1} and 0.3 mgmL^{-1}). The graphene dispersion was taken in the sample cell of isothermal titration calorimeter and the reference cell was filled with Milli-Q water. All the ITC experiments were carried out at a constant temperature 4 ^{0}C. 10 mM solutions of nucleobases (adenine, cytosine, thymine) were made in Milli-Q water. In each experiment, 10 mL of 10 mM nucleobase solution was taken by syringe and added to the sample cell in equal intervals of 3 min. The heat changes was measured after each addition. Control experiments were performed by titrating nucleobases against Milli-Q water under the same conditions and the data obtained were subtracted from the experimental data to remove the dilution effect of nucleobases. Since guanine was insoluble in neutral

water, ITC titrations were also performed using alkaline solutions of all the four DNA nucleobases (10 mM solutions of nucleobases in 30 mM NaOH) keeping all the other conditions same. In order to study the binding of the nucleosides (adenosine, cytidine, thymidine) with graphene, ITC experiments were performed by titrating 10 mM solutions of nucleosides with graphene under conditions similar to those for nucleobases. ITC measurements were also carried out in water using graphene II with nucleobases as well as nucleosides keeping all other conditions same.

In order to study the interaction of graphene with base pairs, ITC experiments were performed with graphene I and the nucleobases pairs in pure water as well as alkaline solutions. In the case of A-T pair, equivalent amounts of A and T were mixed to form 10 mM A- T solutions in pure water. To compare the binding of the two base pairs A-T and G-C, experiments were also performed in alkaline solutions. Binding of the A-T pair in pure water was also examined by titration of this pair with graphene I.

5.4 Results and discussion

We first carried out the study of interaction of graphene I with nucleobases adenine (A), cytosine (C) and thymine (T) in aqueous solution. We could not study the interaction with guanine because of its poor solubility in water. Figure 5.1 shows typical data obtained with 1.0 mgmL^{-1} solutions of graphene in the case of A and T. The raw ITC data for the blank titration of 10 mM A and T against milliQ water being shown in Figures 5.1 a and d. Figures 5.1 b and e show the raw data for the titration of 10 mM A and T solutions against 1.0 mgmL^{-1} graphene solution. The ITC response for the T titration with graphene is exothermic where as in case of A it is endothermic for higher volumes of injection, as can be seen in

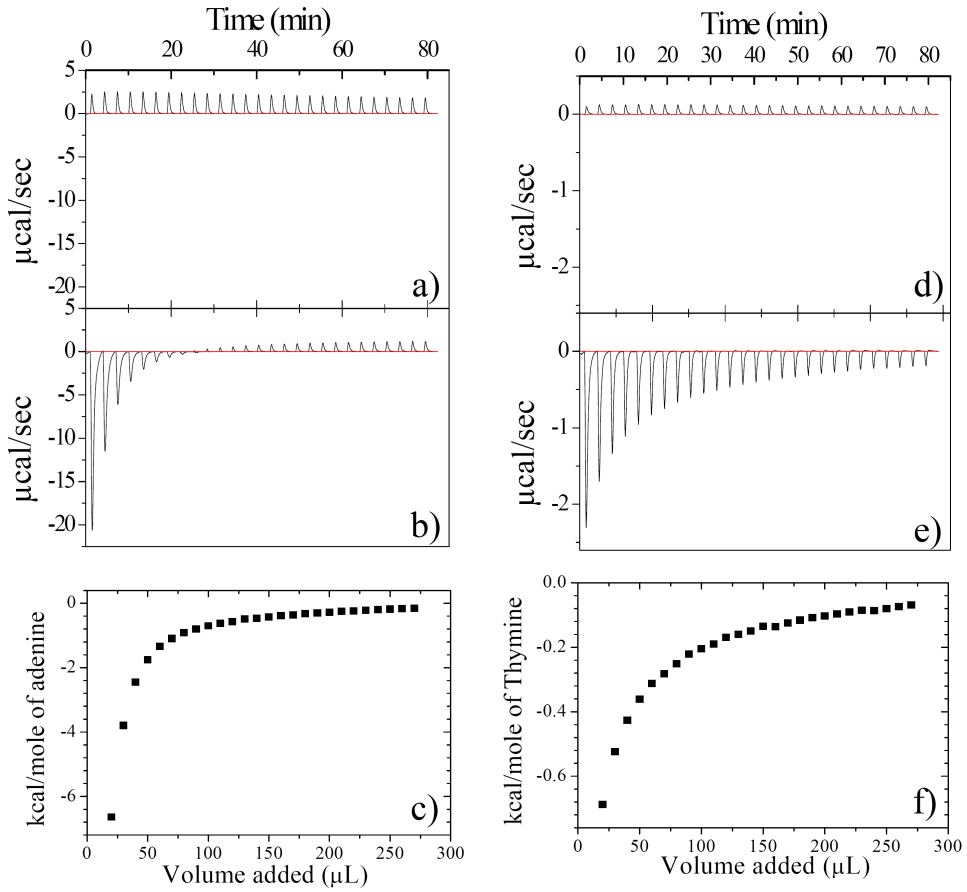

Figure 5.1: ITC data recorded for the interaction of nucleobases with graphene. ITC response for the blank titration with A (a) and T (d). The raw ITC data for the titration of A and T with 1.0 mgmL^{-1} of graphene I is shown in (b) and (e). (c) and (f) show the integrated heat of reaction at each injection for A and T respectively

Figures 5.1 b and e. The blank titration for A also shows higher endothermicity as compared to that with T. In order to eliminate the dilution effects, the heats from the blank titration data were subtracted from the nucleobases-graphene titration data. Figures 5.1 c and f show the integrated heat changes (enthalpy changes in kcal mol^{-1}) after each injection of A and T respectively after correcting for the heat of dilution. The interaction is exothermic for all the three nucleobases, and for different concentrations of graphene. The exothermicity of the peaks reduce

Nucleobase	Graphene I (0.3 $mgmL^{-1}$)	Graphene I (1.0 $mgmL^{-1}$)	Graphene II
Thymine	-0.16	-0.68	-0.42
Cytosine	-0.89	-4.39	-0.29
Adenine	-1.25	-6.64	-0.59

Table 5.1: Graphene-nucleobase interaction energies (in water) in kcal mol^{-1}

with progressive injection as the number of free sites for the binding of nucleobases available on the graphene decreases. Ideally, the heat of reaction curve should be sigmoidal in shape. The limited solubility of the graphene in water does not permit to record the initial part of the sigmoidal curve. The measurement of the absolute binding energy cannot therefore be done from the present data. However, the relative affinities of the different nucleobases can be estimated from the heat liberated in the initial injections since all the experiments were performed under similar conditions. The relative binding energies calculated from the initial points of the integrated heat plots are listed in Table 5.1. Among the three nucleobases, adenine shows the highest interaction energy with graphene and thymine shows the least. This trend in the relative interaction energies ($A > C > T$) was obtained from the experiments performed with both low (0.3 $mgmL^{-1}$) and high (1.0 $mgmL^{-1}$) concentrations of graphene as revealed in Table 5.1. In order to compare the interaction of guanine with A, C and T, we carried out ITC experiments with graphene I in alkaline solutions. The process was found to be exothermic in all the cases as in the case of experiments performed in aqueous solution. The relative binding energies obtained are given in Table 5.2. Here, the order of interaction energies of the four nucleobases with graphene is $G > A > C > T$. It is interesting that this trend nearly parallels that predicted by Antony *et al.* [8] and Gowtham *et al.* [6].

We carried out ITC experiments on the interaction of nucleobases with graphene

Nucleobase	Graphene I (1.0 mgmL^{-1})
Thymine	-4.72
Cytosine	-9.38
Adenine	-11.85
Guanine	-13.45

Table 5.2: Graphene-nucleobase interaction energies (in alkaline solution) in kcal mol^{-1}

II in aqueous solutions keeping all other conditions same. The relative interaction energies of A, C and T obtained with graphene II are given in Table 5.1. Here again, adenine shows the highest binding energy, but cytosine shows a lower binding energy than thymine. The trend in interaction energies is $A > T > C$. It may be noted that theoretical calculations predict the interaction energies to vary as $A > T \approx C$ or $A > T > C$. It is possible that C and T can interchange places in the order of interaction energies with graphene, both being pyrimidines with similar functionalities. Furthermore, the surfaces of the graphene I and II would have differences since the latter was produced by hydrazine reduction of graphitic oxide while the former was obtained by exfoliation. Furthermore, graphene II has a lower surface area.

In order to study the interaction of DNA nucleosides with graphene I, we carried out ITC measurements with 10 mM solutions of adenosine, cytidine and thymidine. The experiments were performed in aqueous solution with two different concentrations of graphene I (0.3 mgmL^{-1} and 1.0 mgmL^{-1}). Figure 5.2 shows typical curves obtained in the ITC experiments for adenosine and thymidine with 1.0 mgmL^{-1} of graphene I solution. The ITC response in the thymidine titration is exothermic where as that in the case of adenosine is endothermic for injections of higher volumes, the blank titration for adenosine showing higher endothermicity compared to that with adenosine-graphene titration. After subtracting the dilution effects,

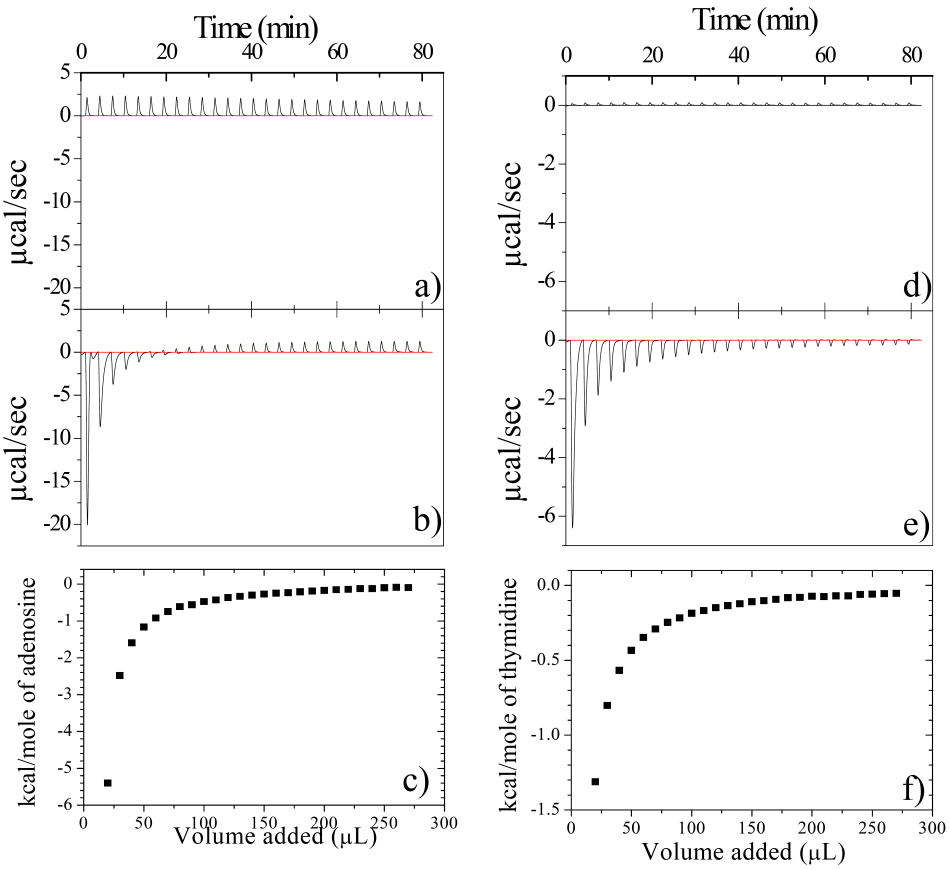

Figure 5.2: ITC data recorded for the interaction of nucleosides with graphene. ITC response for the blank titration with adenosine (a) and thymidine (d). The raw ITC data for the titration of adenosine and thymidine with 1.0 mgmL^{-1} of graphene I is shown in (b) and (e). (c) and (f) show the integrated heat of reaction at each injection for adenosine and thymidine respectively

we obtained the integrated heat change due to each injection of adenosine and thymidine respectively plotted in Figures 5.2 c and f. The process is exothermic for all the three nucleosides and for both the concentrations of graphene. Just as in the case of the bases the exothermicity of peaks reduces with the progressive injection as the number of free sites available on the graphene for the binding of nucleosides decreases. The energies of interaction calculated from the initial points of the integrated heat plot for the three nucleosides are listed in Table 5.3. Among the three nucleosides adenosine showed the highest interaction energy with

Nucleosides	Graphene I (0.3 mgmL^{-1})	Graphene I (1.0 mgmL^{-1})	Graphene II
Thymidine	-0.17	-1.31	-0.15
Cytidine	-0.43	-3.54	-0.25
Adenosine	-0.54	-5.40	-0.46

Table 5.3: Graphene-nucleoside interaction energies (in water) in kcal mol^{-1}

graphene whereas thymidine shows the least. The same trend is obtained with both low (0.3 mgmL^{-1}) and high (1.0 mgmL^{-1}) concentrations of graphene as it is shown in Table 5.3. Thus, the variation in the interaction energies of different nucleosides with graphene I (adenosine > cytidine > thymidine) is same as that with the nucleobases.

We carried out a study of the interaction of nucleosides with graphene II keeping all other conditions the same. The order of the relative interaction energies is adenosine > cytidine > thymidine (Table 5.3), similar to that found with graphene I. The interaction energies of nucleobases with graphene are generally small. They are relatively weak interactions [8]. Calculations on the graphene....Watson-Crick pair complexes show that the base pair hydrogen bonds are barely affected by binding with graphene. However, the binding of A-T and C-G on graphene is found to weaken by 7 and 12% respectively leading to the geometrical anti-cooperativity of the base pair [8]. In order to examine the interaction energies of base pairs with graphene, we have carried out ITC experiments by adding equivalent amounts of relevant nucleobases to graphene I. In Table 5.4, we have given the results obtained with some of the base pairs in both pure water and alkaline solutions. In the case of the A-T base pair, we find that the interaction energy in water is comparable to the sum of interaction energies of the two bases, and slightly higher than that obtained with adenine alone. In alkaline solutions, we could measure the interaction energies of both G-C and A-T pairs. Here, the energies are somewhere in between

Base pair	Graphene I (1.0 mgmL^{-1})
Adenine-Thymine (in water)	-7.75
Adenine-Thymine (in NaOH solution)	-9.73
Guanine-Cytosine (in NaOH solution)	-12.3
Adenosine-Thymidine (in water)	-4.63

Table 5.4: Graphene-base pair interaction energies in kcal mol^{-1}

those of the individual nucleobases. Thus, the interaction energy of the G-C pair is somewhere in between that of G and C while that of the A-T pair is in between that of A and T. The interaction energy of the nucleoside pair adenosine-thymidine is also between that of adenosine and thymidine. That the observed interaction energies of the base pairs are not generally equal to the sum of the interaction energies of the individual nucleobases or nucleosides is probably related to the stereochemistry and orientation of the base pairs. It is possible that the two bases in the pairs do not have the same orientation while the individual ones may lie flat on the graphene surface. It is also to be noted that the G-C pair exhibits greater interaction than the A-T pair. Figure 5.3 summarizes the trends obtained by ITC.

To gain insight into the origin of interaction of nucleobases with graphene, Dr. Maiti of IISc has carried out theoretical calculations. An earlier paper [5] discusses how nucleobases interact with SWNTs, by calculationg the total binding energies for the nanotube-nulcloebases system by adding the Hartree-Fock (HF-quantum chemical), van der Waals (vdW) and solvation energies. HF has been used to calculate the binding energy due to covalent bond or ionic bond between the nucleobases and the nanotube. However, HF is found to be inadequate to calculate the contribution to the binding energy due to dispersive vdW interaction [5, 13, 14]. It has been shown earlier that dispersive vdW interaction is the dominant contribution between the nucleobases and SWNTs [5, 9, 13]. As graphene is also a carbon

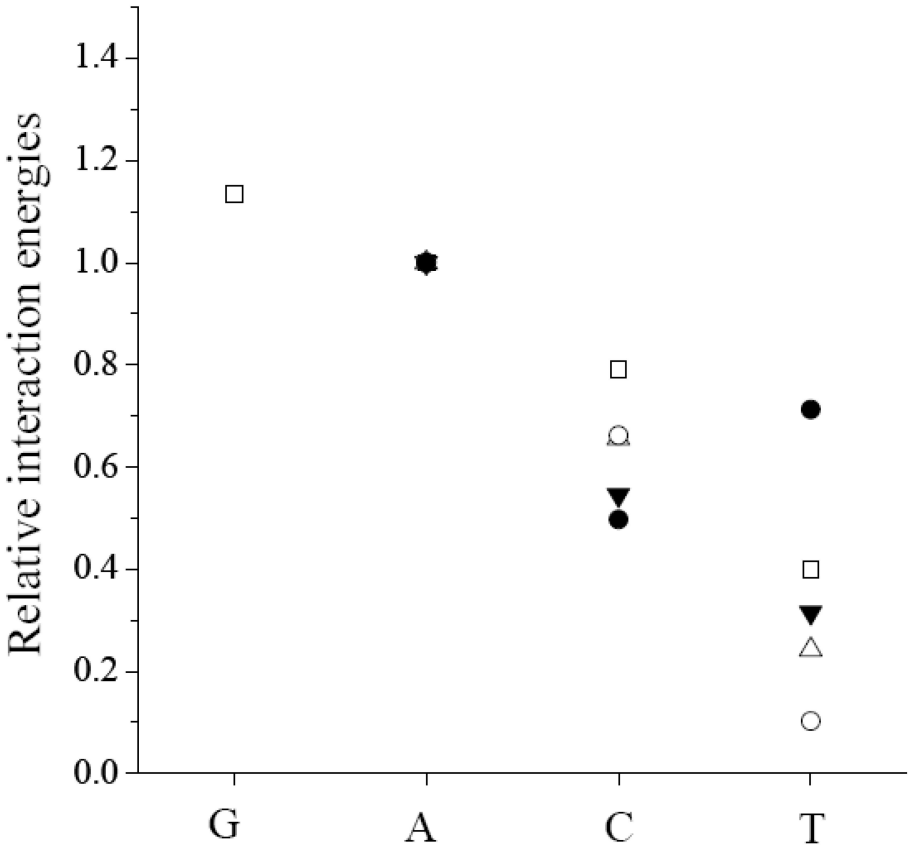

Figure 5.3: Summary of trends in experimental interaction energies of DNA nucleobases and nucleosides with graphene. We have normalized the interaction energies with respect to adenine or adenosine (A) taken as unity. Graphene I (1.0mgmL^{-1}) + Nucleobases in water (open circles), + nucleosides in water (open triangles), + Nucleobases in NaOH (open squares). Graphene II + nucleobases in water (filled circles), + nucleosides in water (filled triangles).

allotrope, it is expected that the vdW interaction would be the main driving force for the binding between graphene and nucleobases. In order to confirm this, we have examined the interaction of adenine with graphene using ab-initio HF calculations and found it to be negligible compared to the vdW intercation. Therefore, for the rest of our calculations we have only calculated vdW interaction between the remaining bases (G, T, C) with graphene and neglect the HF contribution. The vdW contribution of graphene with G, A, T and C bases are, respectively,

-19.10, -17.75, -16.63 and -14.52 kcal mol^{-1} (Table 5.5). Therefore, the binding sequence is $G > A > T > C$. Interestingly, our values of the binding energies are close (G: 24 kcal mol^{-1}, A: 21 kcal mol^{-1}, T: 19 kcal mol^{-1} and C: 18 kcal mol^{-1}) to the values obtained using density functional method [6]. From the optimized structure, we notice that all the nucleobases are parallel with graphene to have maximum vdW interaction between the graphene and nulceobases. The stacking arrangement between graphene and nucleobases is the same as shown in an earlier paper (Figure 3 of Ref. 5) where the MSCFF [15] force field was used. However, in the present paper we have used the AMBER force field which is known to be more accurate. Our optimized structures are similar to the ones in Ref. 6 (shown in Figure 5.4) [6].

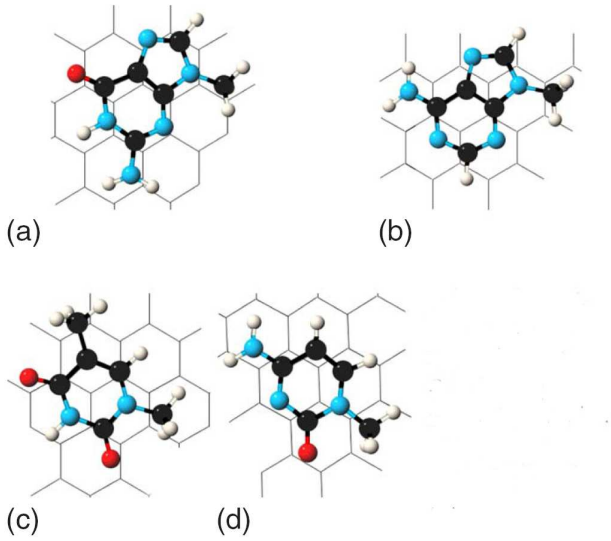

Figure 5.4: Equilibrium geometry of nucleobases on top of graphene: (a) guanine, (b) adenine, (c) thymine and (d) cytosine

In the experimental situation, nucleobases bind with graphene in aqueous solution. To compare the theoretical results with experiment we have carried out the solvation energy calculation using Amber Generalized Born (GB) model [16, 17].

Nucleobase	vdW	SE	Total
Guanine	-19.10	4.00	-15.10
Adenine	-17.75	2.95	-14.8
Thymine	-16.63	1.88	-14.75
Cytosine	-14.52	6.59	-7.93

Table 5.5: Theoretically calculated values of interaction energies (in kcal mol^{-1}) of nucleobases with graphene (Results from Dr. Maiti)

The GB model efficiently describes electrostatics of molecules in water environment and it represents the solvent implicitly as continuum with the dielectric properties of water. For solvation energy calculations, we need to include charges on each atom of graphene as well as nucleobases and the solvation energy is calculated by single point energy calculation. The charges on each carbon atom of graphene as well as nucleobases are calculated using Mulliken population analysis in the HF scheme. The solvation energies found by us are 4.00, 2.95, 1.88 and 6.59 kcal mol^{-1} for G, A, T and C respectively (Table 5.5). The total binding energy is obtained by adding the vdW term to the solvation energy. The energies so found are, -15.1, -14.80, -14.75 and -7.93 kcal mol^{-1} for G, A, T and C respectively (Table 5.5). Thus, the binding sequence remains as $G > A \approx T > C$. This trend is comparable to that found for nucleobases as well as nucleosides experimentally from our ITC experiments.

5.5 Conclusions

In conclusion, DNA nucleobases and nucleosides bind to graphene, the experimental binding energies being generally small. The order of relative binding energies of the nucleobases obtained is best represented by $G > A > C \gtrless T$. Generally, purines interact more strongly than pyrimidines. We can see this clearly from

Figure 5.3 which summarizes the trends obtained experimentally. While nucleosides exhibit a similar trend, the interaction energies of the base pairs are generally between those of the component bases. It is noteworthy that the magnitudes of the interaction energies of nucleobases with SWNTs are comparable to those found with graphene. Isothermal titration calorimetry is clearly a useful technique to study such interactions. Theoretical calculations of Maiti support the experimentally observed trend in interaction energies and suggest the importance of solvation effects.

References

[1] A. Gourishankar, S. Shukla, K. N. Ganesh, and M. Sastry. Isothermal titration calorimetry studies on the binding of DNA bases and PNA base monomers to gold nanoparticles. *J. Am. Chem. Soc*, 126(41):13186–13187, 2004.

[2] Y. V. Shtogun, L. M. Woods, and G. I. Dovbeshko. Adsorption of adenine and thymine and their radicals on single-wall carbon nanotubes. *J. Phys. Chem. C*, 111(49):18174–18181, 2007.

[3] S. Meng, P. Maragakis, C. Papaloukas, and E. Kaxiras. DNA nucleoside interaction and identification with carbon nanotubes. *Nano Lett.*, 7(1):45–50, 2007.

[4] S. Meng, W. L. Wang, P. Maragakis, and E. Kaxiras. Determination of DNA-Base orientation on carbon nanotubes through directional optical absorbance. *Nano Lett.*, 7(8):2312–2316, 2007.

[5] A.Das, A.K. Sood, P. K. Maiti, M. Das, R. Varadarajan, and C.N.R. Rao. Binding of nucleobases with single-walled carbon nanotubes: Theory and experiment. *Chem. Phys. Lett.*, 453(4-6):266 – 273, 2008.

[6] S. Gowtham, R. H. Scheicher, R. Ahuja, R. Pandey, and S. P. Karna. Physisorption of nucleobases on graphene: Density-functional calculations. *Phys. Rev. B*, 76(3):033401(1–4), 2007.

[7] S. Gowtham, R. H. Scheicher, R. Pandey, S. P. Karna, and R. Ahuja. First-principles study of physisorption of nucleic acid bases on small-diameter carbon nanotubes. *Nanotechnology*, 19(12):125701, 2008.

[8] J. Antony and S. Grimme. Structures and interaction energies of stacked graphene-nucleobase complexes. *Phys. Chem. Chem. Phys.*, 10(19):2722–2729, 2008.

[9] S. J. Sowerby, C. A. Cohn, W. M. Heckl, and N. G. Holm. Differential adsorption of nucleic acid bases: Relevance to the origin of life. *Proc. Natl. Acad. Sci. USA*, 98(3):820–822, 2001.

[10] J. E. Ladbury and B. Z. Chowdhry. Sensing the heat: the application of isothermal titration calorimetry to thermodynamic studies of biomolecular interactions. *Chem. Biol.*, 3(10):791–801, 1996.

[11] H. C. Schniepp, J. Li, M.J. McAllister, H. Sai, M. Herrera-Alonso, D. H. Adamson, R. K. Prud'homme, R. Car, D. A. Saville, and I. A. Aksay. Functionalized single graphene sheets derived from splitting graphite oxide. *J. Phys. Chem. B*, 110(17):8535–8539, 2006.

[12] K. S. Subrahmanyam, S. R. C. Vivekchand, A. Govindaraj, and C. N. R. Rao. A study of graphenes prepared by different methods: characterization, properties and solubilization. *J. Mater. Chem.*, 18:1517–1523, 2008.

[13] F. Ortmann, W. G. Schmidt, and F. Bechstedt. Attracted by long-range electron correlation: Adenine on graphite. *Phys. Rev. Lett.*, 95(18):186101, 2005.

[14] R. W. Williams and D. Malhotra. van der waals corrections to density functional theory calculations: Methane, ethane, ethylene, benzene, formaldehyde, ammonia, water, PBE, and CPMD. *Chem. Phys.*, 327(1):54 – 62, 2006.

[15] K. Brameld, S. Dasgupta, and W.A. Goddard. Distance dependent hydrogen

bond potentials for nucleic acid base pairs from ab initio quantum mechanical calculations (LMP2/cc-pVTZ). *J. Phys. Chem. B*, 101(24):4851–4859, 1997.

[16] A. Onufriev, D. Bashford, and D. A. Case. Exploring protein native states and large-scale conformational changes with a modified generalized born model. *Proteins Struct. Funct. Bioinf.*, 55(2):383–394, 2004.

[17] A. Onufriev, D. Bashford, and D.A. Case. Modification of the generalized born model suitable for macromolecules. *J. Phys. Chem. B*, 104(15):3712–3720, 2000.

CHAPTER 6

Synthesis of Inorganic Nanostructures at the Liquid-Liquid Interface*

Summary

Thin films of metallic nickel with a thickness of the order of 20 nm have been prepared at the organic-aqueous interface at room temperature by the reaction of nickel cupferronate $[Ni(C_6H_5N_2O_2)_2]$ in toluene medium and sodium borohydride ($NaBH_4$) in aqueous medium. The films were characterized with transmission electron microscopy, scanning electron microscopy and atomic force microscopy. Thicker Ni films could be prepared by carrying out the reaction at the interface at 60 °C and 80 °C. The Ni nanofilms exhibit superparamagnetic behavior.

Nanowires of CdO have been prepared using the organic-aqueous interface by the reaction of cadmium cupferronate ($Cd(cup)_2$) in toluene medium and sodium hydroxide (NaOH) in the aqueous medium. The $Cd(OH)_2$ nanowires thus formed at the interface were heated at 350 °C for 7 hours to obtain CdO nanowires. The films were characterized using transmission electron microscopy, scanning electron microscopy and X-ray diffraction measurements. Triangular nanostructures of CdO were prepared in the presence of hexadecylamine in the toluene medium keeping other parameters the same. Nanoparticles of CdO were also obtained by the

*A paper based on this work has been published in *Mater Res Bull* **(2011)**

reaction of $Cd(cup)_2$ with hydrogen peroxide (H_2O_2) and ammonium hydroxide (NH_4OH)

6.1 Introduction

Magnetic nanomaterials are of value due to their potential applications in magnetic fluids, magnetic storage, biomedical applications and catalysis [1–4]. In this context, nickel nanostructures have been prepared by various methods employing sputtering, pyrolysis, aqueous and nonaqueous chemical reduction, sonochemical deposition and water-oil microemulsions [5–9]. Huo and Gao [10] prepared Ni nanoparticles by the reduction of nickel acetylacetonate with sodium tetrahydridoborate in the presence of hexadecyl amine and studied their magnetic properties. The synthesis of hcp Ni nanoparticles in polyethylene glycol under refluxing conditions in the presence of oleic acid and oleyl amine has been reported by Tzitzios *et al.* [11]. Reduction of nickel acetylacetonate by hydrazine in oleyl amine also yields hcp or a mixture of hcp and fcc Ni nanoparticles depending on the reaction temperatures [12]. Synthesis and magnetic properties of single-crystalline nanorods and ultra-thin sheets of nickel prepared by the decomposition of nickel acetate in the presence of long-chain amines under solvothermal conditions have been reported by Ghosh *et al.* [13]. Han *et al.* synthesized Ni nanoparticles with fcc and hcp structures by the thermal decomposition of Ni oleate in dodecylamine and octadecene system [14]. Ni nanobelts have been obtained by the reduction of a Ni tartrate complex under surfactant-assisted hydrothermal conditions [15].

Cadmium oxide (CdO) is an important n-type semiconductor with a direct band gap of 2.5 eV and an indirect band gap of 1.98 eV [16]. CdO has high electrical conductivity and carrier concentration because of inherent non stoichiometry [17–19]. The unique combination of high electrical conductivity, high carrier concentration and high transparency in the visible range of electromagnetic spectrum has prompted its applications in solar cells, photoelectrochemical devices, phototran-

sistors, photodiodes, liquid crystal displays, IR detectors, antireflection coatings, gas sensors, etc. [20]. Wu *et al.* [21] prepared a nanometer-sized CdO organosol from an aqueous solution of $Cd(NO_3)_2$, a surfactant and toluene, while Liu *et al.* [15] synthesized CdO nanoneedles by chemical vapour deposition. Zou *et al.* [22] have prepared CdO nanoparticles by the micro-emulsion method employing AOT reverse micelles. CdO nanocrystals have been prepared solvothermally by Ghosh *et al.* [23]. Shi *et al.* synthesized CdO nanodisks by calcination of cadmium hydroxide prepared using a hydrothermal approach [24]. Thin films of CdO nanowires have been deposited onto a glass substrate using chemical vapor deposition method and the optical and electrical properties were measured [25]. Solvothermal synthesis of CdO hollow nanostructures from CdO_2 nanoparticles has been reported by Zhang *et al.* [16]. Formation of CdO films from chemical deposited $Cd(OH)_2$ films has been reported [26]. Mlondo *et al.* have prepared anisotropic CdO nanostructures employing an organic- aqueous interface [27].

6.2 Scope of the present investigations

6.2.1 Ni nanofilms

Most of the synthetic methods for Ni nanostuctures reported in the literature use high temperature, surfactants or long chain amines. It was our interest to prepare Ni nanostructures at room temperature in the absence of any surfactants or amines. For this purpose, we have employed the organic- aqueous interface to prepare thin films of nickel. The organic-aqueous interface has been used to generate various nanostructures, specially single crystalline films of inorganic materials [28]. The synthesis and characterization of nickel nanosheets prepared by the interface

reaction between nickel cupferronate in toluene medium and sodium borohydride in the aqueous medium has been described in this chapter.

6.2.2 CdO nanostructures

Due to the emerging applications of CdO nanostructures, we considered it is useful to prepare them at the liquid-liquid interface. In a typical reaction, cadmium cupferronate in toluene medium was allowed to react with sodium hydroxide in aqueous medium. The films formed at the interface consist of cadmium hydroxide nanowires. Heating the nanostructures of cadmium hydroxide formed to 350 °C yields CdO with similar morphology. Effect of addition of hexadecyl amine to the reaction mixture has also been investigated. The reaction between cadmium cupferronate in toluene medium and ammonium hydroxide in aqueous medium in presence of hydrogen peroxide were carried out.

6.3 Experimental section

Ni nanofilms

Nickel nanofilms were prepared by the reaction of nickel cupferronate ($Ni(Cup)_2$, $Ni(C_6H_5N_2O_2)_2$) as the nickel source and sodium borohydride ($NaBH_4$) as the reducing agent. $Ni(Cup)_2$ was prepared by the reaction of nickel acetate and cupferron at 0 °C. The product formed was filtered, washed with water and dried at 40 °C in an oven. In a typical reaction, 25 mL of 0.1 mM of $Ni(Cup)_2$ in toluene was added slowly to 25 mL of 5 mM of $NaBH_4$ in water. The interface that formed between the two layers turned silverish white after a few hours. The interface was kept undisturbed for 30 hours for the growth of the nickel nanofilm to occur. The

film formed at the interface was lifted onto a silicon substrate for characterization. The film was taken on a holey carbon grid for transmission electron microscopic (TEM) measurements and on a quartz plate for UV-vis spectroscopic measurements. To examine the effect of temperature on the formation of the film, the reaction was carried out at 60 °C and 80 °C keeping the other conditions same.

Field emission scanning electron microscope (FESEM) images were recorded with a FEI NOVA NANOSEM600. Transmission electron microscope (TEM) images were obtained with a JEOL (JEM3010) transmission electron microscope operating with an accelerating voltage of 300 kV. UV-vis absorption spectrum was recorded with a Perkin-Elmer Lamda 900 UV/VIS/NIR spectrometer. Atomic force microscope (AFM) measurements were performed with an Innova atomic force microscope. Magnetic measurements were carried out with a vibrating sample magnetometer in Physical Properties Measurement System (PPMS, Quantum Design, USA).

CdO nanostructures

Nanowires of $Cd(OH)_2$ at the organic- aqueous interface was prepared by the reaction of cadmium cupferronate [$Cd(C_6H_5N_2O_2)_2$, $Cd(cup)_2$] in toluene medium and sodium hydroxide in the aqueous medium. In a typical reaction, 25 mL of 0.12 mM $Cd(cup)_2$ was added slowly to a 25 mL of 3 mM NaOH solution. The interface formed between the two solutions kept undisturbed for 48 hours. A thin transparent film was formed at the interface. The film thus formed was lifted on a silicon substrate for further characterizations. The film lifted on the silicon substrate was heated to 350 °C for 7 hours to form CdO nanowires. To study the effect of amine on the formation of the film, a reaction was carried out taking 0.12 mM

$Cd(cup)_2$ and 6 mM NaOH and 50 mg of hexadecylamine keeping other parameters the same. To prepare the nanoparticles, a reaction was carried out between 25 mL of 0.3 mM $Cd(cup)_2$ and 10 μL each of NH_4OH and H_2O_2 in 25 mL water keeping other parameters the same.

FESEM images were recorded with a FEI NOVA NANOSEM600. TEM images were obtained with an FEI Titan (cube) 80-300 kV aberration-corrected transmission electron microscope. Transmission spectrum was recorded using a Perkin-Elmer Lamda 900 UV/VIS/NIR spectrometer. X-ray diffraction measurements were carried out using Cu-Kα radiation (λ =1.54056 $\mathring{A}$) using a Rigaku-99 instrument.

6.4 Results and discussion

6.4.1 Ni nanofilms

In Figure 6.1a, we show a FESEM image of a typical nickel film formed at room temperature (30 °C) at the interface. The films are fairly continuous covering a large area. Figure 6.1b shows a TEM micrograph of a Ni film. The film is crystalline as can be seen in the selected area electron diffraction (SAED) pattern in the inset in Figure 6.1b. The electron diffraction spots could be indexed on the hexagonal structure ($P6_3/mmc$, a= 2.651 $\mathring{A}$, c= 4.343 $\mathring{A}$, JCPDS No. 45-1027). The TEM image also reveals the presence of small nanoparticles with diameters in the 2-3 nm range. Slightly bigger particles (8-10 nm diameter) were also seen in some parts of the film (indicated by black arrows).

Typical AFM images of Ni films are shown in Figure 6.2. The images reveal that the films are smooth and continuous over wide areas. The three- dimensional

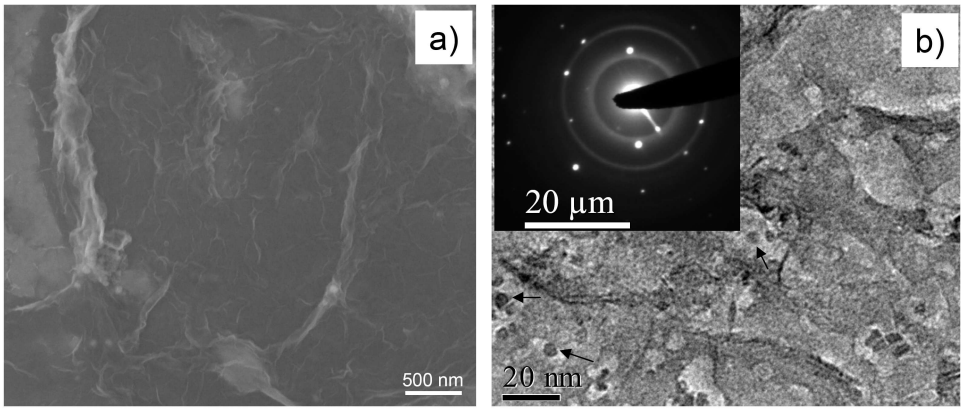

Figure 6.1: (a) FESEM and (b) TEM images of a nickel film formed at the liquid-liquid interface at room temperature. Inset in (b) shows a SAED pattern of the film. The scale bar in the inset is 20 μm.

image of the film in Figure 6.2a and the height profile in Figure 6.2b show that the average thickness of the film is of the order of 20 nm.

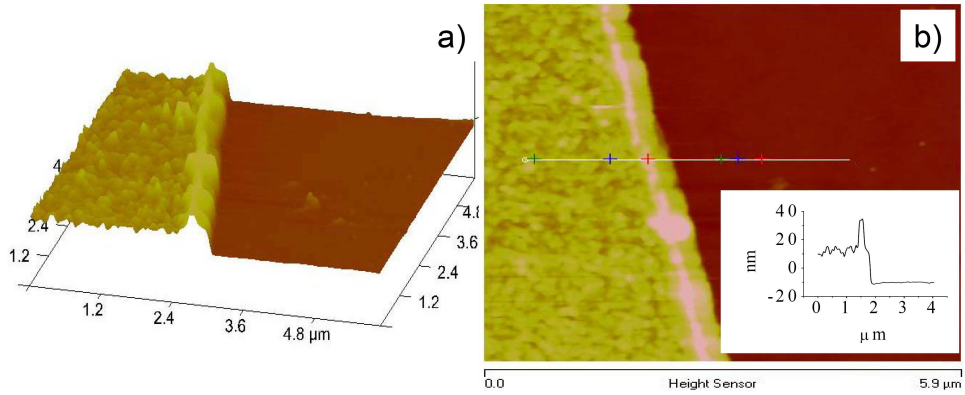

Figure 6.2: a) 3-D AFM image of a nickel film formed at the liquid-liquid interface (b) AFM image showing height profile of a film.

Magnetic properties of the nickel film formed at the interface were measured. In Figure 6.3a, we show the temperature dependence of magnetization under zero-field cooled (ZFC) and field-cooled (FC) conditions at 100 Oe. The ZFC curve shows a maximum at the blocking temperature (T_B) of 13.5 K characteristic of a superparamagnetic material. A T_B in the range of 12-40 K has been reported earlier

in the literature for nickel nanomaterials [10, 29]. The ZFC and FC curves diverge below T_B, characteristic of superparamagnetic materials [30]. The FC curve shows that magnetization continues to increase with decrease in temperature below the T_B. Figure 6.3b shows the field-dependent magnetic behavior of a film at 5 K. The M-H curve shows hysteresis with a saturation magnetization (M_S) of 45 emu/g, which is lower than that of bulk nickel (55 emu/g). Such a reduced value of M_S is expected in a nanofilm. The coercivity at 5 K is 770 Oe whereas the coercivity above T_B is negligible. The magnetic hysteresis disapperas above T_B as expected of a superparamagnet [10, 30, 31]. The present results clearly establish that the nickel film generated at the liquid-liquid interface is superparamagnetic.

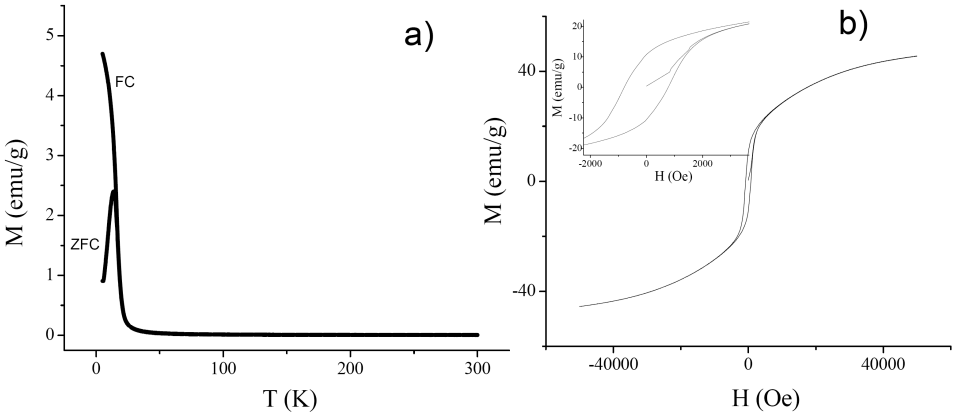

Figure 6.3: (a) Temperature dependence of magnetization for a nickel film formed at the liquid-liquid interface (recorded at 100 Oe). (b) Magnetization as a function of the applied field measured at 5K. The inset shows the enlarged magnetization curve.

In Figure 6.4a, we show the UV-vis spectrum of a nickel film formed at the interface. The spectrum shows a broad, weak feature around 320 nm due to surface plasmon resonance (SPR). There are literature reports of SPR bands of Ni nanoparticles, Ni/SiO_2 glass nanocomposites and Ni implanted alumina in this wavelength region [31–33]. Figure 6.4b shows typical I-V characteristics of a nickel

film. The I-V curve is linear indicating the metallic character of the nickel film.

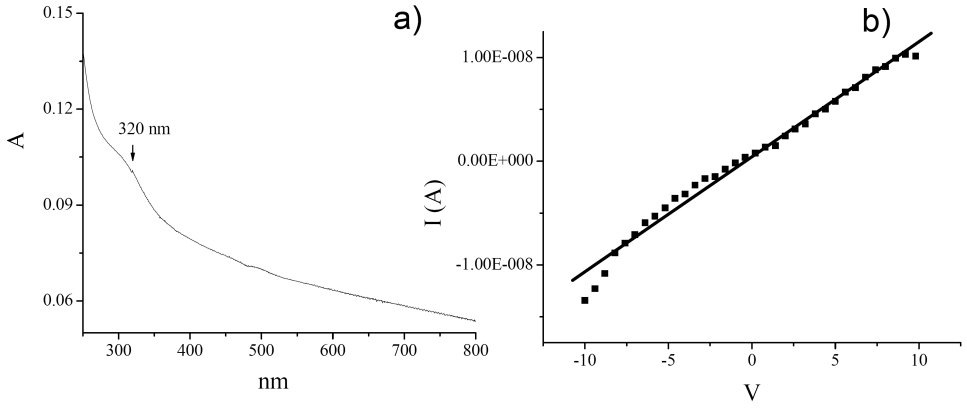

Figure 6.4: (a) UV-vis spectrum of a Ni film formed at the liquid-liquid interface. (b) I-V characteristics of a Ni fim.

Nickel films were also prepared at the liquid-liquid interface at a higher temperature to check the effect of temperature on the film characteristics. In Figure 6.5a, we show a FESEM image of a film formed at the interface at 60 °C. The film

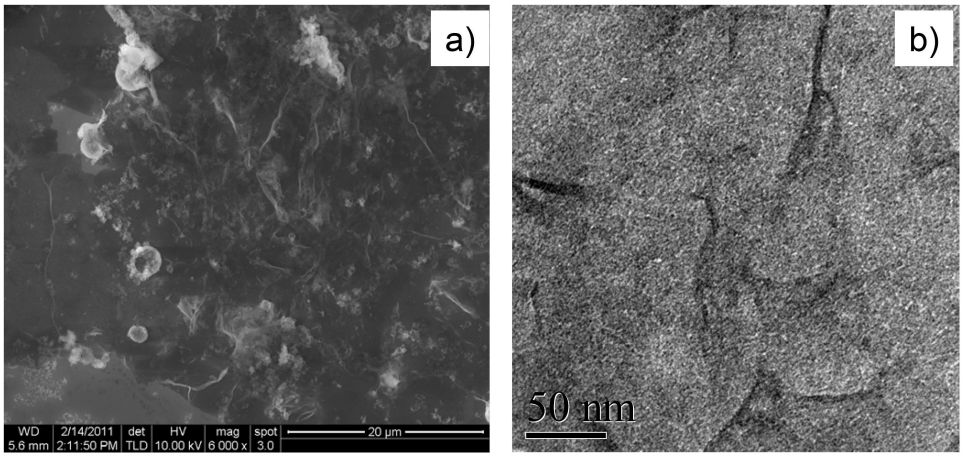

Figure 6.5: (a) FESEM and (b) TEM images of a nickel film formed at the liquid-liquid interface at 60 °C.

appears to be rough compared to that formed at the room temperature. The TEM image of the film shows the presence of small nanoparticles (2-3 nm) as shown in

Figure 6.5b. An AFM image of the film formed at the interface at 60 °C is shown in Figure 6.6. From the z-scale image of the film shown as the inset in Figure 6.6,

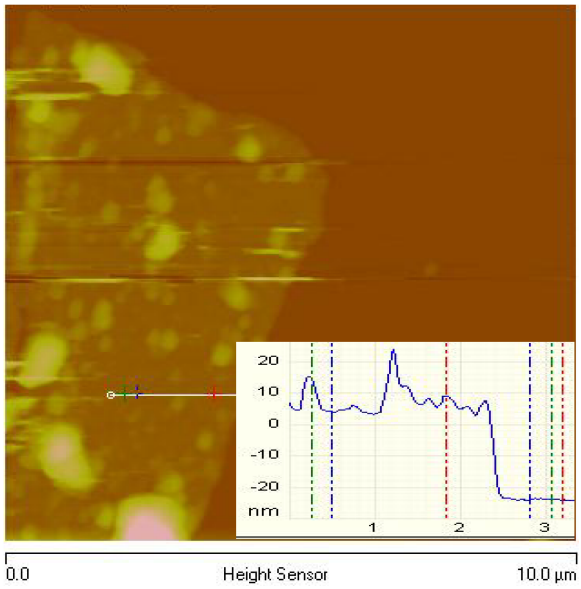

Figure 6.6: AFM image of the film showing the height profile of a Ni film formed at the liquid-liquid interface at 60 °C.

the thickness is estimated to be of the order of 30 nm.

In Figure 6.7a, we show a FESEM image of a film formed at the interface at 80 °C. The film appears to be rougher compared to that formed at the lower temperatures. The TEM image of the film shows the presence of small nanoparticles (2-3 nm) as shown in Figure 6.7b.

An AFM image of the film formed at the interface at 80 °C is shown in Figure 6.8. From the z-scale image of the film shown as the inset in Figure 6.8, the thickness is estimated to be of the order of 50 nm.

6.4.2 CdO nanostructures

Figure 6.9a shows the FESEM images of thin films of $Cd(OH)_2$ nanowires formed at the liquid-liquid interface by the reaction of $Cd(cup)_2$ in toulene medium and

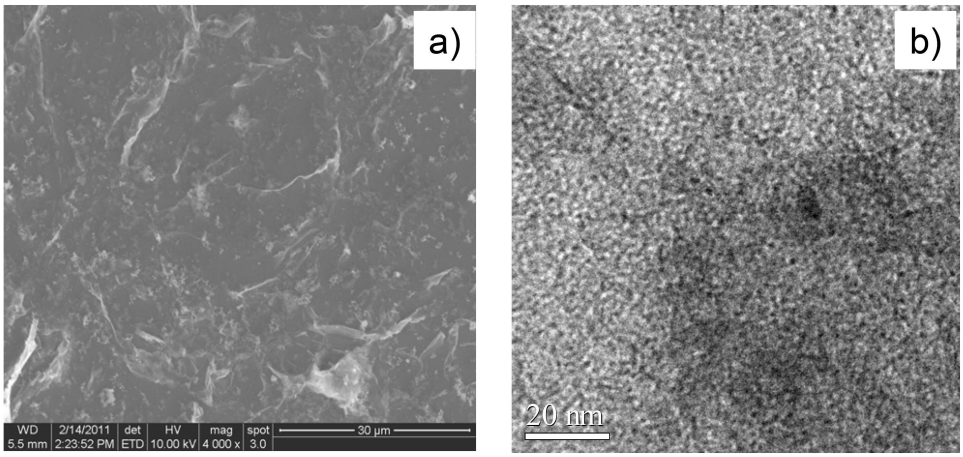

Figure 6.7: (a) FESEM and (b) TEM images of a nickel film formed at the liquid-liquid interface at 80 °C.

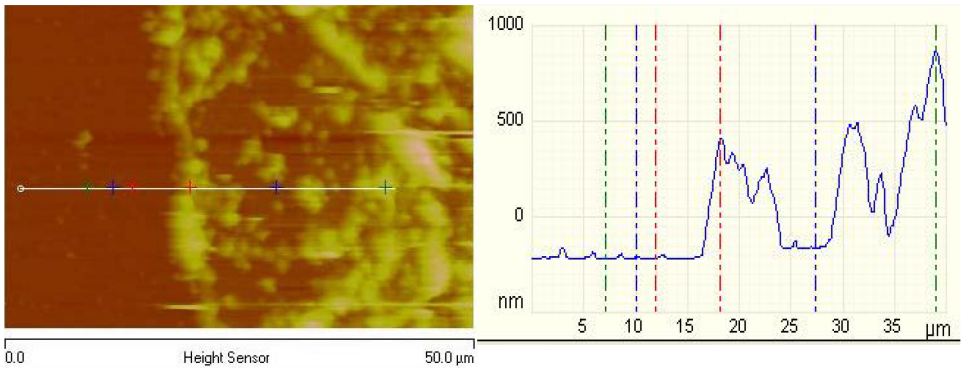

Figure 6.8: AFM image of the film showing the height profile of a Ni film formed at the liquid-liquid interface at 80 °C.

NaOH in aqueous medium. The film contains fairly uniform nanowires of 20-30 nm in diameter and few micrometers in length. The as prepared nanowires were heated at 350 °C for 7 hours to produce CdO nanowires. In Figure 6.9b, we show the typical FESEM images of the CdO nanowires. From the image it is clear that the morphology is retained even after heating of $Cd(OH)_2$ nanostructures.

Figure 6.10a shows the selected area electron diffraction pattern obtained from the films of CdO nanowires. The electron diffraction pattern shows rings indicating the polycrystalline nature of the nanowires. The electron diffraction rings could

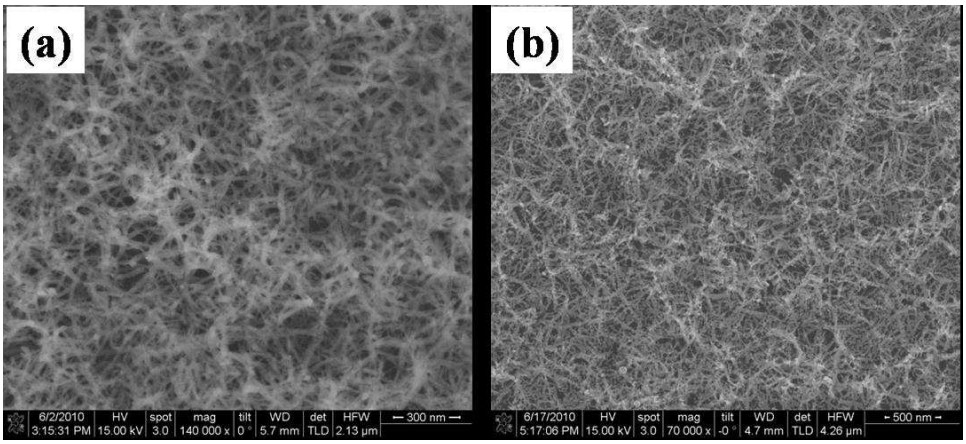

Figure 6.9: FESEM images of (a) $Cd(OH)_2$ nanowires formed at the organic-aqueous interface and (b) CdO nanowires obtained by heating the $Cd(OH)_2$ nanowires at 350 °C for 7 hours.

be indexed on the cubic structure (Fm3m, a= 4.6953 $\mathring{A}$, JCPDS No: 05-0640). In Figure 6.10b, we show the XRD pattern of the film formed at the interface. The XRD pattern confirms the cubic structure.

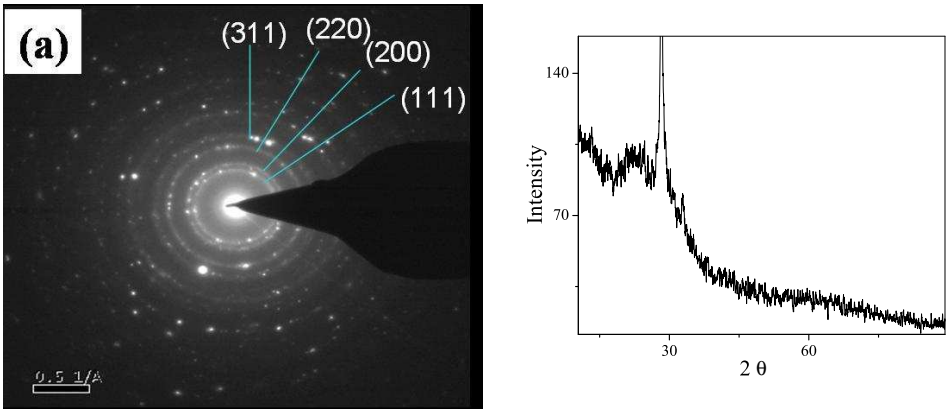

(a) (b)

Figure 6.10: (a) SAED pattern of the CdO nanowires formed at the organic-aqueous interface. XRD pattern of the CdO nanowires.

In Figure 6.11, we show the typical HRTEM images of the film formed at the interface. The nanowires are highly crystalline in nature, as revealed from the HRTEM image. From the lines in the HRTEM, interplanar distance could be

measured. The line spacing of 2.71 and 1.63 $\AA$ obatined from the Figure 6.11 corresponds to the seperation between (111) and (220) planes of the CdO respectively. This again confirms that pure CdO nanowires are formed on heating the $Cd(OH)_2$ nanowires.

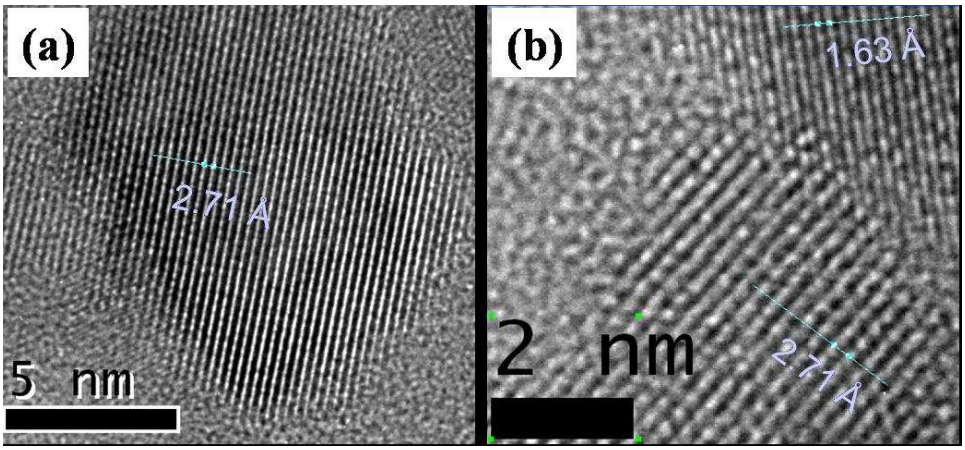

Figure 6.11: HRTEM image of the CdO nanowires.

The transmission spectrum of the CdO films is shown in Figure 6.12. The optical transmittance of the film is high ($\approx 85\%$) as reported earlier in the literature [34]. The I-V curve of the CdO film is shown in Figure 6.13. The I-V behavior indicates that the nanowires are seminconducting in nature.

In Figure 6.14a, we show the FESEM image of the $Cd(OH)_2$ nanostructures formed at the organic- aqueous interface by the reaction of $Cd(cup)_2$ and hexadecylamine in the toluene medium and NaOH in the aqueous medium. The nanostuctures are triangular in morphology. To obtain CdO nanostructure, the as-prepared sample was heated at 350 °C for 4 hours. FESEM images of the CdO nanostructures thus produced are shown in Figure 6.14b. As clearly seen from the FESEM image, the morphology is retained even after heating of the $Cd(OH)_2$ nanostructures.

To produce nanoparticles of CdO, $Cd(cup)_2$ in toluene medium was allowed

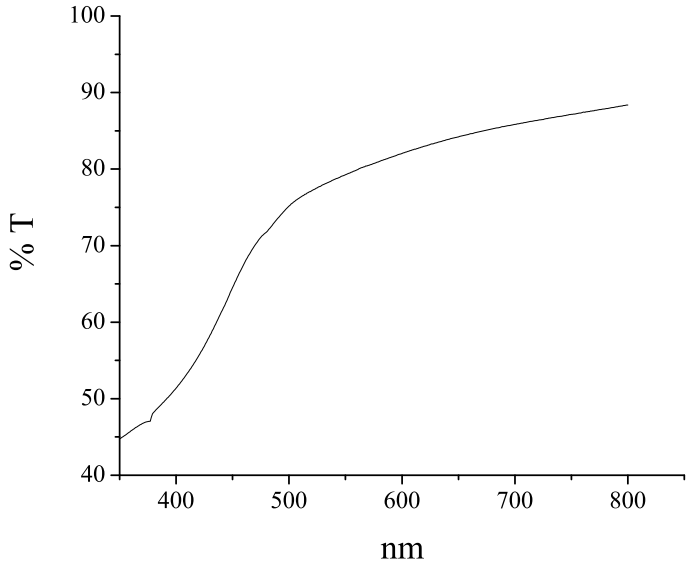

Figure 6.12: The transmittance spectrum of the film of CdO nanowires.

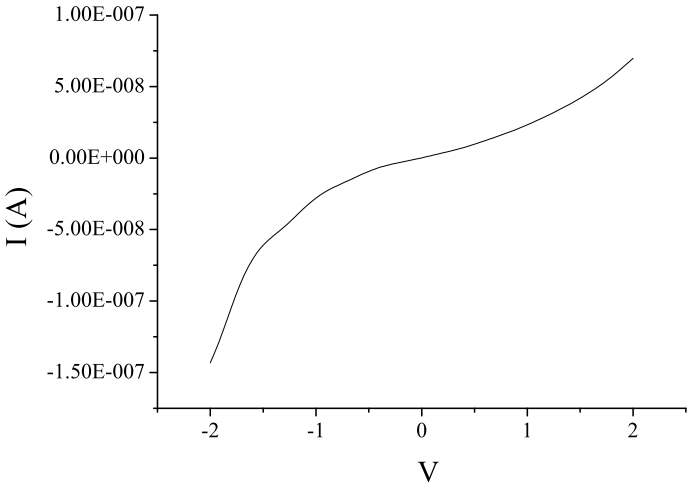

Figure 6.13: The I-V charecterestics of CdO film consists od nanowires.

to react with NH_4OH and H_2O_2 in the aqueous medium. The as prepared film was heated at 450 °C for 4 hours to convert the $Cd(OH)_2$ nanoparticles to CdO. Figure 6.15 shows the FESEM images of the CdO nanoparticles formed. They are

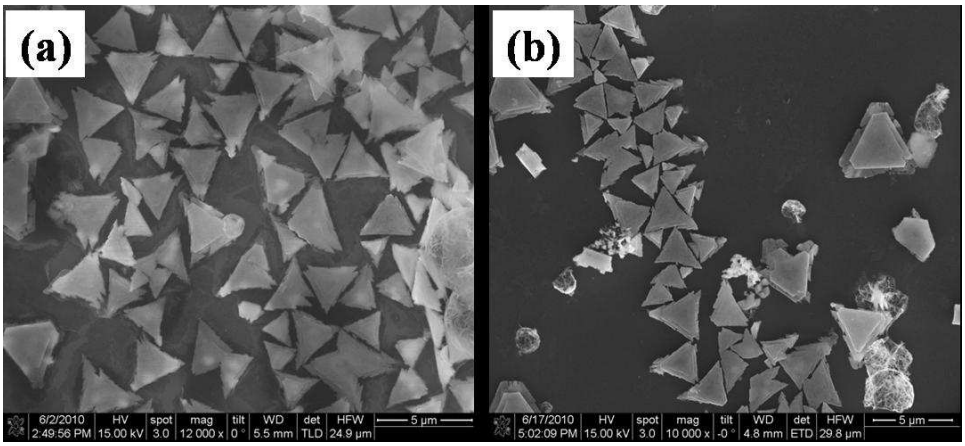

Figure 6.14: FESEM image of (a) $Cd(OH)_2$ nanostructures formed in presence of hexadecyl amine at the organic- aqueous interface and (b) corresponding CdO nanostructured formed by heating the obtained $Cd(OH)_2$ at 350 °C for 4 hours.

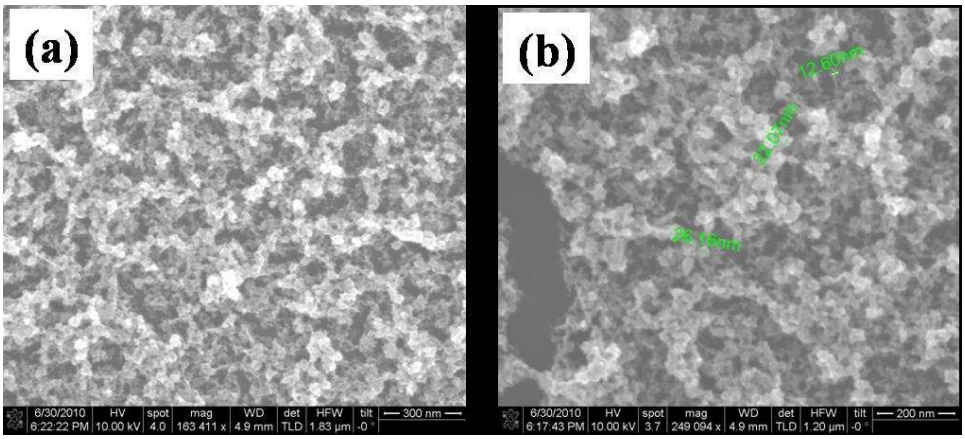

Figure 6.15: FESEM images of CdO nanoparticles obtained by heating the $Cd(OH)_2$ nanostructures formed at the liquid- liquid interface in the presence of H_2O_2 and NH_4OH.

approximately 10-25 nm in diameter.

6.5 Conclusions

The present study demonstrates that the organic-aqueous interface can be used to generate nickel nanofilms by the interface reaction between nickel cupferronate and

sodium borohydride at room temperature. The films prepared at room temperature are $\approx$ 20 nm thick and exhibit superparamagnetism. Ni films prepared at a higher temperatures (60 °C and 80 °C) are thicker compared to those prepared at room temperature.

Various morphologies of CdO nanostructures have been obtained at the organic aqueous interface taking $Cd(cup)_2$ as the precursor in the toluene medium. On reaction with NaOH in the aqueous medium, nanowires of $Cd(OH)_2$ were produced which was converted to CdO nanowires by heating. In the presence of hexadecyl amine, triangular nanostructures of CdO were prepared. Nanoparticles of CdO were synthesized by the reaction of $Cd(cup)_2$ with NH_4OH and H_2O_2 followed by heating of the prepared film. Structural characterizations of the CdO films indicate the cubic structure. Optical and electrical properties of the films have also been measured.

References

[1] M.-P. Pileni. Magnetic fluids: Fabrication, magnetic properties, and organization of nanocrystals. *Adv. Funct. Mater.*, 11(5):323–336, 2001.

[2] S. Sun, C. B. Murray, D. Weller, L. Folks, and A. Moser. Monodisperse FePt nanoparticles and ferromagnetic FePt nanocrystal superlattices. *Science*, 287(5460):1989–1992, 2000.

[3] K. B. Lee, S. Park, and C. A. Mirkin. Multicomponent magnetic nanorods for biomolecular separations. *Angew. Chem. Int. Ed.*, 43(23):3048–3050, 2004.

[4] J. Park, E. Kang, S.U. Son, H.M. Park, M.K. Lee, J. Kim, K.W. Kim, H.-J. Noh, J.-H. Park, C.J. Bae, J.-G. Park, and T. Hyeon. Monodisperse nanoparticles of Ni and NiO: Synthesis, characterization, self-assembled superlattices, and catalytic applications in the Suzuki coupling reaction. *Adv. Mater.*, 17(4):429–434, 2005.

[5] S.-L. Che, K. Takada, K. Takashima, O. Sakurai, K. Shinozaki, and N. Mizutani. Preparation of dense spherical Ni particles and hollow NiO particles by spray pyrolysis. *J. Mater. Sci.*, 34:1313–1318, 1999.

[6] G. B. Thompson, R. Banerjee, X. D. Zhang, P. M. Anderson, and H. L. Fraser. Chemical ordering and texture in Ni-25 at% Al thin films. *Acta Mater.*, 50(3):643 – 651, 2002.

[7] S. H. Wu and D. H. Chen. Synthesis and stabilization of Ni nanoparticles in a pure aqueous CTAB solution. *Chem. Lett.*, 33(4):406–407, 2004.

[8] S. Ramesh, Y. Koltypin, R. Prozorov, and A. Gedanken. Sonochemical deposition and characterization of nanophasic amorphous nickel on silica microspheres. *Chem. Mater.*, 9(2):546–551, 1997.

[9] D. H. Chen and S. H. Wu. Synthesis of nickel nanoparticles in water-in-oil microemulsions. *Chem. Mater.*, 12(5):1354–1360, 2000.

[10] Y. Hou and S. Gao. Monodisperse nickel nanoparticles prepared from a monosurfactant system and their magnetic properties. *J. Mater. Chem.*, 13:1510–1512, 2003.

[11] V. Tzitzios, G. Basina, M. Gjoka, V. Alexandrakis, V. Georgakilas, D. Niarchos, N. Boukos, and D. Petridis. Chemical synthesis and characterization of hcp Ni nanoparticles. *Nanotechnology*, 17(15):3750–3755, 2006.

[12] Y. T. Jeon, J. Y. Moon, G. H. Lee, J. Park, and Y. Chang. Comparison of the magnetic properties of metastable hexagonal close-packed Ni nanoparticles with those of the stable face-centered cubic Ni nanoparticles. *J. Phys. Chem. B*, 110(3):1187–1191, 2006.

[13] S. Ghosh, M. Ghosh, and C. N. R. Rao. Nanocrystals, nanorods and other nanostructures of nickel, ruthenium, rhodium and iridium prepared by a simple solvothermal procedure. *J. Cluster Sci.*, 18:97–111, 2007.

[14] M. Han, Q. Liu, J. He, Y. Song, Z. Xu, and J.M. Zhu. Controllable synthesis and magnetic properties of cubic and hexagonal phase nickel nanocrystals. *Adv. Mater.*, 19(8):1096–1100, 2007.

[15] Z. Liu, S. Li, Y. Yang, S. Peng, Z. Hu, and Y. Qian. Complex-surfactant-assisted hydrothermal route to ferromagnetic nickel nanobelts. *Adv. Mater.*, 15(22):1946–1948, 2003.

[16] Y. C. Zhang and G. L. Wang. Solvothermal synthesis of CdO hollow nanostructures from CdO_2 nanoparticles. *Mater. Lett.*, 62(4-5):673 – 675, 2008.

[17] X. Li, T. A. Gessert, and T. Coutts. The properties of cadmium tin oxide thin-film compounds prepared by linear combinatorial synthesis. *Appl. Surf. Sci.*, 223(1-3):138 – 143, 2004. Proceedings of the Second Japan-US Workshop on Combinatorial Materials Science and Technology.

[18] K. T. Hillie, S. S. Basson, and H. C. Swart. Effect of a CdO coating on the degradation of a ZnS thin film phosphor material. *Appl. Surf. Sci.*, 187(1-2):137 – 144, 2002.

[19] T. K. Subramanyam, S. Uthanna, and B. S. Naidu. Preparation and characterization of CdO films deposited by dc magnetron reactive sputtering. *Mater. Lett.*, 35(3-4):214 – 220, 1998.

[20] B. J. Lokhande, P. S. Patil, and M. D. Uplane. Studies on cadmium oxide sprayed thin films deposited through non-aqueous medium. *Mater. Chem. Phys.*, 84(2-3):238 – 242, 2004.

[21] W. Xiaochun, W. Rongyao, Z. Bingsuo, W. Li, L. Shaomei, X. Jiren, and H. Wei. Optical properties of nanometer-sized CdO organosol. *J. Mater. Res.*, 13(3):604–609, 1998.

[22] B. S. Zou, V. V. Volkov, and Z. L. Wang. Optical properties of amorphous

ZnO, CdO, and PbO nanoclusters in solution. *Chem. Mater.*, 11(11):3037–3043, 1999.

[23] M. Ghosh and C.N.R. Rao. Solvothermal synthesis of CdO and CuO nanocrystals. *Chem. Phys. Lett.*, 393(4-6):493 – 497, 2004.

[24] W. Shi, C. Wang, H. Wang, and H. Zhang. Hexagonal nanodisks of cadmium hydroxide and oxide with nanoporous structure. *Cryst Growth Des.*, 6(4):915–918, 2006.

[25] D.S. Dhawale, A.M. More, S.S. Latthe, K.Y. Rajpure, and C.D. Lokhande. Room temperature synthesis and characterization of CdO nanowires by chemical bath deposition (CBD) method. *Appl. Surf. Sci.*, 254(11):3269 – 3273, 2008.

[26] T.P. Gujar, V.R. Shinde, Woo-Young Kim, Kwang-Deog Jung, C.D. Lokhande, and Oh-Shim Joo. Formation of CdO films from chemically deposited $Cd(OH)_2$ films as a precursor. *Appl. Surf. Sci.*, 254(13):3813 – 3818, 2008.

[27] S. N. Mlondo, E. M. Andrews, P. J. Thomas, and P O'Brien. Deposition of hierarchical $Cd(OH)_2$ anisotropic nanostructures at the water-toluene interface and their use as sacrificial templates for CdO or CdS nanostructures. *Chem. Commun.*, pages 2768–2770, 2008.

[28] C. N. R. Rao and K. P. Kalyanikutty. The liquid-liquid interface as a medium to generate nanocrystalline films of inorganic materials. *Acc. Chem. Res.*, 41(4):489–499, 2008.

[29] F. C. Fonseca, G. F. Goya, R. F. Jardim, R. Muccillo, N. L. V. Carreño,

E. Longo, and E. R. Leite. Superparamagnetism and magnetic properties of Ni nanoparticles embedded in SiO_2. *Phys. Rev. B*, 66(10):104406, 2002.

[30] T. Bala, S. D. Bhame, P. A. Joy, B. L. V. Prasad, and M. Sastry. A facile liquid foam based synthesis of nickel nanoparticles and their subsequent conversion to $Ni_{core}Ag_{shell}$ particles: structural characterization and investigation of magnetic properties. *J. Mater. Chem.*, 14:2941–2945, 2004.

[31] P. K. Verma, A. Giri, N. T. K. Thanh, L. D. Tung, O. Mondal, M. Pal, and Samir K. Pal. Superparamagnetic fluorescent nickel-enzyme nanobioconjugates: synthesis and characterization of a novel multifunctional biological probe. *J. Mater. Chem.*, 20:3722–3728, 2010.

[32] O. A. Yeshchenko, I. M. Dmitruk, A. A. Alexeenko, and A. M. Dmytruk. Optical properties of sol-gel fabricated Ni/SiO_2 glass nanocomposites. *J. Phys. Chem. Solids*, 69(7):1615 – 1622, 2008.

[33] X. Xiang, X. T. Zu, S. Zhu, , and L. M. Wang. Optical properties of metallic nanoparticles in Ni-ion-implanted $\alpha - Al_2O_3$ single crystals. *Appl. Phys. Lett.*, 84(1):52–54, 2004.

[34] S. Aksoy, Y. Caglar, S. Ilican, and M. Caglar. Effect of heat treatment on physical properties of CdO films deposited by sol-gel method. *Int. J. Hydrogen Energy*, 34(12):5191 – 5195, 2009.

CHAPTER 7

Effect of Curcumin and Cu^{2+} and Zn^{2+} Ions on the Fibrillar Aggregates Formed by the Amyloid Peptide and Other Peptides at the Organic-Aqueous Interface*

Summary

A characteristic feature of a perilous neuro-degenerative disease such as the Alzhiemers disease is fibrillar plaque formation by the amyloid (Aβ) peptide. We have modelled the formation and disintegration of fibrils by studying the aggregate structures comprising nanorod bundles and other structures formed by Aβ structural motif diphenylalanine as well as insulin and bovine serum albumin at the organic-aqueous interface. Even small concentrations of curcumin in the organic medium or Cu^{2+} and Zn^{2+} ions in the aqueous medium are found to break down the fibrillar structures.

*A paper based on this work has been published in *Chem. Phys. Lett.* **(2010)**

7.1 Introduction

Many peptides and proteins assemble into filamentous aggregates to form nanofibrils, nanotubes and such ordered nanostructures [1–3]. Of special interest are the peptides giving rise to fibrillar plaque-like aggregates which are histopathological hallmarks of serious diseases such as Alzheimers disease, type II diabetes and prion diseases [4, 5]. The Alzheimers amyloid β-peptide (Aβ) structural motif, diphenylalanine (DPA), has been used as a model peptide to study the aggregation process to form fibrils and nanotubular structures [6]. Thermal, electrical and mechanical properties of the aggregated nanofibrils of DPA have been investigated [5, 7]. DPA as well as insulin and other proteins are also known to form aggregated structures at the organic-aqueous interface [8, 9]. Curcumin and certain other molecules as well as metal ions such as Cu^{2+} and Zn^{2+} are reported to affect the formation of fibrils by Aβ [10, 11]. It is believed that curcumin binds to Aβ and blocks its assembly [12]. Hafner-Bratkovic *et al.* [13] suggest the mechanism of inhibition of amyloid aggregation of Creutzfeld-Jakob disease prion protein by curcumin to proceed through binding of curcumin to the α-helical intermediate. Cu^{2+} ions have been shown to reduce fibrillar aggregation [14]. Reduction in the Aβ burden due to elevated Cu level appears to be connected to the stabilization of brain superoxidedismutase activity or increase in α-secretase mediated cleavage (that result in non-amyloidogenic aggregation) of amyloid precursor protein [15]. Zn^{2+} ions are also reported to bind to the Aβ peptide and inhibit amyloid production via inhibition of β-secretase mediated cleavage (that result in amyloidogenic aggregation) of amyloid precursor protein causing clinically beneficial effects [16]. There are also a few studies reporting an unfavourable effect of these two metal ions resulting in Aβ precipitation and aggregate formation [17]. But to date, there is no clear evidence

to show that supplementation of copper or zinc ions is detrimental or clinically beneficial in the progression of Alzhiemers disease.

7.2 Scope of the present investigations

In order to understand the formation and disintegration of peptide fibrils in biological situations, we have investigated the formation of nanofibrillar aggregates formed by the Aβ-peptide structural motif DPA at the organic-aqueous interface. The effect of curcumin on the formation of the aggregates has bee also investigated by dissolving it in the toluene medium. The interface provides a model comparable to the biological membrane. The effect of Cu^{2+} and Zn^{2+} ions on the formation of the peptide aggregates have been also studied. Present study provides direct electron microscopic evidence for the disintegration of DPA fibrillar aggregates by curcumin and Cu^{2+}/Zn^{2+}. We have corroborated these results by fluorescence and circular dichroism studies and extended the study to the formation of aggregates by insulin and BSA.

7.3 Experimental section

2 mL of 16 mM diphenylalanine (NH_2-L-Phe-L-Phe-COOH; Bachem, Switzerland) in water was taken in a 5 mL sealed beaker to which 2 mL of toluene was added. The dissolution was carried out under sonication followed by heating at 90 °C. The white film formed at the interface was lifted onto a Si (111) substrate after different intervals of time (10, 30, 50, 90, 120 and 150 min) for characterization. 2 mL of different concentrations (1 μM, 100 μM and 6.4 mM) of curcumin in toluene was added to the DPA solution in water keeping the other parameters

the same. DPA fibrils formed at the interface after 10, 30, 50, 90, 120 and 150 min were characterized. The fibrils were also dried, re-dissolved in ethanol with and without one molar equivalent of curcumin and the solutions drop-casted on Si substrates. 6.4 mM $CuCl_2$ or $ZnCl_2$ were taken in the aqueous layer keeping all other parameters constant. The time durations used were 30, 50, 90, 150, 210 min and 16h. Experiments with Cu^{2+} and Zn^{2+} were carried out at room temperature and 90 °C respectively.

To 2 mL of 0.3 mM aqueous solution of bovine serum albumin (Sigma-Aldrich, India) 2 mL of toluene was added. The film formed at the interface after 2 days. 2 mL of 0.1 mM of curcumin in toluene was taken as the organic layer keeping all the other parameters same. In separate experiments, 2 mL of 0.075 mM of $CuCl_2$ or $ZnCl_2$ was taken as the aqueous layer keeping all other parameters the same.

To 2 mL of 1.7 mM aqueous solution (pH 2) of bovine pancreas insulin (Sigma-Aldrich, India) 2 mL of toluene was added and was kept at 40 °C. After 3 days, a thin film was formed at the interface. 2 mL of 0.1 mM of curcumin in toluene was taken as the organic layer keeping all other conditions the same. In separate experiments, 2 mL of 0.64 mM of $CuCl_2$ and $ZnCl_2$ was taken as the aqueous layer keeping all other parameters the same.

Scanning electron microscope (SEM) images of the samples were recorded using a LEICA S440i scanning electron microscope. Field emission scanning electron microscope (FESEM) images were recorded with a FEI NOVA NANOSEM-600. For circular dichroism measurements, 0.32 mM of preformed rods of DPA were taken in ethanol in a 2 mm cuvette and increasing concentrations of $CuCl_2$ or $ZnCl_2$ were added and mixed. CD spectra were recorded with a JASCO (J 810) CD spectrometer to monitor the effect on the secondary structure of DPA rods.

7.4 Results and discussion

Gazit and co-workers [18, 19] have investigated the formation of self-assembled nanostructures of the aromatic dipeptide DPA under various conditions of dissolution, deposition on solid surfaces and vapour deposition yielding forests of nanotubes and nanorods, several micrometers in length and 50 to 300 nm in diameter. Yang *et al.* [11] and Gunnar *et al.* [20, 21] have studied the formation of amyloid (Aβ) fibrils by electron microscopy and atomic force microscopy (AFM) and found to have fibrils of several micrometers in length and less than 10 nm in diameter. The images of typical fibrillar structures are shown in Figure 7.1. Biswas and Rao

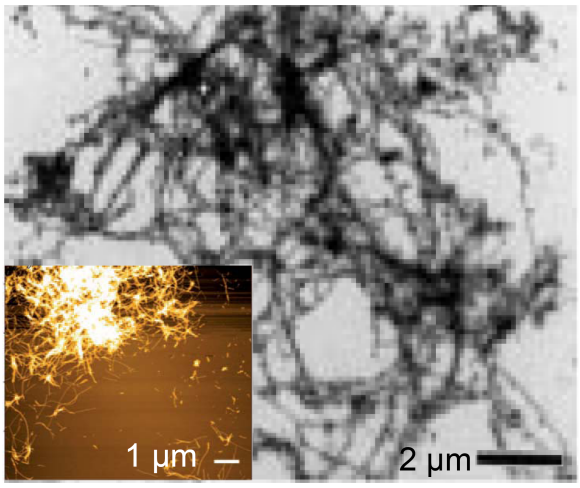

Figure 7.1: (a) Electron microscopic image of the fibrillar structures formed by Aβ40 peptide (under biological condition) [Ref. [11]]. Inset shows an AFM image [Ref. [20]].

[8] have reported the formation of longer (80-100 μm) and thicker (1-1.2μm) 1D DPA fibrils at the toluene-water interface at room temperature. Figure 7.2 shows typical scanning electron microscope (SEM) images of the 1D nanostructures of DPA obtained at the toluene-water interface after 10, 50 and 150 minutes of the aggregation process. DPA forms fairly dense, long micrometer sized entangled fib-

rillar aggregates even within 10 minutes indicating a fast kinetics of the process. Figure 7.2(d) represents the distribution profile of the diameter of the DPA fibrils formed at the interface after 50 minutes. The fibril diameter varies in the range 1-5 μm.

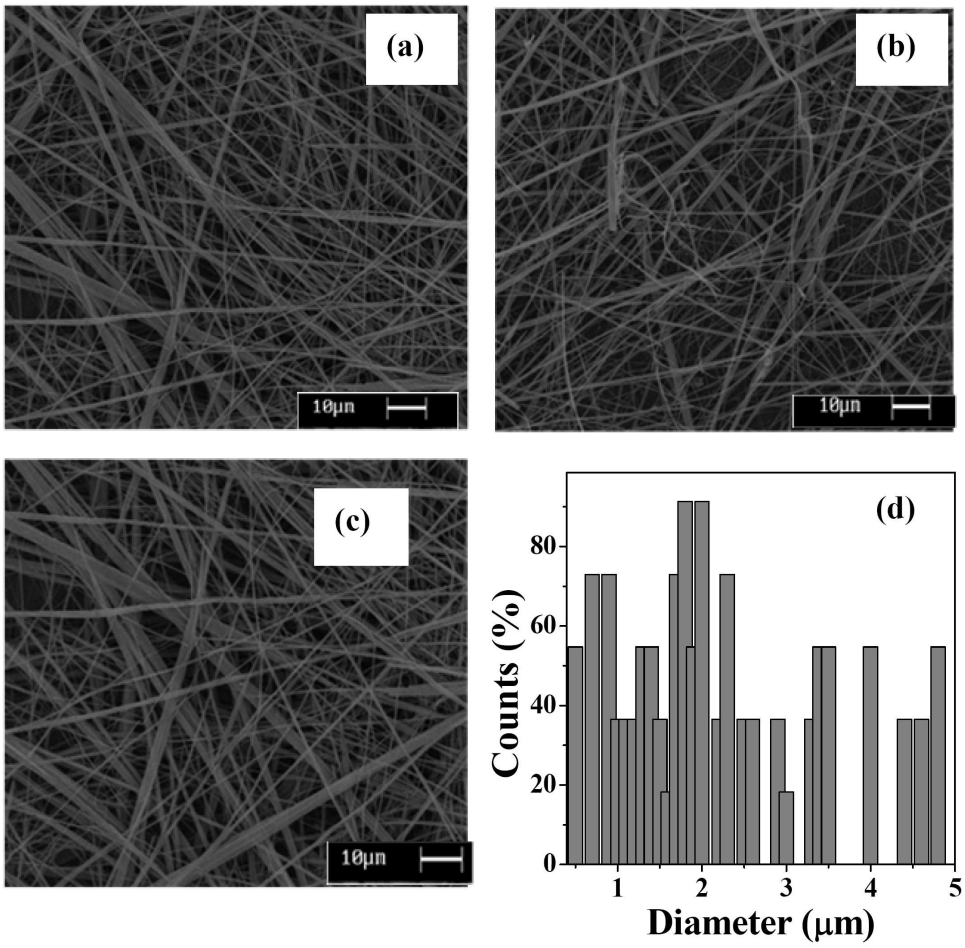

Figure 7.2: SEM image of DPA 1D fibrils obtained at the toluene-water interface after (a) 10 min (b) 50 min and (c) 150 minutes of the aggregation process (d) Distribution profile of the fibril diameter. (Starting concentration of diphenylalanine = 16 mM)

We have carried out an extensive study on the effect of curcumin on DPA fibrils as a function of time as well as curcumin concentration. Figure 7.3 (a) shows the effect of 1μM curcumin on the formation of fibril aggregates after 210 minutes.

The average length of the rods is reduced from 80-100 μm to 0.5-9 μm. At higher concentrations of curcumin the effect is even more remarkable as can be seen from Figure 7.3 (b), where fibril bundles no longer exist. Instead, fragmented flake like structures are observed at 6.4 mM of curcumin within 10 minutes of the reaction. We show the effect of an intermediate concentration of curcumin (0.1 mM) on DPA aggregates in Figure 7.3 (c) and (d) to demonstrate the disintegration of densely aggregated fibrils to form net like structures and shortening of rods even after 10 and 50 minutes. We have also examined the time-dependent evolution of fragmented flake like structures of DPA fibrils in the presence of a higher concentration (6.4 mM) of curcumin.

In order to understand the effect of curcumin on the DPA fibrils, we incubated 1:1 molar equivalent of curcumin with 1μM of preformed DPA rods for 1h. Upon drop casting, only DPA gave the intact rods while the curcumin-DPA rod solution showed the complete absence of fibrillar features as shown in Figure 7.4. Based on these results we conclude that curcumin not only inhibits the aggregation of Aβ peptide structutal motif DPA but also destroys and facilitates the dissolution of the fibrillar structures after its formation. These results are in accord with the effect of phenolic oxime oligomers and multimeric quinacrine conjugates on the Aβ aggregation as shown by Yang *et al.* [11] and Gunnar *et al.* [20, 21].

We examined the effect of Cu^{2+} on the formation of DPA aggregates at the toluene-water interface and found similar fragmented structures when sufficient concentration (6.4 mM) of Cu^{2+} ions was added to the aqueous medium (molar ratio of DPA:Cu^{2+} = 1:0.4). Figure 7.5 (a) and (b) show SEM images of the DPA film formed at the interface after 30 and 50 minutes in the presence of Cu^{2+}. The film has broken rods unlike in the case of DPA alone, the average lengths of the rods being reduced to as low as 1 μm. Similar results were observed when Zn^{2+}

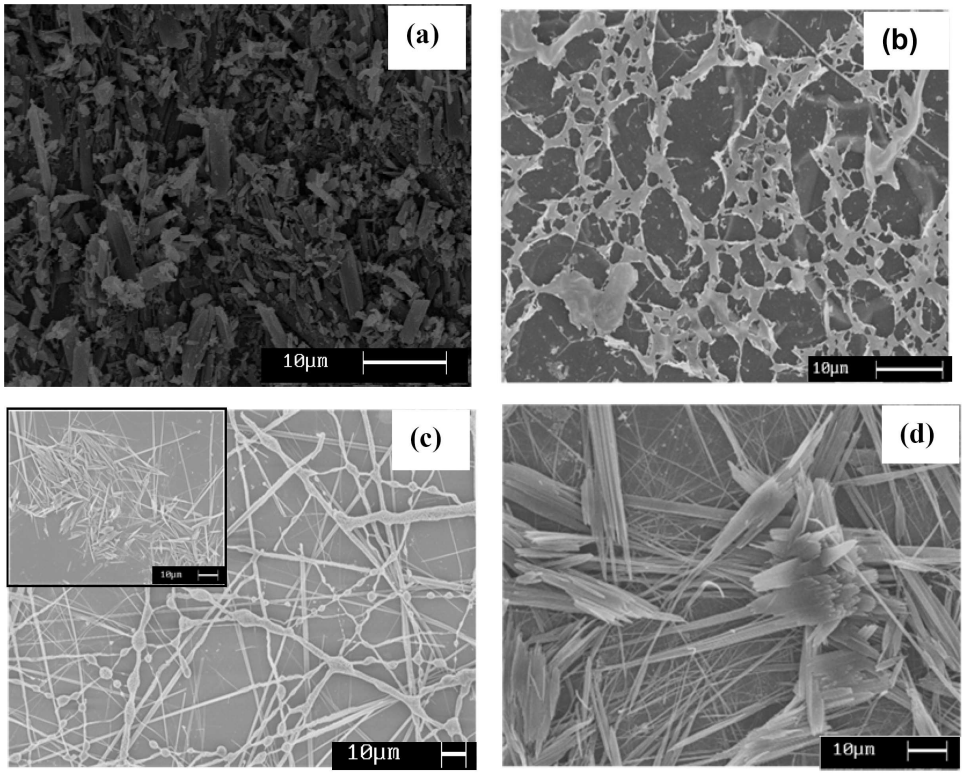

Figure 7.3: SEM image of DPA 1D fibrils obtained at the toluene-water interface at different times after addition of (a) 1 M curcumin (after 210 min), (b) 6.4 mM curcumin (after 30 min), (c) 100 M curcumin (after 10 min) and (d) 100 M curcumin (after 50 min). Inset in (c) is a different section of the same sample (Starting concentration of diphenylalanine = 16 mM).

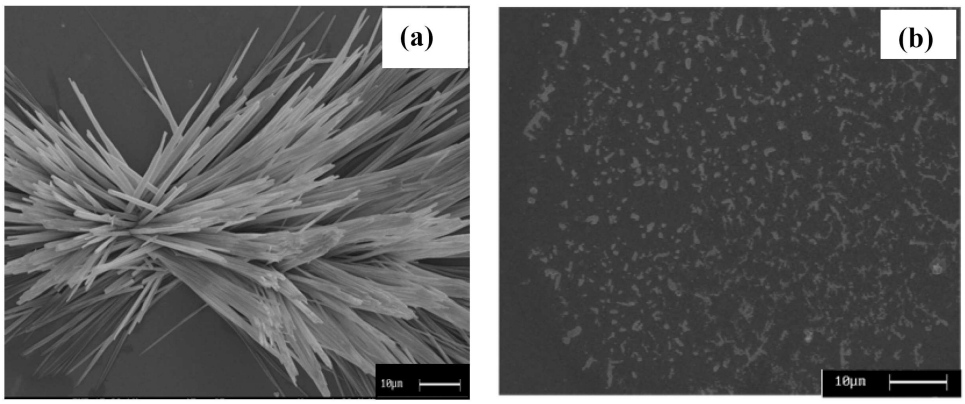

Figure 7.4: SEM image of preformed DPA rods drop-casted on Si substrate (a) before and (b) after 1 h incubation with 1:1 molar equivalent curcumin.

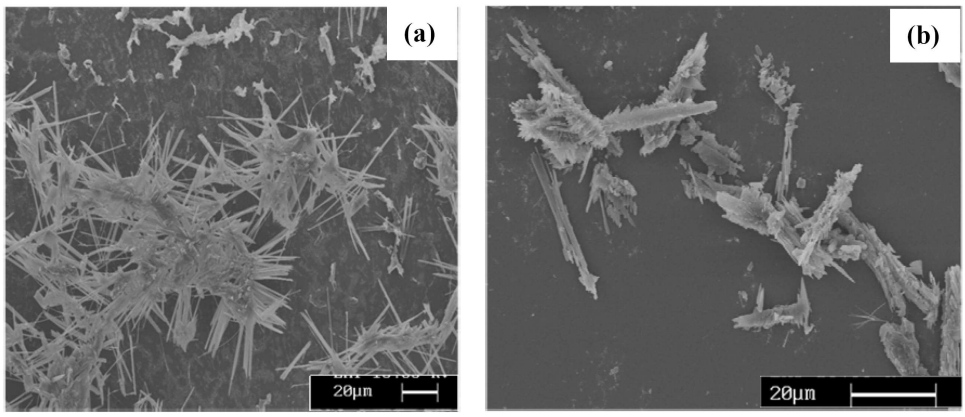

Figure 7.5: SEM image of broken rods of DPA obtained at the toluene-water interface upon addition of 6.4 mM $CuCl_2S$ (a) after 30 min and (b) after 50 min. (Starting concentration of diphenylalanine = 16 mM)

was added to the aqueous medium as shown in Figure 7.6 (a) and (b), and we also noticed the formation of broken tubular structures in the presence of Zn^{2+}. Tubular structure of DPA assembly are reported by Kim *et al.* [22] wherein DPA nanowire morphology can be altered reversibly between nanorods and nanotubes by changing the ionic strength of the solution.

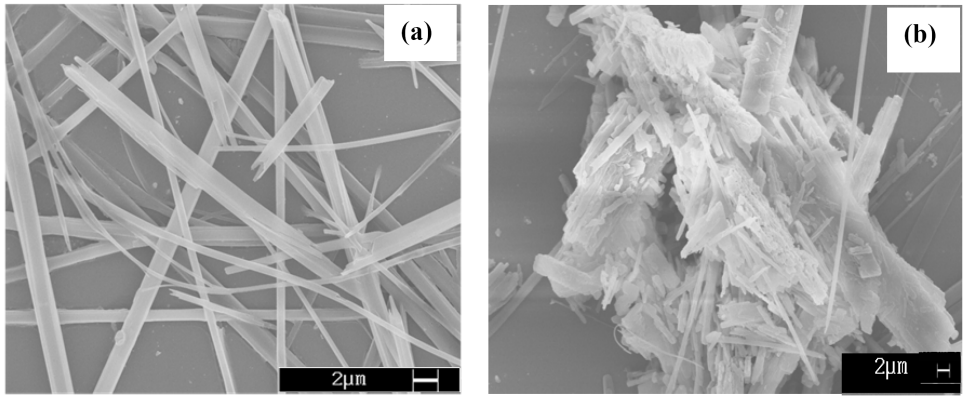

Figure 7.6: SEM image of broken rods of DPA obtained at the toluene-water interface upon addition of 6.4 mM $ZnCl_2S$ (a) after 10 min and (b) after 30 min. (Starting concentration of diphenylalanine = 16 mM)

There are conflicting reports in the literature on the effect of Cu^{2+} and/or Zn^{2+}

on the aggregation behaviour of Aβ peptide [16, 17]. Transmission electron microscopy studies of Kar and Szalai [23] showed that addition of Cu(II) caused some association of Aβ fibrils whereas Perrone *et al.* [24] have shown reduction in Aβ aggregation by transfer of copper from Aβ to human serum albumin. Several other groups have also reported nonfibrillar aggregates at high copper to Aβ ratio [25]. Our study however, shows the breaking down of DPA rods at 0.4 molar equivalents of Cu^{2+} or Zn^{2+} and within a short time of 30 minutes at room temperature. Very short fragments are obtained when the reaction time is increased. After long periods ($\approx$ 16 h), both Cu^{2+} and Zn^{2+} gave rise to broken rods as shown in Figure 7.7. Co-crystallization of curcumin and DPA solutions at 4 °C also yields broken DPA rods.

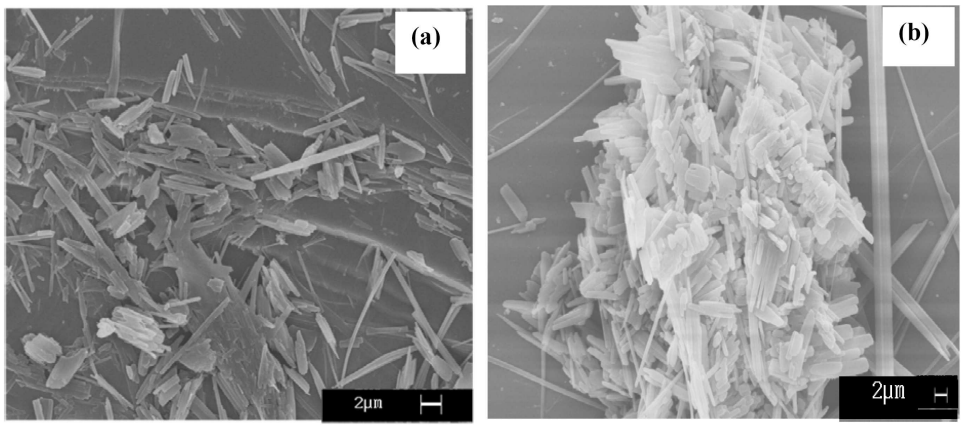

Figure 7.7: SEM image of broken rods of DPA obtained at the toluene-water interface 16 h after addition of (a) 6.4 mM $ZnCl_2$ and (b) 6.4 mM $CuCl_2$.

We have followed the interaction of DPA nanostructures with Cu^{2+} and Zn^{2+} by circular dichroism (CD) experiments using the CD band at 215 nm which is a signature of secondary structure of DPA nanorods [7]. In the presence of high concentrations of these ions (> 1mM), the intensity of the 215nm band decreases significantly indicating conformational changes in the secondary structure of DPA nanostructures.

We have extended our study of the effect of curcumin as well as Cu^{2+} and Zn^{2+} ions on the aggregated structures formed by insulin and BSA. BSA self assembles at a high concentration of 300 μM forming dense layers with globular features as well as elliptical rodlet like structures as shown in Figure 7.7 (a). These structures do not occur in the presence of curcumin or Zn^{2+} ions as can be seen in Figures 7.8 (b) and (c).

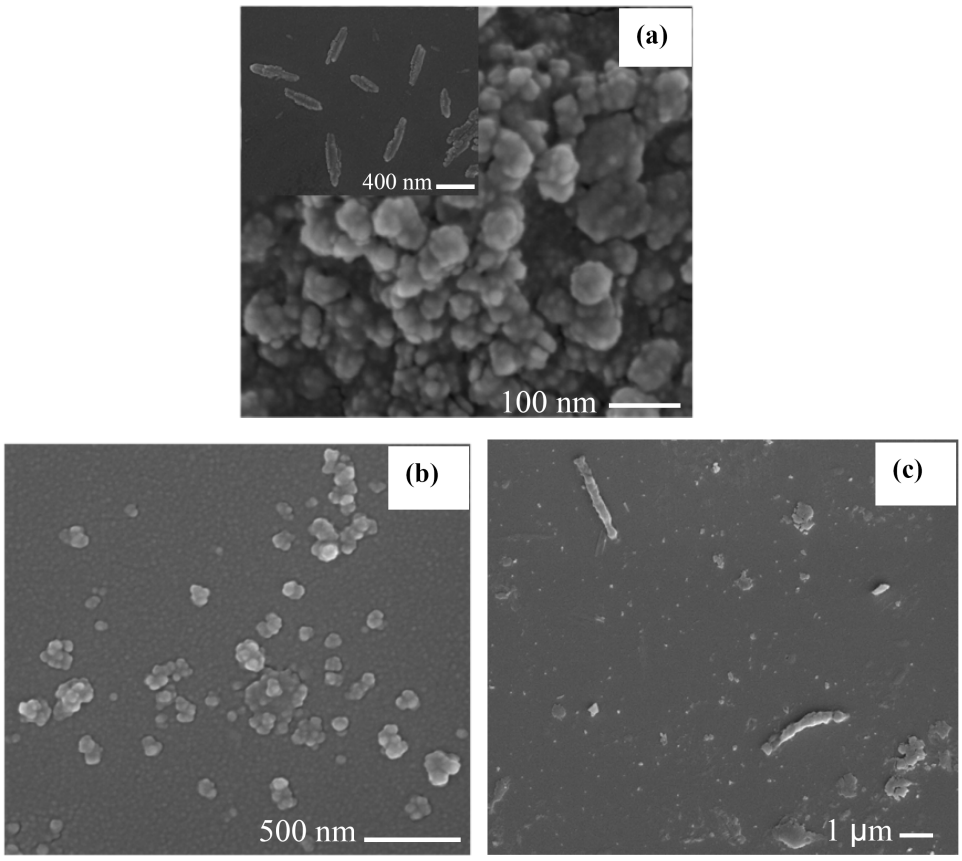

Figure 7.8: FESEM image of Bovine Serum Albumin (BSA, 0.3 mM) assembly obtained at the toluene-water interface after 2 days of the aggregation process: (a) BSA only, (b) after addition of 0.1 mM curcumin and (c) of 0.075 mM $ZnCl_2$. Inset in (a) shows elliptical rodlet structures found in few places of the sample.

Insulin forms a film comprising densely packed interconnected smaller fibril type features at the toluene-water interface as shown in Figure 7.9. Curcumin is reported to have beneficial effect on hyperglycemia and type II diabetes mellitus

by attenuating the effect of insulin [26]. Similarly, stimulatory effect of copper has been implicated in increasing glucose incorporation into the adipose tissue. Zinc-insulin interaction in pancreatic B-cell is known in the literature [27, 28]. We found that the densely packed fibrillar structure of insulin is disrupted in the presence of curcumin giving rise to a widely spaced open structure. Cu^{2+} ions did not show any distinct effect on insulin aggregation. Zinc ions, however, gave rise to spherical and small cylindrical capsule-like structures as shown in Figure 7.9.

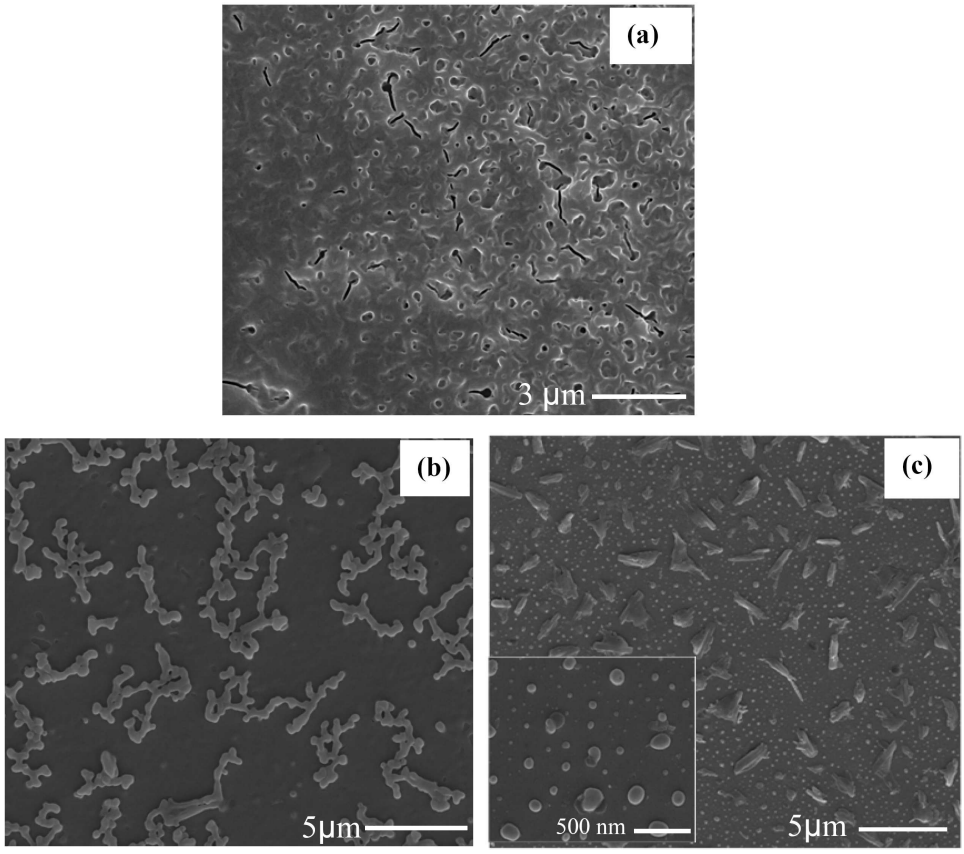

Figure 7.9: Bovine Pancreas Insulin (insulin, 1.7mM) assembly obtained at the toluene-water interface after 3 days of the aggregation process at 40 °C: (a) insulin only, (b) after the addition of 0.1 mM curcumin and (c) 0.64 mM of $ZnCl_2$. Inset in (f) is the high magnification image.

The formation of completely different Zn^{2+}-insulin structures unlike the entangled fibrillar structures formed by insulin could be due to the formation of the

hexamer by Zn^{2+} leading to the precipitation of insulin [28, 29].

7.5 Conclusions

The formation of fibrillar aggregates of Aβ structural motif dephenylalanine including nanorod bundles and other structures at the organic-aqueous interface has been investigated. Our SEM study provides direct evidence of the breakdown of fibrillar aggregates of diphenylalanine, BSA and insulin formed at the organic-aqueous interface in the presence of curcumin, Cu^{2+} and Zn^{2+}. This observation may have implications in understanding Alzheimers disease and type II diabetes mellitus.

References

[1] E Gazit. Self assembly of short aromatic peptides into amyloid fibrils and related nanostructures. *Prion*, 1(1):32–35, 2007.

[2] J. D. Hartgerink, J. R. Granja, R. A. Milligan, and M. R. Ghadiri. Self-assembling peptide nanotubes. *J. Am. Chem. Soc.*, 118(1):43–50, 1996.

[3] S. Vauthey, S. Santoso, H. Gong, N. Watson, and S. Zhang. Molecular self-assembly of surfactant-like peptides to form nanotubes and nanovesicles. *Proc. Natl. Acad. Sci. USA*, 99(8):5355–5360, 2002.

[4] A. Rauk. The chemistry of Alzheimer's disease. *Chem. Soc. Rev.*, 38:2698–2715, 2009.

[5] J.F. Smith, T.P.J. Knowles, C.M. Dobson, C.E. MacPhee, and M.E. Welland. Characterization of the nanoscale properties of individual amyloid fibrils. *Proc. Natl. Acad. Sci. USA*, 103(43):15806–15811, 2006.

[6] C. H. Gorbitz. The structure of nanotubes formed by diphenylalanine, the core recognition motif of Alzheimer's β-amyloid polypeptide. *Chem. Commun.*, pages 2332–2334, 2006.

[7] L. Adler-Abramovich, M. Reches, V. L. Sedman, S. Allen, S. J. B. Tendler, and E. Gazit. Thermal and chemical stability of diphenylalanine peptide nanotubes: implications for nanotechnological applications. *Langmuir*, 22(3):1313–1320, 2006.

[8] K. Biswas and C. N. R. Rao. Nanostructured peptide fibrils formed at the organic-aqueous interface and their use as templates to prepare inorganic nanostructures. *ACS Appl. Mater. Interfaces*, 1(4):811–815, 2009.

[9] C. N. R. Rao and K. P. Kalyanikutty. The liquid-liquid interface as a medium to generate nanocrystalline films of inorganic materials. *Acc. Chem. Res.*, 41(4):489–499, 2008.

[10] F. Peter. Copper and zinc binding to amyloid-β: Coordination, dynamics, aggregation, reactivity and metal-ion transfer. *ChemBioChem*, 10(18):2837–2845, 2009.

[11] F. Yang, G. P. Lim, A. N. Begum, O. J. Ubeda, M. R. Simmons, S. S. Ambegaokar, P. P. Chen, R. Kayed, C. G. Glabe, S. A. Frautschy, and G. M. Cole. Curcumin inhibits formation of amyloid β oligomers and fibrils, binds plaques, and reduces amyloid in vivo. *J. Biol. Chem.*, 280:5892–5901, 2005.

[12] A.R. Ashley and E.G. Jason. Structure-activity relationships of amyloid beta-aggregation inhibitors based on curcumin: Influence of linker length and flexibility. *Chem. Biol. Drug Des.*, 70(3):206–215, 2007.

[13] I. Hafner-Bratkovi, J. Gaperi, L. M. mid, M. Bresjanac, and R. Jerala. Curcumin binds to the α-helical intermediate and to the amyloid form of prion protein a new mechanism for the inhibition of prp^{Sc} accumulation. *J. Neurochem.*, 104(6):1553–1564, 2008.

[14] C. Treiber, M. A. Quadir, P. Voigt, M. Radowski, S. Xu, L. Munter, T. A. Bayer, M.l Schaefer, R. Haag, and G. Multhaup. Cellular copper import by nanocarrier systems, intracellular availability, and effects on amyloid β peptide secretion. *Biochemistry*, 48(20):4273–4284, 2009.

[15] A. L. Phinney, B. Drisaldi, S. D. Schmidt, S. Lugowski, V. Coronado, Y. Liang, P. Horne, J. Yang, J. Sekoulidis, J. Coomaraswamy, M. A. Chishti, D.W. Cox, P. M. Mathews, R. A. Nixon, G. A. Carlson, P. S. George-Hyslop, and

D. Westaway. In vivo reduction of amyloid-β by a mutant copper transporter. *Proc. Natl. Acad. Sci. USA*, 100(21):14193–14198, 2003.

[16] J. Lee, C.H. Kim, D.G. Kim, and Y.S. Ahn. Zinc inhibits amyloid β production from Alzheimer's amyloid precursor protein in SH-SY5Y cells. *Korean J Physiol. Pharmacol.*, 13(3):195–200, 2009.

[17] M. P. Cuajungco, L. E. Goldstein, A. Nunomura, M. A. Smith, J. T. Lim, C. S. Atwood, X. Huang, Y. W. Farrag, G. Perry, and A. I. Bush. Evidence that the β-amyloid plaques of Alzheimer's disease represent the redox-silencing and entombment of Aβ by zinc. *J. Biol. Chem.*, 275:19439–19442, 2000.

[18] L. Adler-Abramovich, D. Aronov, P. Beker, M. Yevnin, S. Stempler, L. Buzhansky, G. Rosenman, and E. Gazit. Self-assembled arrays of peptide nanotubes by vapour deposition. *Nat. Nanotechnol.*, 4(12):849 – 854, 2009.

[19] M. Reches and E. Gazit. Controlled patterning of aligned self-assembled peptide nanotubes. *Nat. Nanotechnol.*, 1(3):195–200, 2006.

[20] T. D. Gunnar, R. Olivier, O. Myriam, D. Pascal, G. Julian, and R. Jean-Louis. Phenolic oxime oligomers inhibit Alzheimer's amyloid fibril formation and disaggregate fibrils in vitro. *ChemBioChem*, 10(8):1325–1329, 2009.

[21] T. D. Gunnar, C. Sabine, O. Myriam, D. Pascal, and G. Julian. A multimeric quinacrine conjugate as a potential inhibitor of Alzheimer's β-amyloid fibril formation. *ChemBioChem*, 9(6):952–963, 2008.

[22] J.Kim, H. Tae Hee, K. Yong-I, P. Ji Sun, C. Jungkweon, G. C. David, K. Sang Ouk, and I. Hyotcherl. Role of water in directing diphenylalanine assembly into nanotubes and nanowires. *Adv. Mater.*, 22(5):583–587, 2010.

[23] J. W. Karr and V. A. Szalai. Cu(II) binding to monomeric, oligomeric, and fibrillar forms of the Alzheimers disease amyloid-β peptide. *Biochemistry*, 47(17):5006–5016, 2008.

[24] L.Perrone, E. Mothes, M. Vignes, A. Mockel, C. Figuero, M. Miquel, M. Maddelein, and P. Faller. Copper transfer from Cu-Aβ to human serum albumin inhibits aggregation, radical production and reduces Aβ toxicity. *ChemBioChem*, 11(1):110–118, 2010.

[25] D. P. Smith, G. D. Ciccotosto, D. J. Tew, M. T. Fodero-Tavoletti, T. Johanssen, C. L. Masters, K. J. Barnham, and R. Cappai. Concentration dependent Cu^{2+} induced aggregation and dityrosine formation of the Alzheimer's disease amyloid-β peptide. *Biochemistry*, 46(10):2881–2891, 2007.

[26] J. Eun-Mi, C. Myung-Sook, J. Un Ju, K. Myung-Joo, K. Hye-Jin, J. Seon-Min, S. Su-Kyung, S. Chi-Nam, and L. Mi-Kyung. Beneficial effects of curcumin on hyperlipidemia and insulin resistance in high-fatfed hamsters. *Metab., Clin. Exp.*, 57(11):1576–1583, 2008.

[27] A. Cohen, E. Miller, and Z. Madar. Is copper effect on glucose incorporation mediated by the insulin receptor in rat adipose tissue? *Acta Diabetol.*, 22(1):47–54, 1985.

[28] S.O. Emdin, G.G. Dodson, J.M. Cutfield, and S.M. Cutfield. Role of zinc in insulin biosynthesis. *Diabetologia*, 19(3):174–182, 1980.

[29] G. Dodson and D. Steiner. The role of assembly in insulin's biosynthesis. *Curr. Opin. Struct. Biol.*, 8(2):189 – 194, 1998.